



Title	Physically-motivated feedback models and the IGM metal enrichment in cosmological hydrodynamic simulations
Author(s)	奥, 裕理
Citation	大阪大学, 2024, 博士論文
Version Type	VoR
URL	https://doi.org/10.18910/96417
rights	
Note	

The University of Osaka Institutional Knowledge Archive : OUKA

<https://ir.library.osaka-u.ac.jp/>

The University of Osaka



大阪大学
OSAKA UNIVERSITY

Physically-motivated feedback models and the IGM metal enrichment in cosmological hydrodynamic simulations

by

Yuri Oku

A thesis submitted in partial fulfillment for the
degree of Doctor of Philosophy

in the
Department of Earth and Space Science
Graduate School of Science
Osaka University

February 2024

Abstract

The elucidation of the structure formation history of the Universe is a major goal in both astrophysics and cosmology, and understanding the formation processes of galaxies, the building blocks of the cosmic large-scale structure, is a central challenge. Cosmological hydrodynamic simulations are widely used as a tool to provide direct theoretical predictions for this challenge. In galaxy formation in the Λ CDM universe, the standard model of modern cosmology, both observation and theory suggest that feedback from astronomical phenomena such as supernovae (SNe) and active galactic nuclei (AGN) is essential. However, dealing directly with pc-scale astrophysical effects in cosmological simulations with computational domains exceeding Mpc is computationally infeasible, and it is necessary to introduce a subgrid model of feedback effects.

Models of feedback are the largest source of uncertainty in cosmological hydrodynamic simulations, and many previous studies have used phenomenological models fine-tuned to reproduce galaxy observations. However, it has recently been pointed out that even models that reproduce galaxy observations fail to reproduce observations of the circumgalactic medium. Models based on pc-scale physics are needed for a comprehensive understanding of galaxy formation and for theoretical predictions for future high-sensitivity observations.

In this study, we develop a physically-motivated SN feedback model based on high-resolution simulations that resolve the pc scale. Considering the physical effects of the SN feedback and numerical constraints, the model incorporates both the mechanical effects of the feedback on the interstellar gas and the effects of the galactic wind on the circumgalactic medium. We then implement this model in the cosmological hydrodynamic simulation code `GADGET4-OSAKA`. We also implement a model of the formation and growth of supermassive black holes, which cause feedback as AGNs, and a chemical evolution model accounting for the metallicity dependence of the initial stellar mass function. We show that this simulation, named `CROCODILE`, generally reproduces observational statistics such as the galaxy mass function.

We analyze the `CROCODILE` dataset to investigate the impact of SN and AGN feedback on metal enrichment in the intergalactic medium. The results show that SN feedback plays a major role in metal enrichment. Additionally, the AGN feedback affects the metal distribution below redshift two and creates characteristic metal enrichment regions on the scale of a few Mpc.

Acknowledgements

I am deeply grateful to Prof. Kentaro Nagamine for his continuous and generous support and encouragement. I am also grateful to the members of my thesis committee, Hironori Matsumoto, Yoshiyuki Inoue, Yoichi Sakawa, and Kento Masuda, for carefully reading this thesis and encouraging my graduation. I would like to express my gratitude to Professors Kengo Tomida, Renyue Cen, and Ikkoh Shimizu for the fruitful discussion we had during our collaboration. I would like to thank Professors Yutaka Fujita, Shinsuke Takasao, and Daisuke Toyouchi for their advice and encouragement in seminars and daily conversations. I also would like to thank postdocs Kei Tanaka, Masato Kobayashi, Pierre Marchand, Jackson Norris, Tomonari Michiyama, Elis Owen, Samuel Barnier, Sdiputa Hensh, and Haruka Washinoue for their guidance and warm encouragement. My thanks also go to Shohei Arata for being my model as a senior Ph.D. student. It was fortunate and was my true pleasure to have shared the days of graduate school with Abednego Wiliardy, Nicolas Ledos, Keita Fukushima, and other students in the theoretical astrophysics group. I would like to thank Secretaries Ms. Mariko Tokiwa and Ms. Hiroko Joh for their support in my research life. I would also like to thank my previous college supervisor, Atsushi Ikeda, for his encouragement. He opened my eyes to research and invited me to the world of numerical simulation.

I am most grateful to my parents, Masato Oku and Kayo Muto, for their warm and continuous support. My graduate school days are not just a time for research but also for looking back and forward at who I am and who I will be. During the hard times, I realized I am always supported by them. Special thanks go to Midori Yokoyama for saving me from those hard times and encouraging me.

I acknowledge the developers of the software used in this work, ATHENA++ ([Stone et al., 2020](#)), CELIB ([Saitoh, 2017](#)), CLASS ([Blas et al., 2011](#)), CLOUDY ([Ferland et al., 2013](#)), GADGET-3,4 ([Springel, 2005](#), [Springel et al., 2021](#)), GRACKLE ([Smith et al., 2017](#)), MUSIC ([Hahn and Abel, 2011](#)), MUSIC2-MONOFONIC ([Michaux et al., 2021](#), [Hahn et al., 2021](#)), NBODYKIT ([Hand et al., 2018](#)), STARBURST99 ([Leitherer et al., 1999](#), [Vázquez and Leitherer, 2005](#), [Leitherer et al., 2010, 2014](#)), STRIPACK ([Renka, 1997](#)), and WVTICS ([Donnert et al., 2017](#), [Arth et al., 2019](#)). I am grateful to Leonard Romano for providing his version of GADGET4-OSAKA code ([Romano et al., 2022a,b](#)), on which my version of GADGET4-OSAKA is based. Our numerical simulations and analyses were carried out on the XC50 systems at the Center for Computational Astrophysics (CfCA) of the National Astronomical Observatory of Japan (NAOJ) and SQUID at the Cybermedia Center, Osaka University as part of the HPCI System Research Project (hp210090, hp220044, hp230089; PI: Kentaro Nagamine). This work is supported by the JSPS KAKENHI Grant Number 21J20930, 22KJ2072.

Contents

Abstract	i
Acknowledgements	ii
List of Figures	vii
List of Tables	ix
Abbreviations	x
1 Introduction	1
1.1 Structure formation in the Λ CDM universe	1
1.2 Galaxy formation and supernova feedback	3
1.2.1 Observational suggestion	3
1.2.1.1 Galaxy stellar mass function	3
1.2.1.2 Galactic wind	4
1.2.1.3 Superbubble	6
1.2.2 Theoretical suggestion	6
1.2.2.1 Cosmological hydrodynamic simulation	7
1.2.2.2 Small-box high-resolution simulation	9
1.2.3 Challenges and future directions	10
1.3 This thesis	12
2 Supernova feedback model	14
2.1 Necessity of feedback model	14
2.2 Main idea of modeling	16
2.3 Mechanical feedback	17
2.3.1 Averaged momentum per SN for a stellar population	17
2.3.2 Shock radius for a star particle	18
2.3.3 Feedback assignment	19
2.4 Galactic wind feedback	21
2.5 Isolated galaxy simulation with GADGET3-OSAKA	22
2.5.1 Simulation Setup	22
2.5.2 Star formation and Stellar feedback	24
2.5.2.1 Star formation	24

2.5.2.2	Stellar feedback	25
	Type II SN feedback	25
	Type Ia SN feedback	25
	Stellar wind from OB stars	25
	AGB feedback	26
2.5.3	Results from GADGET3-OSAKA simulations	26
2.5.3.1	Projection Maps	28
2.5.3.2	Phase Diagrams	30
2.5.3.3	Star Formation Histories	31
2.5.3.4	Kennicutt–Schmidt Relation	31
2.5.3.5	Outflow Profiles of Mass, Energy, Velocity, and Metals	33
2.5.4	Discussion on the SN feedback model	35
3	Method	39
3.1	Initial Condition	39
3.2	Cosmological Hydrodynamic Simulation	40
3.3	Numerical method	41
3.3.1	SPH	41
3.3.1.1	SIMD Vectorization	43
3.3.1.2	Artificial Conduction	43
3.3.1.3	Field Reconstruction	44
3.3.1.4	Jeans pressure floor	44
3.3.1.5	Time Integration	45
3.3.2	Code validation	47
3.3.2.1	Keplerian Disk	47
3.3.2.2	Sedov Explosion	49
3.3.2.3	Cold Blob	51
3.3.2.4	Zeldovich Pancake	54
3.3.2.5	Galaxy Cluster	55
3.4	Subgrid physics	57
3.4.1	Star Formation	58
3.4.2	Core Collapse Supernova	60
3.4.2.1	Mechanical Feedback Model	62
3.4.2.2	Supernova-driven Galactic Wind Model	62
3.4.3	Type-Ia Supernova	63
3.4.4	AGB Stars	64
3.4.5	Black Hole Physics	64
3.4.5.1	Seeding & Repositioning	64
3.4.5.2	Accretion	64
3.4.5.3	Feedback	66
3.4.5.4	Timestepping	66
3.5	Runs	66
3.6	Data Analysis	68
4	General results	71
4.1	Cosmic star formation rate history	71
4.2	Phase diagram	72

4.3	Galaxy Statistics	73
4.3.1	Feedback Model Variation	74
4.3.2	BH Parameter Variation	79
4.3.3	Resolution Variation	82
4.3.4	SN Feedback Energy Yield Variation	82
5	Metal enrichment in the IGM	84
5.1	Visual inspection	84
5.2	Overdensity–metallicity relation	86
5.3	Metal density power spectrum	86
6	Summary and future prospects	91
A	Evolution of a superbubble in idealized ISM	94
A.1	Analytic theory	94
A.1.1	Shell-formation time	94
A.1.1.1	Single SN	94
A.1.1.2	Multiple SNe	96
A.2	ATHENA++ simulation of superbubbles	97
A.2.1	Numerical Method	97
A.2.2	Results from Athena++ simulations	101
A.2.2.1	Results for $n_{\text{H}} = 1 \text{ cm}^{-3}$, $Z = 1 Z_{\odot}$, $\Delta t_{\text{SN}} = 0.1 \text{ Myr}$	101
A.2.2.2	Results for $\Delta t_{\text{SN}} = 0.01 \text{ Myr}$	101
A.2.2.3	Results for $\Delta t_{\text{SN}} = 0.1 \text{ Myr}$	104
A.2.2.4	Results for $\Delta t_{\text{SN}} = 1 \text{ Myr}$	106
A.2.3	Application to SN feedback model in galaxy simulations	107
B	Implementation of supernova feedback	111
	Bibliography	113

List of Figures

1.1	The linear 3D matter power spectrum at $z = 0$	2
1.2	Comparison of dark matter halo mass function and galaxy stellar mass function	4
1.3	M82 galaxy observed by the Hubble Space Telescope	5
1.4	Composite image of N44 superbubble	7
1.5	Comparing the predicted galaxy stellar mass functions from cosmological simulations	8
1.6	Overview of a high-resolution simulation of a kilo-parsec patch of a galactic disk	9
1.7	Comparing the IGM simulated using different subgrid models	11
2.1	Schematic image of the idea of supernova feedback model	17
2.2	Projected gas density plots of the isolated galaxies	28
2.3	Projected temperature (density-weighted) of the isolated galaxies	29
2.4	Projected metallicity (density-weighted) of the isolated galaxies	29
2.5	Large-scale, edge-on view of metal column density	30
2.6	Phase diagram of the gas in the isolated galaxies	30
2.7	SFR as a function of time for the isolated galaxy simulations	31
2.8	The Kennicutt–Schmidt relation of the simulated galaxies	32
2.9	Mass, energy, and metal loading factors vs. the height above the galactic plane	33
2.10	Same as Figure 2.9 but measured with spheres of different radii up to 200 kpc, centered at the galactic center	36
3.1	Surface density of the simulated Keplerian disk	48
3.2	Density slice through the center of the simulated Sedov blast wave	49
3.3	The results from the Keplerian disk and Sedov blast tests	50
3.4	Density slice through the mid-plane of the cold blob test	52
3.5	Cloud remaining fraction as a function of time in the cold blob test	53
3.6	Density projection of the simulated Zeldovich pancake	55
3.7	Density, temperature, and velocity profiles of the Zeldovich pancake at $z = 0$	56
3.8	Projected density-weighted temperature of the simulated cluster	57
3.9	Radial profiles of density, temperature, entropy, and pressure of the cluster test	58
3.10	Stellar initial mass function and supernova energy yield adopted in this work	61
3.11	Projected image of the Fiducial run	70
4.1	Cosmic star formation rate density of CROCODYLE	72

4.2	Phase diagram of the Fiducial run	73
4.3	Galaxy stellar mass function at $z = 0.1, 1, 2.3, 6$	74
4.4	Redshift evolution of the star formation main sequence of the simulated galaxies	76
4.5	Redshift evolution of the mass–metallicity relation	77
4.6	Redshift evolution of the BH mass–stellar mass relation	78
4.7	Halo baryon fraction, f_{baryon} , normalized by the cosmic mean baryon fraction, $\Omega_{\text{baryon}}/\Omega_{\text{matter}}$, vs. halo mass at $z = 0$	80
4.8	Comparing the $M_{\text{BH}}-M_*$ relation, stellar mass function, and star-formation main sequence for the runs with different BH parameters	81
4.9	Galaxy stellar mass functions of the runs with different resolutions	82
4.10	Galaxy stellar mass function of the L25N256 and L25N256NoZdepSN runs	83
5.1	The density-weighted projection of metallicity	85
5.2	Metallicity as a function of dark matter and gas overdensity at $z = 2.3$	87
5.3	Metallicity as a function of dark matter and gas overdensity at $z = 0$	88
5.4	Power spectra of the metal density field at $z = 2.3$ and 0	89
A.1	Cooling curves used in the superbubble simulations	99
A.2	Slice plot of gas number density and temperature distribution	102
A.3	Phase diagram of gas in a superbubble simulation	103
A.4	Evolution of superbubble as a function of radius	104
A.5	Time evolution of mass, energy, and momentum of the superbubble for SN injection time intervals of $\Delta t_{\text{SN}} = 0.01$ Myr	105
A.6	Same as Figure A.5, but for SN injection time interval $\Delta t_{\text{SN}} = 0.1$ Myr	106
A.7	Same as Figure A.5, but for SN injection time interval $\Delta t_{\text{SN}} = 1$ Myr	107
A.8	Evolution of R_{hot} normalized by $R_{\text{sf,m}}$, versus time normalized by $t_{\text{sf,m}}$	108
A.9	Evolution of momentum p normalized by $p_{\text{sf,m}}$, versus time normalized by $t_{\text{sf,m}}$	108
B.1	Schematic description of the spherical superbubble feedback model	112

List of Tables

2.1	List of isolated galaxy simulations used in this chapter.	27
3.1	Numerical settings of the models used in the test simulations	47
3.2	List of common parameters for subgrid physics	59
3.3	List of cosmological simulations	67
A.1	Initial conditions of the suprebubble simulations.	100

Abbreviations

Λ CDM Λ cold dark matter.

AGB asymptotic giant branch.

AGN active galactic nucleus.

BH black hole.

CCSN core-collapse supernova.

CGM circumgalactic medium.

CIC cloud-in-cell.

CMB cosmic microwave background.

EoS equation of state.

FoF Friend-of-Friends.

HN hypernova.

ICMF initial stellar cluster mass function.

IGM intergalactic medium.

IMF initial mass function.

IR infrared.

ISM interstellar medium.

LMC Large Magellanic Cloud.

LRG luminous red galaxies.

PDS pressure-driven snowplow.

SFR star formation rate.

SN supernova.

SPH smoothed particle hydrodynamics.

sSFR specific star formation rate.

SSP simple stellar population.

UV ultraviolet.

YMC young massive star cluster.

To My Parents

Chapter 1

Introduction

1.1 Structure formation in the Λ CDM universe

Within the Λ cold dark matter (Λ CDM) model, the theory of structure formation in the universe has been extensively developed. The time evolution of the universe is dictated by the Friedmann equation, which is the reduced form of Einstein's equation on the Friedmann–Lemaitre–Robertson–Walker metric, a metric on a homogeneous and isotropic universe,

$$H^2 = \frac{8\pi G}{3c^2}\rho + \frac{\Lambda c^2}{3} - \frac{Kc^2}{a^2}. \quad (1.1)$$

where H is the Hubble parameter, ρ is the energy density of matter, Λ is the cosmological constant, K is the curvature of the universe, and a is the scale factor. The (flat) Λ CDM model is the case where we have non-zero Λ , the matter in the universe is composed of ‘cold’ dark matter, i.e., the kinetic energy of dark matter is much less than the mass energy, and the universe is flat, i.e., $K = 0$.

This model gives robust predictions of the distribution of matter on large scales, where the gravitational influence of dark matter is the major driver of these distributions (e.g., Blumenthal et al., 1984, Davis et al., 1985, Ostriker and Steinhardt, 1995, Perlmutter et al., 1998, Bahcall et al., 1999). Figure 1.1 shows the matter power spectrum at $z = 0$. The data points are inferred from observations on different scales and at different redshifts; the cosmic microwave background (CMB) on scales of $\gtrsim 10$ Mpc at $z \sim 1100$, the luminous red galaxies (LRG) on scales of ~ 10 Mpc at $z \sim 0.35$, the cosmic shear (weak gravitational lensing) on scales of ~ 1 Mpc at $z = 0.2$ -1.3, and the Ly α forest on scales of ~ 1 Mpc at $z = 2.2$ -4.6. Given the cosmological parameters calibrated to the *Planck* CMB observation, the theoretical expectation from Λ CDM model consistently reproduces these observations.

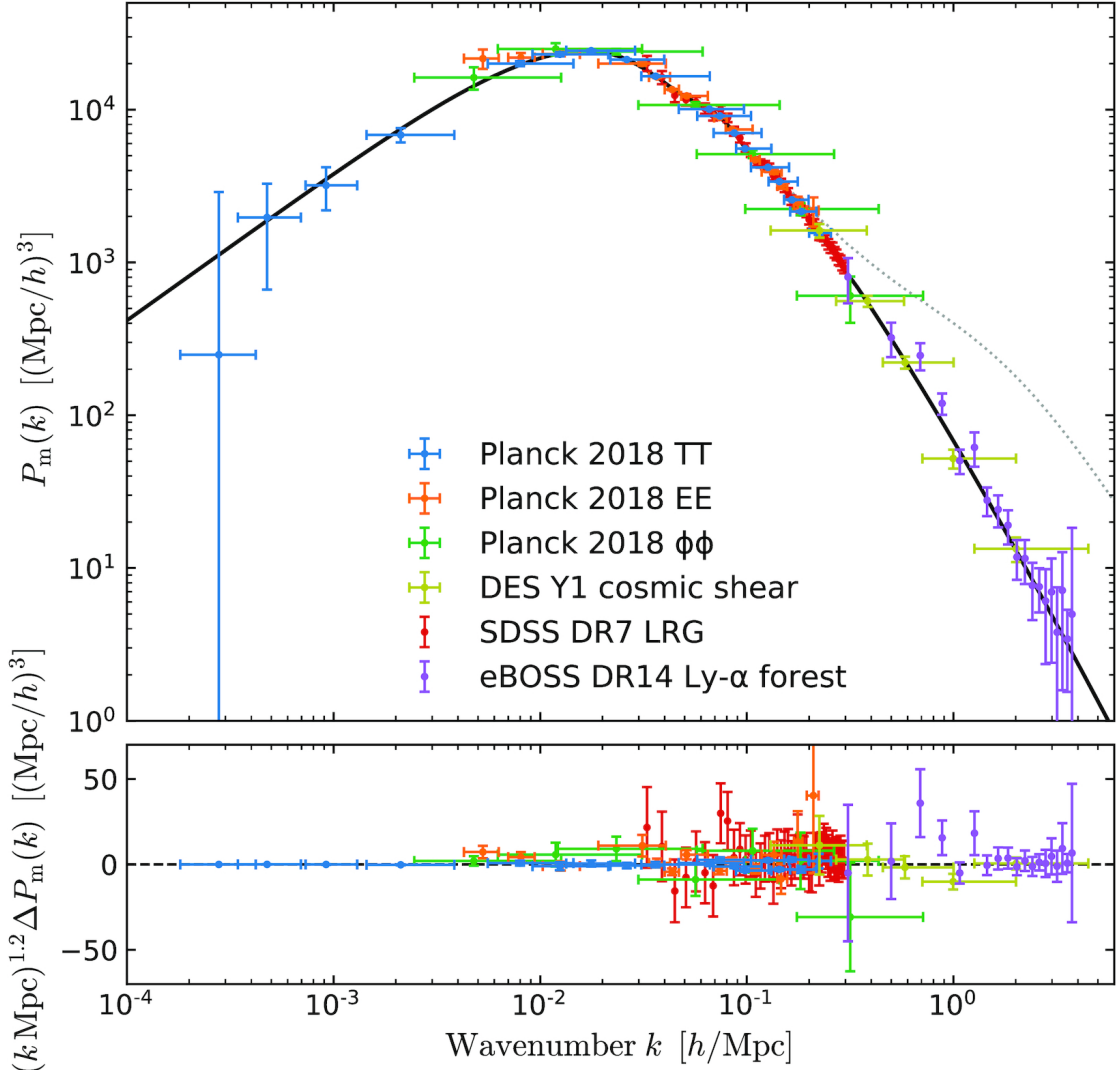


FIGURE 1.1: Top: The linear 3D matter power spectrum at $z = 0$. Data points show inferences of the 3D linear matter power spectrum from *Planck CMB* data on the largest scales (Planck Collaboration et al., 2020), SDSS galaxy clustering (Reid et al., 2010) on intermediate scales, SDSS Ly α clustering (Abolfathi et al., 2018) and DES cosmic shear data (Troxel et al., 2018) on the smallest scales. The solid black line is the theoretical expectation given the best-fitting *Planck 2018 ΛCDM* model. The dotted line for reference shows the theoretical spectrum, including non-linear effects. Bottom: Deviation of the data from the *Planck* best-fitting ΛCDM 3D matter power spectrum.

Reprinted from Figure 1 of Chabrier et al. (2019) with permission.

However, this model faces difficulties at smaller scales. Here the influences of astrophysical and hydrodynamical processes become increasingly important. This adds complexity to our understanding of the distribution of baryonic matter and the evolution and formation of galaxies and black holes throughout cosmic history.

1.2 Galaxy formation and supernova feedback

A [supernova \(SN\)](#) is a massive explosion with a typical energy of 10^{51} erg, but it affects only several tens of parsec of the [interstellar medium \(ISM\)](#), which is three orders of magnitude smaller than the size of a galaxy, e.g., the radius of Milky Way is ~ 10 kpc. [SN](#) is still important as a feedback source due to its collective effect. In our Milky Way Galaxy, the typical number of star formation rate is $1 M_{\odot} \text{yr}^{-1}$, the occurrence rate of [SN](#) per stellar mass is $10^{-2} M_{\odot}^{-1}$, and the rotation time of the galactic disk is 200 Myr. Combining these numbers, we obtain 2×10^6 [SNe](#) per galactic rotation, whose energy is comparable to the gravitational bounding energy of a galaxy. This nature of [SN](#) feedback as a collective effect of numerous [SN](#) explosions and its spatial and temporal scales makes it difficult to obtain direct observational evidence nor perform direct simulations to draw a comprehensive picture of [SN](#) feedback.

In this section, I summarize the observational and theoretical implications of how [SN](#) feedback affects galaxy formation.

1.2.1 Observational suggestion

In this subsection, I describe observations related to [SN](#) feedback, starting from statistics of the stellar mass of galaxies, then the galactic wind of an individual galaxy, and finally, a superbubble formed by [SN](#) explosions.

1.2.1.1 Galaxy stellar mass function

The existence of the astrophysical feedback effect is realized by the fact that star formation is inefficient in galaxies. Figure 1.2 compares the dark matter halo mass function and galaxy stellar mass functions in the nearby universe ($z \sim 0.1$). The dashed black line is the mass function of baryons in dark matter halos. One would expect that the dashed black line corresponds to the galaxy stellar mass function, assuming gas is converted to stars without feedback. However, Figure 1.2 shows that the dashed black line deviates from the observed galaxy stellar mass function, and star formation is more inefficient

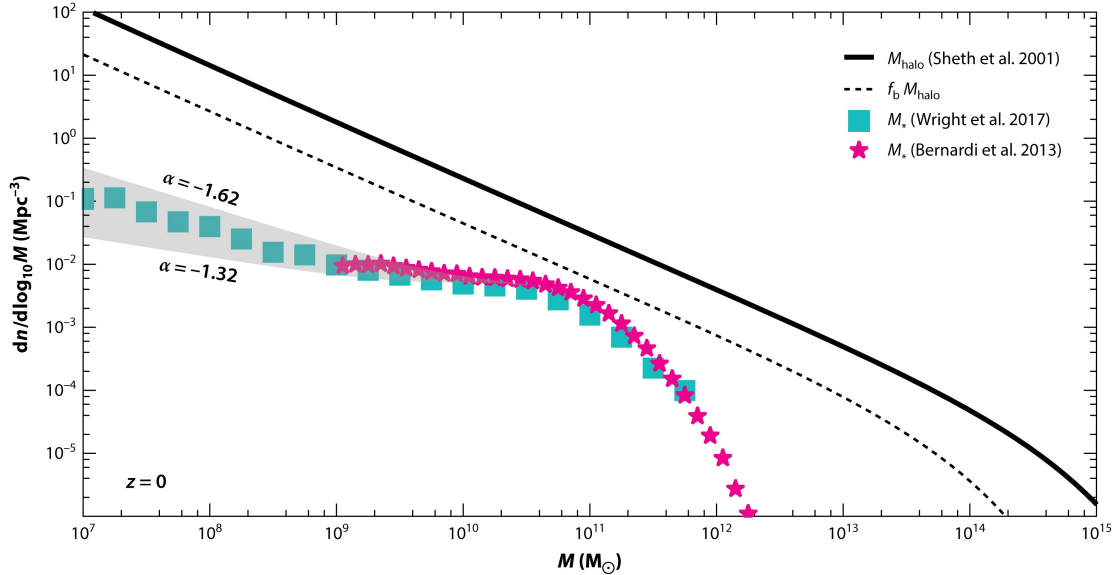


FIGURE 1.2: Comparing the dark matter halo mass function with galaxy stellar mass function. The thick black solid line is a theoretical dark halo mass function by [Sheth et al. \(2001\)](#), and the dashed black line is shifted by the baryon mass fraction. The observed galaxy stellar mass function is from [Bernardi et al. \(2013, magenta star\)](#) and [Wright et al. \(2017, cyan box\)](#). Reprinted from Figure 5 of [Bullock and Boylan-Kolchin \(2017\)](#) with permission.

than naively expected. This inefficiency suggests the existence of astrophysical feedback suppressing star formation.

There are some possible sources of feedback, e.g., stellar radiation, stellar wind, [SN](#), and [active galactic nucleus \(AGN\)](#). Among these possibilities, the [SN](#) is considered a dominant feedback source ([Dekel and Silk, 1986](#)). The galaxy stellar mass function suggests the existence of feedback, but it does not tell us about the physical process of feedback.

1.2.1.2 Galactic wind

A more direct observational evidence of [SN](#) feedback is the galactic winds. The galactic winds are the outflowing gas from galaxies driven by [SN](#) explosions, and they are observed in nearby and distant universes. Figure 1.3 shows the optical image of M82 galaxy, which has prominent galactic wind features due to its central starburst and subsequent [SN](#) explosions. The image is taken by the *Hubble* space telescope, and the orange filaments above and below the stellar disk indicate the hydrogen H α emission from the galactic wind.

There are observations at multiple wavelengths, from X-ray to radio, tracing hot plasma to cold molecular cloud, for the M82 galaxy. [Shopbell and Bland-Hawthorn \(1998\)](#)



FIGURE 1.3: Observed image of M82 galaxy by the *Hubble* Space Telescope. The image is composed of four images taken with different filters; the red, green, and blue images are taken with wide band filters around 814, 555, and 435 nm, respectively, which capture starlight, and the orange image is taken with a narrow band filter at 658 nm, which captures the H α line. From <https://hubblesite.org/contents/media/images/2006/14/1876-Image.html>. Image courtesy of NASA, ESA, and The Hubble Heritage Team (STScI/AURA). Acknowledgment: J. Gallagher (University of Wisconsin), M. Mountain (STScI), and P. Puxley (National Science Foundation). Public domain.

observed warm ($\sim 10^4$ K) ionized gas emitting H α , [N II], and [O III] spectral lines in optical wavelength. They measured the velocity of the outflowing optical filaments as seen in Figure 1.3 to be ~ 600 km s $^{-1}$. Also, from their measurement of mass and length of filament, the mass outflow rate is estimated to be $\sim 7 M_{\odot}$ yr $^{-1}$, comparable to the star formation rate of M82. Strickland and Heckman (2009) observed hot ($\gtrsim 10^7$ K) plasma in X-ray. Their measurement showed that the wind velocity of hot gas is ~ 2000 km s $^{-1}$, considerably higher than that of warm ionized medium, and the mass outflow rate is $\sim 2 M_{\odot}$ yr $^{-1}$. Salak et al. (2013) observed cold (~ 10 K) molecular gas using CO emission line. The measured wind velocity was ~ 200 km s $^{-1}$, and the mass outflow rate is estimated to be $\sim 100 M_{\odot}$ yr $^{-1}$, considerably higher than those of hot and ionized gas. These observations show that the galactic wind is multiphase in nature, with the hotter phase flowing faster and being less massive, while the colder phase has a

slower velocity and is more massive.

The different properties of different phases result in different feedback impacts on galaxy formation. The wind velocity of the hot phase is larger than the escape velocity of M82, and the hot phase can entrain mass, energy, and metals to the [intergalactic medium \(IGM\)](#). The cold phase has a smaller velocity, but it expels a lot of gas out from the galaxy. The mass loading efficiency of galactic wind is characterized by a ratio between the mass outflow rate and the star formation rate of the galaxy, which is termed mass loading factor, $\eta_m = \dot{M}_{\text{wind}}/\dot{M}_*$. The cold phase has $\eta_m \sim 10$, meaning that the gas, the fuel of star formation, is lost at a rate of 10 times faster than star formation. This massive outflow is considered to be one of the major mechanisms of supernova feedback, but its contribution is still under debate. The massive outflow can halt star formation by removing star-forming gas, but the gas falls back in a timescale of the order of Gyr, which is 10 times shorter than the cosmic age. Therefore, the galactic wind alone would not be enough to explain the low star formation efficiency in galaxies.

1.2.1.3 Superbubble

Stars are born in molecular clouds and form star clusters, and massive stars with more than $8 M_\odot$ typically explode as core-collapse [SN](#) at the end of their life. In star clusters, multiple [SNe](#) occur clustered in space and time, and the clustered [SN](#) explosions form a large bubble called superbubble. The left panel in Figure 1.4 shows the N44 superbubble in the [Large Magellanic Cloud \(LMC\)](#). There are contributions of stellar radiations and winds to form the superbubble, but the X-ray emission inside the superbubble indicates the energetic [SN](#) explosions in the past. The superbubble expands driven by the pressure of internal hot gas and sweeps up the surrounding [ISM](#). The superbubble eventually mixes with [ISM](#), adding kinetic energy to drive interstellar turbulence.

The size of the superbubble is approximately 300 pc, and in the right panel of Figure 1.4, it is compared with the size of entire [LMC](#), whose diameter is roughly 4 kpc. Superbubbles are commonly observed in star-forming regions, and indeed many superbubbles can be found in the right panel of Figure 1.4. Although each superbubble is small compared to the galaxy, multiple superbubbles occur across it, affecting its evolution.

1.2.2 Theoretical suggestion

In this subsection, I describe the theoretical works of feedback using simulations.

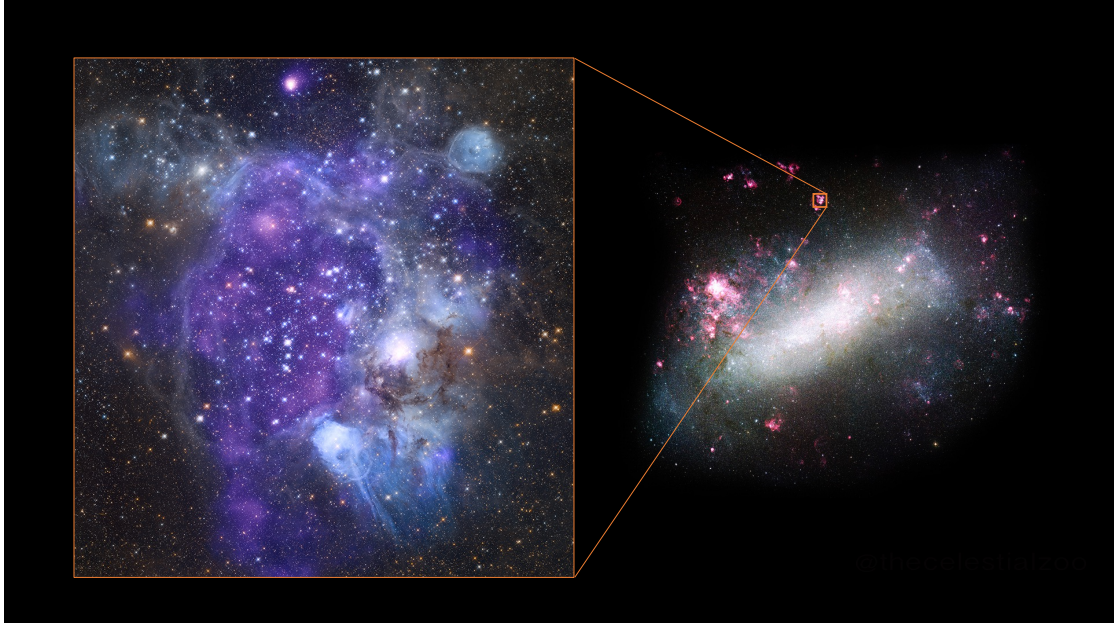


FIGURE 1.4: Left: The composite image of the N44 superbubble in the LMC. The purple and pink colors are X-ray images taken by the *Chandra* satellite, and the orange and light blue colors are optical images taken by the *Hubble* satellite. Credit: Enhanced Image by Judy Schmidt (CC BY-NC-SA) based on images provided courtesy of NASA/CXC/SAO & NASA/STScI. Right: The telescopic photograph of the LMC. Credit: Pablo Carlos Budassi, CC BY-SA 4.0, via Wikimedia Commons

1.2.2.1 Cosmological hydrodynamic simulation

The galaxy formation involves multiple astrophysical phenomena in the cosmological framework. To tackle these complexities, a powerful and direct approach has emerged in the form of cosmological hydrodynamical simulations. These simulations integrate gravity and hydrodynamics within the Λ CDM cosmology, while incorporating a range of astrophysical effects. This method has proved instrumental in advancing our comprehensive understanding of structure formation (for a technical review, see Vogelsberger et al., 2020).

Recent advances in cosmological hydrodynamical simulations have successfully reproduced key observed galaxy statistics, such as the galaxy stellar mass function as shown in Figure 1.5. Pioneering simulations like Illustris (Genel et al., 2014), Magneticum (Hirschmann et al., 2014), EAGLE (Schaye et al., 2015), MassiveBlack-II (Khandai et al., 2015), Horizon-AGN (Kaviraj et al., 2017), MUFASA (Davé et al., 2016), Romulus (Tremmel et al., 2017), IllustrisTNG (Pillepich et al., 2018a), SIMBA (Davé et al., 2019), ASTRID (Bird et al., 2022), FIREbox (Feldmann et al., 2023), MillenniumTNG (Pakmor et al., 2023), and FLAMINGO (Schaye et al., 2023) have shown remarkable

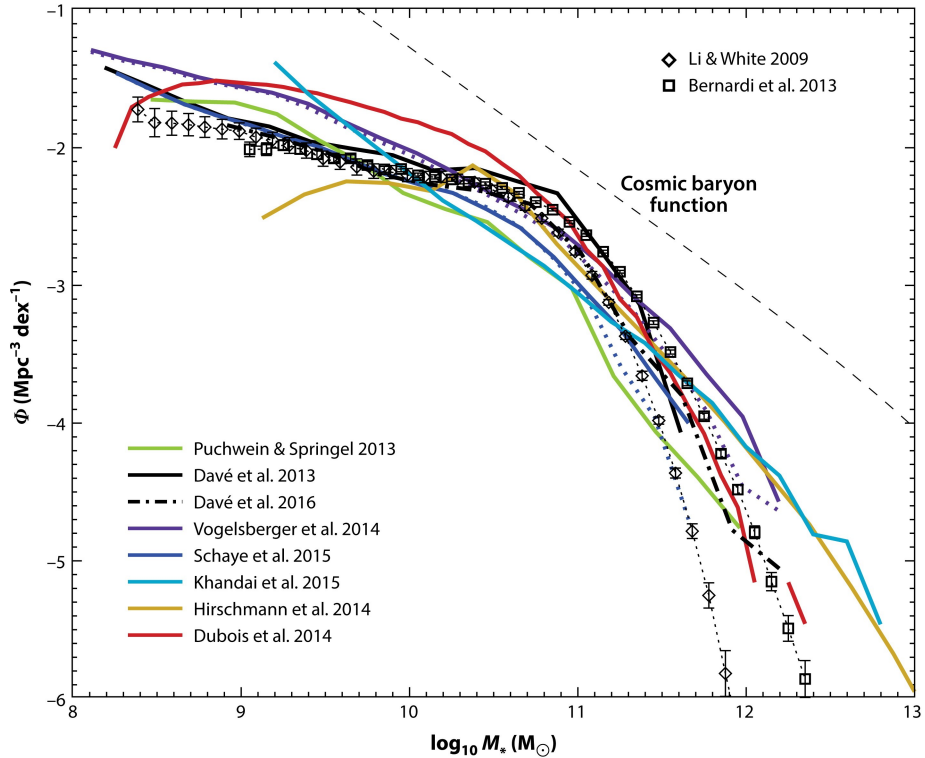


FIGURE 1.5: Comparing the predicted galaxy stellar mass functions from cosmological simulations at $z = 0$. The thick lines are the results of cosmological situations, and the dotted lines with points are observed galaxy stellar mass functions. The predicted galaxy abundance can vary by an order of magnitude, but they show general agreement with observations. Reprinted from Figure 4 of [Naab and Ostriker \(2017\)](#) with permission.

agreement with the observed galaxy stellar mass functions at various redshifts, but obtaining a perfect match at every redshift remains an ongoing challenge, reflecting the complexity and dynamic nature of galaxy evolution.

These simulations adopt the concordance Λ CDM cosmology and include a number of sophisticated subgrid models, including radiative cooling, extragalactic ultraviolet (UV) background radiation, star formation, and SN feedback. In addition, several of these simulations also integrate AGN feedback, adding a further layer of sophistication and fidelity to the simulation of galactic behavior and evolution.

The diverse but consistent success of several independent simulation projects, each using different subgrid models, has fostered a broad consensus within the scientific community. This consensus highlights the critical role of SN and AGN feedback in galaxy formation. The capability of these simulations to faithfully reproduce observed galaxy stellar mass functions, particularly through the calibration of feedback models, further underlines the central role of these phenomena in galaxy formation ([Somerville and Davé, 2015](#), [Naab and Ostriker, 2017](#)).

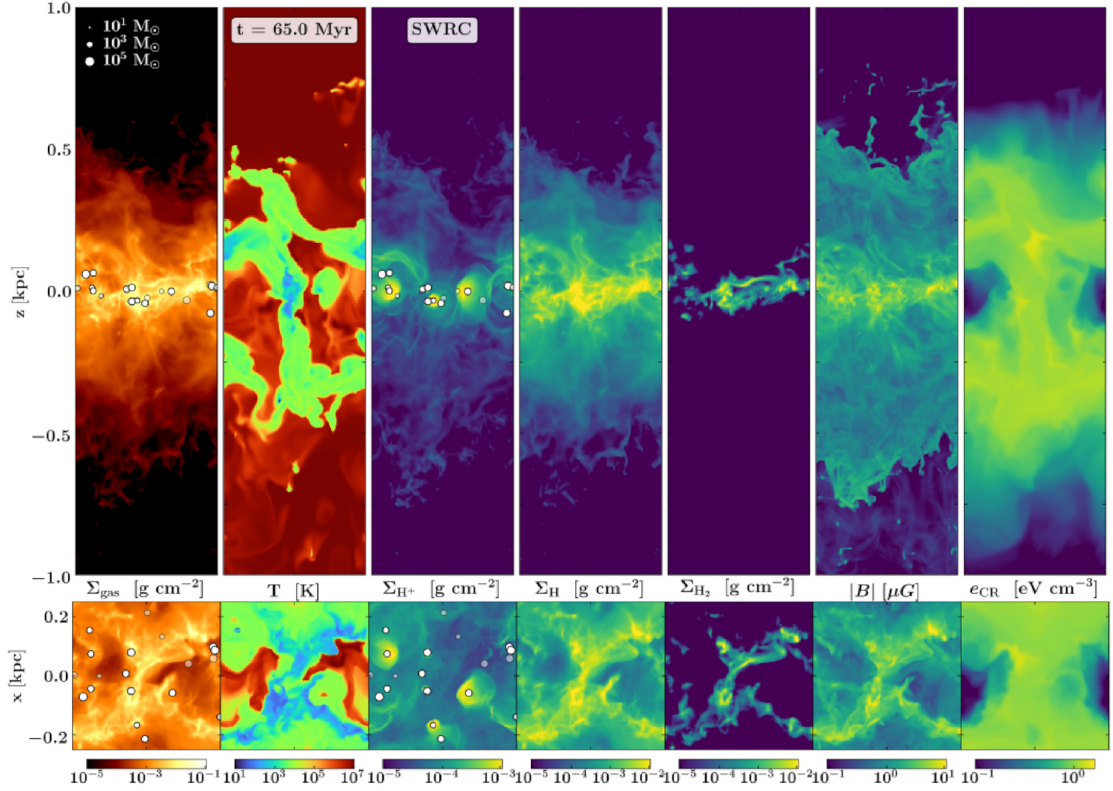


FIGURE 1.6: Overview of the SILCC high-resolution simulation. The simulation box has a size of $0.5 \text{ kpc} \times 0.5 \text{ kpc} \times 4 \text{ kpc}$ and the resolution is 4 pc. Shown are the edge-on (top row) and face-on (bottom row) views of the total gas column density, temperature, ionized-, atomic-, and molecular hydrogen column densities, magnetic field strength, and cosmic ray energy density. The white circles in the first and third panels indicate star clusters with different masses. Reprinted from Figure 1 of Rathjen et al. (2021) with permission.

1.2.2.2 Small-box high-resolution simulation

The drawbacks of cosmological simulation are its low resolution and dependency on subgrid modeling. The small-box high-resolution simulations have a resolution of an order of 1 pc, small enough to resolve the Sedov–Taylor phase of a [SN](#) remnant, and they predict the outcome of feedback activities without depending on subgrid treatments, although sacrificing the spatial scale and cosmological context.

Figure 1.6 shows the overview of the SILCC simulation (Rathjen et al., 2021), simulating the [ISM](#) at solar neighborhood condition with star formation and stellar feedback in forms of stellar winds, ionizing radiation, [SN](#), and cosmic rays. The resolution is high enough to resolve individual [SN](#) remnant, and a highly structured and turbulent multiphase [ISM](#) is naturally generated by the stellar feedback. They showed clustered [SNe](#) drives multiphase galactic wind, consistently with the observational facts as described in Section 1.2.1.2 and 1.2.1.3

[Ostriker and Kim \(2022\)](#) have investigated how the physical state of [ISM](#) is set by stellar feedback by analyzing their TIGRESS high-resolution simulations. They formulated the pressure balance of gravity, thermal pressure, and turbulent pressure due to momentum injection by [SN](#) feedback, finding agreement of their theory with simulations and observations. Their result indicates that the [SN](#) feedback maintains the suppressed star formation in the galactic disk by driving turbulence.

As described above, the high-resolution simulations give us deep insight into feedback physics. However, they neglect some important processes in galaxy evolution, like the recycling of outflowing gas, cosmic inflow, galactic merger, and the redshift evolution of galactic morphology due to their limited box size.

1.2.3 Challenges and future directions

As described in Section 1.2.2.1, cosmological simulations have successfully reproduced the observed galaxy stellar mass function (Section 1.2.1.1), and as described in Section 1.2.2.2, small-box high-resolution simulations have reproduced superbubble formed by clustered [SN](#) (Section 1.2.1.3) and the [SN](#)-driven multiphase galactic wind (Section 1.2.1.2). However, there are still disagreements between simulations and observations about the properties of [circumgalactic medium \(CGM\)](#) and [IGM](#).

Figure 1.7 shows the physical state of [IGM](#) of cosmological simulations using ASTRID (Bird et al., 2022, Ni et al., 2022), IllustrisTNG (Weinberger et al., 2017, Pillepich et al., 2018b), and SIMBA (Davé et al., 2019) models, performed as a part of CAMELS project (Ni et al., 2023). The [IGM](#) temperature of the SIMBA run is visibly higher than those of others, reflecting the treatment of subgrid [SN](#) and [AGN](#) feedback. The difference between the ASTRID and TNG run is minor, but the cosmic filament is more diffused in the TNG run.

[Butler Contreras et al. \(2023\)](#) have used the CAMELS project data set (Villaescusa-Navarro et al., 2023) to study the O VII column density at low redshift ($z < 0.3$) in simulations performed with the same code used for the IllustrisTNG and SIMBA simulations, and compared with the stacked *Chandra* observations of X-ray absorption lines on a line of sight of a background quasar from Kovács et al. (2019). They found that for a given H I column density, SIMBA predicts a lower O VII column density than the IllustrisTNG model by order of magnitude. They also found that the O VII column density in the simulations is lower than that observed by Kovács et al. (2019) by more than an order of magnitude, even for all ranges of [SN](#) and [AGN](#) feedback parameters explored in CAMELS.

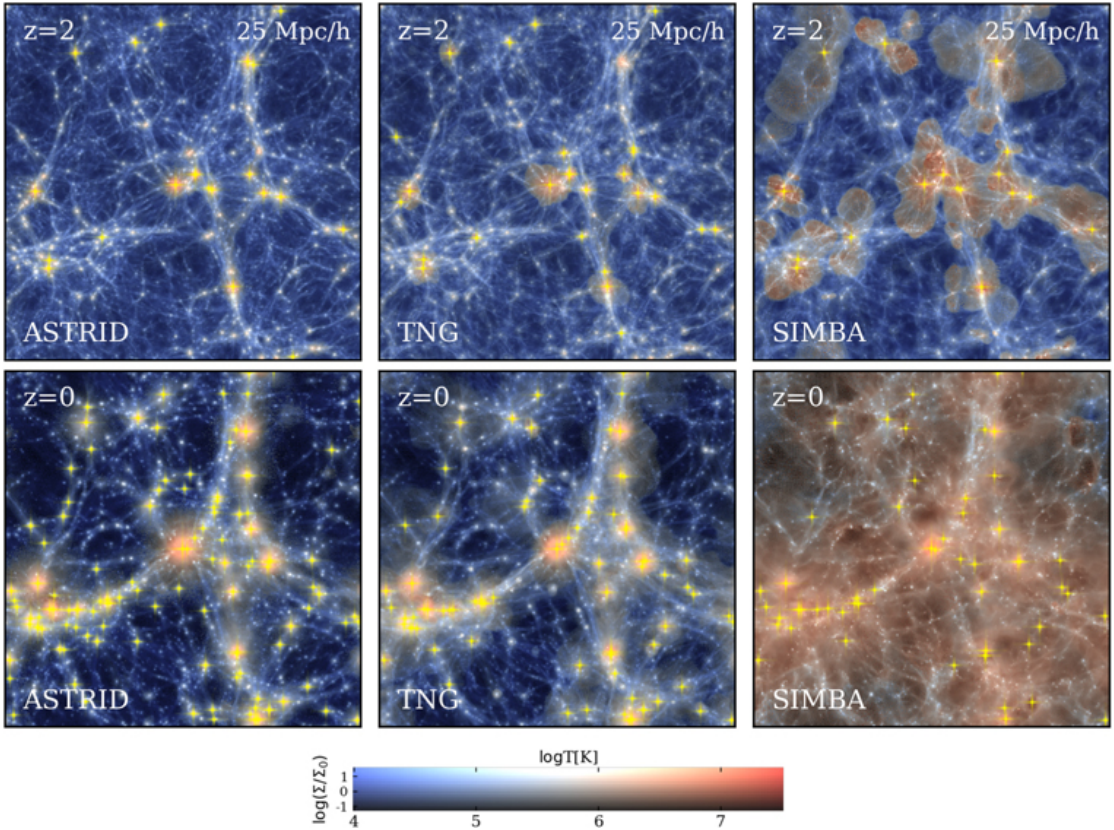


FIGURE 1.7: Comparison of the **IGM** simulated using ASTRID, IllustrisTNG, and SIMBA models. The intensity indicates the gas density, and the color indicates temperature (as indicated by the 2D color map) over the full box comoving volume of $(25 h^{-1} \text{ Mpc})^3$ at $z = 2$ (top panels) and $z = 0$ (bottom panels). The locations of massive BHs with $M_{\text{BH}} > 10^8 M_{\odot}$ are marked by the yellow spikes. Reprinted from Figure 1 of [Ni et al. \(2023\)](#). CC BY 4.0.

[Strawn et al. \(2024\)](#) have analyzed a series of zoom-in simulations performed as part of the AGORA project ([Roca-Fàbrega et al., 2021](#)). These simulations were performed using a variety of simulation codes, both grid-based and particle-based, with various feedback models calibrated to match the values of the stellar-to-halo mass ratio predicted by the semi-empirical models. They have investigated column densities of four ions, namely Si IV, C IV, O VI, and Ne VIII, in the **CGM**. They found that there were considerable differences in the ion column densities between the simulations and the observations. At $z = 3$, the simulations differed by three orders of magnitude from the observations. They also found the ion column densities from the grid-based code generally to be higher than those from the particle-based code, with varying scatter due to different feedback prescriptions. The discrepancy in the properties of the **CGM** and **IGM** found in these works is due to the feedback models used in the simulations. Therefore, it is necessary to improve the feedback modeling based on small-scale physics.

The discrepancy seen in the **IGM** property in the simulations, in turn, indicates that the study of the **IGM** offers a distinct and robust means of constraining feedback physics.

Especially, the spatial distribution and abundance patterns of metals in the IGM serve as historical records of feedback activities. It is still a challenge to observe dilute IGM. However, it is possible to perform ‘IGM tomography,’ an observational technique to reconstruct the three-dimensional distribution of foreground absorbers from absorption lines on multiple lines of sight of galaxies and quasars (Lee et al., 2014, 2018, Newman et al., 2020). The advent of future wide-field and high-spectral-resolution IGM tomography utilizing advanced multiplexed fiber spectrographs such as Subaru/PFS (Greene et al., 2022), WHT/WEAVE (Jin et al., 2023), VLT/MOONS (Cirasuolo et al., 2014), MSE (The MSE Science Team et al., 2019), ELT/ANDES (Maiolino et al., 2013) and ELT/MOSAIC (Japelj et al., 2019) promises to revolutionize our understanding. These innovative tools are expected to reveal the intricate three-dimensional metal distribution within the IGM, providing unprecedented insights into the formation of cosmic structures.

Predicting the matter distribution from numerical simulations is necessary for deducing information on feedback physics from IGM tomographic observations. Nagamine et al. (2021) have highlighted the potential of IGM tomography as a powerful tool for probing feedback. They have used the GADGET3-OSAKA cosmological simulation (Shimizu et al., 2019) and revealed variations in the Ly α optical depth on small scales. These variations were affected by the details of the feedback model, as well as the treatment of gas self-shielding, star formation, and UV background radiation. While Nagamine et al. (2021) focused primarily on the distribution of neutral hydrogen, investigation of the metal distribution can give further insight into the feedback physics.

1.3 This thesis

In this thesis, I describe the development of a physically-motivated SN feedback model based on high-resolution simulations and cosmological simulation using the model. This thesis is based on our following two papers.

In Oku et al. (2022), we developed a SN feedback model based on high-resolution simulations. The adiabatic phase of a SN remnant is rarely resolved in cosmological simulations, and then the hydro-solver cannot resolve the conversion between kinetic and thermal energy. We thus consider the kinetic and thermal feedback effect of SN feedback respectively (see also Chaikin et al., 2023). The kinetic feedback takes into account the momentum of a superbubble formed by clustered SNe, driving interstellar turbulence. The thermal feedback accounts for the fact that some superbubbles break out of the galactic disk to generate hot galactic winds, as observed in M82 (Strickland and Heckman, 2009). In simulations of Milky Way-mass isolated galaxies, we have shown that the

kinetic feedback supports a galactic disk against gravitational collapse to suppress star formation, and the thermal feedback drives the hot metal-rich galactic wind.

In [Oku and Nagamine \(2024\)](#), we have introduced the CROCODYLE¹ (Cosmological hydROdynamical simulation of struCture fOrmation and feeDback physIcs in gaLaxy Evolution) cosmological simulation. This CROCODYLE is performed using the GADGET4-OSAKA smoothed particle hydrodynamics (SPH) code ([Romano et al., 2022a,b](#)), a modified version of GADGET-4, [Springel et al. 2021](#)), which features our updated **SN** feedback model developed in [Oku et al. \(2022\)](#) and includes the active galactic nuclei (AGN) feedback model following [Rosas-Guevara et al. \(2015\)](#), [Schaye et al. \(2015\)](#), [Crain et al. \(2015\)](#). [Oku and Nagamine \(2024\)](#) have demonstrated CROCODYLE’s capability in reproducing essential galaxy statistics and investigated the impacts of **SN** and **AGN** feedback on the metal enrichment of the **IGM**.

This thesis is organized as follows: Chapter 2 describe the development of our **SN** feedback model. Chapter 3 details the methodology of our cosmological simulation CROCODYLE, including the numerics and the subgrid models for stellar feedback and black holes. In Chapter 4, we present the results of our CROCODYLE simulations, with a focus on the basic statistical properties of galaxies to validate our simulation framework. In Chapter 5, we analyze the distribution of metals in the **IGM** in CROCODYLE. We highlight the impact of **SN** and **AGN** feedback, and this section serves as a preliminary study, setting the theoretical groundwork for future tomographic surveys. Our findings are summarized, and future research directions are outlined in Chapter 6. Additionally, Appendix A discusses the evolution of a superbubble in idealized **ISM**, which serves as a basis of our **SN** feedback model. Appendix B describes the technical details of introducing feedback in simulation.

¹Named in homage to Osaka University’s official mascot, Dr. Wani, a crocodile (<https://www.osaka-u.ac.jp/sp/drwani/en/>)



OSAKA UNIVERSITY mascot Dr. Wani as a science member

Chapter 2

Supernova feedback model

In this chapter, we discuss the supernova feedback model developed in [Oku et al. \(2022\)](#).

2.1 Necessity of feedback model

Due to a lack of resolution, it is challenging to spatially and temporally resolve [SN](#) explosions in galaxy formation simulations. [SN](#) explosions were modeled as thermal energy injections in the early days of cosmological galaxy simulation (i.e., the 1990s) ([Cen and Ostriker, 1992](#), [Katz et al., 1996](#), [Cen and Ostriker, 1999](#)). However, the thermal energy was dissipated and radiated away as soon as it was injected due to low resolution (i.e., the overcooling problem, [Katz, 1992](#)).

Here, we analytically calculate the mass resolution requirement for thermal and kinetic feedback. [Dalla Vecchia and Schaye \(2012\)](#) estimated the resolution necessary for effective thermal feedback. They compared the sound-crossing time, t_s , with the cooling time, t_c . The sound-crossing time across a scale of spatial resolution $\Delta x = (m_{\text{gas}}/\rho)^{1/3}$ is

$$t_s = \frac{\Delta x}{c_s} = \left(\frac{\mu m_{\text{H}}}{\gamma k_{\text{B}} T} \right)^{\frac{1}{2}} \left(\frac{m_{\text{gas}}}{\rho} \right)^{\frac{1}{3}} \\ = 1.0 \times 10^5 \text{ yr} \times \left(\frac{\mu}{0.59} \right)^{\frac{1}{6}} \left(\frac{T}{10^{7.5} \text{ K}} \right)^{-\frac{1}{2}} \left(\frac{m_{\text{gas}}}{10^4 \text{ M}_{\odot}} \right)^{\frac{1}{3}} \left(\frac{n_{\text{H}}}{1 \text{ cm}^{-3}} \right)^{-\frac{1}{3}}, \quad (2.1)$$

where c_s is the local sound speed. The cooling time is

$$t_c = \frac{n k_{\text{B}} T}{(\gamma - 1) \Lambda_{ff}}, \quad (2.2)$$

where Λ_{ff} is the cooling rate by bremsstrahlung. Here, the cooling time of gas with $T > 10^7 \text{ K}$ is considered, where bremsstrahlung is the dominant cooling process. Note

that this cooling time is not the cooling time of a point explosion, i.e., the shell-formation time for a [SN](#) remnant. We compare the sound-crossing time to the cooling time for a gas particle with fixed density to evaluate if the heated gas particle cools down within the simulation time step. The overcooling can be avoided if the cooling time is longer than the simulation time step. However, as discussed later in this section, avoiding overcooling does not ensure that we resolve the Sedov–Taylor phase.

The cooling rate by bremsstrahlung is ([Draine, 2011](#))

$$\Lambda_{ff} = 1.14 \times 10^{-23} \text{ erg cm}^{-3} \text{ s}^{-1} \left(\frac{n_{\text{H}}}{1 \text{ cm}^{-3}} \right)^2 \left(\frac{T}{10^{7.5} \text{ K}} \right)^{1/2}, \quad (2.3)$$

where we have assumed that the number density ratio of hydrogen to helium is 10:1, the plasma is fully ionized, and the gaunt factor is 1.19. Combining Eq. (2.2) and (2.3), we obtain the cooling time as:

$$t_c = 4.2 \times 10^7 \text{ yr} \left(\frac{n_{\text{H}}}{1 \text{ cm}^{-3}} \right)^{-1} \left(\frac{T}{10^{7.5} \text{ K}} \right)^{1/2}. \quad (2.4)$$

The ratio between the sound-crossing and cooling times is:

$$\frac{t_c}{t_s} = 4.2 \times 10^2 \times \left(\frac{\mu}{0.59} \right)^{-\frac{1}{6}} \left(\frac{n_{\text{H}}}{1 \text{ cm}^{-3}} \right)^{-\frac{2}{3}} \left(\frac{T}{10^{7.5} \text{ K}} \right) \left(\frac{m_{\text{gas}}}{10^4 \text{ M}_\odot} \right)^{-\frac{1}{3}}. \quad (2.5)$$

The thermal feedback becomes effective if the cooling time is sufficiently longer than the sound-crossing time, $t_c/t_s > 10$, which translates to

$$T > 7.5 \times 10^5 \text{ K} \left(\frac{\mu}{0.59} \right)^{1/6} \left(\frac{n_{\text{H}}}{1 \text{ cm}^{-3}} \right)^{2/3} \left(\frac{m_{\text{gas}}}{10^4 \text{ M}_\odot} \right)^{1/3}. \quad (2.6)$$

The criterion temperature $T = 7.5 \times 10^5 \text{ K}$ is lower than the temperature where metal line radiative cooling dominates over bremsstrahlung. Therefore, thermal feedback is effective when it is energetic enough to heat a gas particle to $T > 10^{7.5} \text{ K}$.

The condition for kinetic feedback is more stringent than that for thermal feedback. [Kim and Ostriker \(2015\)](#) performed 3D simulations using the ATHENA code ([Stone et al., 2008](#)) and studied the resolution dependence of the terminal momentum of a [SN](#) remnant. They showed that the criterion for the terminal momentum to be converged within 25% is $\Delta x/R_{\text{sf}} < 1/3$, where Δx is the spatial resolution, and R_{sf} is the shell-formation radius (Eq. A.7). This criterion can be converted to the mass resolution requirement in [SPH](#):

$$\frac{(m_{\text{gas}}/\rho)^{1/3}}{23E_{51}^{0.29}n_0^{-0.42}\Lambda_{6,-22\text{pc}}^{-0.13}} < \frac{1}{3}, \quad (2.7)$$

where m_{gas} is the SPH particle mass. Solving this inequation for m_{gas} , we obtain

$$m_{\text{gas}} < 6.6 M_{\odot} \left(\frac{\mu}{0.59} \right) n_0^{-0.26} E_{51}^{0.87} \Lambda_{6,-22}^{-0.39} \quad (2.8)$$

[Hu \(2019\)](#) investigated the resolution dependence of the terminal momentum of a [SN](#) remnant. They used their modified version of GADGET-3 [SPH](#) code and simulated the remnant formed by a [SN](#) explosion with $E_{\text{SN}} = 10^{51}$ erg in a uniform medium of $n_{\text{H}} = 1 \text{ cm}^{-3}$ at four mass resolutions, $m_{\text{gas}} = 0.1, 1, 10, \text{ and } 100 M_{\odot}$. They found the convergence of the terminal momentum in the cases of $m_{\text{gas}} = 0.1, \text{ and } 1 M_{\odot}$. The terminal momentum in the case of $m_{\text{gas}} = 10 M_{\odot}$ was about 15% smaller than that for $m_{\text{gas}} = 0.1, \text{ and } 1 M_{\odot}$, and this result is roughly consistent with the criterion in Eq. (2.8). The reason for the 15% convergence of the terminal momentum in the case of $m_{\text{gas}} = 10 M_{\odot}$ might be because the spatial resolution of [SPH](#) becomes better in a dense shell. In the case of lowest resolution at $m_{\text{gas}} = 100 M_{\odot}$, the terminal momentum is underestimated by a factor of three due to overcooling.

We can also solve Eq. (2.7) for $E (= E_{51} \times 10^{51} \text{ erg})$ to find the injection energy large enough to generate an explosion that can be resolved with the given mass resolution m_{gas} :

$$E > 4.5 \times 10^{54} \text{ erg} \left(\frac{\mu}{0.59} \right)^{-1.2} \left(\frac{m_{\text{gas}}}{10^4 M_{\odot}} \right)^{1.2} n_0^{0.30} \Lambda_{6,-22}^{0.45}, \quad (2.9)$$

and obtain the temperature at which the criterion is satisfied:

$$T = \frac{\mu m_{\text{H}}}{(\gamma - 1)} \frac{E}{m_{\text{gas}} k_{\text{B}}} > 1.6 \times 10^9 \text{ K} \left(\frac{\mu}{0.59} \right)^{-0.2} \left(\frac{m_{\text{gas}}}{10^4 M_{\odot}} \right)^{0.2} n_0^{0.3} \Lambda_{6,-22}^{0.45}. \quad (2.10)$$

This temperature is much higher than the temperature needed for the thermal feedback to be effective (Eq. 2.6), meaning that the condition for kinetic feedback is more difficult to realize in actual simulations.

2.2 Main idea of modeling

To model [SN](#) feedback, we must consider what to model. As described in Figure 2.1, [SN](#) feedback affects galaxy evolution via both kinetic feedback (driving turbulence) and thermal feedback (generating hot bubbles and outflows). When the resolution is high enough to resolve the Sedov–Taylor phase, its kinetic and thermal energies get converted to one another, and the difference between the thermal and kinetic form, or a combination of both forms, is negligible ([Durier and Dalla Vecchia, 2012](#)). However, in most cases of cosmological galaxy simulations, such small scales cannot be resolved as we described in Section 2.1. Hence, we need to include both kinetic and thermal feedbacks in the



FIGURE 2.1: Schematic image of the idea of supernova feedback model.

SN feedback model. We note that simply distributing thermal energy is ineffective (Hu, 2019) because it leaves the mass of the SN ejecta unresolved in simulations, as long as we use simple stellar population (SSP) approximation and the particle masses of stars and gas are comparable (Dalla Vecchia and Schaye, 2012). Therefore, the effective modeling of thermal feedback is necessary.

2.3 Mechanical feedback

In this section, we develop a mechanical feedback model based on high-resolution superbubble simulation using ATHENA++ code. The simulation is performed as a part of my master thesis work, and the details of the simulation, as well as the basic analytic theory of superbubble evolution, is described in Appendix A to avoid the duplication in theses in main contents and clarify the contribution made in PhD course.

2.3.1 Averaged momentum per SN for a stellar population

From the fitting function in Appendix A.2.3, we derive the expression for momentum of a superbubble per SN, averaged over an initial stellar cluster mass function (ICMF). We assume the ICMF to be described by the power-law $dN/dM_c \propto M_c^{-2}$ with high-mass cutoff, where M_c is the mass of the stellar cluster (Krumholz et al., 2019) and stellar initial mass function (IMF) is fixed. We also assume SNe occurs at a constant rate. The ICMF can be translated to an SN number function (probability distribution function of the number of SN explosions occurring in a stellar cluster)

$$\frac{dN}{dN_{\text{SN}}} = AN_{\text{SN}}^{-2}, \quad (2.11)$$

where N_{SN} is the number of **SN** explosions occurring in a stellar cluster and A is the normalization factor. The range of the number of **SN** explosions is assumed as $N_{\text{SN}} = N_{\text{SN,min}} - N_{\text{SN,max}}$, where we adopt the range of $(N_{\text{SN,min}}, N_{\text{SN,max}}) = (1, 500)$, and the normalization factor is $A = 1/\ln 500$. The value of $N_{\text{SN,max}} = 500$ is the number of **SN** explosions expected to happen in the largest **young massive star cluster (YMC)** in the Milky way with a mass of $M = 5 \times 10^4 \text{ M}_\odot$ (Portegies Zwart et al., 2010). The choice of high-mass cutoff has little effect on the result since such high-mass **YMCs** are rare objects. The **SN** interval is obtained by dividing their duration by their number, $\Delta t_{\text{SN}} = (t_{\text{SN,end}} - t_{\text{SN,start}})/N_{\text{SN}}$, where $t_{\text{SN,start}}, t_{\text{SN,end}}$ are the times at the first and the last Type II **SN** after the formation of the stellar cluster, i.e., the minimum and the maximum lifetimes of stars causes Type II **SNe**. The lifetimes of stars depend on their mass and metallicity. We calculate **SNe** duration using CELIB¹ (Saitoh, 2017), which compute it using the metallicity-dependent stellar lifetime table by Portinari et al. (1998). We assume the mass range of the progenitors of Type II **SNe** to be $13\text{--}40 \text{ M}_\odot$. In the range of $Z = 10^{-6}\text{--}10^{-2}$, **SNe** duration is

$$t_{\text{SN,end}} - t_{\text{SN,start}} \sim 1.2 \times 10^7 \text{ yr.} \quad (2.12)$$

Single **SN** explosion energy is set to 10^{51} erg. The average momentum per **SN** is

$$\hat{p}(n_0, Z) = \int_{N_{\text{SN,min}}}^{N_{\text{SN,max}}} p(n_0, Z, \Delta t_{\text{SN}}(N'_{\text{SN}})) \frac{dN}{dN'_{\text{SN}}} dN'_{\text{SN}}. \quad (2.13)$$

The final integral is well-fitted by the following function:

$$\hat{p}(n_0, Z) = 1.75 \times 10^5 \text{ M}_\odot \text{ km s}^{-1} n_0^{-0.05} \Lambda_{6,-22}^{-0.17}, \quad (2.14)$$

and the momentum input by \mathcal{N}_{SN} **SNe** (superbubble momentum, p_{SB}) is estimated as

$$p_{\text{SB}}(\mathcal{N}_{\text{SN}}, n_0, Z) = \mathcal{N}_{\text{SN}} \hat{p}(n_0, Z). \quad (2.15)$$

Here, we used a slightly different font of \mathcal{N}_{SN} for the total number of **SNe** for a star particle in the simulation (i.e., a collection of stellar clusters, rather than a population of stars in a single stellar cluster).

2.3.2 Shock radius for a star particle

We similarly calculate the shock radius of **SN** feedback of a star particle. Assuming that stellar clusters follow the power-law **ICMF**, we determine the shock radius of the **SN**

¹<https://bitbucket.org/tsaitoh/celib>

feedback as the radius of a sphere whose volume is the sum of those of the superbubbles. We first consider the averaged volume shocked by **SN** feedback *per SN* considering the variation of superbubbles created by a range of star clusters:

$$\hat{V}(n_0, Z) = \int_{N_{\text{SN}, \text{min}}}^{N_{\text{SN}, \text{max}}} \frac{4}{3} \pi R(n_0, Z, \Delta t_{\text{SN}}(N'_{\text{SN}}))^3 \frac{dN}{dN'_{\text{SN}}} dN'_{\text{SN}}. \quad (2.16)$$

Then the effective radius is obtained as

$$\hat{R}(n_0, Z) = \left(\frac{3\hat{V}}{4\pi} \right)^{1/3} = 61 \text{ pc } n_0^{-0.22} \Lambda_{6,-22}^{-0.04}, \quad (2.17)$$

and the shock radius by \mathcal{N}_{SN} **SNe** is calculated as

$$R(\mathcal{N}_{\text{SN}}, n_0, Z) = \mathcal{N}_{\text{SN}}^{1/3} \hat{R}(n_0, Z). \quad (2.18)$$

Here, \mathcal{N}_{SN} is meant to be the number of **SNe** occurring in the stellar population of a star particle. Since Eq. (2.16) gives the averaged superbubble volume *per SN*, the effective volume for \mathcal{N}_{SN} **SNe** for a star particle would be $\mathcal{N}_{\text{SN}} \hat{V}$ and the effective radius would be $\mathcal{N}_{\text{SN}}^{1/3} \hat{R}$ as given in Eq. (2.18).

2.3.3 Feedback assignment

We use the ‘Spherical superbubble model’ described in Appendix B to assign physical quantities related to feedback. Using the superbubble momentum p_{SB} computed in Eq. (2.15), we deposit the following momentum on the i -th gas particle:

$$\Delta \mathbf{p}_i = p_{\text{SB}} \frac{\Omega_i}{4\pi} \mathbf{n}_i, \quad (2.19)$$

where \mathbf{n}_i is the normal vector of the face on the Voronoi polyhedron. When the number of neighboring gas particles falls below four (which prevents the construction of a Voronoi polyhedron), we inject the same amount of momentum and determine \mathbf{n}_i so that the total momentum is conserved. The total momentum of the surrounding gas should be conserved before and after the **SN** event. For this, we compute the total momentum input as:

$$\Delta \mathbf{p}_{\text{tot}} = \sum_i \Delta \mathbf{p}_i, \quad (2.20)$$

and modify momentum input to i -th gas particle to

$$\Delta \mathbf{p}'_i = \Delta \mathbf{p}_i - \frac{\Omega_i}{4\pi} \Delta \mathbf{p}_{\text{tot}}. \quad (2.21)$$

The kinetic energy input by momentum kick may exceed the [SN](#) energy input due to particle distribution. Thus, we limit the momentum input to each neighboring particle based on the Sedov–Taylor solution. The resulting momentum input is:

$$\Delta\mathbf{p}_i'' = \frac{\Delta\mathbf{p}_i'}{|\Delta\mathbf{p}_i'|} \min \left(|\Delta\mathbf{p}_i'|, \sqrt{2(m_i + \Delta m_i)\Delta E_{\text{kin},i}} \right), \quad (2.22)$$

where m_i is the mass of the i -th gas particle and $\Delta E_{\text{kin},i}$ is the solid-angle-weighted kinetic energy from [SN](#) feedback. $\Delta E_{\text{kin},i}$ is given as

$$\Delta E_{\text{kin},i} = \epsilon_{\text{kin}} E_{\text{SN}} \frac{\Omega_i}{4\pi}, \quad (2.23)$$

where ϵ_{kin} is a fraction of the [SN](#) energy deposited as kinetic energy, and we adopt $\epsilon_{\text{kin}} = 0.3$ as the default value ([Shimizu et al., 2019](#)). Equation (2.22) essentially corresponds to equation (A1) in [Kimm and Cen \(2014\)](#) and equation (32) in [Hopkins et al. \(2018\)](#).

The momentum input above is calculated with respect to the frame moving with the star particle. To ensure exact conservation, we require a term accounting for the relative motion between the gas and the star ([Hopkins et al., 2018](#)). Finally, the momentum input boosted back to the simulation frame is

$$\Delta\mathbf{p}_i''' = \Delta\mathbf{p}_i'' + \Delta m_i \mathbf{v}_{\text{star}}, \quad (2.24)$$

where \mathbf{v}_{star} is the star velocity.

In summary, we first compute $\Delta\mathbf{p}_i$ for the momentum that we want to assign the neighboring gas particles with. Then $\Delta\mathbf{p}_i'$ makes it isotropic, and we ensure energy conservation by $\Delta\mathbf{p}_i''$. Finally, $\Delta\mathbf{p}_i'''$ takes care of the motion of the originating stellar particle. By giving $\Delta\mathbf{p}_i''$, the momentum feedback is basically guaranteed to be isotropic, energy-conserving, and momentum-conserving.

To be more specific, it is possible that momentum conservation could be broken when the second term in the RHS of Eq. (2.22) is chosen. However, such a situation does not arise very often because we do not have sufficient to resolve the Sedov–Taylor phase. In fact, we have checked our isolated galaxy simulations performed in Section 2.5, the second term was chosen only $3.4 \times 10^{-5}\%$ of the cases for the Fiducial run, and $1.1 \times 10^{-4}\%$ for the High-reso run.

2.4 Galactic wind feedback

Several groups have studied the [SN](#)-driven outflow using high-resolution small-box simulations. [Hu \(2019\)](#) investigated [SN](#)-driven outflow of a dwarf galaxy. They showed the entropy $S \equiv k_B T n^{1-\gamma}$ of the hot outflow to be $10^8 - 10^9 k_B \text{ K cm}^2$, and it is almost constant after being launched from the galaxy. Although their result is on a dwarf galaxy, the energy loading factor and specific energy of the hot outflow by [Hu \(2019\)](#) are similar to those of a Milky-way-mass galaxy ([Li et al., 2017](#), [Armillotta et al., 2019](#), [Kim and Ostriker, 2018](#), [Kim et al., 2020b](#)), according to [Li and Bryan \(2020\)](#).

It is suggested that the hot outflow is driven by buoyancy and its entropy is its fundamental physical quantity; if the entropy of the hot bubble is higher than that of the surrounding [CGM](#), the hot bubble becomes buoyant and drives the outflow ([Bower et al., 2017](#)). [Keller et al. \(2020\)](#) analytically calculated the entropy of superbubbles and the virialized Milky-way-mass halos to be about $10^8 k_B \text{ K cm}^2$. The buoyancy-driven outflow framework is supported by the MUGS2 simulations ([Keller et al., 2015, 2016](#)), and the framework may explain the ineffectiveness of [SN](#) feedback in halos more massive than $10^{12} M_\odot$ ([Keller et al., 2020](#)).

In this work, we update the stochastic thermal feedback model ([Dalla Vecchia and Schaye, 2012](#)) by using the entropy of hot outflow S_{OF} as a free parameter, setting $S_{\text{OF}} = 10^8 k_B \text{ K cm}^2$ as the default value. When [SN](#) feedback occurs, thermal energy is stochastically injected to heat neighboring particles to target entropy, S_{OF} . The thermal energy required to heat the i -th gas particle is

$$\Delta E_{\text{req},i} = \frac{1}{\gamma - 1} \frac{m_i}{\mu m_H} n_i^{2/3} S_{\text{OF}}, \quad (2.25)$$

where n_i is the number density of the i -th gas particle. The probability of injecting thermal energy is the ratio between the solid-angle-weighted thermal energy from [SN](#) feedback (Appendix B),

$$\Delta E_{\text{th},i} = \epsilon_{\text{th}} E_{\text{SN}} \frac{\Omega_i}{4\pi}, \quad (2.26)$$

and the required thermal energy:

$$P_i = \frac{\Delta E_{\text{th},i}}{\Delta E_{\text{req},i}}, \quad (2.27)$$

where $\epsilon_{\text{th}} = 1 - \epsilon_{\text{kin}}$ is a fraction of the [SN](#) energy deposited as thermal energy, and we adopt $\epsilon_{\text{th}} = 0.7$ as the default value ([Shimizu et al., 2019](#)). We draw a random number $0 < \theta_i < 1$ for each gas particle, and inject thermal energy $\Delta E_{\text{req},i}$ to i -th gas particle if $\theta_i < P_i$. When $P_i > 1$, we simply inject a thermal energy of $\Delta E_{\text{th},i}$ to the i -th gas particle.

The original stochastic thermal feedback model by [Dalla Vecchia and Schaye \(2012\)](#) uses temperature increase ΔT as a free parameter and stochastically heats gas that magnitude. Their default value $\Delta T = 10^{7.5}$ K was set for a numerical reason; the expectation value for the number of heated gas particles per [SN](#) is about 1. If this value is much smaller than 1, most [SN](#) feedback events do not inject energy into their surroundings, leading to poor sampling of the [SN](#) feedback cycle ([Schaye et al., 2015](#)). Although they provide a good reason to use ΔT as a parameter for their stochastic feedback model, the outflow properties depend on ΔT ([Dalla Vecchia and Schaye, 2012](#)), and a better parameter choice is desired. In this work, we use outflow entropy as a free parameter, motivated by the high-resolution simulations ([Hu, 2019](#)) and buoyancy-driven outflow framework ([Bower et al., 2017, Keller et al., 2020](#)).

2.5 Isolated galaxy simulation with GADGET3-OSAKA

In this section, we implement the [SN](#) feedback model based on the high-resolution ATHENA++ simulations described in the earlier sections and demonstrate its effect on star formation and galactic outflow in an isolated galaxy simulation.

2.5.1 Simulation Setup

We use the GADGET3-OSAKA cosmological [SPH](#) code ([Aoyama et al., 2017, Shimizu et al., 2019](#)), which is a modified version of GADGET-3 (originally described in [Springel 2005](#), as GADGET-2²). We solve the [SPH](#) equation of motion, following the entropy-conserving, density-independent [SPH](#) formulation ([Hopkins, 2013, Saitoh and Makino, 2013](#)):

$$\frac{d\mathbf{v}_i}{dt} = - \sum_j m_j (S_i S_j)^{1/\gamma} \left[\frac{f_{ij} \bar{P}_i}{\bar{P}_i^{2/\gamma}} \nabla_i W(r_{ij}, h_{\text{sml},i}) + \frac{f_{ji} \bar{P}_j}{\bar{P}_j^{2/\gamma}} \nabla_i W(r_{ij}, h_{\text{sml},j}) \right], \quad (2.28)$$

$$f_{ij} = 1 - \frac{h_{\text{sml},i}}{3S_j^{1/\gamma} \rho_i} \frac{\partial \bar{P}_i^{1/\gamma}}{\partial h_{\text{sml},i}} \left(1 + \frac{h_{\text{sml},i}}{3\rho_i} \frac{\partial \rho_i}{\partial h_{\text{sml},i}} \right)^{-1}, \quad (2.29)$$

where m_i , \mathbf{v}_i , S_i , $h_{\text{sml},i}$, and \bar{P}_i denote the mass, velocity, entropy (defined as $S \equiv \bar{P}/\rho^\gamma$), smoothing length, and smoothed pressure defined as

$$\bar{P}_i = \left[\sum_j m_j S_j^{1/\gamma} W(r_{ij}, h_{\text{sml},i}) \right], \quad (2.30)$$

²<https://wwwmpa.mpa-garching.mpg.de/gadget/>

of the i -th gas particle, respectively. In this formulation, the thermal energy of a particle is computed from its entropy and smoothed pressure. When thermal feedback injects energy, updating entropy assuming fixed pressure leads to the wrong result because the smoothed pressure field itself depends on the entropy. Therefore, we use an iterative method to calculate entropy change by energy injection from feedback and energy dissipation by radiative cooling (Schaye et al., 2015, Borrow et al., 2021). The self-gravity of SPH and collisionless particles are also considered. We adopt the quintic B-spline kernel (Schoenberg, 1946, Morris, 1996), and set the number of neighboring particles for each SPH particle to $N_{\text{ngb}} = 128 \pm 8$. Our code includes the time-step limiter (Saitoh and Makino, 2009, Durier and Dalla Vecchia, 2012).

Radiative cooling is calculated using the GRACKLE-3 chemistry and cooling library³ (Smith et al., 2017), which solves non-equilibrium primordial chemistry and cooling for the H, D, and He species, including molecular H₂ and HD. The library also includes tabulated rates of metal cooling calculated with the photoionization code CLOUDY (Ferland et al., 2013) and photoheating and photoionization from the UV background radiation, and we adopt the UV background value at $z = 0$ by Haardt and Madau (2012). We applied a nonthermal Jeans pressure floor that forces the local Jeans length to be resolved to avoid artificial numerical fragmentation (Hopkins et al., 2011, Kim et al., 2016):

$$P_{\text{Jeans}} = \frac{1}{\gamma\pi} N_{\text{Jeans}}^2 G \rho_{\text{gas}}^2 \Delta x^2, \quad (2.31)$$

where $\gamma = 5/3$ is the adiabatic index, $N_{\text{Jeans}} = 4$ is the Jeans number adopted from Truelove et al. (1997), G is the gravitational constant, and ρ_{gas} is the gas density. Δx is chosen from the larger one of either the gravitational softening length of an SPH particle or the spatial resolution of hydrodynamics $(m_{\text{gas}}/\rho_{\text{gas}})^{1/3}$, where m_{gas} is the mass of the gas particle.

We used an initial condition taken from the AGORA project⁴ (Kim et al., 2016). The galaxy has properties characteristic of Milky Way-mass galaxies at redshift $z \sim 1$. The galaxy is composed of the following components: a dark matter halo with $M_{\text{DM}} = 1.25 \times 10^{12} M_{\odot}$, a stellar disk with $M_{\text{disc}} = 4.30 \times 10^9 M_{\odot}$, a stellar bulge with $M_{\text{bulge}} = 3.44 \times 10^{10} M_{\odot}$, and a gas disk with $M_{\text{gas}} = 8.59 \times 10^9 M_{\odot}$. The total mass of the galaxy is $1.3 \times 10^{12} M_{\odot}$. In the fiducial run, we employed 10^5 dark matter particles, 10^5 gas (SPH) particles, and 10^5 and 1.25×10^4 collisionless particles representing the stars in the disk and the bulge, respectively. We also added a hot gaseous halo following Shin

³<https://grackle.readthedocs.io>

The default solar metallicity in GRACKLE-3 is $Z_{\odot} = 0.0134$. This value is smaller than the value of Z_{\odot} that was used in Eq. (A.10) by a factor of 1.45. This difference will affect the calculation of terminal momentum in Eq. (A.16), however the power index on $\Lambda_{6,-22}$ term is small so that the impact on the value of $p_{\text{sf},m}$ is negligible.

⁴<http://www.AGORAsimulations.org>

et al. (2021). We randomly sampled 4×10^4 dark matter particles and added gas particles with the same mass as that of originally existing gas particles at the same position as those sampled dark matter particles. We adopt a fixed gravitational softening length of $\epsilon_{\text{grav}} = 80$ pc. We allowed the minimum gas smoothing length to reach 10 percent of the spline size of gravitational softening $2.8 \epsilon_{\text{grav}}$.⁵ We first evolve the system to 0.5 Gyr adiabatically for relaxation to set up the initial condition, and then evolve it to 1 Gyr with the sub-grid physics including cooling, UV background heating, star formation, and stellar feedback.

2.5.2 Star formation and Stellar feedback

2.5.2.1 Star formation

We assume star formation to occur when the gas number density $n > 10 \text{ cm}^{-3}$ and temperature $T < 10^4 \text{ K}$. We use the same star formation prescription as Shimizu et al. (2019), a Schmidt-type star formation law (Schmidt, 1959). The star formation rate (SFR) density is (Cen and Ostriker, 1992, Katz, 1992, Nagamine et al., 2001, Springel and Hernquist, 2003, Stinson et al., 2006, Kim et al., 2014, 2016)

$$\dot{\rho}_* = \epsilon_* \frac{\rho_{\text{gas}}}{t_{\text{ff}}}, \quad (2.32)$$

where ϵ_* is the star formation efficiency, ρ_{gas} is the gas density, and $t_{\text{ff}} = \sqrt{3\pi/(32G\rho_{\text{gas}})}$ is the local free-fall time. We adopt $\epsilon_* = 0.05$. The star particles are stochastically spawned from gas particles to follow the SFR density. Each gas particle can spawn a maximum of n_{spawn} star particles. The initial mass of the star particle is defined as $m_* = m_{\text{gas}}/n_{\text{spawn}}$, where m_{gas} is the mass of the gas particle. We have adopted $n_{\text{spawn}} = 2$ throughout this paper, using a SSP approximation and assuming each star particle to consist of a cluster of stars whose mass function follows the Chabrier IMF (Chabrier, 2003) with a mass range of $0.1\text{-}100 \text{ M}_\odot$.

⁵We use the definitions of the smoothing length and the gravitational softening length in GADGET-2 code (Springel, 2005) in this paper; the gravitational softening length is equivalent to the Plummer softening length, while the smoothing length is the kernel size beyond which kernel value vanishes (see also Appendix C in Kim et al., 2016). We define the SPH spatial resolution as the smoothing length widely used in literature, $\Delta x = \eta(m/\rho)^{1/3}$ (see e.g., Rosswog, 2009, for review). The parameter η is usually set to $\eta \sim 1.3$, but we set it to $\eta = 1$ for simplicity. In our GADGET3-OSAKA simulation, we adopt the quintic spline kernel and $N_{\text{ngb}} = 128$. If we consider the quintic spline kernel to truncate at $3h$ as in Price (2012) (see also Dehnen and Aly, 2012, for another definition of the smoothing length in terms of the smoothing kernel), we set to $\eta = 1.04$ in our simulation, effectively.

2.5.2.2 Stellar feedback

We consider stellar wind from massive stars, Type II **SNe**, Type Ia **SNe**, and stellar wind from the **asymptotic giant branch (AGB)** stars as stellar feedback while distributing the physical quantities from them using the spherical superbubble model (Appendix B). We use CELIB to calculate time and metallicity-dependent mass, metal, and energy input from Type II **SNe**, Type Ia **SNe**, and **AGB** stars (see Shimizu et al., 2019, figure 1). To deposit energy and metals gradually rather than at a single instant, we divide each feedback from the star particle into n_{fb} events and adopt $n_{\text{fb}} = 8$ throughout this paper (Shimizu et al., 2019).

Type II SN feedback We assume the range of the progenitor mass to be $13 - 40 \text{ M}_\odot$ and the **hypernova (HN)** fraction to be $f_{\text{HN}} = 0.05$. In the case of solar metallicity, the specific energy of Type II **SNe** is $\epsilon_{\text{SNII}} = 7.19 \times 10^{48} \text{ erg M}_\odot^{-1}$. We assume the **SN** energy to be 10^{51} erg and estimate shock radius and momentum input from **SN** feedback using equations (2.18) and (2.15). When **SN** feedback occurs at a low-density void formed by previous feedback events, we may overestimate the shock radius. Thus, we set an upper limit on the mass enclosed inside the shock radius $M(R_{\text{max}}) = 2 \times 10^3 m_*/n_{\text{fb}}$. This limit comes from a rough estimate of the **SN** remnant mass at fade away under an assumption that the terminal momentum per **SN** is $p \sim 2 \times 10^5 \text{ M}_\odot \text{ km s}^{-1}$, the sound speed of star-forming cloud is $c_s \sim 1 \text{ km s}^{-1}$, and the **SN** rate is $N_{\text{SN}} \sim m_*/(100 \text{ M}_\odot)$.

Type Ia SN feedback We adopted the delay-time distribution function with a power law of t^{-1} for Type Ia **SNe** event rate (e.g., Totani et al., 2008, Maoz and Mannucci, 2012), using equations (2.18) and (2.15) to estimate shock radius and momentum input, although Type Ia **SN** explosions are intermittent. One can estimate the momentum input from a single Type Ia **SN** using equation (A.9), assuming the **SN** remnant formed by a single **SN** to acquire about 77 % of its terminal momentum by the shell-formation time (Kim and Ostriker, 2015). For Type Ia **SN** feedback, we ignore thermal feedback because the formation of a hot bubble by stochastic thermal feedback represents superbubble formation by clustered Type II **SNe**. We used the same upper limit as Type II **SN** feedback on the shock radius.

Stellar wind from OB stars For stellar wind feedback from OB stars, we consider only mechanical feedback. We calculated the energy of the stellar wind from OB star using STARBURST99⁶ (Leitherer et al., 1999, Vázquez and Leitherer, 2005, Leitherer et al.,

⁶<https://www.stsci.edu/science/starburst99/docs/default.htm>

2010, 2014) and set the specific energy of stellar wind to $\epsilon_{\text{SW}} = 1.5 \times 10^{48} \text{ erg M}_{\odot}^{-1}$. Assuming 30 % of the energy turns into kinetic energy, we estimate the shock radius and momentum input using the equation (2.18) and (2.15) by setting $N_{\text{SN}} = m_* \epsilon_{\text{SW}} / (10^{51} \text{ erg})$. Here we choose to use the equation of superbubble momentum because the specific luminosity of stellar wind and Type II SNe are similar (e.g., Agertz et al., 2013). We set an upper limit on the mass enclosed inside the shock radius $M(R_{\text{max}}) = 2 \times 10^2 m_*/n_{\text{fb}}$. This limit is one order smaller than that of SN feedback because the amount of energy injected by stellar winds is about one order smaller than that injected by SNe. The adopted numbers above translates to a specific momentum injection rate of $\dot{p}/M \sim 100 \text{ km s}^{-1} \text{ Myr}^{-1}$. However, Lancaster et al. (2021b) have shown that the wind specific momentum injection rate from O star winds in a cluster is $\dot{p}/M \sim 10 \text{ km s}^{-1} \text{ Myr}^{-1}$ due to fractal mixing boundary layer. Our model here can be regarded as an upper limit of O star winds.

We do not use our stochastic thermal feedback model for OB stars because ionization heating is limited to $2 \times 10^4 \text{ K}$ by hydrogen recombination, and heating to higher temperature is unphysical. Just heating to $2 \times 10^4 \text{ K}$ is ineffective due to overcooling. In reality, radiation pressure and ionization heating form low-density H II bubbles, but we don't have a reasonable subgrid model for the bubble formation process.

AGB feedback For stellar wind from AGB stars, we only consider mass and metal input. We cannot resolve the circumstellar envelope of an AGB star at $R \lesssim 1 \text{ pc}$ (e.g., Höfner and Olofsson, 2018). In our simulations, a star particle represents a star cluster; however, in reality, stars are dispersed. To account for this, we consider the star particle to be representative of stars in the surrounding gas with a mass of $100 m_*$, assuming the star formation efficiency to be $\epsilon_* \sim 0.01$. Thus, we set the mass enclosed inside the shock radius of the AGB feedback to $M(R_{\text{shock}}) = 100 m_*$ and distribute the mass and metals to gas particles inside the shock radius. We do not consider the mechanical feedback from stellar winds because it is slower ($\sim 10 \text{ km s}^{-1}$) than (and negligible in comparison to) SN feedback. However, we add a boost-back momentum for momentum conservation. If the relative velocity between the star and gas particles is large, the boost-back momentum can have a significant impact (Hopkins et al., 2018, Su et al., 2019).

2.5.3 Results from GADGET3-OSAKA simulations

To explore the thermal and mechanical feedback effects, we ran five simulations with different feedback settings, as summarized in Table 2.1. We retained the amount of mass and metals ejected by SNe and AGB stars and changed only the energy and momentum injection models. When feedback is turned off, its energy is reduced. All simulations have AGB feedback.

TABLE 2.1: List of isolated galaxy simulations used in this chapter.

Run Name	Feedback Type				Note
	Type II SN mechanical FB	Type II SN thermal FB	Stochastic thermal FB	Type Ia & OB star mechanical FB	
Fiducial	✓	✓	✓	✓	Fiducial run with all feedback models
Non-stochastic	✓	✓	✓	✓	Fiducial but thermal energy is distributed without stochastic treatment
SNII-kinetic		✓			Type II SN mechanical feedback only
SNII-thermal			✓		Type II SN thermal feedback only
No-FB					No feedback

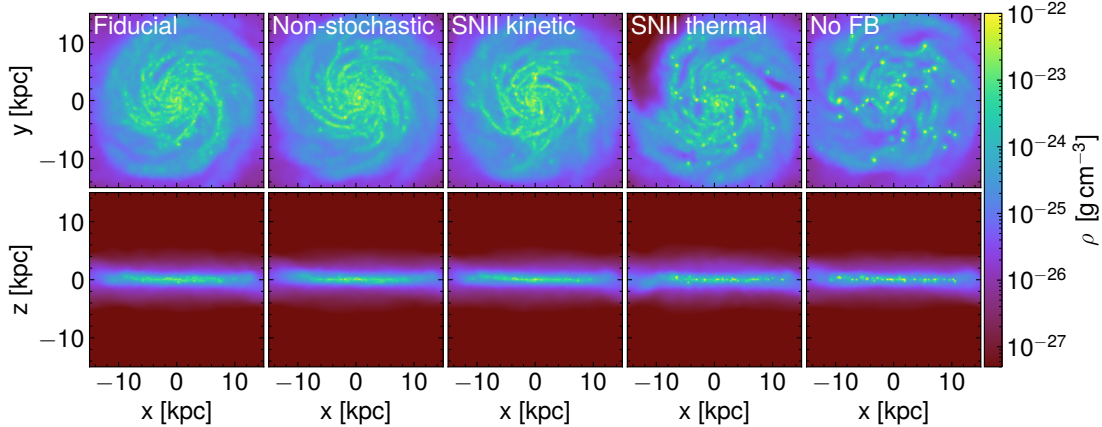


FIGURE 2.2: Projected gas density plots of the isolated galaxies in given Table 2.1 at $t \simeq 1$ Gyr in $30 \text{ kpc} \times 30 \text{ kpc}$ images. The top and bottom rows depict face-on and edge-on images, respectively. Here, we plot $\sum \rho^2 / \sum \rho$ to enhance the contrast and to use the same density-weighted method for both temperature and metallicity.

2.5.3.1 Projection Maps

Figures 2.2, 2.3, and 2.4 show the density-weighted projection plots of density, temperature, and metallicity of the simulated galaxies at $t \simeq 1$ Gyr. Galaxies are centered at the density-weighted center of gas mass,

$$\mathbf{r}_{\text{center}} = \frac{\sum_i \rho_i m_i \mathbf{r}_i}{\sum_i \rho_i m_i}. \quad (2.33)$$

In Figure 2.2, one can see that the density structure in the presence of mechanical feedback differs from that in its absence. The gas disk is maintained for 1 Gyr in three runs with Type II SN mechanical feedback (Fiducial, Non-stochastic, and SNII-kinetic), while the gas disks become clumpy in the other two runs. This result suggests that the galactic disk is supported against gravity by the turbulence driven by mechanical feedback. Comparing the Fiducial and Non-stochastic runs, the effect of stochastic thermal feedback is not clearly seen in the density distribution.

Figure 2.3 shows the density-weighted temperature. One can see the hot bubbles formed by the stochastic thermal feedback inside the gas disks in the Fiducial and SNII-thermal runs, which escape from the galactic disk to produce the hot outflow. This feature is observed in X-ray by Nakashima et al. (2018), who suggested that the hot, gaseous halo of the Milky Way is formed by the hot outflow resulting from stellar feedback. The low-density regions created by mechanical feedback or gas depletion are shown as $\sim 10^6$ K because we set the initial temperature of the halo to 10^6 K.

The density-weighted metallicity is depicted in Figure 2.4. It should be noted that we did not change the metal injection model, and that these five runs are different at the

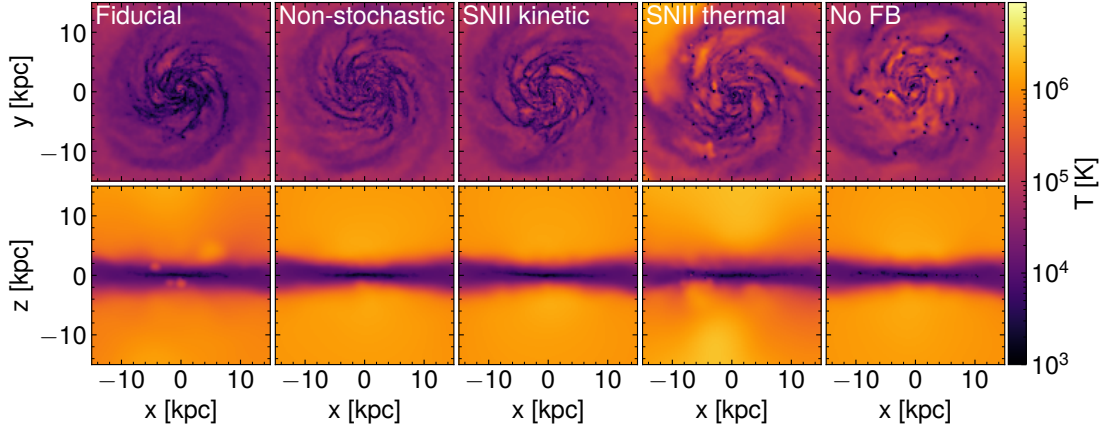


FIGURE 2.3: Projected temperature (density-weighted) of the isolated galaxies given in Table 2.1 at $t \simeq 1$ Gyr. The top and bottom rows depict face-on and edge-on images. The hot gas above the disk in the No-FB run is due to the galactic halo gas with $T = 10^6$ K implemented in the initial condition.

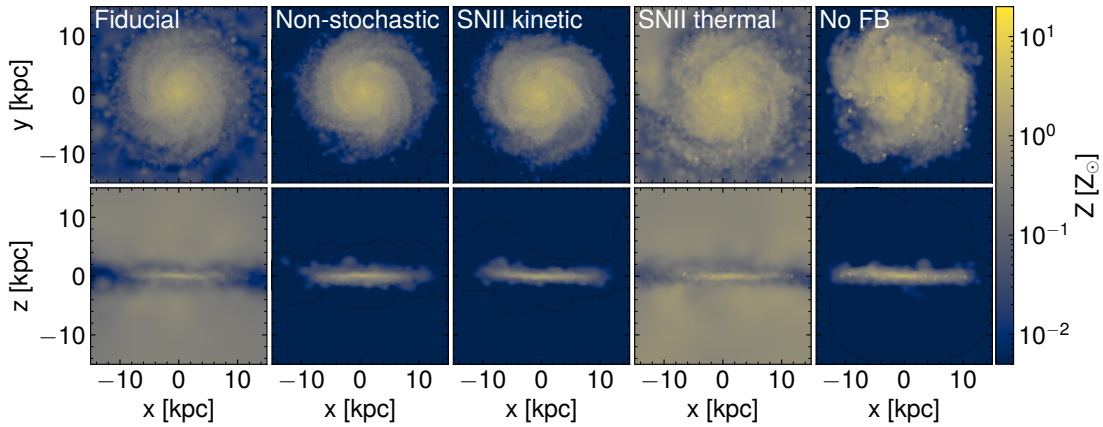


FIGURE 2.4: Projected metallicity (density-weighted) of the isolated galaxies given in Table 2.1 at $t \simeq 1$ Gyr. The top and bottom rows depict face-on and edge-on images. Metals carried by the outflows are visible above and below the disk.

models of energy and momentum injection. The metal distribution above the galactic disks in the presence of stochastic thermal feedback differs from that in its absence. We also indicate the distribution of metals on the virial radius (205 kpc) scale in Figure 2.5. Metal outflows were not observed in the Non-stochastic run. This result is consistent with those of [Shin et al. \(2021\)](#), who demonstrated that metal outflow is suppressed by ram pressure from the hot gaseous halo using GADGET2 code with a simple thermal dump [SN](#) feedback model. On the other hand, the Fiducial run shows the metal outflows beyond the virial radius. We will further compare our work with that of [Shin et al. \(2021\)](#) in Section 2.5.3.5.

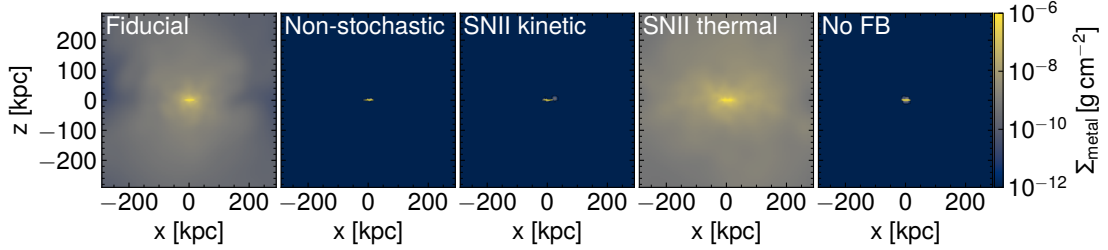


FIGURE 2.5: Large-scale, edge-on view of metal column density at $t \simeq 1$ Gyr. It is clear that the metals are carried over large distances in the Fiducial and SNII-thermal runs.

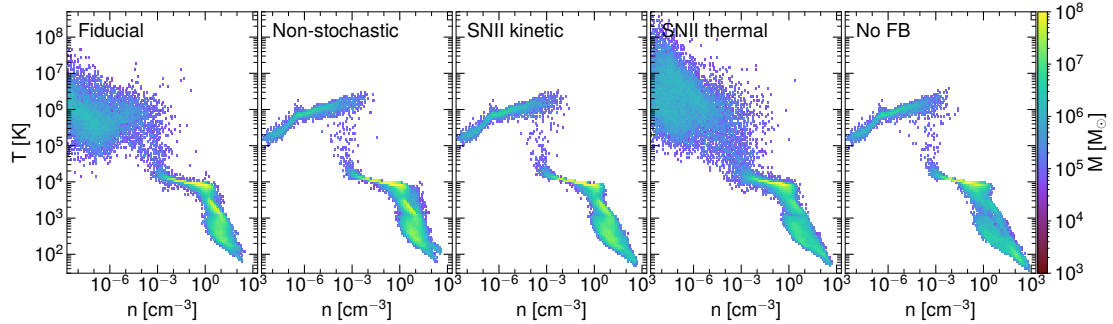


FIGURE 2.6: Phase diagram of the gas in the isolated galaxies given in Table 2.1 at $t \simeq 1$ Gyr. The dense, cold gas ($T < 10^3$ K) in the galactic disk is visible on the lower right corner. The hot, tenuous gas heated by feedback adiabatically cools and then joins the hot gaseous halo in the upper left region with $T \sim 10^6$ K. The hot component is most visible in the SNII-thermal run due to the highest star formation rate and subsequent strong thermal feedback. The hot gas seen in the No-FB run is due to the hot halo implemented in the initial condition.

2.5.3.2 Phase Diagrams

Figure 2.6 shows the phase diagrams of simulated galaxies at $t \simeq 1$ Gyr. The dense, cold gas ($T < 10^3$ K) in the galactic disk is visible in the lower right corner. In three runs with mechanical [SN](#) feedback (Fiducial, Non-stochastic, and SNII-kinetic), two-phase [ISM](#) of the warm ($T \sim 2 \times 10^3$ K) and cold ($T \sim 3 \times 10^2$ K) phases were observed. Compared with them, the warm phase is less visible and the cold gas is more condensed at a lower temperature ($T < 10^2$ K) in SNII-thermal and No-FB runs. The hot, tenuous gas heated by thermal feedback adiabatically cools and joins the hot gaseous halo in the upper left region with $T \sim 10^6$ K. We do not see a difference in the upper left gas distributions of the Non-stochastic and No-FB runs, which indicates ineffective thermal feedback in the Non-stochastic run. The hot component is most visible in the SNII-thermal run due to its higher star formation rate and subsequent thermal feedback.

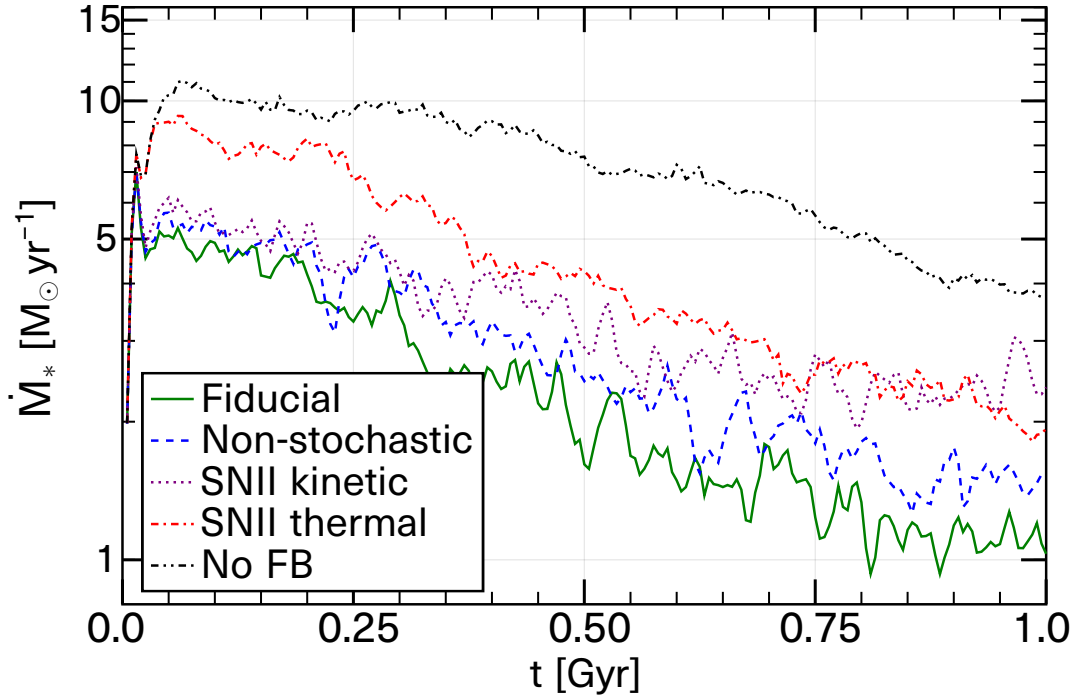


FIGURE 2.7: **SFR** as a function of time for the isolated galaxy simulations given in Table 2.1. The No-FB run has the highest **SFR**, and the SNII-thermal run shows weak suppression of **SFR**. In other runs, **SFR** is suppressed by the mechanical **SN** feedback efficiently.

2.5.3.3 Star Formation Histories

Figure 2.7 depicts the star formation history of the simulated galaxy. Star formation is suppressed in all the runs with feedback compared to the No-FB run. The thermal feedback suppresses star formation, and the mechanical feedback suppresses it further. Star formation rate in the Fiducial and Non-stochastic runs are slightly lower than that in the SNII-kinetic run because the mechanical feedback from Type Ia **SNe** and OB stars are not considered in the SNII-kinetic run. In our previous work Shimizu et al. (2019), we observed an ‘initial star burst’ which occurs just after the beginning of the simulations due to the collapse of gas without feedback. This phenomenon is weakened in this work because we first adiabatically evolve the initial condition to 0.5 Gyr for relaxation and then plot the star formation history with an interval of 5 Myr, which is approximately equal to the lifespan of a massive star.

2.5.3.4 Kennicutt–Schmidt Relation

Figure 2.8 shows the Kennicutt–Schmidt relations of the simulated galaxies given in Table 2.1 at $t = 1$ Gyr calculated with $500 \text{ pc} \times 500 \text{ pc}$ patches up to the galactic radius of $R = 10 \text{ kpc}$. The results from our simulations agree with the observed range by Bigiel

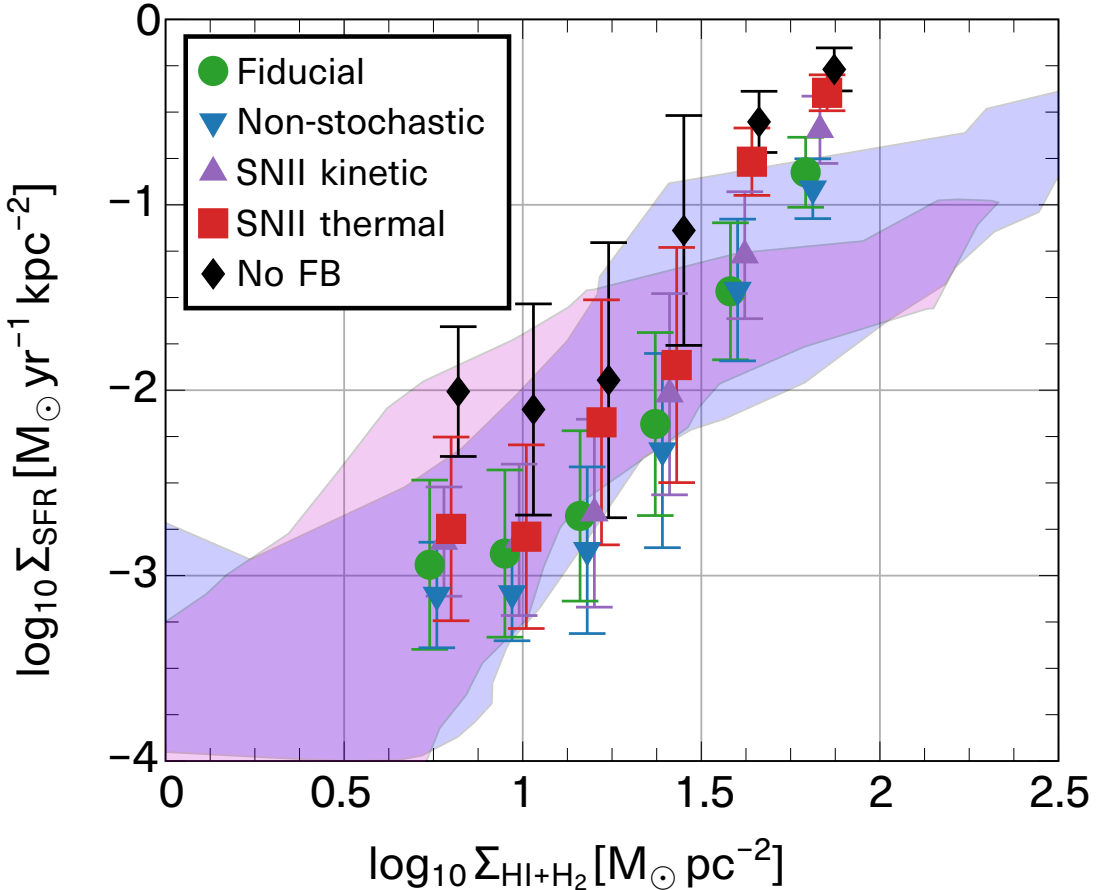


FIGURE 2.8: The Kennicutt–Schmidt relation of the simulated galaxies given in Table 2.1 at $t \simeq 1$ Gyr, calculated with $500 \text{ pc} \times 500 \text{ pc}$ patches. Colored regions depict the observational data of nearby spiral galaxies (blue: [Schruba et al. 2011](#); magenta: [Bigiel et al. 2008](#)).

[et al. \(2008\)](#), [Schruba et al. \(2011\)](#) with a similar slope and normalization, which is encouraging. The three runs with mechanical feedback (Fiducial, Non-stochastic, and SNII-kinetic) show similar results, and their star formation rate density is lower by a factor of 2–3 than that of No-FB run. The SNII-thermal run is inbetween No-FB and other runs consistently with Fig. 2.7. The simulated data fluctuates as a function of time but on average stays within the observed range. The Fiducial and Non-stochastic runs have the lowest Σ_{SFR} among all runs due to low SFR , as shown in Fig. 2.7.

The simulation data point corresponding to the highest gas column density is above the observed data; at this point, it is unclear if our results will turn over at higher column densities due to limitations in our resolution. The cut-off at the lower end of the simulation data is determined by mass resolution and by how well we can track star formation in a low-density region, which will be explored in future works.

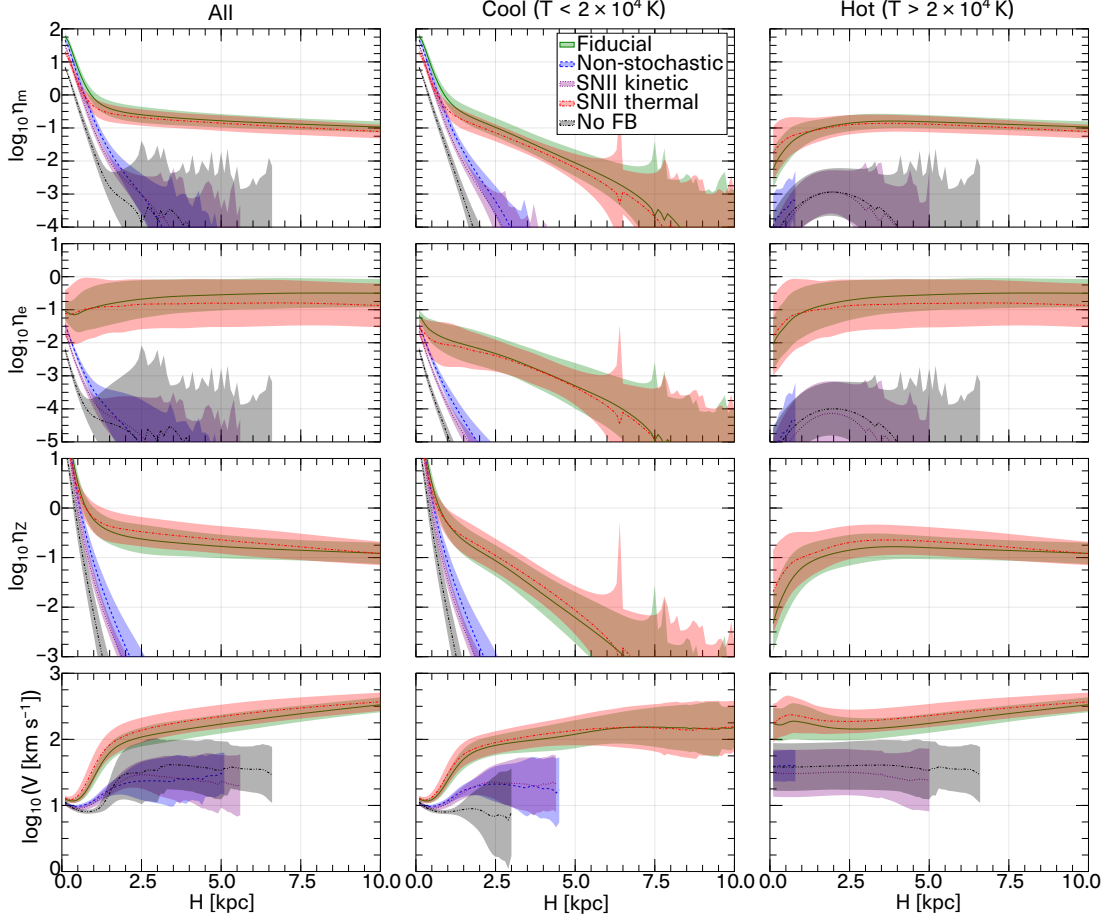


FIGURE 2.9: Mass (top row), energy (second row), and metal (third row) loading factors vs. the height above the galactic plane. The fourth row depicts outflow velocity vs. the height above the galactic plane. All quantities are measured using cylinders of different heights and a 10 kpc radius and averaged over $t = 0.5 - 1.0$ Gyr. The lines indicate the average values during this time period, with $\pm 1\sigma$ shade for time variation.

2.5.3.5 Outflow Profiles of Mass, Energy, Velocity, and Metals

The outflow rate of physical value X at a height H above the galactic plane is

$$\dot{X}_{\text{out}}(H) = \int \rho_X v_z dS_H = \int_{S_H} \sum_i X_i v_{i,z} W(r_{ij}, h_{\text{sml},i}) dr_j, \quad (2.34)$$

where S_H , ρ_X , and v_z denote the plane at height H , the density of X , and velocity in the z -direction, while W indicates the kernel function used in the simulation. Other symbols, such as r_{ij} , $v_{i,z}$, and $h_{\text{sml},i}$ denote the distance from the i -th gas particle to r_j , the z -direction outflow velocity, and the smoothing length of the i -th gas particle, respectively. We rewrite this equation as follows, to compute the outflow rate from

simulation snapshots (Shimizu et al., 2020):

$$\dot{X}_{\text{out}}(H) = \sum_i X_i v_{i,z} \int_0^{\sqrt{h_{\text{sml},i}^2 - \zeta_i^2}} 2\pi \xi W \left(\sqrt{\zeta_i^2 + \xi^2}, h_{\text{sml},i} \right) d\xi, \quad (2.35)$$

where $\zeta_i = |z_i - H|$ and z_i is the z coordinate of i -th particle.⁷ To evaluate the intrinsic outflow, we take the summation over those outflowing gas particles that have non-zero metallicity. Since the metallicity is initially zero and metal mixing between gas particles is not considered, such particles are considered as metal-enriched outflows.

We depict the outflow profiles of mass, energy, and metal loading factor

$$\eta_m = \frac{\dot{M}_{\text{out}}}{\dot{M}_*}, \quad (2.38)$$

$$\eta_e = \frac{\dot{E}_{\text{out}}}{\epsilon_{\text{SNII}} \dot{M}_*}, \quad (2.39)$$

$$\eta_Z = \frac{\dot{M}_{Z,\text{out}}}{\mu_{Z,\text{SN}} \dot{M}_*}, \quad (2.40)$$

averaged over $t = 0.5 - 1.0$ Gyr, in Fig. 2.9. Here, \dot{M}_{out} , \dot{E}_{out} , and $\dot{M}_{Z,\text{out}}$ are the outflow rates of mass, energy, and metals, while \dot{M}_* is the star formation rate and $\mu_{Z,\text{SN}} = 0.01$ is the specific metal mass released by Type II SNe. We also compute density-weighted, average outflow velocity,

$$V_{\text{out}}(H) = \frac{\int \rho v_z dS_H}{\int \rho dS_H} = \frac{\sum_i m_i v_{i,z} \int_0^{\sqrt{h_{\text{sml},i}^2 - \zeta_i^2}} 2\pi \xi W \left(\sqrt{\zeta_i^2 + \xi^2}, h_{\text{sml},i} \right) d\xi}{\sum_i m_i \int_0^{\sqrt{h_{\text{sml},i}^2 - \zeta_i^2}} 2\pi \xi W \left(\sqrt{\zeta_i^2 + \xi^2}, h_{\text{sml},i} \right) d\xi}, \quad (2.41)$$

where m_i is the mass of the i -th gas particle. The profiles of the total mass and the metal loading factor are high at low altitudes, decrease rapidly to $H \sim 1.0$ kpc, and become flatter at $H \gtrsim 1.0$ kpc.

At $H \lesssim 1.0$ kpc, the cool ($T < 2 \times 10^4$ K) component dominates mass outflow (higher η_m in the top middle panel of Fig. 2.9), which is slow ($V \lesssim 30 \text{ km s}^{-1}$) and falls back to the galaxy. We see that the mass loading factor of cool outflow in the runs with feedback is greater by ~ 0.8 dex over that of No-FB run.

⁷We used the quintic B-spline kernel function in our simulations. In this case, the integral accounting for the cross-section of the SPH particle and the plane of height H can be analytically calculated as

$$\int_0^{\sqrt{h^2 - \zeta^2}} 2\pi \xi W \left(\sqrt{\zeta^2 + \xi^2}, h \right) d\xi = f_{\frac{1}{3},1}(\zeta, h) + f_{-2,\frac{2}{3}}(\zeta, h) + f_{5,\frac{1}{3}}(\zeta, h), \quad (2.36)$$

where

$$f_{a,b}(\zeta, h) = \frac{3^9 a}{359 h^2} \left(b - \frac{\zeta}{h} \right)_+^6 \left(\zeta + \frac{h}{7} \left(b - \frac{\zeta}{h} \right)_+ \right). \quad (2.37)$$

Here, $(\cdot)_+ \equiv \max(0, \cdot)$.

At $H \gtrsim 2.5$ kpc, the hot ($T > 2 \times 10^4$ K) component dominates outflow. We see that the mass loading factor of hot outflow in runs with stochastic thermal feedback (Fiducial and SNII-thermal) is much higher than that of others, which indicates that stochastic thermal feedback launches hot outflow. Non-stochastic and SNII-kinetic runs shows much weaker hot outflow, demonstrating that simply distributing thermal energy from SN feedback is ineffective in launching hot outflow. The outflow profile of Fiducial run is qualitatively consistent with high-resolution small-box simulations solving a patch of galactic disk (Kim et al., 2020b).

Figure 2.10 shows the outflow profiles up to 200 kpc. We calculate the outflow rates at the surface of a sphere with a radius R centered at the galactic center, and show the loading factors and outflow velocity of all components. The hot component dominates at $R > 10$ kpc with cool component disappearing at large R . We see the outflow is accelerated towards large R and reaches $\gtrsim 560$ km s $^{-1}$ at $R = 200$ kpc. The mass loading factor of Fiducial run at $R = 200$ kpc is $\eta_m \sim 0.3$. In all the panels the SNII-thermal model shows somewhat higher loading factors and outflow velocity than the Fiducial run, which is due to higher SFR in the former model as was shown in Fig. 2.7.

For the presented isolated galaxy test, we followed Shin et al. (2021) in adding a gaseous halo to the initial condition. As shown in Fig. 2.9, metals are transported via the hot outflow driven by thermal feedback, while the cool outflow cannot transport metals beyond $H = 5$ kpc. This is because the hot outflow driven by thermal feedback is not impeded by the ram pressure of the gaseous halo $P_{\text{ram}} = \rho v^2$ due to its higher thermal pressure. On the other hand, the cool outflow is decelerated by the ram pressure of the gaseous halo because it is not accelerated after its initial launch by momentum feedback.

Our stochastic thermal feedback model heats the gas particles up to a higher temperature than simple thermal dump models do, driving hot outflow without increasing the total SN feedback energy by hand. The discrepancy in metal outflow between mesh-based (ENZO) and particle-based (GADGET-2 and GIZMO) simulations reported by Shin et al. (2021) could be due to the difference in mass resolution; particle-based simulations fix the mass resolution, but mesh-based simulations do not fix it and can effectively heat gas cells at low-density voids created by previous SN feedback events.

2.5.4 Discussion on the SN feedback model

In our model, we assume that the superbubbles spread isotropically. However, when the ISM is highly non-uniform, the superbubbles spread selectively towards the low-density channel (Ohlin et al., 2019). In particular, when the superbubbles break out, the kinetic feedback to the local star formation may be weaker, as the energy flows out of the galaxy

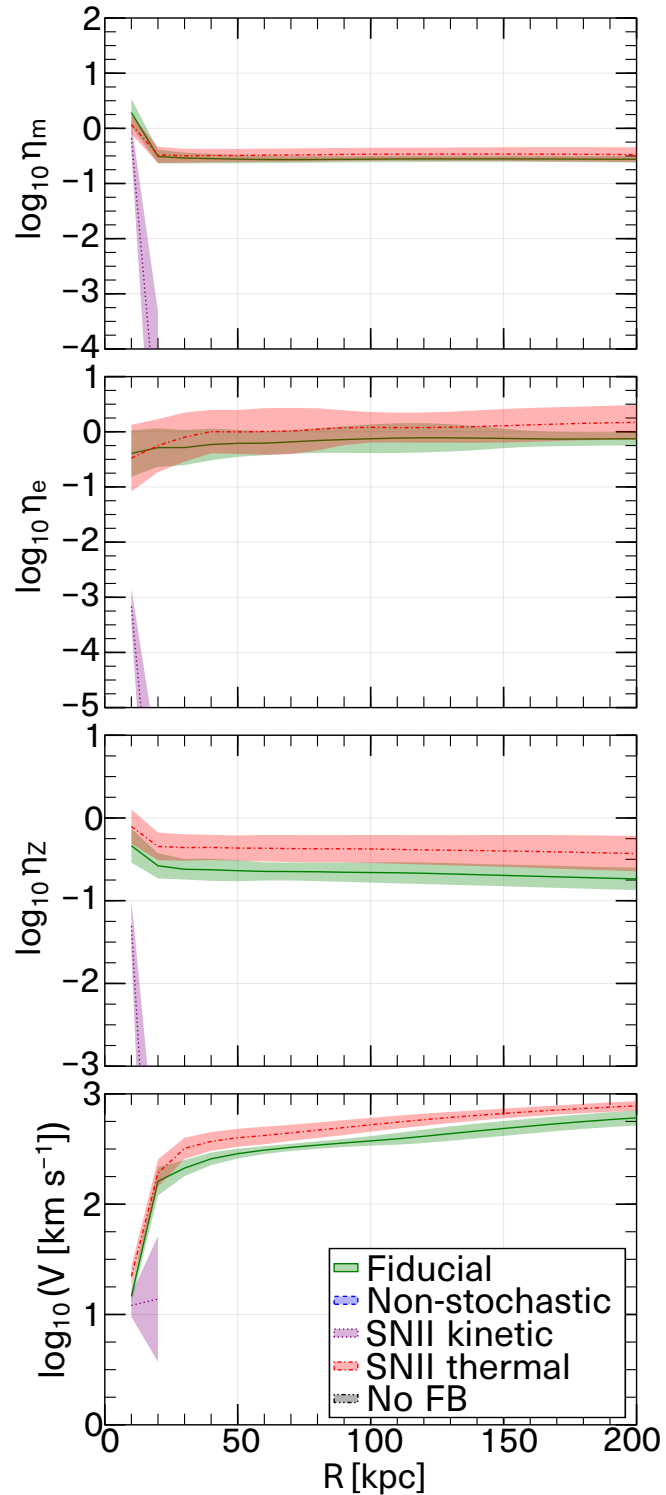


FIGURE 2.10: Same as Figure 2.9 but measured with spheres of different radii up to 200 kpc, centered at the galactic center and averaged between $t = 0.5 - 1.0$ Gyr. The lines show the average during this time period with $\pm 1\sigma$ shade for the time variation.

before the superbubbles gain momentum (Fielding et al., 2018). Although our feedback model considers the non-uniformity of the [ISM](#) via anisotropic particle distribution, the impact of non-uniform [ISM](#) needs to be examined in the future with a more realistic setup and a higher resolution. For example, an analytical model considering the effect of superbubble breakout could be incorporated to construct a more realistic feedback model (Orr et al., 2022b).

There are several different weighting schemes to distribute mechanical feedback in particle simulation such as Hopkins et al. (2018), Hu (2019), Marinacci et al. (2019). However, the detailed distribution of particles on sub-resolution scales is somewhat random, and the exact weighting scheme does not matter very much in the final outcome as long as it is isotropic.

The models of Kimm and Cen (2014) and Hopkins et al. (2018) estimated the momentum by scaling that of isolated supernova explosions. However, the superbubble momentum also depends on the time interval of supernova explosions as we show in this work. Here we develop a more realistic model by using a universal scaling relation for the superbubble terminal momentum and radius, and this is where our model is different from Kimm and Cen (2014) and Hopkins et al. (2018).

In addition to momentum feedback, thermal feedback was also considered by Kimm and Cen (2014) and Hopkins et al. (2018), where they simply injected thermal energy. However, thermal feedback will not work if the model is not constructed to avoid overcooling (Hu, 2019). Therefore, in our model, we adopt a stochastic thermal feedback model. In the isolated galaxy test, we show that the thermal outflow is driven by the stochastic model.

Dalla Vecchia and Schaye (2012) constructed a stochastic thermal feedback model with temperature rise, ΔT , as a free parameter. However, the temperature is not constant during the evolution of high-temperature bubbles formed by supernova explosions. Therefore, a parameter survey is necessary to determine ΔT , and using temperature as a model parameter is not so ideal as we discuss in Section 2.4. Instead, we use entropy as a parameter in our model. Since the high-temperature outflow gas expands adiabatically, the entropy is constant and its value can be determined based on high-resolution simulations.

In our model, we also provide momentum feedback in addition to thermal feedback. As shown in the isolated galaxy test, thermal feedback can only suppress star formation weakly. This is because the spatial resolution required to solve for the time evolution of [SN](#) remnant is more stringent than the mass resolution required to resolve for hot [SN](#) bubbles (Section 2.1).

Our thermal feedback model heats gas particles up to a fixed entropy, which means denser gas particles are heated to higher temperatures. In high- z galaxies where the gas density is higher than in the local ones, our thermal feedback would become stronger. [Arata et al. \(2020\)](#) performed cosmological galaxy simulations using the stochastic thermal feedback model by [Dalla Vecchia and Schaye \(2012\)](#), with $\Delta T = 10^{7.5}$ K and studied metal-emission lines from high- z galaxies. They showed that the radial profile of [C II] surface brightness of simulated galaxies is lower at outer radius than observation. This discrepancy could be resolved by our stronger thermal feedback. In future works, we will investigate the impact of our [SN](#) feedback model in a cosmological context.

Our [SN](#) feedback model injects both terminal momentum and thermal energy from [SNe](#), which may overestimate the feedback effect. In reality, some [SN](#) energy is used to drive a superbubble and the other is used to accelerate outflows after the break-out of the superbubble. [Orr et al. \(2022b\)](#) developed an analytic model for clustered [SNe](#) in a galactic disk, and their model predicts that the superbubble is more likely to break out in an environment with rich gas and short dynamical times, which is consistent with observations and simulations ([Orr et al., 2022a](#)). Their model could be incorporated into our [SN](#) feedback model in the future.

Chapter 3

Method

In this chapter, we describe the methodology of the cosmological hydrodynamic simulation.

3.1 Initial Condition

We generate an initial condition using MUSIC2-MONOFONIC¹ (Michaux et al., 2021, Hahn et al., 2021). The phase fixing technique (Angulo and Pontzen, 2016) is used to suppress the impact of cosmic variance, but we run only a single simulation for each model and do not include paired simulations for the analyses in this paper. We adopt the following cosmological parameters from Planck Collaboration et al. (2020), $(\Omega_m, \Omega_b, \Omega_\Lambda, h, n_s, 10^9 A_s) = (0.3099, 0.0488911, 0.6901, 0.67742, 0.96822, 2.1064)$.² The initial condition is generated at $z_{\text{ini}} = 39$ using the third-order Lagrangian perturbation theory. The transfer function at z_{ini} is obtained by back-scaling the transfer function at reference redshift $z_{\text{ref}} = 2$ computed by Boltzmann code CLASS³ (Blas et al., 2011). The simulation box size is $L_{\text{box}} = 50 h^{-1} \text{cMpc}$, and the total number of particles is $N_p = 2 \times 512^3$; the initial particle mass of dark matter and gas is $m_{\text{DM}} = 6.74 \times 10^7 h^{-1} \text{M}_\odot$ and $m_{\text{gas}} = 1.26 \times 10^7 h^{-1} \text{M}_\odot$, respectively.⁴

¹The code's website is <https://bitbucket.org/ohahn/monofonic/src/master/>

²The best-fit parameters of the baseline model 2.20 base_plikHM_TTTEEE_lowl_lowE_lensing_-post_BAO_Pantheon of Planck 2018 cosmological parameter table as of May 14, 2019 (https://wiki.cosmos.esa.int/planck-legacy-archive/images/b/be/Baseline_params_table_2018_68pc.pdf).

³The code's website is <http://class-code.net/>

⁴cMpc denotes Mega parsec in comoving coordinate.

3.2 Cosmological Hydrodynamic Simulation

We use the cosmological N-body/[SPH](#) code GADGET4-OSAKA (Romano et al., 2022a,b), which is a privately developed branch of GADGET-4⁵ (Springel et al., 2021). The GADGET-4 is the successor of the GADGET-3 (last described in Springel, 2005, as GADGET-2), on which our GADGET3-OSAKA is based. GADGET-4 has improved performance and some useful modules for large-scale cosmological simulation over the earlier implementation.

The Newtonian gravity for dark matter and baryons is solved via

$$\Delta\Phi = 4\pi G\rho, \quad (3.1)$$

using the third-order TreePM method (Xu, 1995, Bagla, 2002, Springel, 2005). The same gravitational softening length is used for all particle types, and it is set to $\epsilon_{\text{grav}} = 3.38 h^{-1} \text{ ckpc}$ but limited to physical $0.5 h^{-1} \text{ kpc}$ at all times.

The [SPH](#) method (for reviews, see Rosswog, 2009, Springel, 2010a, Price, 2012) is used to solve the governing equations of hydrodynamics,

$$\frac{d\rho}{dt} = -\rho\nabla \cdot \mathbf{v} - \mathcal{S} + \mathcal{I}, \quad (3.2)$$

$$\frac{d\mathbf{v}}{dt} = \frac{\nabla P}{\rho} + \mathcal{K}, \quad (3.3)$$

$$\frac{du}{dt} = -\frac{P}{\rho}\nabla \cdot \mathbf{v} + \Gamma - \Lambda + \mathcal{T}, \quad (3.4)$$

where ρ , P , and \mathbf{v} are density, pressure, and velocity, respectively, and $\frac{d}{dt} = \frac{\partial}{\partial t} + \mathbf{v} \cdot \nabla$ is the material derivative. The integration is carried out on the expanding comoving coordinate. The \mathcal{S} and \mathcal{I} in the equation of continuity (3.2) denote gas mass converted to stars and mass injected from [SNe](#) and [AGB](#) stars. The \mathcal{K} in the equation of motion (3.3) denotes momentum injection by [SN](#) feedback, and \mathcal{T} in the energy equation (3.4) denotes thermal energy injection by [SN](#) and [AGN](#) feedback. The treatment of \mathcal{S} , \mathcal{I} , \mathcal{K} , and \mathcal{T} are described in the following subsections. The next subsection 3.3 describes the details and development of numerical treatment of hydrodynamics.

The heating rate, Γ , and the cooling rate, Λ , are computed using the GRACKLE⁶ library (Smith et al., 2017), which solves the non-equilibrium primordial chemistry network of 12 chemical species, H, D, He, H₂, HD, and their ions, with radiative cooling by metals and photo-heating and photo-ionization by uniform [UV](#) background. The metal cooling rate is precomputed using the photoionization code CLOUDY (Ferland et al., 2013), and the

⁵The code's website is <https://wwwmpa.mpa-garching.mpg.de/gadget4/>

⁶The code's website is <https://grackle.readthedocs.io/en/latest/>

UV background model by [Haardt and Madau \(2012\)](#) is assumed. In GRACKLE, we set the parameters related to the onset of UV background to `UVbackground_redshift_on=8` and `UVbackground_redshift_fullon=6`, and then the cosmic reionization occurs at $z \sim 7$. Our simulations do not include the heating by the cosmic ray and stellar radiation, and we ignore the self-shielding of the UV background by atomic hydrogen to avoid overcooling of neutral gas.

We follow 12 chemical elements, H, He, C, N, O, Ne, Mg, Si, S, Ca, Fe, and Ni, produced by core-collapse SNe, type-Ia SNe, and AGB stars. The metallicity floor is $Z_{\text{floor}} = 10^{-6} Z_{\odot}$, where $Z_{\odot} = 0.0134$ is the solar metallicity ([Asplund et al., 2009](#)).

GADGET4-OSAKA solves the production and destruction of dust as described in [Romano et al. \(2022a\)](#) following the full dust grain size distribution; however, we do not focus on dust in this work and omit the description of the dust module here. The analysis of dust will be made in our future work.

We use the Smagorinsky-Lilly type turbulent metal and dust diffusion model ([Smagorinsky, 1963](#), [Shen et al., 2010](#), [Romano et al., 2022a](#)) with a diffusion parameter $C_{\text{diff}} = 2 \times 10^{-4}$.

The non-thermal Jeans pressure floor ([Hopkins et al., 2011](#), [Kim et al., 2016](#)) is applied to avoid artificial fragmentation as described in Section 3.3.1.4. The lower limit of the temperature is set to the higher value of the CMB temperature and $T_{\text{min}} = 15$ K, and the upper limit is set to $T_{\text{max}} = 10^9$ K.

The simulations presented in this chapter are performed at the SQUID supercomputer at Cybermedia Center, Osaka University, equipped with dual Intel Xeon Platinum 8368 processors (2.4 GHz) per compute node. Running the Fiducial model took 1.12×10^5 CPU hours.

3.3 Numerical method

We here describe the numerical methodology of the cosmological hydrodynamics simulation by GADGET4-OSAKA.

3.3.1 SPH

We determine the smoothing length by

$$\frac{4}{3} \pi h_i^3 n_i = N_{\text{ngb}}, \quad (3.5)$$

where

$$n_i = \sum_{j=1}^N W_{ij}(h_i) \quad (3.6)$$

is the **SPH** particle number density, and $W_{ij}(h_i) \equiv W(|\mathbf{r}_i - \mathbf{r}_j|; h_i)$ is the kernel function. We use the Wendland C4 kernel function (Wendland, 1995, Dehnen and Aly, 2012) with neighbor number $N_{\text{ngb}} = 120 \pm 2$.

We use the pressure-energy formulation of **SPH** (Hopkins, 2013, Saitoh and Makino, 2013). The equation of motion of **SPH** particle is

$$\frac{dv_i}{dt} = - \sum_{j=1}^N m_j \left[f_{ij} \frac{u_j}{u_i} \frac{\bar{P}_i}{\bar{\rho}_i^2} \nabla_i W_{ij}(h_i) + f_{ji} \frac{u_i}{u_j} \frac{\bar{P}_j}{\bar{\rho}_j^2} \nabla_j W_{ij}(h_j) \right]. \quad (3.7)$$

The energy equation is

$$\frac{du_i}{dt} = \sum_{j=1}^N m_j f_{ij} \frac{u_j}{u_i} \frac{\bar{P}_i}{\bar{\rho}_i^2} (\mathbf{v}_i - \mathbf{v}_j) \nabla_i W_{ij}(h_i), \quad (3.8)$$

where

$$\bar{P}_i = \sum_{j=1}^N (\gamma - 1) m_j u_j W_{ij}(h_i) \quad (3.9)$$

is the smoothed pressure, $\bar{\rho}_i = \bar{P}_i/[(\gamma - 1)u_i]$ is the internal-energy-weighted smoothed density, and

$$f_{ij} = \left[\frac{h_i}{3(\gamma - 1)n_i m_j u_i} \frac{\partial \bar{P}_i}{\partial h_i} \right] \left(1 + \frac{h_i}{3n_i} \frac{\partial n_i}{\partial h_i} \right)^{-1} \quad (3.10)$$

is the grad- h term, which accounts for the variation of the smoothing length.⁷

We did not use the pressure-entropy formulation, another pressure-based **SPH** variant implemented in original GADGET-4. The pressure-entropy **SPH** cannot correctly increase or decrease energy without a costly iterative treatment when energy is added or reduced by subgrid physics (Borrow et al., 2021). This is because the smoothed density $\bar{\rho}_i = (1/A_i^{1/\gamma}) \sum_j m_j A_j^{1/\gamma} W_{ij}(h_i)$ is coupled to the entropy A_i , and one cannot change the particle's energy $u_i = A_i \bar{\rho}_i^\gamma$ as desired by simply updating entropy. In the pressure-energy formulation, each **SPH** particle explicitly has an internal energy variable, and modifying the energy is straightforward.

⁷Note that entropy and energy are simultaneously conserved in the pressure-energy **SPH** formulation derived from Lagrangian (Hopkins, 2013).

3.3.1.1 SIMD Vectorization

To execute large-scale simulations, it is necessary to improve the computational efficiency of the simulation code. We vectorized the density and hydro force evaluation kernel using the AVX-512 vector extension instruction set, which can perform arithmetic or logical instruction for eight 64-bit double variables in a single instruction (single instruction, multiple data; SIMD). The **SPH** calculation consists of a doubly-nested loop; 1) for all active particles, 2) we take kernel-weighted sums. [Springel et al. \(2021\)](#) reported that the original GADGET-4 code shows no significant improvement in the computational speed using the AVX2 instruction set. This would be likely because they vectorized the innermost **SPH** loop, where the memory bandwidth limits the calculation speed. Instead, we vectorize the outer loop by simultaneously processing a group of **SPH** particles ([Barnes, 1990](#)).

At the beginning of every **SPH** evaluation loop, we form groups consisting of, at most, eight particles using the indices of **SPH** particles. The indices are assigned using the Peano-Hilbert curve when the domain decomposition is carried out, and the particles that are close on the index list are also close in positions ([Springel et al., 2005](#)). To form groups, we check particles in the order of indices and add a particle to a group if their regions to search for neighbors overlap each other. We find twice the speed up of calculation in a realistic cosmological zoom-in simulation.

3.3.1.2 Artificial Conduction

We include artificial conduction, a diffusive term of internal energy, for a better capturing of pressure discontinuity, i.e., shocks. We implemented the artificial conduction of the following form ([Price, 2008](#)), which conserves the internal energy within the kernel:

$$\frac{du_i}{dt} = \sum_j m_j \alpha_{\text{cond},ij} v_{\text{sig},ij} \frac{u_i - u_j}{\rho_{ij}} \nabla_i \bar{W}_{ij}, \quad (3.11)$$

where m and u denote mass and internal energy, $\rho_{ij} = (\rho_i + \rho_j)/2$ denotes the mean density of particle i and j , and $\bar{W}_{ij} = [W_{ij}(h_i) + W_{ij}(h_j)]/2$ denotes the symmetrized kernel between i and j .

We use the conduction limiter proposed by [Borrow et al. \(2022\)](#) for the conduction coefficient $\alpha_{\text{cond},ij}$, which is computed as

$$\alpha_{\text{cond},ij} = \frac{\alpha_{\text{cond},i} P_i + \alpha_{\text{cond},j} P_j}{P_i + P_j} \quad (3.12)$$

with

$$\alpha_{\text{cond},i} = \alpha_{\text{cond}} \left(1 - \frac{\alpha_{\text{max},i}}{\alpha_{\text{visc}}} \right) \quad (3.13)$$

and

$$\alpha_{\text{max},i} = \max_{r_{ij} < h_i} \alpha_{\text{tdav},j} \quad (3.14)$$

where α_{cond} and α_{visc} are constant coefficients of artificial conduction and viscosity, α_{tdav} is the time-dependent coefficient of artificial viscosity, and P is thermal pressure. In this work, we use constant viscosity with field reconstruction as discussed below, but we also compute the time-dependent coefficient α_{tdav} to limit the artificial conduction at shocks. We use the default time-dependent coefficient in GADGET-4, which was originally proposed by [Hu et al. \(2014\)](#).

For the conductivity signal velocity, we use the expression commonly used for simulations with self-gravity ([Wadsley et al., 2008](#)):

$$v_{\text{sig},ij} = \frac{|\mathbf{r}_{ij} \cdot \mathbf{v}_{ij}|}{r_{ij}}. \quad (3.15)$$

3.3.1.3 Field Reconstruction

Field reconstruction is commonly used in the finite-volume scheme. [Frontiere et al. \(2017\)](#) and [Rosswog \(2020\)](#) used velocity field reconstruction in [SPH](#) to reduce excessive artificial diffusion and showed encouraging results. Similar improvement is obtained by [Price and Laibe \(2020\)](#), who used a reconstructed velocity field to compute drag force between gas and dust particles in two-fluid [SPH](#) simulations.

We compute the artificial viscosity with velocities linearly reconstructed at the particle mid-point ([Frontiere et al., 2017](#), [Rosswog, 2020](#)). The high-order estimator of the velocity gradient by [Hu et al. \(2014\)](#) is used to reconstruct the velocity field.

3.3.1.4 Jeans pressure floor

The non-thermal Jeans pressure floor is introduced to avoid numerical fragmentation. This additional pressure term can be interpreted as unresolved interstellar turbulence and allows us to follow the thermal evolution of atomic gas to low temperature.

The floor is usually implemented as

$$P_{\text{hydro}} = \max\{P, P_{\text{Jeans}}\}, \quad (3.16)$$

and

$$P_{\text{Jeans}} = (\gamma\pi)^{-1} G N_{\text{Jeans}}^2 \rho^2 \Delta x^2, \quad (3.17)$$

where $\gamma = 5/3$ is the adiabatic index, $N_{\text{Jeans}} = 4$ is the Jeans number (Truelove et al., 1997), and $\Delta x = \max(\epsilon_{\text{grav}}, (m/\rho)^{1/3})$ is the local resolution, which is the larger of the gravitational softening length and the mean particle separation. The P is the particle's pressure, and P_{hydro} is the pressure used in the hydro force evaluation. This implementation works as intended in the density-based SPH formulation; however, care is necessary when used with the pressure-based formulation.

The pressure used in the pressure-based SPH (Eq. 3.9) is obtained from the kernel sum of internal energy. Modifying the pressure alone causes inconsistency between the internal energy and pressure. The appropriate implementation is to introduce a floor in the internal energy.⁸ For each SPH particle, we store floored internal energy, $u_{\text{hydro}} = \max\{u, P_{\text{Jeans}}/[(\gamma - 1)\rho]\}$, where $\rho = \sum_j^N m_j W_{ij}(h_i)$ is physical density, in addition to the original internal energy. We use the floored internal energy to compute the smoothed pressure and hydro force. The original internal energy is kept to compute gas temperature.

3.3.1.5 Time Integration

In GADGET-4, the hydrodynamical force is integrated using the second-order predictor-corrector method (Springel et al., 2021). In the following, we call the integration width on the timeline a time step, and the point on the timeline where a previous time step ends and the next step begins a synchronization point.

We use the time step limiter that wakes up inactive SPH particles to force a time step constraint (Saitoh and Makino, 2009, Durier and Dalla Vecchia, 2012). For the constraint, we use the signal velocity timestep limiter (Springel, 2010b, Springel et al., 2021) instead of constraining the neighbor's time step within a fixed factor of difference. The signal velocity limiter is more general and flexible than the fixed factor limiter, as demonstrated in Springel (2010b). The implementation of the signal velocity time step limiter in the original GADGET-4 is one-sided, and information on neighboring particles is used to constrain the new time step of a particle. We extended the limiter to a mutual constraint in our GADGET4-OSAKA; when the particle i is updated, we search its neighbor j and impose the time step constraint $\Delta t_j < C_{\text{CFL}} \Delta t_j^{\text{signal}}$, where

$$\Delta t_j^{\text{signal}} = \frac{2h_j + r_{ij}}{c_i^{\text{snd}} + c_j^{\text{snd}} - \mathbf{r}_{ij} \cdot \mathbf{v}_{ij}/r_{ij}}, \quad (3.18)$$

⁸In the density-based SPH, modifying the particle's pressure is equivalent to modifying its internal energy.

and $\mathbf{r}_{ij} = \mathbf{r}_i - \mathbf{r}_j$, $\mathbf{v}_{ij} = \mathbf{v}_i - \mathbf{v}_j$, $r_{ij} = |\mathbf{r}_{ij}|$, and c_i^{snd} is the sound speed of i -th particle. This wake-up scheme ensures that all **SPH** particles maintain the signal velocity time step criterion even when the velocity and the sound speed of neighboring particles are updated due to feedback.

The evaluation of $\Delta t_j^{\text{signal}}$ is carried out by walking on the oct-tree used for the neighbor search of **SPH** particles. For each node of the oct-tree, we store the maximum signal time step $\Delta t_{\max}^{\text{signal}}$, the maximum of $d^{\text{signal}} = c^{\text{snd}} \Delta t^{\text{signal}} - 2h$, the maximum sound speed c_{\max}^{snd} , and the maximum and the minimum of velocity in x-, y-, and z-direction ($v_{\max}^x, v_{\min}^x, v_{\max}^y, v_{\min}^y, v_{\max}^z, v_{\min}^z$) of **SPH** particles in the node. When we encounter a node in the tree walk, we compute the node opening criterion,

$$d_{\min} < d_{\max}^{\text{signal}} + \Delta t_{\max}^{\text{signal}} (c_i^{\text{snd}} - v_{\min}^{\text{rel}}), \quad (3.19)$$

where $v_{\min}^{\text{rel}} = \min_j (\mathbf{r}_{ij} \cdot \mathbf{v}_{ij} / r_{ij})$ is the minimum relative velocity, i.e., the largest approaching velocity, between particle i and particles in the node, which can be constrained using the maximum and minimum velocity of particles in the node. The d_{\min} is the smallest distance from the particle i to the node. If the opening condition is fulfilled, we open the node and continue walking on its daughter nodes. When we encounter a particle j , we compute Eq. (3.18) and update $\Delta t_j^{\text{signal}}$ if it is smaller. If $C_{\text{CFL}} \Delta t_j^{\text{signal}}$ is smaller than particle j 's time step Δt_j , we flag the particle. At the beginning of every synchronization point, we check flagged particles and wake them up if it is the point where a particle with the time step of $C_{\text{CFL}} \Delta t_j^{\text{signal}}$ should be synchronized.

We note that the tree walk is carried out along with the evaluation of $\Delta t_i^{\text{signal}}$, and its node opening criterion is

$$d_{\min} < d_i^{\text{signal}} + \Delta t_i^{\text{signal}} (c_{\max}^{\text{snd}} - v_{\min}^{\text{rel}}). \quad (3.20)$$

We actually open the tree node if the criteria (3.19) or (3.20) are fulfilled, and when we encounter a particle, we compute $\Delta t_i^{\text{signal}}$ and update if it is smaller.

We also note that the number of neighbor particles can be large when there are particles with high temperatures and/or high relative velocities. In GADGET-4, the default tree walk method is to build a local essential tree, which requires a memory buffer to allocate data of tree nodes and particles on other memory space. When we have a large number of neighbors, the construction of the local essential tree can fail due to memory shortage. We thus implemented the tree-based time step limiter using the generic communication pattern, a C++ class of MPI communication routine available in GADGET-4. The tree walk can be costly when we have many neighbors, but the signal velocity time step

TABLE 3.1: Numerical settings of the models used in the test simulations. (1) Model name. (2) The [SPH](#) formulation (Section 3.3.1). (3) Check list of the usage of the artificial conduction (Section 3.3.1.2). (4) Check list of the usage of the velocity field reconstruction (Section 3.3.1.3).

Name (1)	SPH formulation (2)	Artificial conduction (3)	Velocity field reconstruction (4)
PU_AC_Rec	Pressure-Energy	✓	✓
PU_AC	Pressure-Energy	✓	
PU_Rec	Pressure-Energy		✓
PU	Pressure-Energy		
PE_AC_Rec	Pressure-Entropy	✓	✓
DE_AC_Rec	Density-Entropy	✓	✓

limiter chooses the optimal time step for each particle, and unnecessary calculation can be avoided to reduce the computational cost.

In addition to the signal velocity time step constraint, we activate particles that can be subject to stellar or [AGN](#) feedback. At the beginning of a synchronization point, we drift neighbor particles around the feedback site and find particles that will receive feedback energy. The neighbor particles are woken up if they are inactive. This ensures that the feedback effect is reflected in hydrodynamics without delay.

3.3.2 Code validation

In this subsection, we demonstrate the performance of the above numerical treatment using five test problems. We perform simulations with six different models of numerical settings as summarized in Table 3.1. We compare our fiducial model PU_AC_Rec with other runs without artificial conduction, velocity field reconstruction, or using different [SPH](#) formulation.

3.3.2.1 Keplerian Disk

The Keplerian disk is a two-dimensional hydrodynamical test for the conservation of angular momentum and numerical diffusion by artificial viscosity and conductivity. The excess in numerical diffusion breaks the conservation of angular momentum and leads to the disruption of the disk. The initial condition has the same density profile as that used by [Hopkins \(2015\)](#) and [Hosono et al. \(2016\)](#);

$$\Sigma = \begin{cases} (r/0.5)^3 & (r < 0.5) \\ 1 & (0.5 < r < 2) \\ [1 + (r - 2)/0.1]^{-3} & (r > 2) \end{cases} \quad (3.21)$$

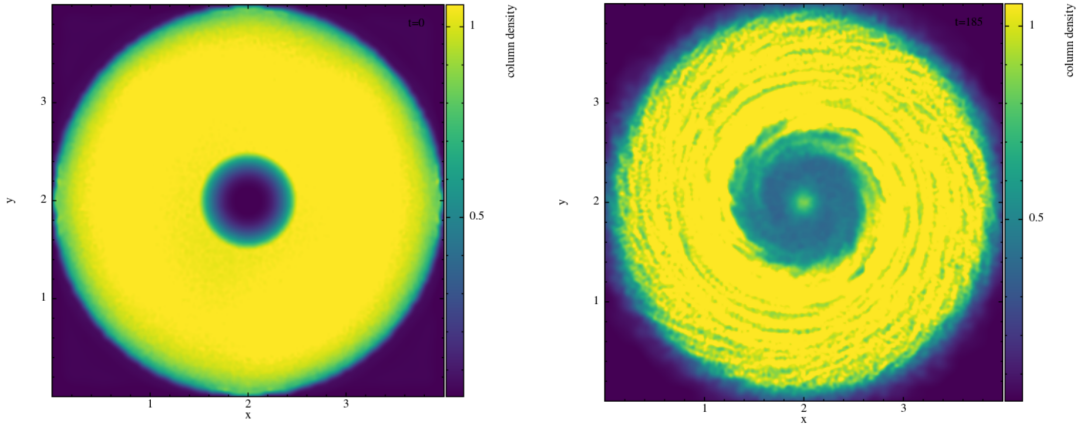


FIGURE 3.1: Surface density of simulated Keplerian disk at initial condition (left) and at the termination of the simulation when the L1 error of azimuthal velocity exceeds 0.01 (right).

where Σ is the gas surface density and r is the distance from the center. The disk is cold ($P = 10^{-6}$) and is subject to the external Keplerian potential

$$\Phi = -(r^2 + \epsilon^2)^{-1/2}, \quad (3.22)$$

where $\epsilon = 0.25$ is the gravitational softening length. The corresponding rotational velocity is

$$v_r = |\mathbf{r}|(r^2 + \epsilon^2)^{-3/4}. \quad (3.23)$$

We generate the initial condition using the glass-like initial condition generator WVTICs⁹ (Donnert et al., 2017, Arth et al., 2019). The box length is 4 in unit length, and 46,560 SPH particles are employed. We monitor the L1 error of azimuthal velocity

$$L1 = \frac{1}{N} \sum_{0.5 < r < 2.0}^N \frac{|v_{j,\phi} - v_r(r_j)|}{v_r(r_j)}, \quad (3.24)$$

where $v_{j,\phi}$ is the azimuthal velocity of j -th particle and $v_r(r_j)$ is the rotational velocity at the radius of j -th particle, and terminates the simulation when $L1$ exceeds 0.01.

The left panel of Figure 3.1 shows the surface density of the simulated Keplerian disk at the initial condition, whose density profile follows equation (3.21). The right panel of Figure 3.1 shows the surface density at the termination of the simulation. The excess artificial viscosity causes the loss of angular momentum of gas at the inner edge of the disk, and then the gas losing its angular momentum forms a gas clump at the center.

⁹The code's website is <https://github.com/jdonnert/WVTICs>

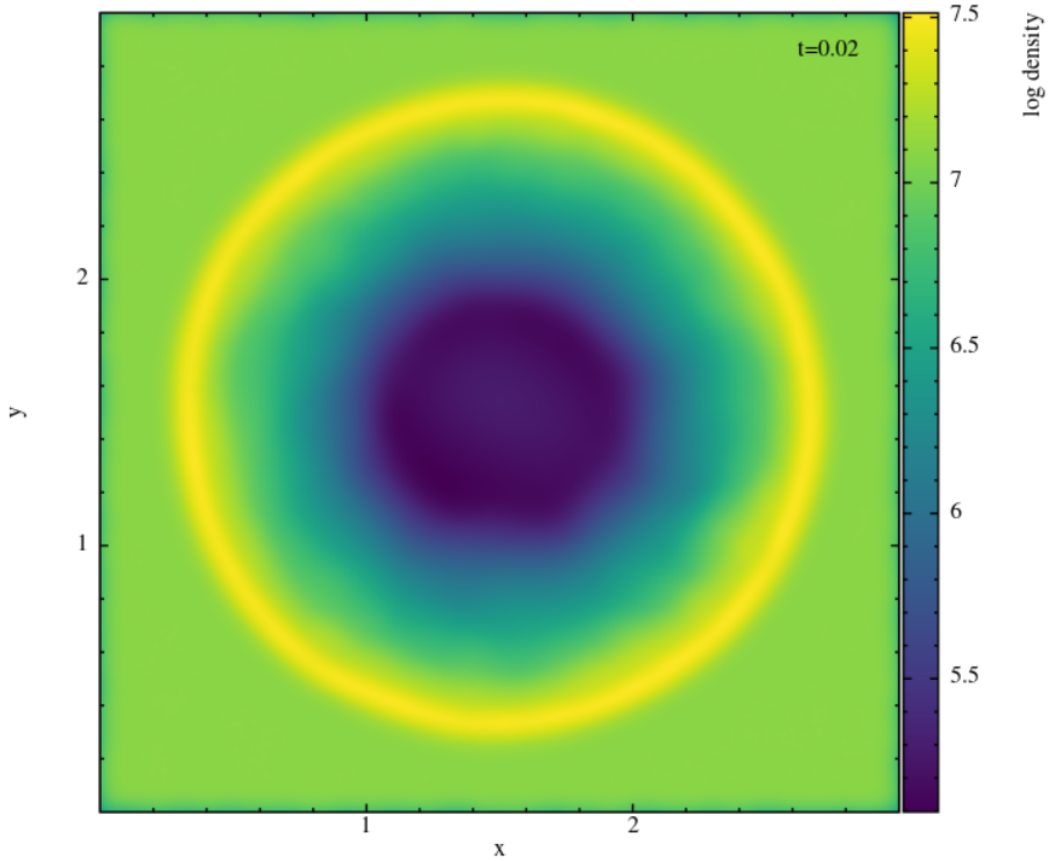


FIGURE 3.2: Density slice through the center of the simulated Sedov blast wave at $t = 20$ Myr.

In the next subsubsection, we show the result of the Keplerian disk test in combination with the Sedov Blast test.

3.3.2.2 Sedov Explosion

The Sedov blast is a three-dimensional hydrodynamical test of shock capturing, conservation, and integration stability. The blast wave should evolve following the Sedov–Taylor solution.

We use the initial condition generator WVTICS to generate the initial condition, which is identical to that used by [Hopkins \(2013\)](#) and [Hu et al. \(2014\)](#). The box length is $L = 3$ kpc, and 64^3 SPH particles are employed. The thermal energy of $E = 6.78 \times 10^{53}$ erg is injected into the 63 central particles with a top-hat profile in a homogeneous density field of $n = 0.5 \text{ cm}^{-3}$. The ambient temperature is $T = 10$ K with adiabatic index $\gamma = 5/3$ and mean molecular weight $\mu = 1$.

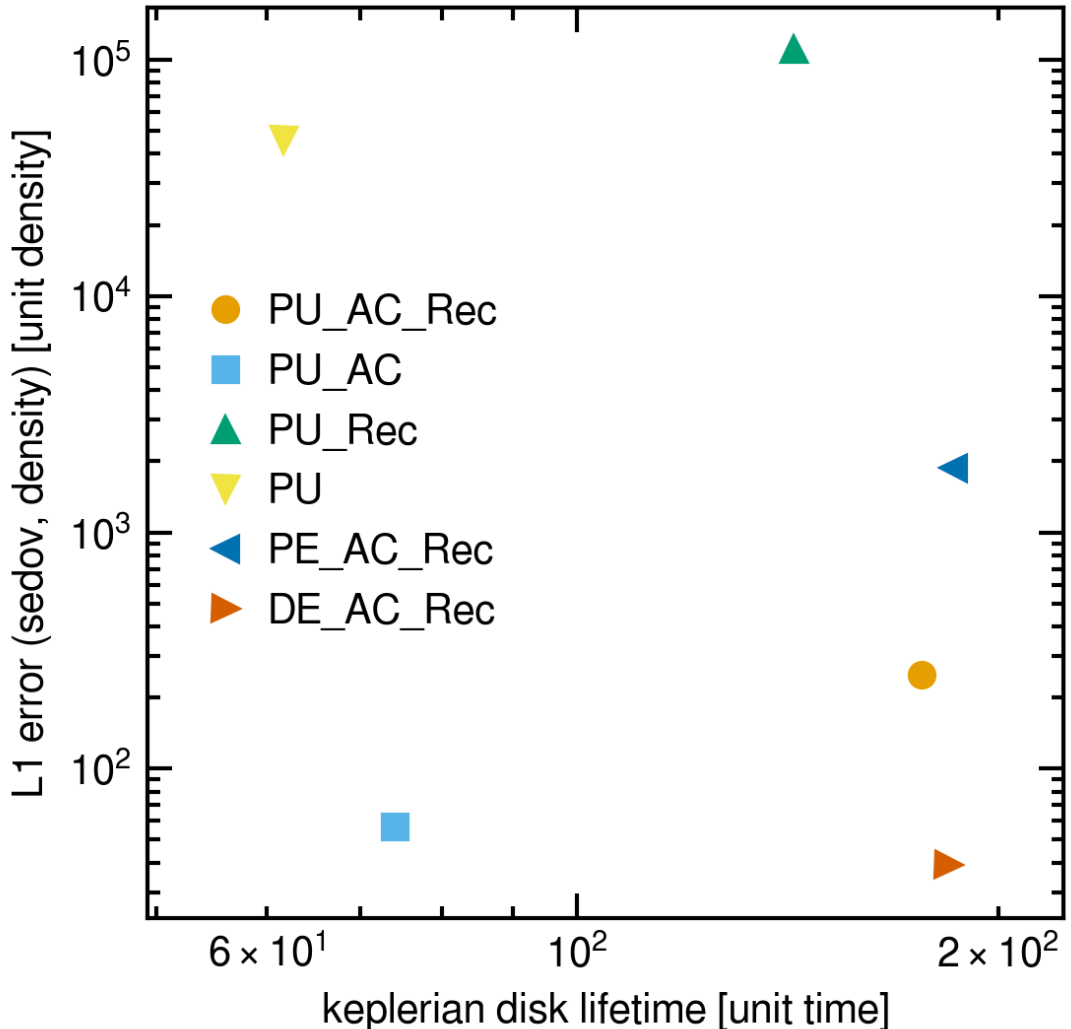


FIGURE 3.3: The comparison of the performance of the six numerical models in the Keplerian disk and Sedov blast tests. The x-axis shows the lifetime of the Keplerian disk, and the longer lifetime indicates the better angular momentum conservation. The y-axis shows the L1 error of density in the Sedov blast test, and the smaller L1 error indicates higher accuracy in the treatment of shocks. The models located in the bottom right perform nicely in both tests.

We calculate the Sedov–Taylor solution by numerical integration of the dimensionless equation of continuity, equation of motion, and energy equation on spherical coordinate and compare it with the snapshot at $t = 20$ Myr to compute the L1 error of density, pressure, and radial velocity. The L1 error is computed on the range $[0, 1.1R_{\text{shock}}]$, where R_{shock} is the radius of the shock front. First, the range is linearly-equally divided into 20 bins and L1 error of X ($X = \rho, p$, or v)

$$L1_i = \frac{1}{N_i} \sum_{r_j \in [r_i, r_{i+1})}^{N_i} \frac{|X_j - X_{ST}(r_j)|}{X_{ST}(r_j)} \quad (3.25)$$

is computed for each bin, where $X_{ST}(r)$ is the value of X of the Sedov–Taylor solution obtained by linear interpolation of the result of the numerical integration. Then the L1 error is computed as

$$L1 = \frac{1}{20} \sum_i^{20} L1_i. \quad (3.26)$$

Figure 3.2 shows the density slice through the center of the simulated Sedov blast at $t = 20$ Myr. The blast wave expands isotropically in the uniform medium.

Figure 3.3 compares the results using the six models in the Keplerian disk and Sedov blast tests. In the Keplerian disk test, the artificial viscosity causes a loss of angular momentum, but in the Sedov explosion test, artificial viscosity is necessary to capture the shock. Triggering the artificial viscosity only when necessary is key to obtaining high performance in both tests. Our fiducial model PU_AC_Rec shows a long lifetime of the Keplerian disk and low L1 error in the Sedov blast test. Similar results are obtained with the DE_AC_Rec and PE_AC_Rec models. This is achieved using velocity field reconstruction, which reduces the artificial viscosity where the velocity field is smooth. This can be confirmed by comparing the PU_AC_Rec and PU_AC run; the PU_AC_Rec has more than twice the lifetime of the Keplerian disk but keeps the same order of the L1 error in the Sedov blast test.

In the formulation of pressure-based [SPH](#), we have assumed a smooth pressure field, which is not the case for the shock front. The large L1 error of the PU and PU_Rec run results from the error at the huge pressure jump. This can be mediated by artificial conduction, which smoothes the pressure discontinuity. The comparison between PU_AC_Rec and PU_AC runs shows that artificial conduction reduces error in resolving the shock with a minor effect in the Keplerian disk test.

3.3.2.3 Cold Blob

The cold blob is a three-dimensional hydrodynamic problem proposed by [Agertz et al. \(2007\)](#) to test the capability of the hydro solver to handle Rayleigh–Taylor and Kelvin–Helmholtz instabilities. A spherical cloud of gas is placed in a wind tunnel with periodic boundary conditions, and the cloud is disrupted through hydrodynamical instabilities. This test is designed to capture the same physical processes that occur during the formation and evolution of astrophysical structures and does not have an exact analytic solution. It is known that different hydro solvers show diverging results on this test as shown by [Hopkins \(2015\)](#) and [Braspenning et al. \(2023\)](#).

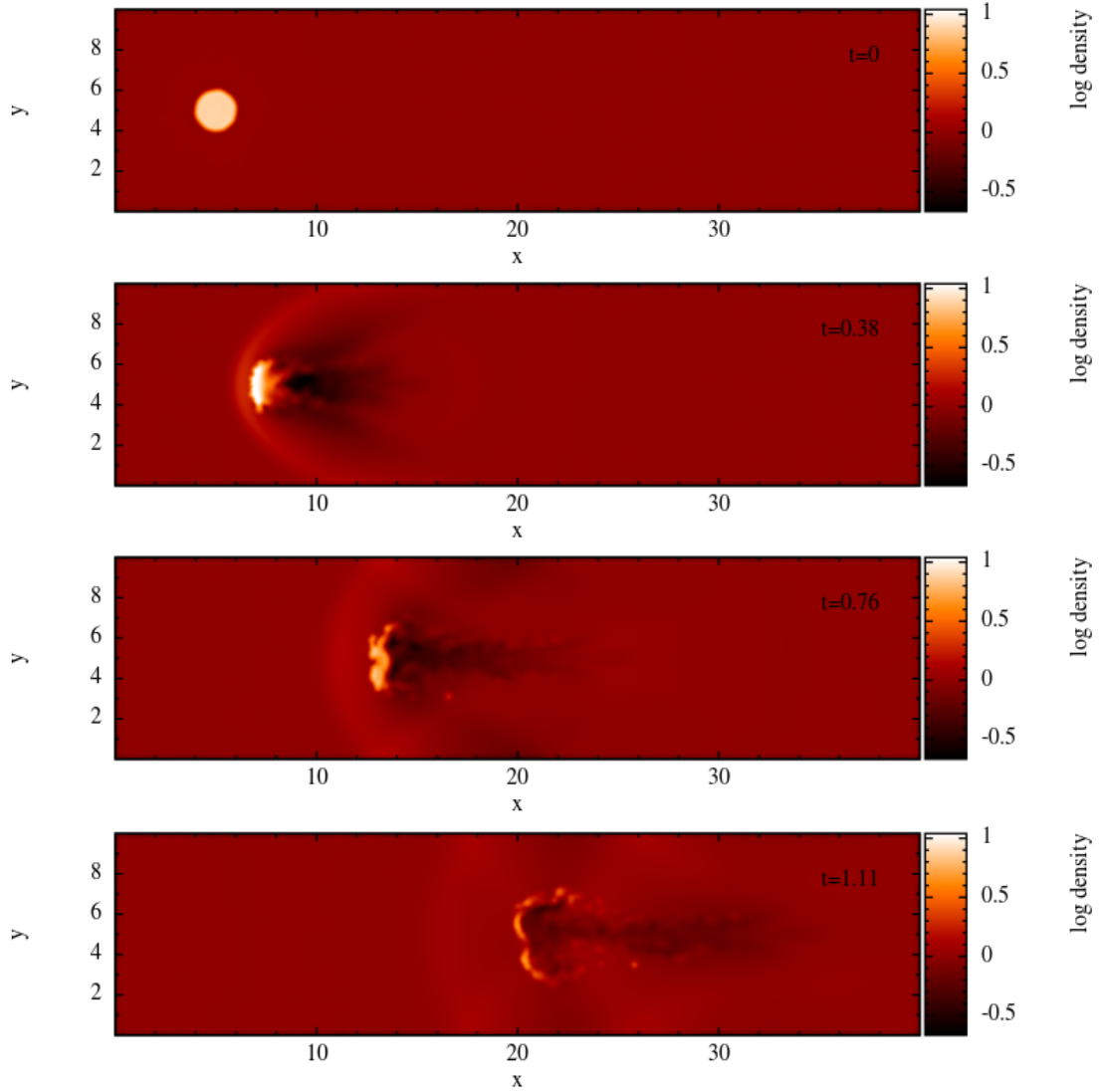


FIGURE 3.4: Density slice through the mid-plane of cold blob test at $t = 0, 1 t_{\text{KH}}, 2 t_{\text{KH}}$, and $3 t_{\text{KH}}$ (from top to bottom).

The initial conditions for the blob test are set up in the following way. The simulation box has a size of $(L_x, L_y, L_z) = (40, 10, 10)$ with periodic boundaries, and a cloud with radius 1 is centered at $(5, 5, 5)$. The densities of the cloud and the ambient gas are $\rho_{\text{cl}} = 10$ and $\rho_{\text{amb}} = 1$, respectively. The specific internal energies of the cloud and the ambient gas are set to $u_{\text{cl}} = 9$ and $u_{\text{amb}} = 90$, respectively, so that the cloud and the ambient gas are in pressure equilibrium. The cloud is stationary, and the velocity of the ambient gas is $\mathbf{v} = (27, 0, 0)$, corresponding to $\mathcal{M} = 2.7$ with adiabatic gamma $\gamma = 5/3$ and mean molecular weight $\mu = 1$.

Figure 3.4 shows the time evolution of the blob. The blob is disrupted by the Rayleigh–Taylor and Kelvin–Helmholtz instabilities caused by the surrounding flow.

Figure 3.5 show the cloud remaining fraction. The cloud is defined as being any gas that

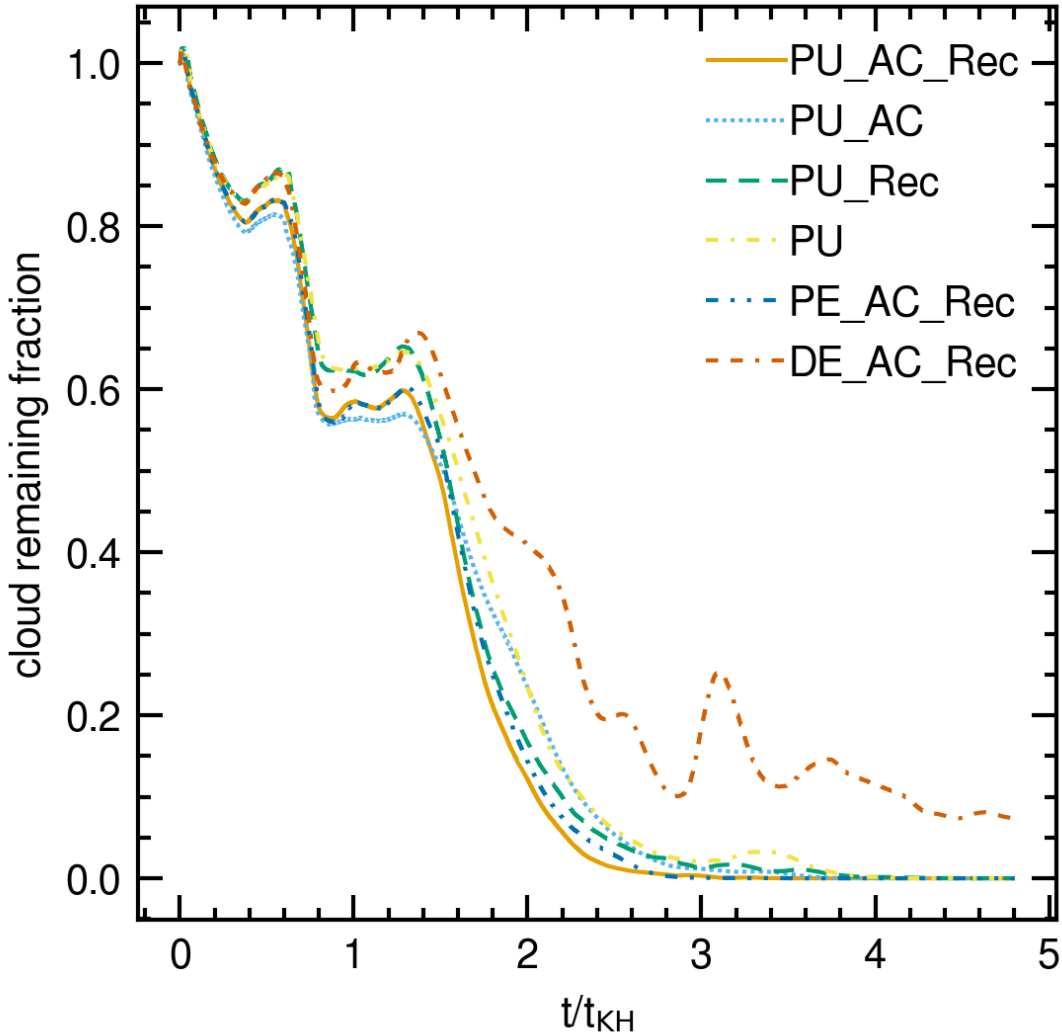


FIGURE 3.5: Cloud remaining fraction as a function of time in the cold blob test.

satisfies $u < 0.9 u_{\text{amb}}$ and $\rho > 0.64 \rho_{\text{cl}}$. The cloud is disrupted at the time when the KHI mode of cloud size has grown fully. The timescale of disruption is often called t_{KH} , and its analytically estimated value is (Agertz et al., 2007)

$$t_{\text{KH}} = 1.6 \tau_{\text{cr}} = 3.2 \frac{R_{\text{cl}} \chi^{0.5}}{v} \sim 0.375 \left(\frac{R_{\text{cl}}}{1} \right) \left(\frac{\chi}{10} \right)^{0.5} \left(\frac{v}{27} \right), \quad (3.27)$$

where τ_{cr} is the cloud crushing time, and R_{cl} , v , and χ are cloud radius, flow speed, and density ratio between the cloud and surroundings, respectively.

In the runs except for the DE_AC_Rec run, the cloud fully disrupts at $t \sim 2 t_{\text{KH}}$, consistent with the results from grid-based codes (Hopkins, 2015). The DE_AC_Rec run has a long disruption time because the density-based **SPH** formulation assumes a smooth density field. This assumption is broken at the contact discontinuity, and the density-based **SPH** is not good at solving the instabilities occurring there. In the other

runs using the pressure-based **SPH** formalism, there are only minor differences due to the usage of artificial conduction and velocity field reconstruction.

3.3.2.4 Zeldovich Pancake

The Zeldovich pancake is a three-dimensional test of cosmological hydrodynamics and cosmological integration. A single Fourier mode density perturbation of box size in a baryonic Einstein-de Sitter universe evolves from redshift 99 to 0.

The initial condition is almost identical to that used by [Hopkins \(2015\)](#). The simulation box has size of $L_{\text{box}} = 64 h^{-1} \text{ Mpc}$ with periodic boundary, and the density parameters are $(\Omega_m, \Omega_b, \Omega_\Lambda) = (1, 1, 0)$. The number of particles is 64^3 . The gas is non-radiative; thus, the setup is independent of the Hubble constant. First, a three-dimensional uniform density field with glass (not grid) particle distribution is generated. Then, the particles are assigned velocities, and their positions are shifted using the Zeldovich approximation. The shifted particle x-coordinate on Eulerian comoving coordinate and x-direction peculiar velocity is

$$x(q, z) = q - \frac{1 + z_c}{1 + z} \frac{\cos(kq)}{k}, \quad (3.28)$$

$$v(q, z) = -H_0 \frac{1 + z_c}{\sqrt{1 + z}} \frac{\cos(kq)}{k}, \quad (3.29)$$

where q is the Lagrangian coordinate, $z_c = 1$ is the redshift at the collapse of the perturbation, k is the wave number of the perturbation, and $H_0 = 100 h \text{ km s}^{-1} \text{ Mpc}^{-1}$ is the current Hubble constant. The Lagrangian coordinate q is the Eulerian coordinate of the unperturbed initial particle position. This Fourier mode collapses at $x = L_{\text{box}}/2$ at $z = 1$. Here, note again that the Hubble constant is included in the length unit, and thus, the setup is independent of h . The initial gas temperature is uniformly set to 100 K. The perturbation is in the x-direction, the density is uniform in the yz-plane, and the velocity in the y- and z-direction is zero.

Figure 3.6 shows the time evolution of the Zeldovich pancake. Starting from the condition of almost uniform but with a single Fourier mode, the perturbation grows and collapses at $z = 0$, forming a thin plane, the Zeldovich pancake.

We randomly sample ~ 2000 particles and output their x-coordinates, density, temperature, and x-velocity at $z = 0$. The x-coordinate is shifted by $-L_{\text{box}}/2$ so that the pancake comes at $x = 0$. The gas is assumed to be primordial with hydrogen mass fraction $X = 0.76$ and helium mass fraction $Y = 1 - X$, and temperature is computed assuming full ionization if $T > 10^4 \text{ K}$ and atomic otherwise.

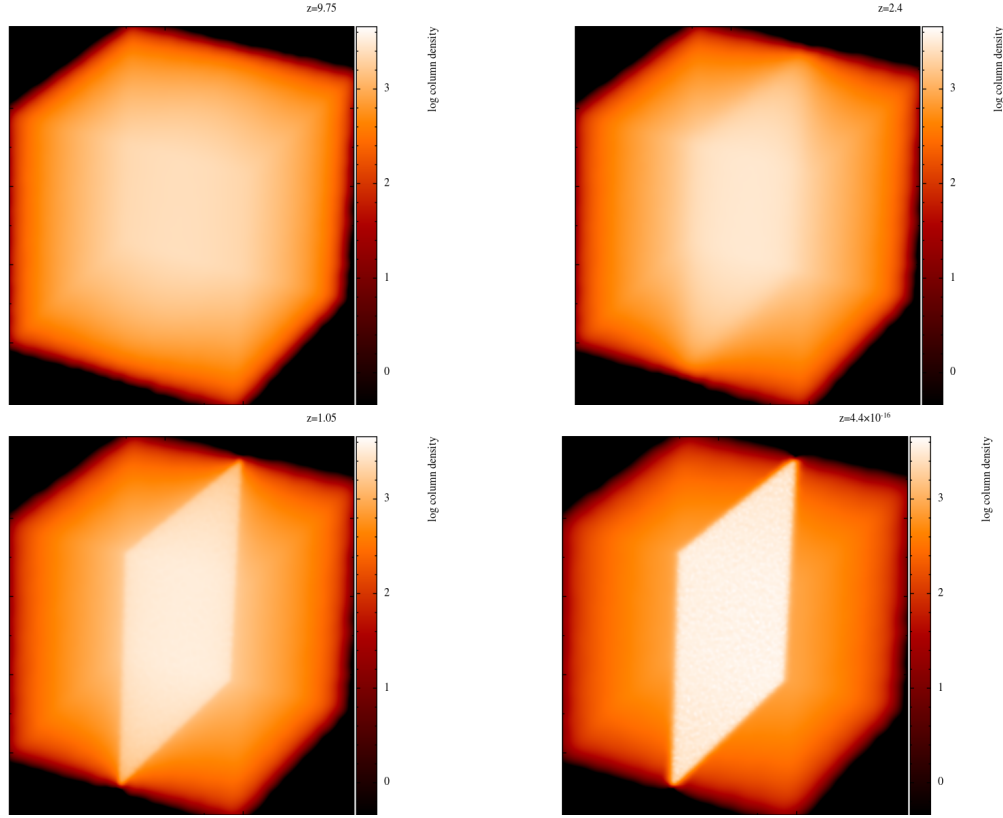


FIGURE 3.6: Density projection of the simulated Zeldovich pancake at $z = 9.75, 2.4, 1.05$, and 0 (from top left to bottom right).

The output is compared with the reference result of 1D piecewise parabolic method simulation with high resolution (8194 grids) taken from GIZMO’s test problem suite.¹⁰

Figure 3.7 shows the density, temperature, and velocity profiles at $z = 0$. All runs show agreement with the reference data, indicating the high accuracy of the cosmological integration of the hydro solver of GADGET4-OSAKA code.

3.3.2.5 Galaxy Cluster

The cluster test is a zoom-in simulation of a galaxy cluster with a total mass of $\sim 10^{15} M_{\odot}$ at $z = 0$. This test is similar to the simulations performed in the Santa Barbara Cluster Comparison Project by Frenk et al. (1999). It is known that the central part of the entropy profiles of simulated clusters differs among different hydro schemes, and no agreed results have been obtained yet. Therefore, this test cannot be used to validate the code, but it is interesting to see how different the profiles are between different hydro settings. Interested readers are referred also to Springel (2010b), Hopkins (2015), and Sembolini et al. (2016).

¹⁰The test suite is in the documentation of the GIZMO code, whose website is http://www.tapir.caltech.edu/~phopkins/Site/GIZMO_files/gizmo_documentation.html.

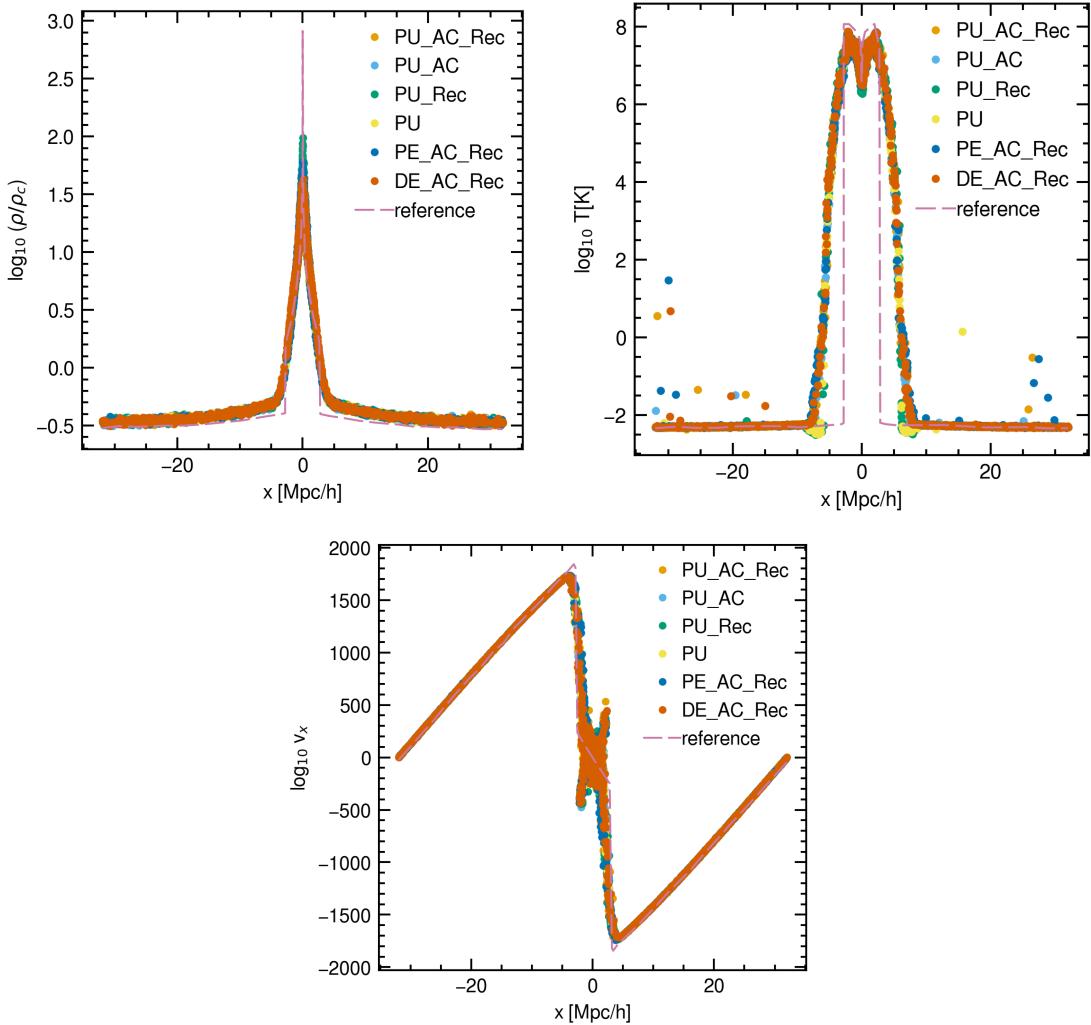


FIGURE 3.7: Density (top left), temperature (top right), and velocity (bottom) profiles of the Zeldovich pancake at $z = 0$. Each point indicates the x -position and each property of a sampled particle. The pink dashed line is the reference result of the 1D Piecewise Parabolic Method (PPM) simulation with high resolution (8194 grids).

The initial condition is generated using the cosmological initial condition generator MUSIC¹¹ (Hahn and Abel, 2011) with parameters used in Fukushima et al. (2023) but with reduced resolution. The adopted cosmological parameters largely follow those from Planck Collaboration et al. (2016), ($\Omega_m, \Omega_\Lambda, \Omega_b, h, \sigma_8, n_s$) = (0.3089, 0.6911, 0.0486, 0.6774, 0.811, 0.961). The size of the simulation box is $L = 100 h^{-1}$ Mpc, and the finest refinement level is 8, resulting in the particle mass of baryon and dark matter are $8.04 \times 10^8 h^{-1} M_\odot$ and $4.31 \times 10^9 h^{-1} M_\odot$, respectively.

Figure 3.8 shows the time evolution of the simulated cluster. We do not include any astrophysical effects, including cooling and feedback, and the gas is heated by the virial shock for its thermal pressure to balance with gravity.

¹¹The code's website is <https://bitbucket.org/ohahn/music/src/master/>.

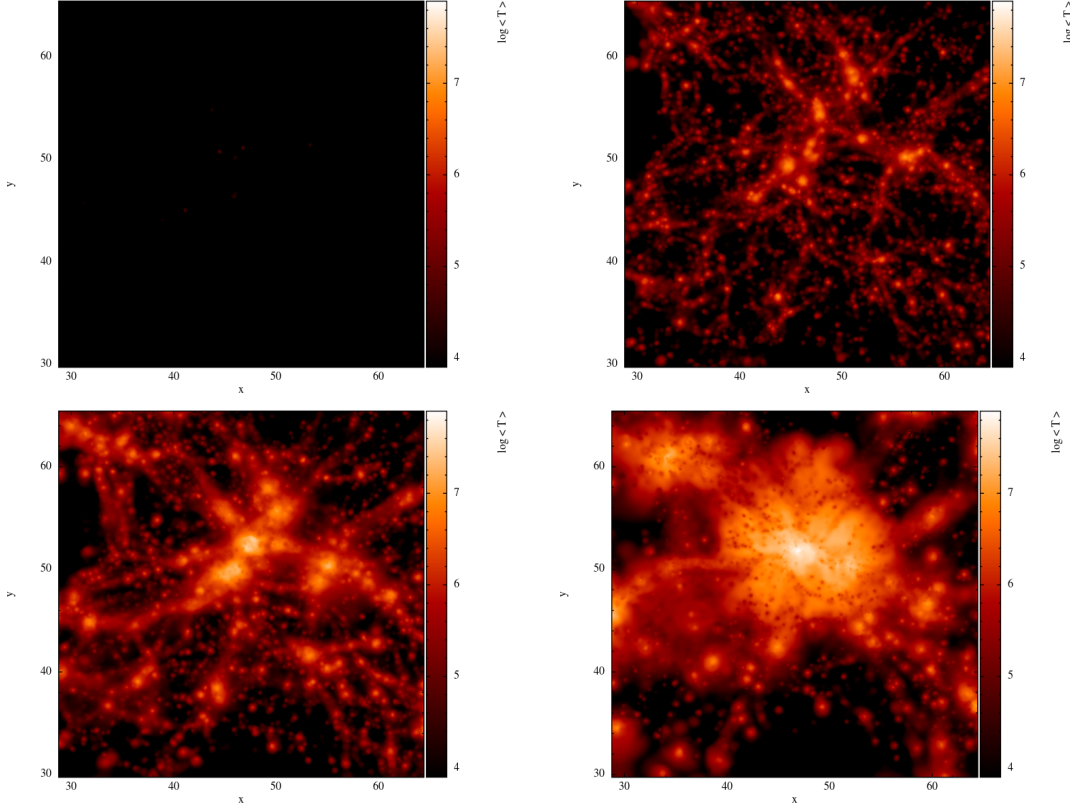


FIGURE 3.8: Projected density-weighted temperature of the simulated cluster at $z = 9.75, 2.4, 1.05$, and 0 (from top left to bottom right).

Figure 3.9 shows the radial profiles of density, temperature, entropy, and pressure at $z = 0$. The density profiles of dark matter are consistent with each other among the simulations, and the gas density at the center is slightly higher in the PU and PU_Rec runs than in others. The PU and PU_Rec runs have lower temperature and entropy at the cluster center than the other runs. The higher entropy in runs with artificial conduction suggests that artificial conduction promotes the diffusion of cold clumps. The pressure profiles are consistent among the simulations because they have the same gravitational potential due to dark matter, and gas has to be in equilibrium with gravity by its thermal pressure. The different entropy profiles indicate the effect of artificial conduction in cluster evolution, but there is no analytical solution nor fiducial simulation result, and we cannot conclude which model is better in this comparison.

3.4 Subgrid physics

In the following subsections, we describe our treatment of subgrid star formation, stellar feedback, and **black hole (BH)** physics. In this work, **SNe** and **AGB** stars are considered as sources of stellar feedback, while early stellar feedback, e.g., stellar radiation and

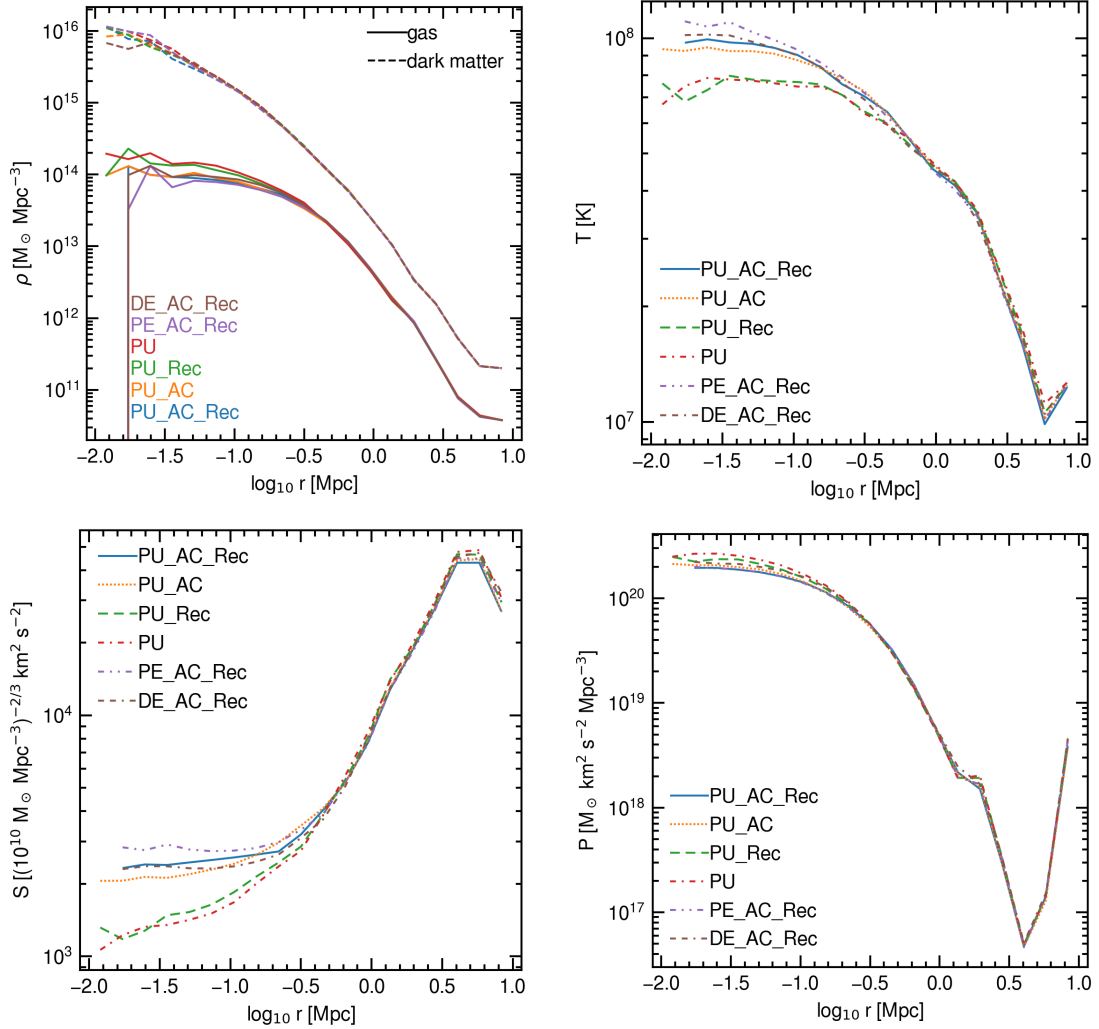


FIGURE 3.9: Radial profiles of density, temperature, entropy, and pressure (from top left to bottom right) of the cluster test at $z = 0$.

stellar wind, is neglected. The adopted values of parameters introduced in the following subsections are summarized in Table 3.2.

3.4.1 Star Formation

We assume star formation to occur when the hydrogen number density is higher than the threshold density, $n_{\text{thres}} = 0.1 \text{ cm}^{-3}$, and the temperature is lower than the threshold temperature, $T_{\text{thres}} = 10^4 \text{ K}$. Each gas particle is allowed to spawn n_{spawn} star particles at most, and the mass of the star particle is $m_* = m_{\text{gas}}/n_{\text{spawn}}$, where m_{gas} is the mass of the gas particle, and $n_{\text{spawn}} = 2$.

We use the **SSP** approximation; a star particle represents a cluster of stars with the same metallicity, and their mass function follows an adopted **IMF**. For the **IMF**, its

TABLE 3.2: List of common parameters for subgrid physics

Parameter	Adopted value	Description
n_{thres}	0.1 cm^{-3}	Lower density threshold to allow star formation
T_{thres}	10^4 K	Upper temperature threshold to allow star formation
ϵ_*	0.01	Star formation efficiency
n_{spawn}	2	Maximum number of stars spawned from one gas particle
$N_{\text{ngb,fb}}$	8 ± 2	Number of gas particles subject to feedback
$n_{\text{event,snii}}$	2	SNII feedback event number
$n_{\text{event,snia}}$	8	SNIa feedback event number
$n_{\text{event,agb}}$	8	AGB feedback event number
$M_{\text{seedng,FoF}}$	$10^{10} h^{-1} \text{ M}_\odot$	FoF mass threshold to seed BH
$M_{\text{seedng,star}}$	$10^8 h^{-1} \text{ M}_\odot$	FoF stellar mass threshold to seed BH
ϵ_r	0.1	Radiative efficiency of BH
ϵ_{FB}	0.15	AGN feedback efficiency
ΔT_{AGN}	$10^{8.5} \text{ K}$	AGN feedback temperature

dependence on metallicity and redshift is considered based on the star cluster formation simulation by Chon et al. (2022). They have investigated IMF at a metallicity range of $10^{-4} \leq Z/Z_\odot \leq 10^{-1}$ and redshift range of $0 \leq z \leq 20$ and quantified the mass fraction of excess component from a Salpeter-like component,

$$f_{\text{massive}} = 1.07(1 - 2^x) + 0.04 \times 2.67^x \times z, \quad (3.30)$$

with $x = \min\{1 + \log_{10}(Z/Z_\odot), 0\}$, where z is the redshift. The metallicity range investigated by Chon et al. (2022) is limited to $Z \leq 0.1 Z_\odot$, and we use the value of f_{massive} at $Z = 0.1 Z_\odot$ for the higher metallicity because IMF at $Z = 0.1 Z_\odot$ and $z = 0$ is already similar to present day Salpeter-like IMF. Figure 3.10 shows the variation of IMF depending on f_{massive} . We first assume the Chabrier IMF (Chabrier, 2003) with stellar mass range $0.1 \text{ M}_\odot < M < 100 \text{ M}_\odot$, and then add a log-flat component at $5 \text{ M}_\odot < M < 100 \text{ M}_\odot$ with mass fraction f_{massive} to allow for a treatment of top-heavy IMF.

When a star particle is spawned from a gas particle, f_{massive} is computed from the metallicity of the gas particle and the redshift at that time, which is used later for computing energy and metal yield by SNe and AGB stars. In computing the metal and energy yields, we use the metallicity of the star particle with a floor of $Z_{\text{yield,floor}} = 0.03 Z_\odot$. This metallicity floor is introduced to consider the metal enrichment by unresolved early star formation, and the $Z_{\text{yield,floor}}$ is similar to the observed metallicity of galaxies with $M_* \sim 10^7 \text{ M}_\odot$.

The star formation rate for a gas particle follows the local Schmidt law (Schmidt, 1959),

$$\dot{\rho}_* = \epsilon_* \frac{\rho}{t_{\text{ff}}}, \quad (3.31)$$

where $t_{\text{ff}} = \sqrt{3\pi/32G\rho}$ is the local free fall time and $\epsilon_* = 0.01$ is the star formation efficiency. Star particles are spawned stochastically (Katz, 1992, Springel and Hernquist, 2003, Shimizu et al., 2019) following the star formation rate.

3.4.2 Core Collapse Supernova

When a massive star ($\gtrsim 8 M_{\odot}$) ends its life, its major path is to explode as **core-collapse supernova (CCSN)**. Typically, there is one massive star per $100 M_{\odot}$ stars, and the kinetic energy of a supernova is 10^{51} erg; the specific **SN** energy is $\zeta_{\text{SN}} = 10^{49} \text{ erg } M_{\odot}^{-1}$. However, the specific energy can vary due to multiple factors, e.g., stellar **IMF**, lower and upper limits of **SN** progenitor mass, and energy per **SN**. The specific **SN** energy adopted in previous works varies by more than a factor of two (Keller and Kruijssen, 2022).

Some supernovae, called hypernovae (**HNe**) or superluminous supernovae, have an order of higher explosion energy of 10^{52} erg. The number fraction of **HNe** in a solar metallicity environment is about one per cent, but it is observationally suggested that the **HN** fraction increases at subsolar metallicity (Moriya et al., 2018, Gal-Yam, 2019). From a cosmological hydrodynamic simulation of galaxies, Kobayashi et al. (2006) suggested that the **HN** fraction of 50% is necessary to explain the zinc abundance.

In this work, we use the yield model by Nomoto et al. (2013), which covers the progenitor mass range of $13\text{--}40 M_{\odot}$. We assume that some **CCSNe** with progenitor masses of $20\text{--}40 M_{\odot}$ explode as **HNe**, and its number fraction in that mass range is 50% at $Z < 10^{-3}$ and 1% otherwise. We generate a yield table as a function of stellar age using the chemical evolution library CELIB (Saitoh, 2017). The bottom panel of Figure 3.10 shows the specific energy of **CCSNe** as a function of metallicity in our model. A low-metallicity star's specific energy is higher due to top-heavy **IMF** and higher **HN** fraction.

We divide the Type-II **SN** feedback from a star particle into $n_{\text{event,snii}}$ events so that the **SN** energy and metal yields are deposited gradually rather than instantaneously (Shimizu et al., 2019), and in this work, we adopt $n_{\text{event,snii}} = 2$. The **SN** feedback event occurs following the yield table, considering the stellar age. The energy and metal output of **SN** is distributed to surrounding $N_{\text{ngb,fb}} = 8 \pm 2$ gas particles using the feedback model developed in Oku et al. (2022) with some updates, as we briefly summarize in the following. The model consists of two components: local mechanical feedback and galactic wind feedback.

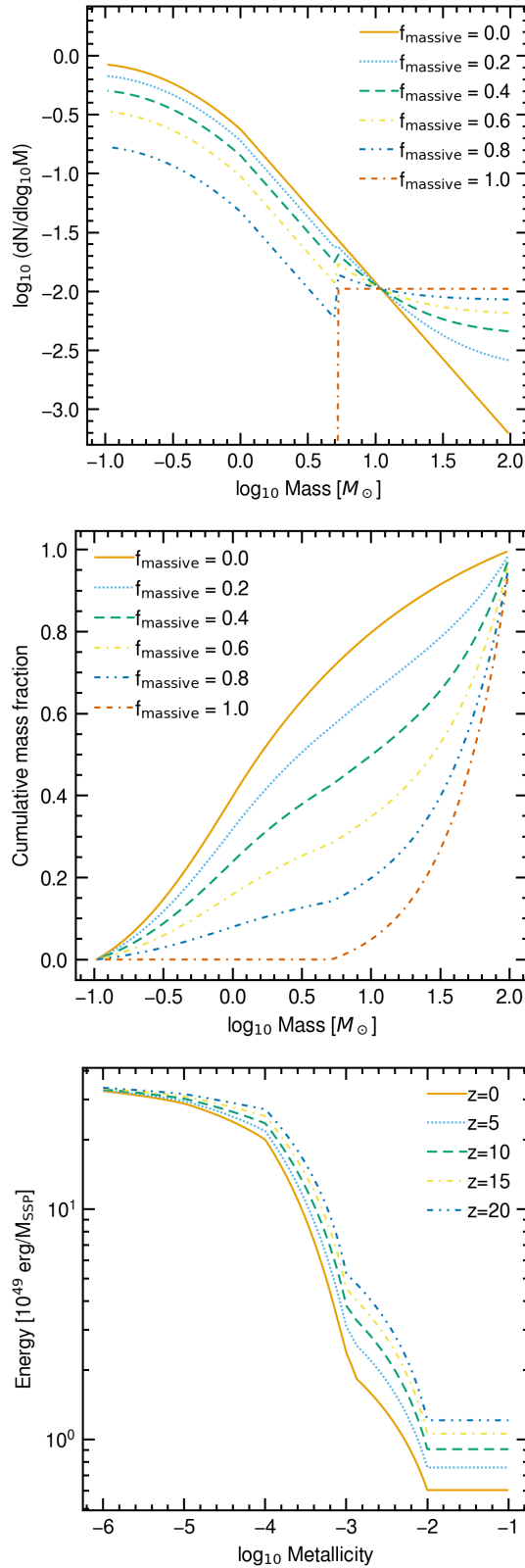


FIGURE 3.10: *Top panel:* Metallicity- and redshift-dependent IMF assumed in this work. *Middle:* Cumulative mass fraction of the stars following the IMFs shown in the top panel. *Bottom:* Metallicity- and redshift-dependent specific energy of Type-II supernova.

3.4.2.1 Mechanical Feedback Model

The mechanical feedback model accounts for the momentum injection by **SN** remnants acquired in the unresolved Sedov–Taylor and pressure-driven snowplow phases. [Oku et al. \(2022\)](#) have performed three-dimensional hydrodynamic simulations using ATHENA++ code ([Stone et al., 2020](#)) to investigate the momentum of superbubble formed by clustered **SN** explosions in a variety of density and metallicity environments with different intervals of **SN** explosions. The terminal momentum obtained in the simulations is normalized over an initial mass function of star clusters and finally translated into the terminal momentum per **SN**,

$$\hat{p} = 1.75 \times 10^5 M_{\odot} \text{ km s}^{-1} n_0^{-0.05} \Lambda_{6,-22}^{-0.17}, \quad (3.32)$$

where $n_0 = n_{\text{H}}/(1 \text{ cm}^{-3})$, and $\Lambda_{6,-22} = \max\{1.9 - 0.85(Z/Z_{\odot}), 1.05\} \times (Z/Z_{\odot}) + 10^{-1.33}$ is the value of cooling function of [Sutherland and Dopita \(1993\)](#) at 10^6 K normalized by $10^{-22} \text{ erg s}^{-1} \text{ cm}^3$. For every feedback event, the local density and metallicity are computed, and the **SN** energy is translated to momentum using Eq. (3.32) assuming that the energy per **SN** is 10^{51} erg .

The momentum is distributed to surrounding particles with weights calculated using Voronoi tessellation. Metals from Type-Ia **SNe**, Type-II **SNe**, and **AGB** stars are distributed using the same weights. When coupling the feedback momentum to surrounding particles, we limit the momentum if necessary to ensure manifest energy conservation considering the relative velocity of star and gas particles for individual coupling events (see Appendix B1 of [Hopkins et al., 2023b](#)). We did not consider the manifest conservation of total energy and linear momentum of multiple feedback events as discussed in Appendix B3 of [Hopkins et al. \(2023b\)](#), and this would be a task for future development of GADGET4-OSAKA, while its effect would be small in our low-resolution simulation where most of **SN** event is at the momentum-conserving limit on the resolved scale.

3.4.2.2 Supernova-driven Galactic Wind Model

The galactic wind model accounts for the hot ($T \gtrsim 10^6 \text{ K}$) galactic wind driven by **SNe**. We use the scaling relations by [Kim et al. \(2020a\)](#) to determine mass, energy, and metal loading factors from metallicity and star formation surface density. The star formation surface density is estimated as $\Sigma_{\text{SFR}} = \rho_{\text{SFR}} H$, where ρ_{SFR} is the star formation rate density and $H = \rho/|\nabla\rho|$ is the gas scale height obtained using the Sobolev-like approximation. The model provides the scaling relations for cool ($T \lesssim 10^4 \text{ K}$) and hot ($T \gtrsim 10^6 \text{ K}$) galactic outflows based on the TIGRESS simulation ([Kim et al., 2020b](#)), and we employ the model for hot phase.

In our previous work (Oku et al., 2022), we used a constant entropy wind based on the galactic wind property in the high-resolution dwarf galaxy simulation by Hu (2019) assuming a fixed energy loading factor $\eta_e = 0.7$. By updating our model as described above, we no longer have to assume η_e , thus reducing one free parameter.

Our simulation has the mechanical feedback model, which drives the cool wind, and we did not use the wind model for the cool phase. The galactic wind model for the hot phase is necessary for low-resolution simulations that cannot resolve the Sedov–Taylor phase because the mechanical feedback model is for the snowplow phase where the **SN** bubble has cooled down, and treatment to avoid overcooling is necessary to produce hot galactic wind (Oku et al., 2022).

We follow the TWIND sampling procedure described in Appendix B of Kim et al. (2020a) to sample wind particles and determine their temperature, metallicity, and wind velocity except for the first step. For the first step, we obtain the mass of the hot wind as $M_{\text{hot}} = \tilde{\eta}_M^{\text{hot}}(m_*/n_{\text{event,snii}})(\zeta_{\text{SN}}/\zeta_{\text{TIGRESS}})$, where $\tilde{\eta}_M^{\text{hot}}$ is the mass loading factor obtained as a function of Σ_{SFR} . The second term represents the stellar mass contributing to one feedback event. The third term is a factor considering the difference in the energy yield, where ζ_{SN} and ζ_{TIGRESS} are the specific **SN** energy adopted in our simulation and the TIGRESS framework (Kim and Ostriker, 2017, Kim et al., 2020a). The specific **SN** energy adopted in our simulation is redshift- and metallicity-dependent as shown in Fig. 3.10, and $\zeta_{\text{TIGRESS}} = 1.05 \times 10^{49} \text{ erg M}_{\odot}^{-1}$.

The sampled particles are flagged as wind particles and kicked at the wind velocity in random directions isotropically. We assume that wind particles represent the hot galactic wind flowing through unresolved low-density channels, and we disable their hydrodynamical interaction and cooling to avoid the wind particles being affected by **ISM**. We re-couple the wind particle to hydrodynamics and enable cooling after its density falls below 0.05 times the threshold density of star formation or 0.025 times the current Hubble time has elapsed, following the criteria used in the IllustrisTNG model (Pillepich et al., 2018b).

3.4.3 Type-Ia Supernova

For Type-Ia **SNe**, the element yield table by Seitenzahl et al. (2013) is used in combination with a power-law delay-time distribution function of $\Psi(t) = 4 \times 10^{-13} \text{ SN yr}^{-1} \text{ M}_{\odot}^{-1} (t/1 \text{ Gyr})^{-1}$ with minimum delay of 40 Myr (Maoz and Mannucci, 2012). We divide the Type-Ia **SN** feedback from a star particle into $n_{\text{event,snia}} = 8$ events. The energy per Type-Ia **SN** is fixed to 10^{51} erg, and we use Eq. (3.32) to convert the energy to feedback momentum. We did not consider thermal galactic wind feedback for Type-Ia **SNe** because their degree

of clustering is low, and they are not considered to be the major driver of the galactic wind.

3.4.4 AGB Stars

For **AGB** stars, two yield tables are combined to cover the mass range of $1\text{--}8 M_\odot$; [Karakas \(2010\)](#) table is used in $M_*/M_\odot \in [1, 6]$, [Doherty et al. \(2014\)](#) table in $M_*/M_\odot \in [7, 8]$, and we linearly interpolate between them. We do not consider the mechanical feedback due to the stellar wind of **AGB** stars. We divide the **AGB** feedback from a star particle into $n_{\text{event,agb}} = 8$ events.

3.4.5 Black Hole Physics

For the supermassive **BHs**, we largely follow the model used in the EAGLE project ([Schaye et al., 2015](#), [Crain et al., 2015](#)). The model consists of seeding using the **Friend-of-Friends (FoF)** halo finder, torque-limited Bondi–Hoyle accretion, and thermal quasar feedback, as summarized below.

3.4.5.1 Seeding & Repositioning

We regularly run the **FoF** halo finder with an interval of $\Delta \ln a = 0.005$, where $a = 1/(1+z)$ is the scale factor, and convert the gas particle with a minimum gravitational potential in the halo to a **BH** particle if the total mass of the halo is larger than $M_{\text{seeding,FoF}} = 10^{10} h^{-1} M_\odot$, stellar mass in the halo is larger than $M_{\text{seeding,star}} = 10^8 h^{-1} M_\odot$, and does not contain **BHs**.

If a **FoF** halo contains **BH** particles and the **BHs** are within three times the gravitational softening length of **BH** particles from the star particle with minimum potential, the **BH** particles are repositioned and assigned the velocity of the **FoF** halo.

3.4.5.2 Accretion

The mass accretion rate onto **BH** is computed by the Eddington-limited Bondi rate. The Bondi rate ([Bondi, 1952](#)) is

$$\dot{M}_{\text{Bondi}} = \frac{4\pi G^2 M_{\text{BH}}^2 \rho}{(c_s^2 + v_{\text{BH}}^2)^{3/2}}, \quad (3.33)$$

where G is the gravity constant, M_{BH} is the **BH** mass, and v_{BH} is the velocity of the **BH** relative to the surrounding medium. We set v_{BH} to zero because the velocities of **BH** particles are set by hand when repositioned. In computing the sound speed c_s , we assume the effective [equation of state \(EoS\)](#) used in the EAGLE project, i.e., $c_s = \sqrt{\gamma(k_{\text{B}}/\mu_{\text{a}}m_{\text{p}})T_{\text{eos}}}$, where $\gamma = 5/3$ is the adiabatic index, k_{B} is the Boltzmann constant, $\mu_{\text{a}} = 1.2285$ is the mean molecular weight of primordial atomic gas, m_{p} is the proton mass, and $T_{\text{eos}} = 8 \times 10^3 \text{ K} (n_{\text{H}}/0.1 \text{ cm}^{-3})^{1/3}$ is the temperature derived from the [EoS](#). The [EoS](#) is used only in computing the **BH** accretion rate for consistency with the accretion model of the EAGLE simulation.

The Eddington accretion rate is

$$\dot{M}_{\text{Eddington}} = \frac{4\pi GM_{\text{BH}}m_{\text{p}}}{\epsilon_r c\sigma_{\text{T}}}, \quad (3.34)$$

where $\epsilon_r = 0.1$ is the radiative efficiency of **BH**, c is the speed of light, and σ_{T} is the Thomson cross section. The accretion rate is the minimum of the Bondi rate and the Eddington rate

$$\dot{M}_{\text{acc}} = \min(\dot{M}_{\text{Eddington}}, C\dot{M}_{\text{Bondi}}), \quad (3.35)$$

where $C = \min(C_{\text{visc}}^{-1}(c_s/v_{\phi})^3, 1)$ is a factor to limit the Bondi rate considering the angular momentum and the viscosity of the accretion disk on a subgrid scale ([Rosas-Guevara et al., 2015](#)). We set the model parameter C_{visc} to 200π in our fiducial run, and v_{ϕ} is the rotation speed of gas around the **BH**.

We use the subgrid **BH** mass to follow the growth of **BH** ([Springel et al., 2005](#)). Each **BH** particle has particle mass, m_{part} , and subgrid **BH** mass, M_{BH} ; the former is used in the computation of gravitational force and potential, and the latter is used for the calculation of the accretion rate onto the black hole. The mass growth rate of the **BH** is

$$\dot{M}_{\text{BH}} = (1 - \epsilon_r)\dot{M}_{\text{acc}}. \quad (3.36)$$

The **BH** particles swallow the surrounding gas particles stochastically following their subgrid **BH** mass. For each gas particle j around the **BH**, we compute a probability

$$p_{j,\text{acc}} = \frac{w_j \Delta m}{\rho}, \quad (3.37)$$

where w_j is the kernel weight of the gas particle relative to the **BH**, $\Delta m = \max(M_{\text{BH}} - m_{\text{part}}, 0)$ is the mass increment from the **BH** particle mass to the subgrid mass, and ρ is the gas density at the position of the **BH**. We then draw a uniform random number $x_j \in [0, 1]$, and the **BH** absorbs the gas particle with conserving mass and momentum if $x_j < p_{j,\text{acc}}$.

3.4.5.3 Feedback

The **AGN** feedback is modeled by stochastic thermal energy injection. Each **BH** particle has an energy reservoir, and we increase it at a rate of $\dot{E}_{\text{res}} = \epsilon_r \epsilon_{\text{FB}} \dot{M}_{\text{acc}} c^2$, where $\epsilon_{\text{FB}} = 0.15$ is the efficiency of converting **AGN** radiation to thermal energy via radiative pressure. When E_{res} is large enough to increase the temperature of a gas particle by ΔT_{AGN} , the **BH** is allowed to distribute feedback energy stochastically. Similarly to the treatment of accretion, for each gas particle j around the **BH**, we compute a probability

$$p_{j,\text{FB}} = \frac{(\gamma - 1) \mu_i m_p w_j E_{\text{res}}}{k_B \Delta T_{\text{AGN}} \rho}, \quad (3.38)$$

where $\mu_i = 0.588$ is the mean molecular weight of a primordial ionized gas, and draw a uniform random number $y_j \in [0, 1]$. The thermal energy of

$$E_{j,\text{FB}} = \frac{m_j k_B \Delta T_{\text{AGN}}}{(\gamma - 1) \mu m_p} \quad (3.39)$$

is added to the gas particle if $y_j < p_{j,\text{FB}}$, and then we reduce E_{res} by $E_{j,\text{FB}}$.

3.4.5.4 Timestepping

The timestep size of a black hole is limited to constrain the accreting mass and feedback energy per time step. The accretion timestep is determined to limit the mass growth rate of a black hole per time step to less than 10% and the number of **SPH** particles swallowed by a black hole to one:

$$\Delta t_{\text{acc}} = \min \left\{ 0.1 \frac{\dot{M}_{\text{BH}}}{\dot{M}_{\text{BH}}}, \frac{\bar{m}_{\text{gas}}}{\dot{M}_{\text{BH}}} \right\}, \quad (3.40)$$

where \bar{m}_{gas} is the mean gas particle mass. The feedback timestep is determined as

$$\Delta t_{\text{FB}} = 0.3 \frac{N_{\text{ngb,BH}} \bar{m}_{\text{gas}} k_B \Delta T_{\text{AGN}}}{(\gamma - 1) \mu m_p \dot{E}_{\text{res}}}, \quad (3.41)$$

such that the fraction of neighboring **SPH** particles that receive feedback energy is less than 30% within the kernel. We use the shortest of Δt_{acc} , Δt_{FB} , and the gravitational timestep size of the black hole particle.

3.5 Runs

We conduct simulations with varied feedback settings, black hole accretion parameters, and resolution as summarized in Table 3.3.

TABLE 3.3: List of simulations. The columns list (1) the run name; (2) the box size in comoving Mpc, L_{box} ; (3) the number of particles employed in the run, N_{particle} ; (4) the subgrid viscous parameter for **BH** accretion, C_{visc} ; (5) the subgrid mass of **BH** seed, m_{seed} ; (6-8) the checklist of feedback modules activated in the run, (6) the mechanical feedback from core-collapse **SNe** (see Section 3.4.2.1), (7) the **SNe**-driven galactic wind model (see Section 3.4.2.2), and (8) **AGN** feedback (see Section 3.4.5.3); (9) the stellar **IMF**; (10) the number fraction of **HN**e.

Name (1)	L_{box} (2)	N_{particle} (3)	C_{visc} (4)	m_{seed} (5)	Feedback Type				
					SN Mechanical (6)	SN GalWind (7)	AGN (8)	Stellar IMF (9)	HN fraction (10)
Fiducial	50	2×512^3	200π	1×10^5	✓	✓	✓	variable ^a	Z-dependent ^b
NoSNGalWind	50	2×512^3	200π	1×10^5	✓	✓	✓	variable	Z-dependent
AGNOnly	50	2×512^3	200π	1×10^5		✓	✓	variable	Z-dependent
SNOnly	50	2×512^3	200π	1×10^5	✓		✓	variable	Z-dependent
NoFB	50	2×512^3	200π	1×10^5			✓	variable	Z-dependent
LowCvisc	50	2×512^3	2π	1×10^5	✓	✓	✓	variable	Z-dependent
LowCviscLowMseed	50	2×512^3	2π	1×10^4	✓	✓	✓	variable	Z-dependent
L25N512	25	2×512^3	200π	1×10^5	✓	✓	✓	variable	Z-dependent
L25N256	25	2×256^3	200π	1×10^5	✓	✓	✓	variable	Z-dependent
L25N128	25	2×128^3	200π	1×10^5	✓	✓	✓	variable	Z-dependent
L25N256NoZdepSN	25	2×256^3	200π	1×10^5	✓	✓	✓	Chabrier	0.01

^aThe metallicity- and redshift-dependent IMF (see Section 3.4.1)

^bThe redshift-dependent HN fraction (see Section 3.4.2)

The Fiducial run considers the two-component **SN** feedback and **AGN** feedback. The NoSNGalWind run does not use the **SN**-driven hot galactic wind model. It is presented to show the effect of explicit modeling of the galactic wind in comparison to the Fiducial run. The AGNonly and SNonly runs only consider **AGN** and **SN** feedback, respectively, and are performed to investigate the impact of these feedbacks. The NoFB run does not consider any feedback and is presented as a baseline to show the impact of feedback in comparison to other runs.

The LowCvisc and LowCviscLowMseed runs adopt black hole accretion parameters different from the Fiducial run. In these two runs, we adopt $C_{\text{visc}} = 2\pi$ (same value as the fiducial EAGLE simulation), which is 100 times smaller than the one adopted in the Fiducial run. The parameter C_{visc} modulates the limiting value of parameter C in Eq. 3.35 through the accretion suppression factor of $C_{\text{visc}}^{-1}(c_s/v_\phi)^3$, which is usually less than unity. The lower C_{visc} results in a higher suppression factor (Rosas-Guevara et al., 2015, Schaye et al., 2015, Crain et al., 2015), which allows **BHs** to accrete at near Bondi rate, hence faster and earlier growth at $M_* \simeq 10^9 - 10^{10} \text{ M}_\odot$ as we will see in Section 4.3.2. The LowCviscLowMseed adopts the **BH** seed mass of $M_{\text{seed}} = 10^4 h^{-1} \text{ M}_\odot$, 10 times smaller than that used in the other two runs.

The L25N512, L25N256, and L25N128 runs have different mass resolutions and are performed to investigate the dependence on resolution. The size of the simulation box of the L25N256 run is $25 h^{-1} \text{ cMpc}$, and the number of employed particles is 2×256^3 , as the name indicates. The L25N256 run has the same resolution as the Fiducial run (i.e., L50N512). The L25N512 and L25N128 have eight times better and worse mass resolution than the L25N256 run. The same configurations and parameters are employed in the three runs except for the gravitational softening length. In the L25N256 run, we use the same gravitational softening length as the Fiducial run, and we set it to twice as small and as large in the L25N512 and L25N128 runs.

Finally, in the L25N256NoZdepSN run, the stellar **IMF** is fixed to the Chabrier **IMF**, and the hypernova fraction is set to 0.01, independent of metallicity and redshift. This is different from our fiducial treatment used in L25N256, where the specific energy of Type-II **SN** is higher for lower metallicity stars as shown in Fig. 3.10 due to metallicity- & redshift-dependent **IMF** and hypernova fraction.

3.6 Data Analysis

Simulation data is analyzed by on-the-fly **FoF** and the SUBFIND group and substructure finder (Springel et al., 2001, 2021). For visualization and further data analysis, we

generate a uniform three-dimensional cartesian mesh covering the entire simulation box with 1024^3 voxels, assign particle data, and take projections on the fly. The [cloud-in-cell \(CIC\)](#) assignment is used for dark matter and star particles, and the [SPH](#) kernel weight is used for gas particles. The [SPH](#) particle data is assigned to the mesh, conserving the total mass, metal mass, and internal energy. For only data analysis purposes, we set a floor in the [SPH](#) smoothing length at $(\sqrt{3}/2)L_{\text{voxel}}$, where L_{voxel} is the size of a voxel, so that there are some voxel centers within the smoothing length from each [SPH](#) particle. We then assign mass of $m_i W_{ij}(h_i) / \sum_k^N W_{ik}(h_i)$ to j -th voxel from i -th particle, where m_i and h_i are the mass and smoothing length of the i -th particle, and $W_{ij}(h_i) = W(r_{ij}; h_i)$ is the kernel weight with r_{ij} being the distance from i -th particle to the center of j -th voxel. The metal mass and internal energy are assigned to voxels in the same manner, and the metallicity and temperature of each voxel are calculated using the mass, metal mass, and internal energy of the voxel. This mesh generator module is useful for the post-process analysis of the [IGM](#) presented in Section 5.1.

Figure 3.11 shows the density projection image of the Fiducial run at $z = 0$. The baryonic cosmic web, composed of intermediate-temperature ($10^{4.5} \text{ K} < T < 10^{5.5} \text{ K}$) filaments and high-temperature nodes, is apparent. The rest of the cosmic volume is filled with low-temperature voids. ¹²

¹²The movie is available at <https://www.yurioku.com/research/>

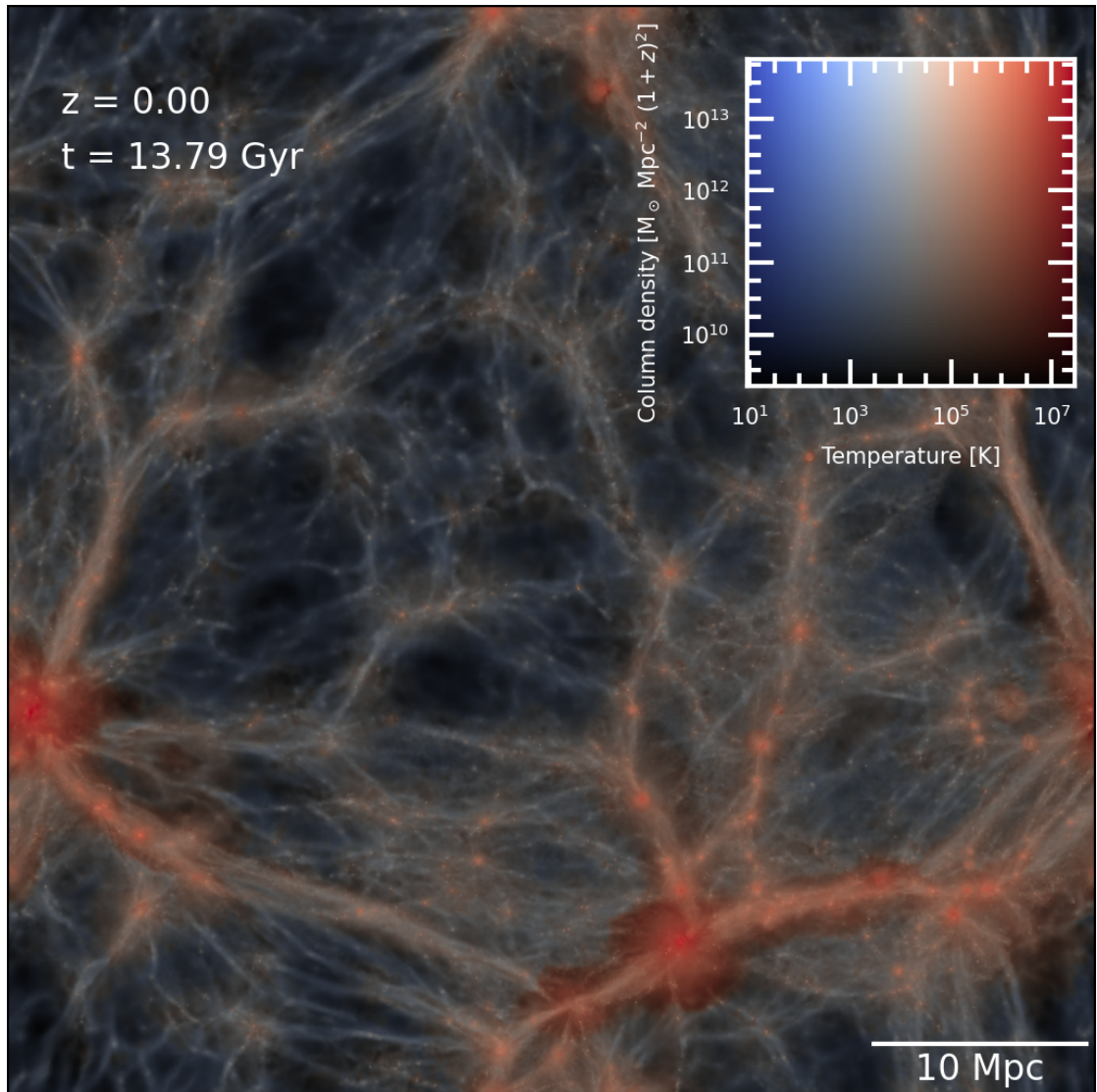


FIGURE 3.11: Projected image through a $6.25 h^{-1} \text{ cMpc}$ slice of the Fiducial run. The color and intensity indicate temperature and density, as shown by the color map at the top right corner of the image

Chapter 4

General results

In this chapter, we show the general results from the CROCODYLE simulation dataset.

4.1 Cosmic star formation rate history

Figure 4.1 shows the history of cosmic star formation rate density of CROCODYLE simulations. The black dashed line is the best-fitting function to the [UV](#) and [infrared](#) ([IR](#)) observations at $0 < z < 8$ by [Madau and Dickinson \(2014\)](#),

$$\psi = 0.015 \frac{(1+z)^{2.7}}{(1+(1+z)/2.9)^{5.6}} \text{ M}_\odot \text{ yr}^{-1} \text{ cMpc}^{-3}, \quad (4.1)$$

which peaks at $z \sim 1.8$. The Fiducial run generally captures the trend of the observational best-fit function. Three runs with mechanical [SN](#) feedback suppress star formation at high redshift and have a peak of cosmic [SFR](#) density at $z \sim 2$, and others produce more stars at high redshift and have a peak at $z \sim 3$. Comparing Fiducial and SNonly runs, the [SFR](#) of the Fiducial run is lower at $z < 2$, indicating the suppression of star formation by [AGN](#) feedback. The small bump at $z = 7$ is due to the reionization, after which the [UV](#) background radiation ionizes neutral hydrogen and suppresses star formation.

We note that this is not a direct comparison; our simulation results show the actual [SFR](#) while the observational best-fit function is obtained from [SFR](#) estimated from [UV](#) or [IR](#) luminosity function under an assumption of fixed [IMF](#). Our simulation adopts metallicity- and redshift-dependent [IMF](#), and further analysis is necessary for direct comparison. At high redshift, dwarf galaxies with low metallicity are the major place of star formation, where the [IMF](#) is top-heavy and more [UV](#) photon is produced for a given [SFR](#). We expect

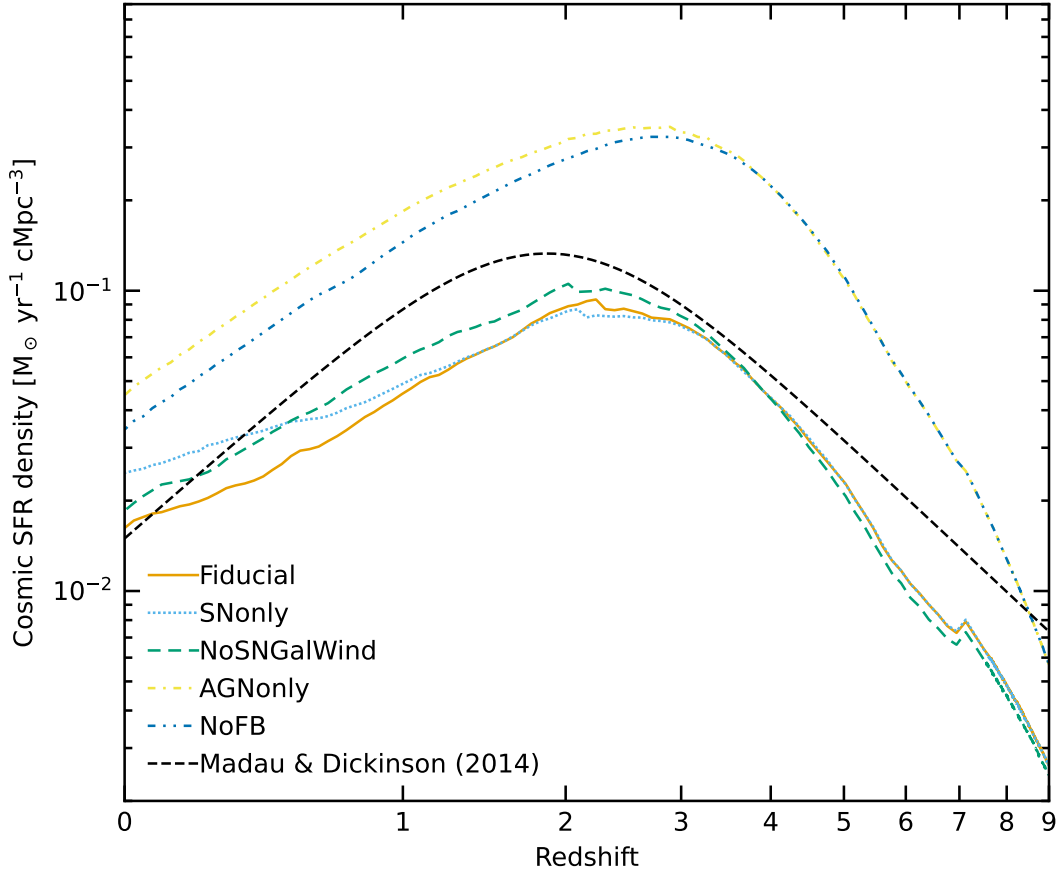


FIGURE 4.1: The history of cosmic star formation rate density of CROCODILE simulation. The black dashed line is the fitting function to [UV](#) and [IR](#) observations by [Madau and Dickinson \(2014\)](#).

the discrepancy between the Fiducial simulation and observations to be smaller when they are compared in terms of [UV](#) luminosity density.

4.2 Phase diagram

Figure 4.2 shows the phase diagram of the Fiducial run at $z = 0$. The cold and dense gas is the star-forming gas in the interstellar medium in galaxies, and the hot and tenuous gas is the circumgalactic medium heated by virial shock and feedback. The cold and tenuous gas is the intergalactic medium at photoionization equilibrium of [UV](#) background radiation and Compton cooling off of the cosmic microwave background and has a slope of $1/1.7$ ([Hui and Gnedin, 1997](#), [McQuinn, 2016](#)).

Unlike some previous cosmological simulations e.g., EAGLE and IllustrisTNG, we did not use an effective [EoS](#) for unresolved multiphase [ISM](#). We instead use the non-thermal

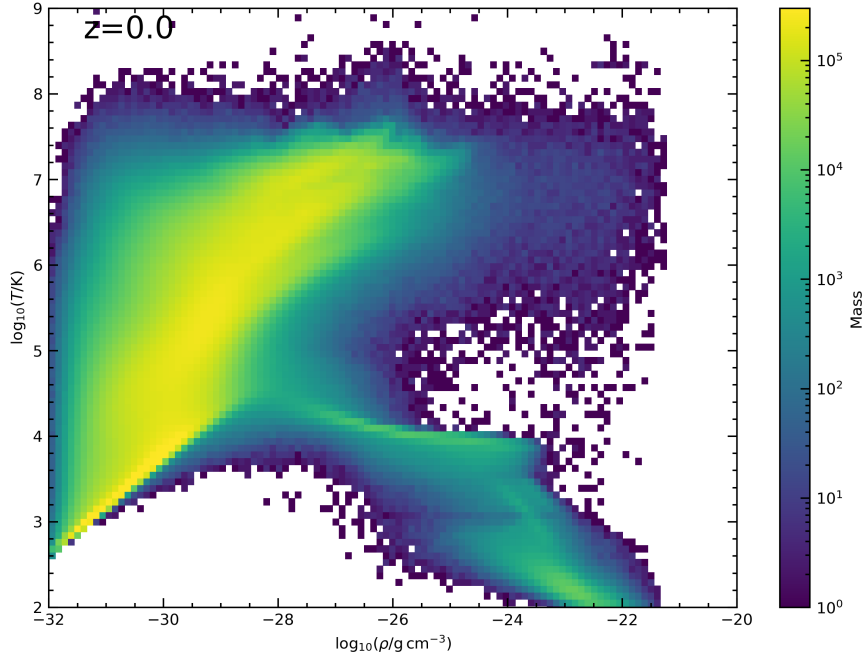


FIGURE 4.2: Phase diagram of the Fiducial run at $z = 0$. The color shows the mass in each bin.

pressure floor to track the gas cooling down to 100 K. This treatment enables us to obtain a realistic phase diagram.

4.3 Galaxy Statistics

This section compares the statistical properties of galaxies formed in our simulations. In the following subsections, we compare simulations focusing on the feedback model variation, **BH** model parameters, resolution, and **SN** feedback energy variation. We examine the stellar mass, **SFR**, gas-phase metallicity, and the most massive black hole mass in galaxies, identified as subhalos by the SUBFIND algorithm. The stellar mass presented in the following is the mass of stars within twice half-stellar-mass radius; for each collection of stellar particles in a subhalo, we compute the radius of a sphere enclosing half of its mass and then obtain the stellar mass within the twice half-stellar-mass radius. The **SFR** of a galaxy is the sum of the gas particles' **SFR**, computed using Eq. 3.31, in the subhalo. The gas-phase metallicity of a galaxy is an **SFR**-weighted average of the metallicity of gas particles in the subhalo, intended for comparison with observations where metallicity is measured using nebular lines from ionized regions around young stars in star-forming regions. In the following figures, we show various quantities as a function

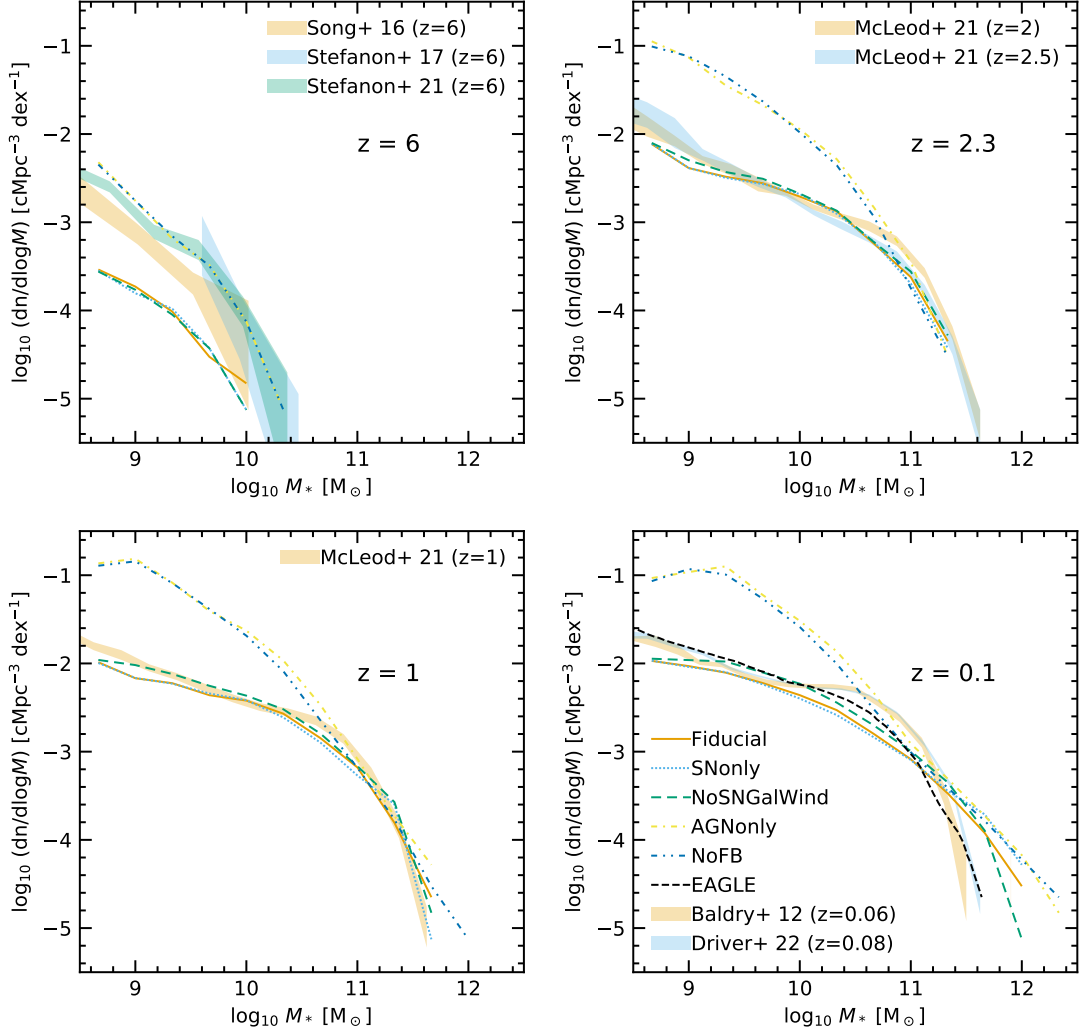


FIGURE 4.3: Galaxy stellar mass function at $z = 0.1, 1, 2.3, 6$. The black dashed line in the bottom right panel is for the Ref run of EAGLE simulation (Schaye et al., 2015). The shaded regions are the observational constraints on SMF from Song et al. (2016), Stefanon et al. (2017, 2021) at $z = 6$, McLeod et al. (2021) at $z = 1, 2$, and 2.5 , and Baldry et al. (2012) and Driver et al. (2022) around $z = 0.1$.

of galaxy stellar mass above $M_* = 10^{8.5} M_\odot$ because the mass of each stellar particle is $9.1 \times 10^6 M_\odot$.

4.3.1 Feedback Model Variation

Figure 4.3 shows the galaxy stellar mass function at $z = 6, 2.3, 1$, and 0.1 . The shaded regions are the observational constraints on the stellar mass function from Song et al. (2016), Stefanon et al. (2017, 2021) at $z = 6$, McLeod et al. (2021) at $z = 1, 2$, and 2.5 , and Baldry et al. (2012) and Driver et al. (2022) around $z = 0.1$.

The Fiducial, SNonly, and NoGalWind runs show suppressed star formation compared to runs without **SN** mechanical feedback (AGNonly and NoFB) at $M_* < 10^{11} M_\odot$, leading to a better consistency with the observation at $z = 2.3$ and 1 . This indicates that the **SN** mechanical feedback is the dominant feedback source for the low-mass galaxies.

At $z \sim 6$, our **SN** feedback model appears to be a bit too strong, leading to an underprediction of galaxies with $M_* < 10^{9.5} M_\odot$ despite the good agreement in the star-formation main sequence (top left panel of Figure 4.4). Interestingly, runs without **SN** mechanical feedback demonstrate a closer agreement with observational data. Moreover, recent observations by the *James Webb Space Telescope (JWST)* have unveiled more numerous massive galaxies at $z > 7$ than expected from cosmological simulations (Harikane et al., 2023, Bouwens et al., 2023, Finkelstein et al., 2023, Chemerynska et al., 2023, Yung et al., 2024). At $z \gtrsim 6$, the discrepancy between our simulation results and observational data becomes more pronounced. Dekel et al. (2023) have introduced the concept of a ‘feedback-free starburst’ scenario. This theory suggests that gas in high- z halo can be efficiently converted into stars with minimal feedback effects, primarily due to the conditions of high density and low metallicity prevalent at these early cosmic times. The closer agreement of the NoFB run with observations lends support to this feedback-free starburst hypothesis. However, it remains uncertain whether this scenario can consistently account for the observed stellar mass function at lower redshifts. This uncertainty points to a potentially critical area of investigation in understanding the evolution of galaxies across different epochs.

At $z = 0.1$, the Fiducial run nicely reproduces the low-mass end of the observed stellar mass function. Both our simulations and the EAGLE simulation decrease towards a higher mass end with a slightly steeper slope than the observed exponential cutoff at $M_* \sim 10^{11.5} M_\odot$, but capture the cutoff mass range relatively well.

Figure 4.4 shows the star-formation main sequence at $z = 6, 2.3, 1$, and 0.1 . The points and error bars show the median **SFR** values and 16th and 84th percentile for each stellar mass bin in our simulations. The shaded regions are the observational constraints from Salmon et al. (2015) at $z = 6$, Karim et al. (2011) at $z = 2.25, 1.1, 0.9$, and 0.3 , Tomczak et al. (2016) at $z = 2.25, 1.125$, and 0.875 , and Whitaker et al. (2012) at $z = 0 - 0.5$. We display only the star-forming galaxies, selected by a criterion **specific star formation rate (sSFR) > 10⁻² Gyr⁻¹**, because the observed data are also for star-forming galaxies.

At $z = 6$, the simulations show similar star-formation main sequences with each other. The runs without stellar feedback show lower **SFR** than the observed star-formation main sequences for a given stellar mass at lower redshifts. This indicates that stellar feedback is necessary to sustain star formation activity by driving interstellar turbulence and galactic wind to delay the depletion of gas in the dark matter halo and produce

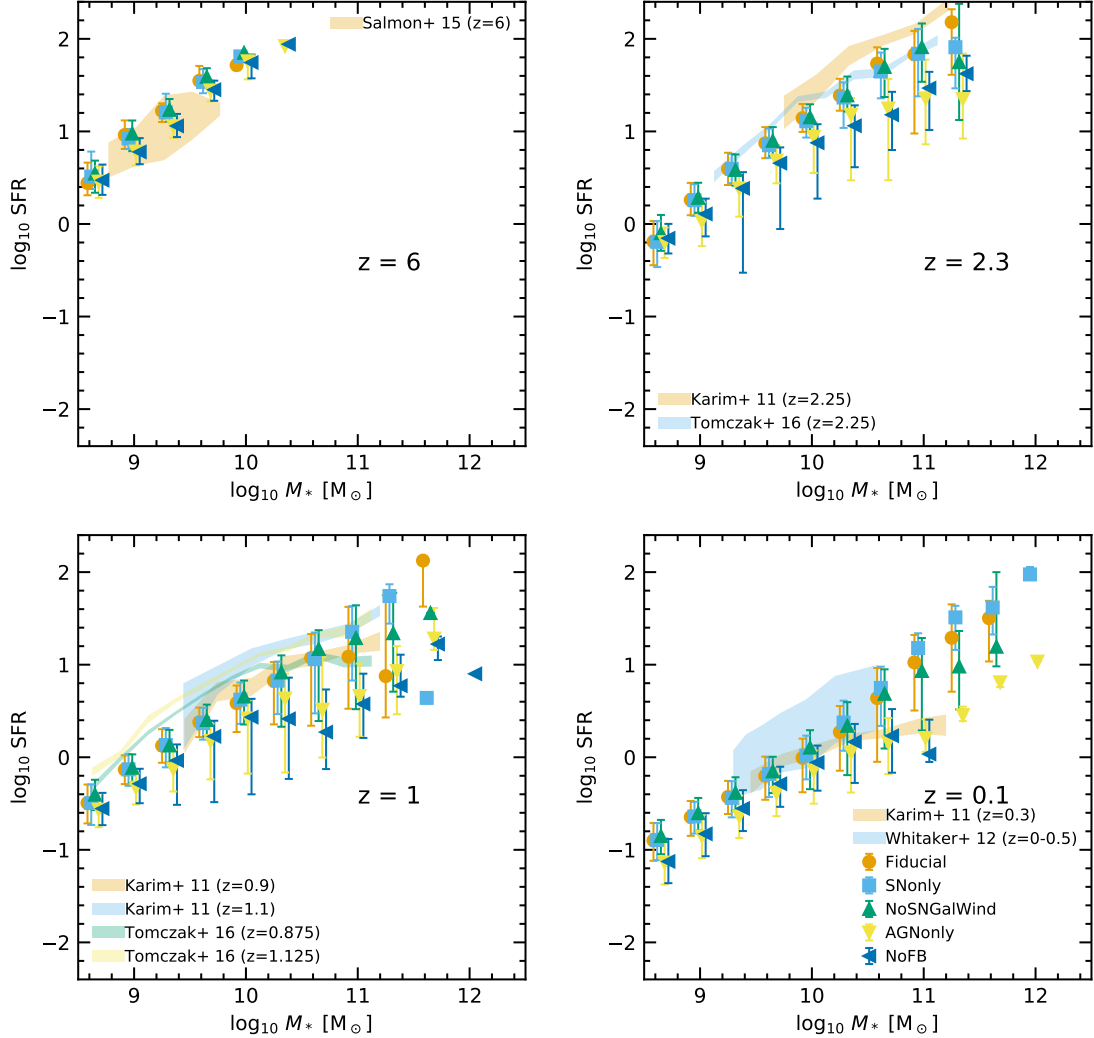


FIGURE 4.4: Redshift evolution of the star formation main sequence of the simulated galaxies with $\text{sSFR} > 10^{-2} \text{ Gyr}^{-1}$. The points and error bars show the median SFR values and 16th and 84th percentile for each stellar mass bin in our simulations. The shaded regions are the observational constraints from [Salmon et al. \(2015\)](#) at $z = 6$, [Karim et al. \(2011\)](#) at $z = 2.25, 1.1, 0.9$, and 0.3 , [Tomczak et al. \(2016\)](#) at $z = 2.25, 1.125$, and 0.875 , and [Whitaker et al. \(2012\)](#) at $z = 0 - 0.5$.

star-forming galaxies at $z = 0$. Runs with stellar feedback show a nice agreement with observations.

Figure 4.5 shows the mass-metallicity relations at $z = 6, 2.3, 1$, and 0.1 . The metallicity of simulated galaxies is computed with the total metal mass in the gaseous phase. The points and error bars show the median metallicity values and 16th and 84th percentile for each stellar mass bin in our simulations. The shaded regions are observational constraints from [Sanders et al. \(2021\)](#), [Strom et al. \(2022\)](#) at $z = 2.3$ and [Andrews and Martini \(2013\)](#), [Tremonti et al. \(2004\)](#) at $z = 0.1$. The galaxies in the runs without stellar feedback have higher metallicity at $M_* \lesssim 10^9 M_\odot$, which indicates that stellar feedback expels metals from galaxies.

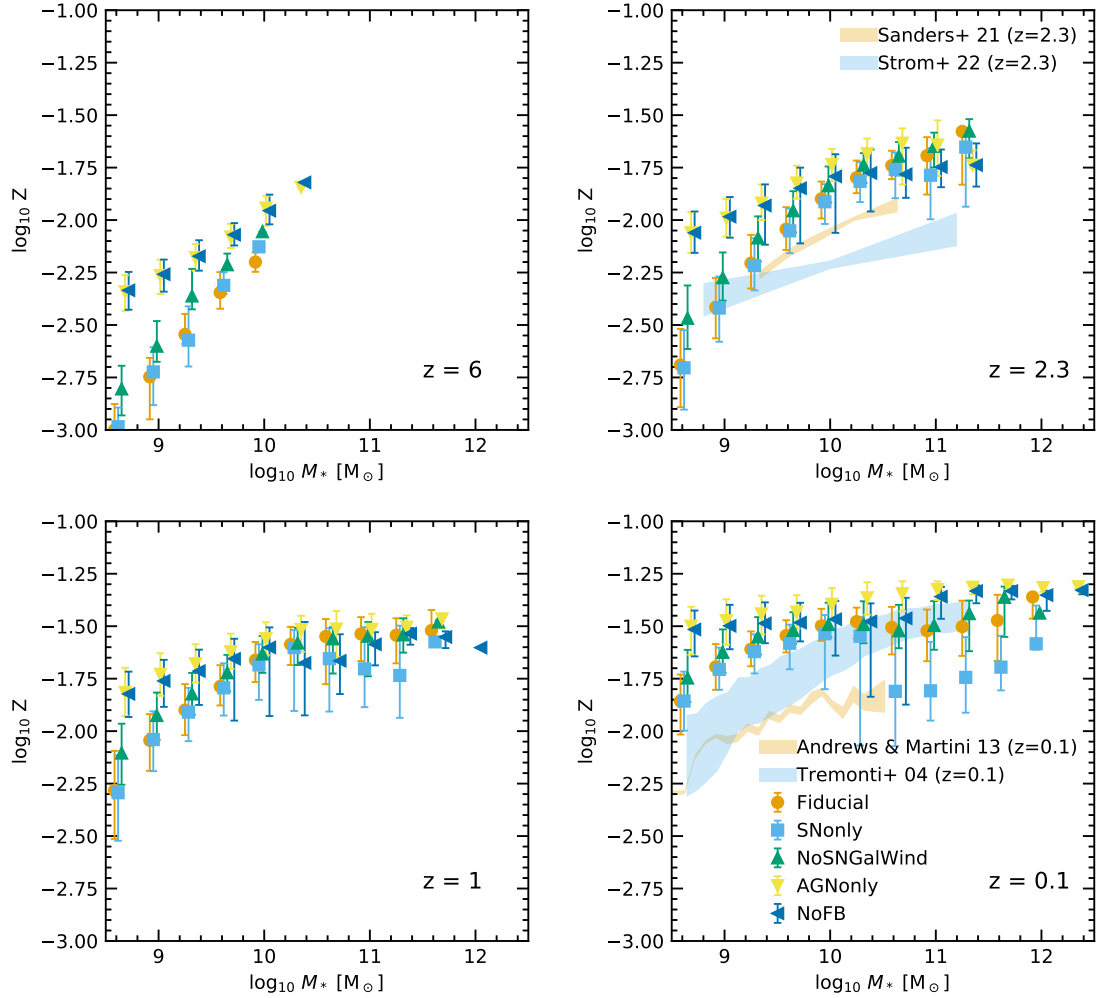


FIGURE 4.5: Redshift evolution of the mass–metallicity relation. The points and error bars show the median metallicity values and 16th and 84th percentile for each stellar mass bin in our simulations. The shaded regions are observational constraints from Sanders et al. (2021), Strom et al. (2022) at $z = 2.3$ and Andrews and Martini (2013), Tremonti et al. (2004) at $z = 0.1$.

One can see that the NoSNGalWind run has slightly higher metallicity than the Fiducial run. This is because of the metal reduction by the galactic wind in the Fiducial run. The typical metal loading factor of our galactic wind model is 0.3, corresponding to 0.15 dex, which can explain the difference between the NoSNGalWind and Fiducial run. The difference among the models is small at $M_* \gtrsim 10^{10} M_{\odot}$ because the feedback effect is weaker at the massive end, where the gravitational binding energy is stronger.

The metallicity of simulated galaxies of $M_* \sim 10^{10} M_{\odot}$ is 0.2 dex higher than the mass–metallicity relation by Sanders et al. (2021) at $z = 2.2$, and 0.4 dex higher than the mass–metallicity relation by Andrews and Martini (2013) at $z = 0.1$. This can be due to either inefficient metal ejection by the galactic wind or insufficient gas mass in the

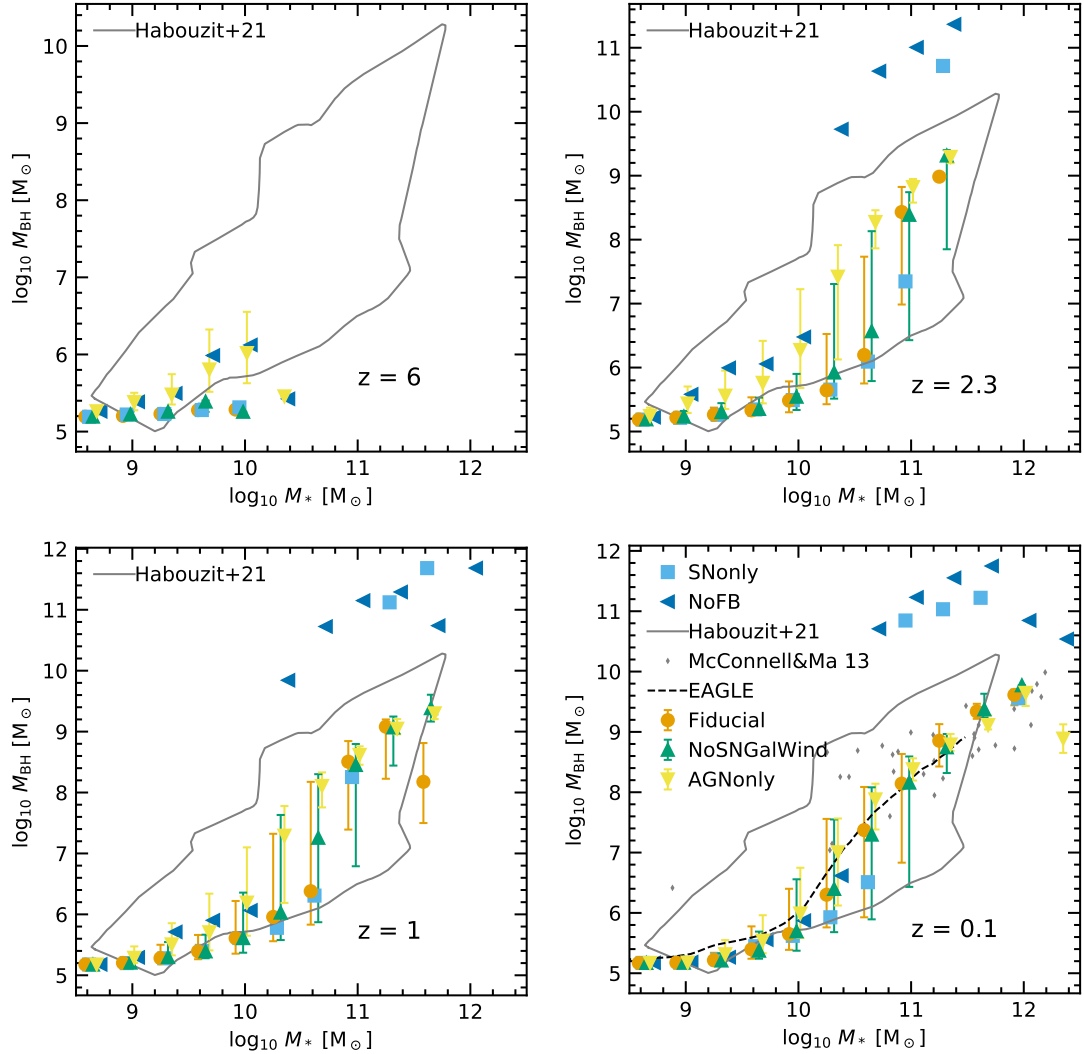


FIGURE 4.6: Redshift evolution of the **BH** mass–stellar mass relation. The points and error bars show the median value and 16th and 84th percentile of the most massive **BH** mass in the galaxies in each stellar mass bin. For the SOnly and NoFB runs, we omit the error bars for clarity. The black dashed line shows the median of the EAGLE Ref run. The region indicated by the gray solid line covers the majority of local observational constraints compiled by [Habouzit et al. \(2021\)](#). The gray diamonds are observational data by [McConnell and Ma \(2013\)](#).

simulated galaxies at low redshift. We will investigate the galactic outflow properties in our simulations by comparing them with recent IFU data in our future work.

Figure 4.6 shows the **BH** mass as a function of galaxy total stellar mass. The points and error bars show the median value and 16th and 84th percentile of the most massive **BH** mass in the galaxies in each stellar mass bin. The region indicated by the black solid line is the observational constraint at $z = 0$ compiled by [Habouzit et al. \(2021\)](#). The gray diamonds are observational data by [McConnell and Ma \(2013\)](#).

The runs with **AGN** feedback have lower **BH** masses at $z \lesssim 3$ because the gas around

BHs is blown away by the **AGN** feedback. In the runs with **AGN** feedback, the $M_{\text{BH}} - M_*$ relation is consistent with observations, and the medians are almost at the lower edge of the observationally constrained region at $10^9 M_\odot < M_* < 10^{10.5} M_\odot$. This behavior is sensitive to the choice of subgrid parameters of black holes, as demonstrated in Section 4.3.2.

The AGNonly run also shows higher **BH** mass than the Fiducial run, indicating that the stellar feedback inhibits the gas accretion onto **BHs** and suppresses **BH** growth. The difference between the AGNonly and Fiducial run is noticeable at $M_* \sim 10^9 M_\odot - 10^{11} M_\odot$ at $z > 1$, where stellar feedback is considered to be playing the major role in regulating the galaxy formation, while the results from the two runs converge at the massive end.

Figure 4.7 shows the halo baryon fraction f_{baryon} normalized by the cosmic mean baryon fraction, $\Omega_{\text{baryon}}/\Omega_{\text{matter}}$, versus halo mass at $z = 0$. For the Fiducial run, the f_{baryon} increases monotonically as the halo mass increases. The baryon mass is reduced for low-mass halos due to **SN** feedback. Comparing the Fiducial and NoSNGalWind runs, there are only minor differences, which indicate that the hot galactic wind plays a minor role and the kinetic feedback is dominant in ejecting baryons out from halos. Comparing the Fiducial and SOnly runs, the SOnly run has higher f_{baryon} at $M_h > 10^{12} M_\odot$, indicating the **AGN** impact of ejecting gas from halos. The f_{baryon} of the Fiducial run is consistent with the observational estimate by Das et al. (2023) while EAGLE and TNG underpredict f_{baryon} . These simulations adopt **SN** and **AGN** feedback models that are too strong in driving the galactic outflows to suppress star formation by removing gas in halos. The momentum-based kinetic **SN** feedback model in our simulation is moderate in driving the galactic outflow for galaxies with $M_h \sim 10^{12.5} M_\odot$, and the baryons are kept in **CGM**.

4.3.2 BH Parameter Variation

Figure 4.8 again shows the $M_{\text{BH}} - M_*$ relation, stellar mass function, and star-formation main sequence, but for the runs with different **BH** parameters, Fiducial, LowCvisc, and LowCviscLowMseed, at $z = 2.3$ and 0.1 .

Panels A and B show the $M_{\text{BH}} - M_*$ relation. The C_{visc} controls the onset of the **BH** growth, and the **BH** mass starts to increase at $M_* \sim 10^9 M_\odot$ for runs with low C_{visc} ($= 2\pi$) and at $10^{10} M_\odot$ for the runs with our default C_{visc} ($= 200\pi$) at $z = 0.1$. The simulation data points of the Fiducial run are around the bottom of the region indicated by Habouzit et al. (2021), while those by the LowCvisc run are around the top of the region. At $M_* > 10^{11} M_\odot$, it is interesting to see that the $M_{\text{BH}} - M_*$ relation for all three simulations agree due to the self-regulated growth of **BH**.

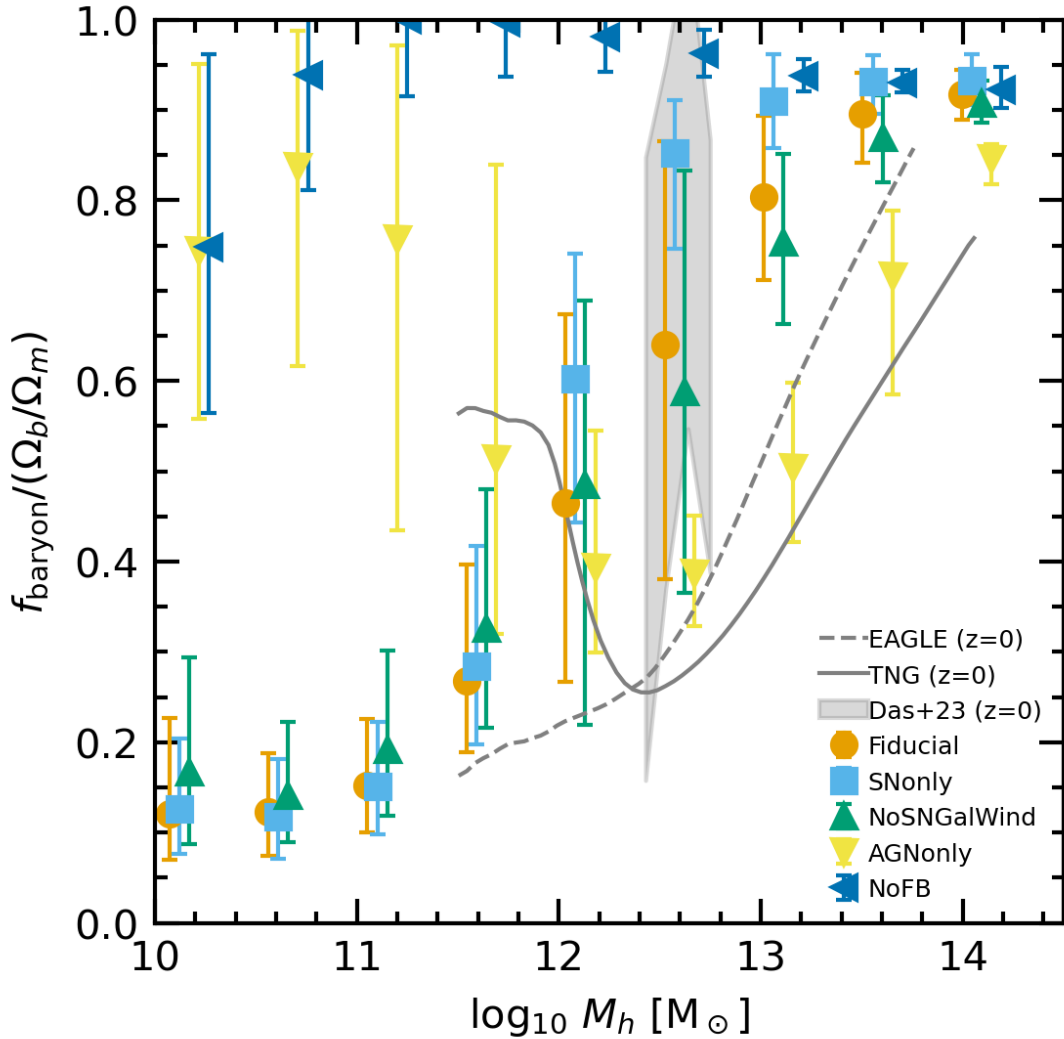


FIGURE 4.7: Halo baryon fraction, f_{baryon} , normalized by the cosmic mean baryon fraction, $\Omega_{\text{baryon}}/\Omega_{\text{matter}}$, vs. halo mass at $z = 0$. The points and error bars show the median value and 16th and 84th percentile of the mass of baryons (star and gas) in the halos in each halo mass bin. The gray dashed and solid lines are the median lines of the EAGLE-Ref and TNG-100 simulations taken from [Davies et al. \(2020\)](#). The gray-shaded region is estimated baryon fraction by the observation of thermal Sunyaev–Zel’dovich effect ([Das et al., 2023](#)).

Panels C and D show the stellar mass function. By comparing with panels A and B, one can see that the stellar mass function rapidly declines at the same mass scale where the **BH** mass rapidly increases. The stellar mass function of the LowCvisc run is lower than other runs at $M_* > 10^{9.5} M_\odot$ due to the early growth of **BHs** and subsequent **AGN** feedback. In the LowCviscLowMseed run, the **BH** growth is delayed due to the smaller **BH** seed mass, as seen in the upper panels, and it shows a similar stellar mass function to the Fiducial run.

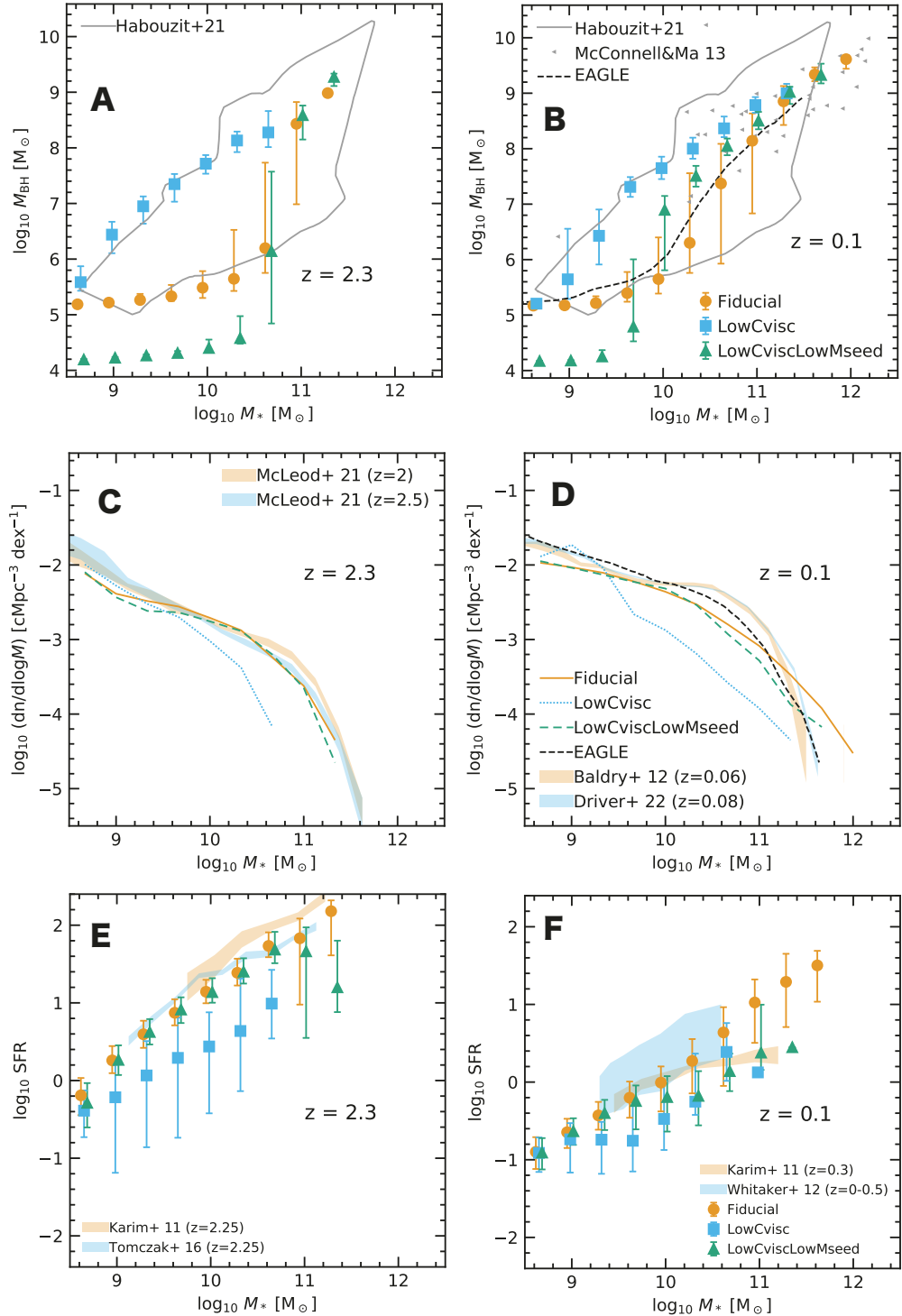


FIGURE 4.8: Comparing the $M_{\text{BH}}-M_{*}$ relation, stellar mass function, and star-formation main sequence for the runs with different BH parameters, Fiducial, LowCvisc, and LowCviscLowMseed, at $z = 2.3$ and 0.1 .

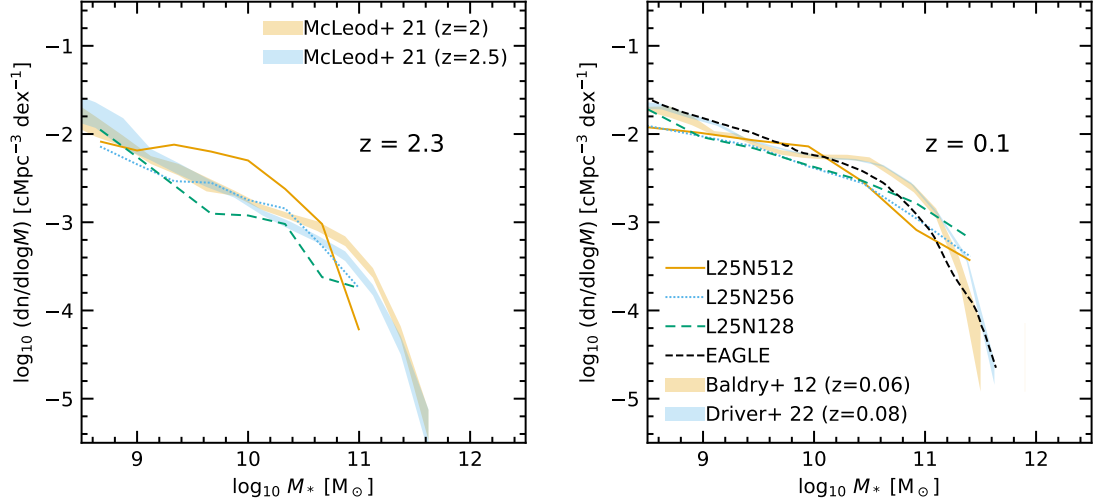


FIGURE 4.9: Galaxy stellar mass functions of the runs with different resolutions, L25N512, L25N256, and L25N128 at $z = 2.3$ and 0.1 .

We can also see the impact of **AGN** feedback on the star formation activity in the star-formation main sequence shown in panels E and F. The slope of the star-formation main sequence becomes shallower at the same stellar mass where the **BH** begins to grow rapidly.

4.3.3 Resolution Variation

Figure 4.9 shows the stellar mass functions of the runs with different resolutions, L25N512, L25N256, and L25N128. We used the same subgrid and numerical parameters except for the gravitational softening length in these runs. They roughly converge and agree with the observed stellar mass function. The stellar mass function slightly increases with increasing resolution at $z = 2.3$. This is attributed to the density dependence of the star formation efficiency; higher resolution simulations can resolve higher density star-forming clouds, which have shorter star formation timescales.

4.3.4 SN Feedback Energy Yield Variation

Figure 4.10 shows the stellar mass function of the L25N256 and L25N256NoZdepSN runs at $z = 2.2$ and 0.1 . In the L25N256 run, we used the metallicity- and redshift-dependent **SN** energy yield model, which has increasing specific **SN** energy towards lower **SN** progenitor metallicity as shown in Fig. 3.10. In the L25N256NoZdepSN run, the specific **SN** energy is fixed to $\zeta_{\text{SN}} \simeq 6 \times 10^{48} \text{ erg M}_{\odot}^{-1}$. One can see that the L25N256NoZdepSN run completely overpredicts the number of low-mass galaxies. This indicates that the **SN**

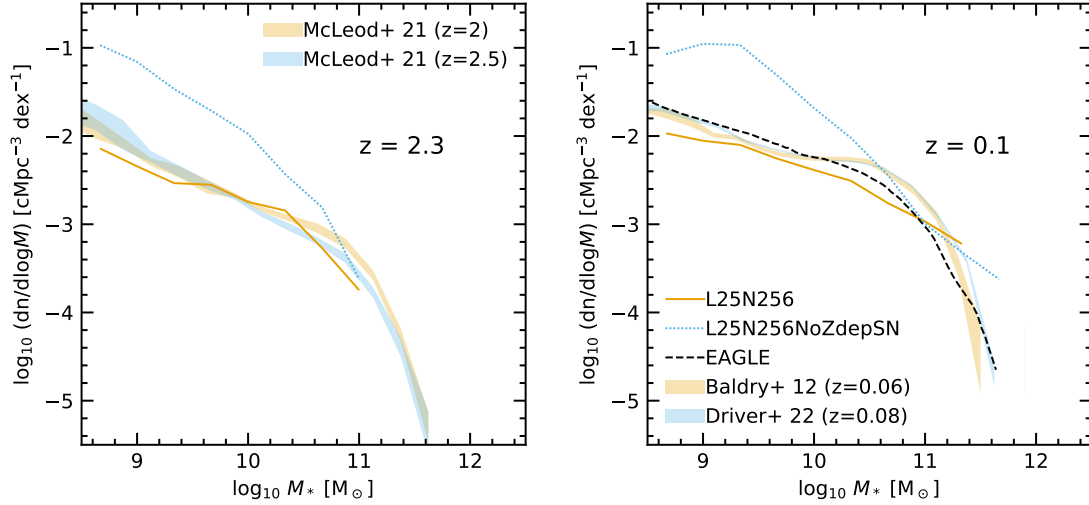


FIGURE 4.10: Galaxy stellar mass function of the L25N256 and L25N256NoZdepSN runs at $z = 2.3$ and 0.1 .

feedback with the above constant ζ_{SN} is not strong enough to suppress star formation and reproduce the observed stellar mass function.

Chapter 5

Metal enrichment in the IGM

In this chapter, we analyze the distribution of metals in the **IGM** and show the impact of **SN** and **AGN** feedback by comparing simulations with varying feedback models.

5.1 Visual inspection

Figure 5.1 shows the density-weighted projections of metallicity at $z = 2.3$ and 0 .¹ Metals are distributed following the large-scale structure with visible differences due to feedback settings.

The effect of explicit modeling of **SN**-driven galactic wind can be seen in the comparison between the Fiducial and NoSNGalWind runs. The **SN**-driven metal-rich galactic wind spread metals on $\lesssim 100$ kpc scale in the Fiducial run more uniformly than in the NoSNGalWind run.

Comparing the Fiducial and SNonly runs clarifies the role of **AGN** outflow in the chemical enrichment of the **IGM**. The high-metallicity bubbles of a size of a few Mpc are formed by **AGN** feedback in the Fiducial run at $z = 0$, but they are not visible in the SNonly run. We modeled **AGN** feedback as an isotropic thermal energy injection, however the hot bubble cannot expand into the direction of the galactic disk. Therefore, the metal-rich **AGN** outflow naturally expands in the bipolar direction above and below the galactic disk.

In the NoFB case, metals produced in galaxies remain there, and the distribution of metals follows that of galaxies at $z = 2.3$. It is interesting to see that metals are somewhat spread at $z = 0$, which is likely due to the hydrodynamical effect in galaxy

¹The movie is available at <https://www.yurioku.com/research>

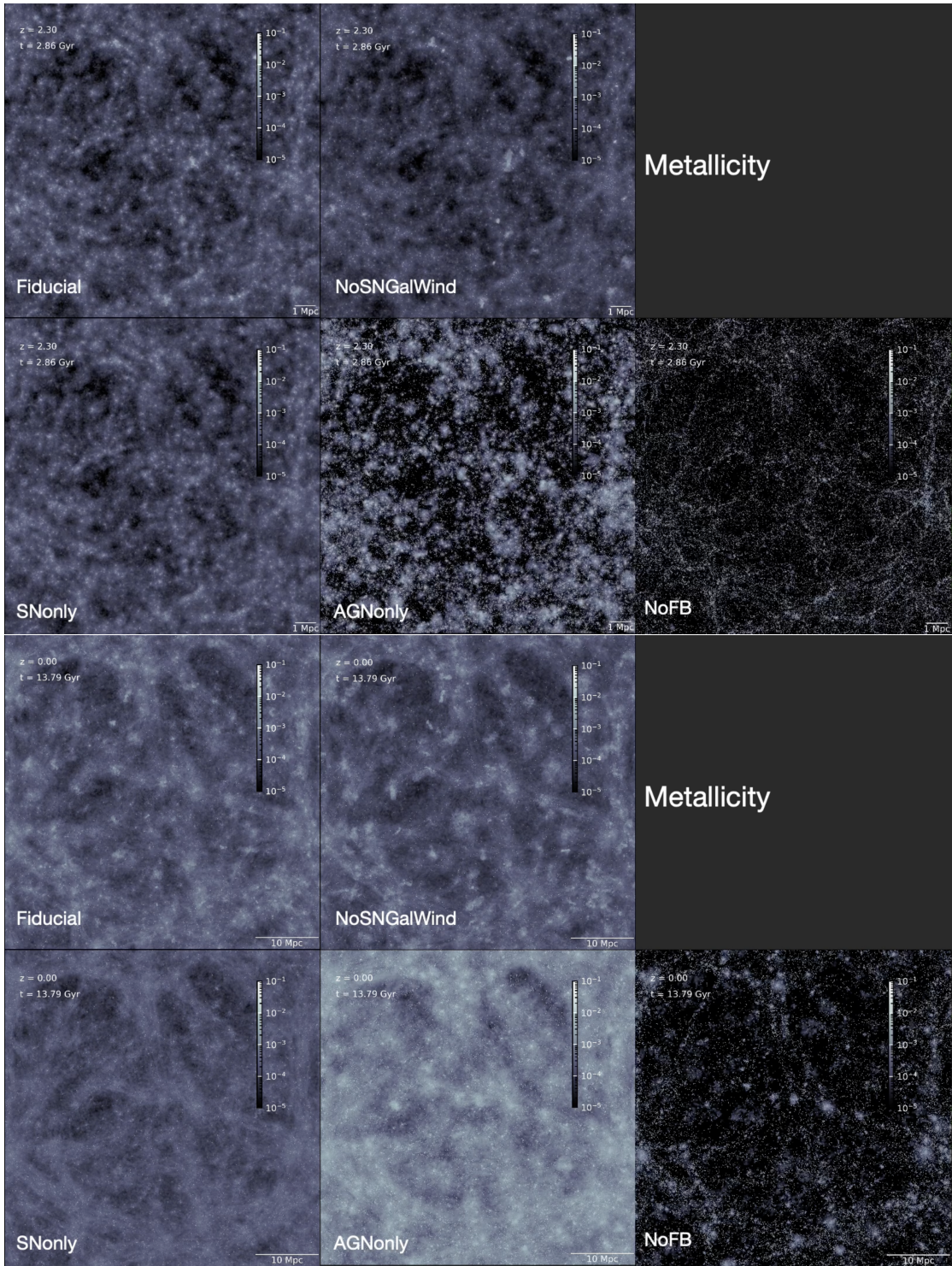


FIGURE 5.1: The density-weighted projection of metallicity at $z = 2.3$ (top two rows) and 0 (bottom two rows).

mergers, galaxy collision, and ram pressure stripping. In other runs, feedback spread metals out to **CGM** and **IGM**.

The AGNonly run shows a distinctively higher metallicity than other runs at $z = 0$ because star formation efficiency is higher due to the lack of **SN** feedback, more metals are produced by stars, and **AGN** feedback spreads metals to **IGM**. The **AGN** feedback begins to have an effect at $z \sim 2$, and the metal enrichment in the void region is delayed from other runs with **SN** feedback at $z = 2.3$.

5.2 Overdensity–metallicity relation

Figure 5.2 and 5.3 show the **IGM** metallicity as a function of the dark matter and gas overdensity. The black dashed line shows the best-fit line for the observational estimate of the metallicity–overdensity relation from the carbon abundance in the Ly α forest (Schaye et al., 2003), $[\text{C}/\text{H}] = -3.47 + 0.08(z - 3) + 0.65(\log \delta - 0.5)$, where δ is the baryon overdensity and z is the redshift. We generate a uniform cartesian mesh with 512^3 voxels and compute dark matter density, gas density, and gas metallicity as described in Section 3.6. The Fiducial, NoSNGalWind, and SNonly run show similar results, indicating that the **SN** mechanical feedback is the dominant mechanism to enrich the **IGM** among other feedback processes. The slope of these runs shows a good agreement with the observation, which is encouraging. Compared to the Fiducial run, the AGNonly run shows higher metallicity at higher overdensity at $z = 2.3$, because more metals are produced and confined in galaxies due to the absence of stellar feedback. Below $z \sim 2$, the **AGN** feedback kicks in and spreads metals to **IGM** and increases metallicity at low overdensity regions, which cannot be seen in the NoFB run.

5.3 Metal density power spectrum

Figure 5.4 shows the power spectra of the metal density field at $z = 2.3$ and 0, which allows us to examine the different effects of feedback models statistically. We use the cosmological analysis toolkit NBODYKIT² (Hand et al., 2018) to compute the power spectra on 1536^3 mesh, and the upper limit of the abscissa (wavenumber) is cut off at $k = k_{\text{Nyq}}/4$, where $k_{\text{Nyq}} = \pi N_{\text{mesh}}/L_{\text{box}}$ is the Nyquist frequency.

At $z = 2.3$, the Fiducial run has lower power at $k > 3 \text{ } h \text{ cMpc}^{-1}$ compared to the NoSNGalWind run, indicating that the galactic wind transport metals and smooth out the metal distribution in **CGM**. The effect of **AGN** can be seen around $k \sim 3 \text{ } h \text{ cMpc}^{-1}$

²The code’s website is <https://nbodykit.readthedocs.io/en/latest/>

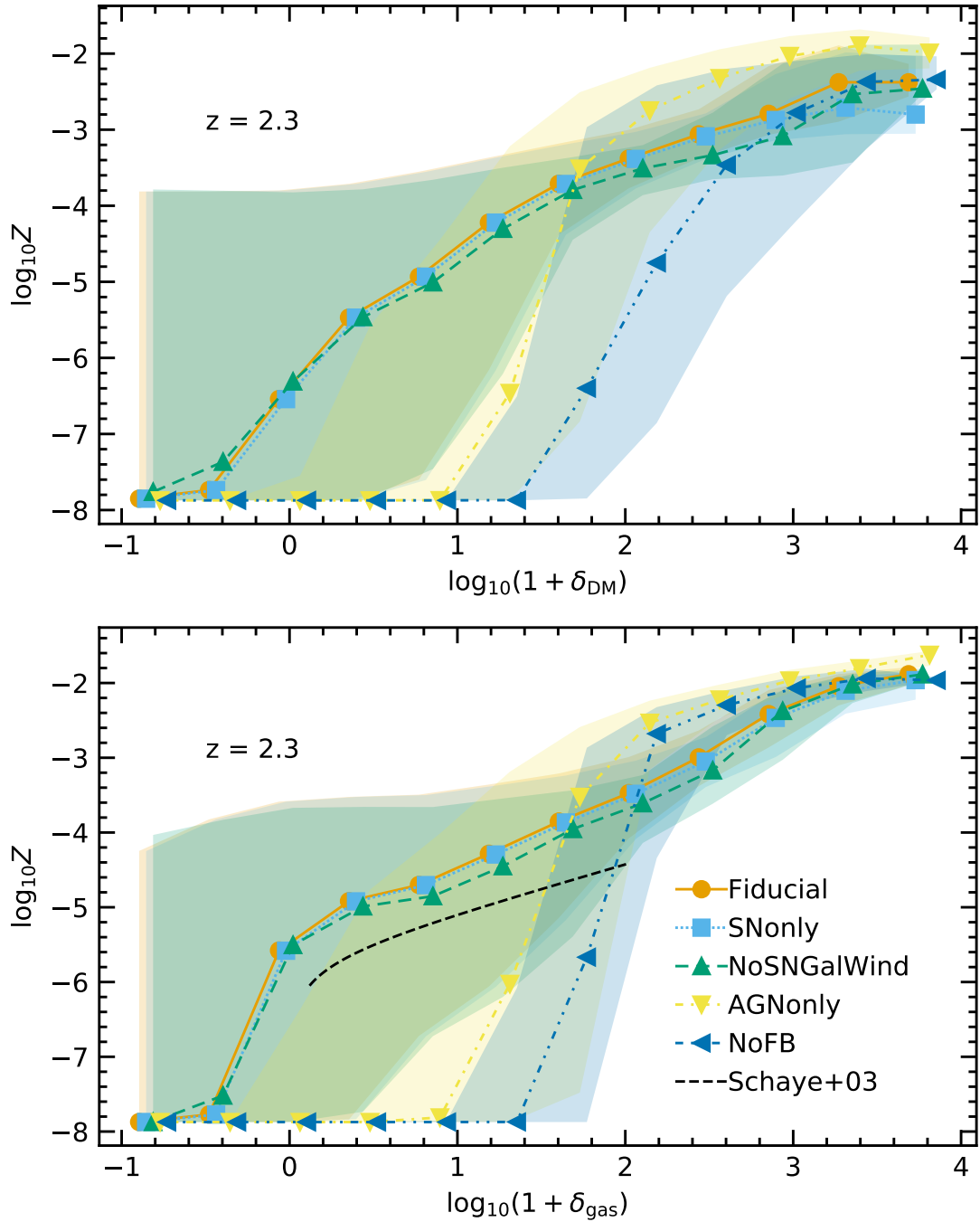
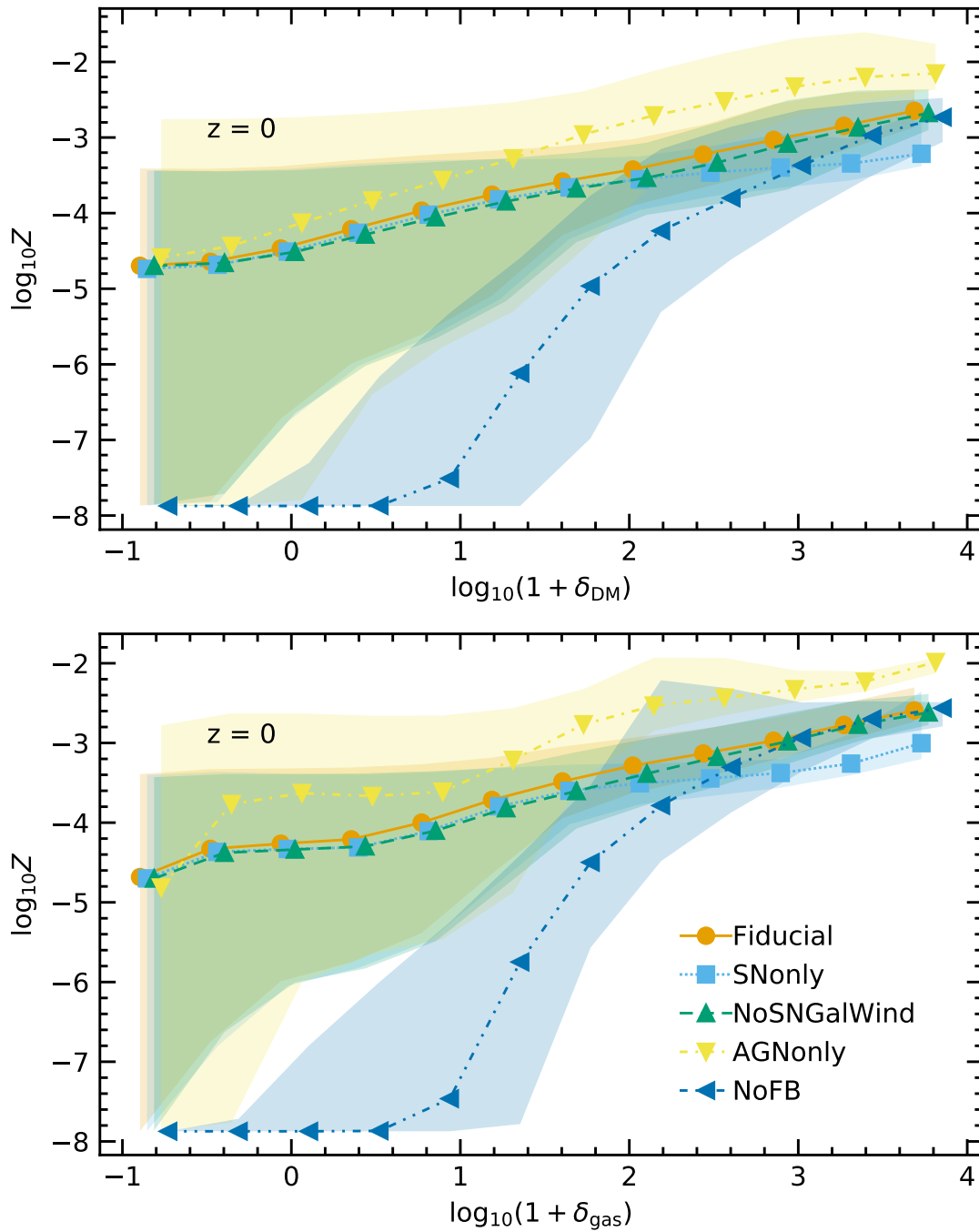


FIGURE 5.2: Metallicity as a function of dark matter (top) and gas (bottom) overdensity at $z = 2.3$. The points and shades indicate the median value and 16th and 84th percentile of the metallicity. The black dashed line shows the observational estimate of the metallicity–overdensity relation using Ly α forest (Schaye et al., 2003).

FIGURE 5.3: Same as Fig. 5.2 but at $z = 0$.

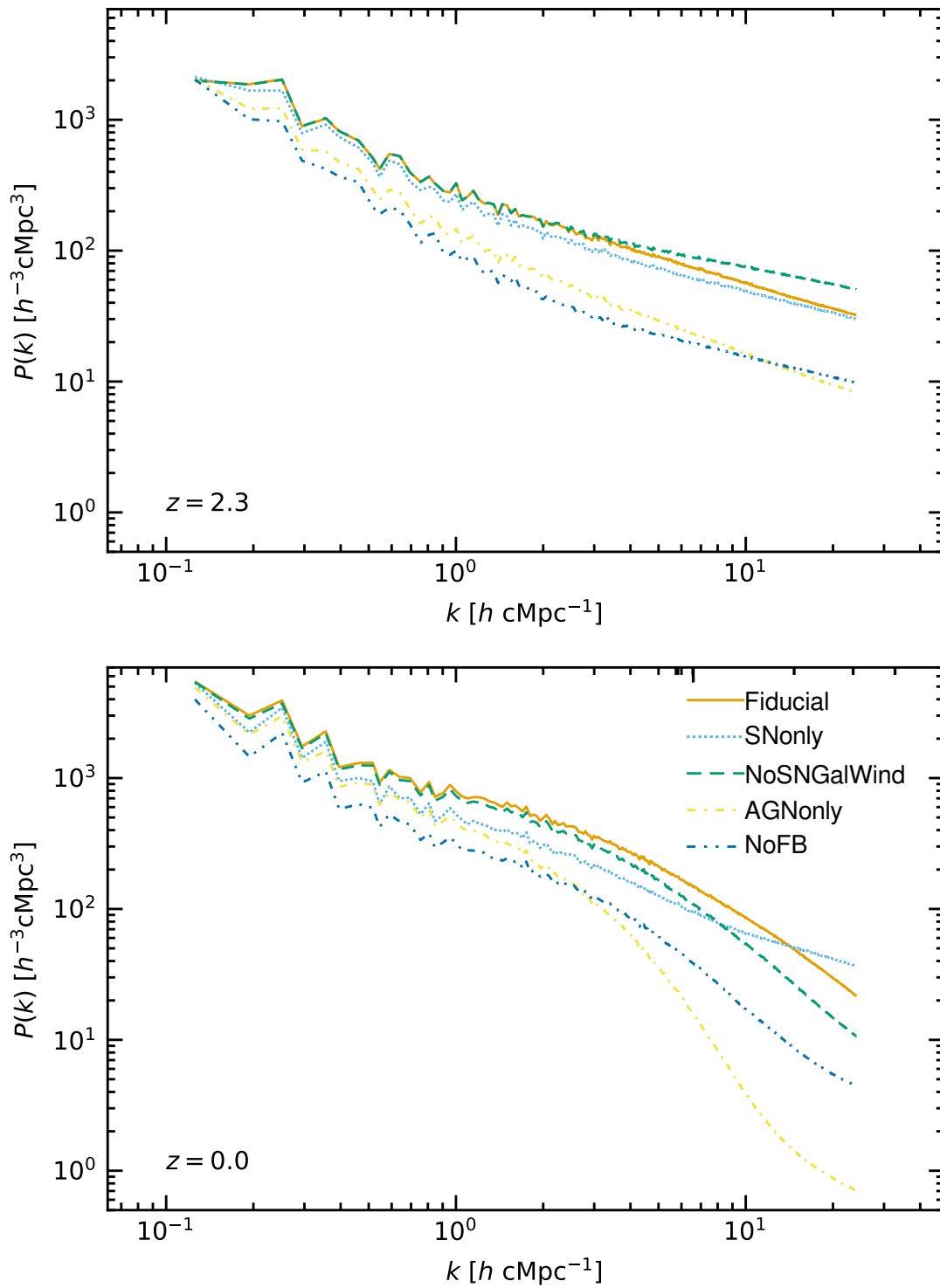


FIGURE 5.4: Power spectra of the metal density field at $z = 2.3$ (top) and 0 (bottom). The upper limit of the abscissa (wavenumber) is cut off at $k = k_{\text{Nyq}}/4$, where k_{Nyq} is the Nyquist frequency.

as a slight enhancement of the power in the Fiducial run relative to the SOnly run due to the **AGN**-driven outflows entraining metals out to a few Mpc scale.

At $z = 2.3$, metals are more diffused in the Fiducial run compared to the NoSNGalWind run, hence lower power on small scales. On the other hand, at $z = 0$, the effect of the **AGN** outflow is stronger, and metals are more diffused in the NoSNGalWind run than in the Fiducial run, leading to a lower power on small scale in the NoSNGalWind run.

Chapter 6

Summary and future prospects

In this thesis, we develop a physically-motivated [supernova \(SN\)](#) feedback model based on high-resolution simulations. We then introduce a new suite of cosmological hydrodynamical simulations CROCODYLE, powered by the GADGET4-OSAKA code utilizing the supernova feedback model. Our simulations also feature an updated chemical evolution model, which integrates a metallicity- and redshift-dependent [initial mass function \(IMF\)](#) based on the star cluster formation simulation by [Chon et al. \(2022\)](#), along with a metallicity-dependent [hypernova \(HN\)](#) fraction. This refinement significantly enhances the specific [SN](#) energy of low-metallicity stars by more than an order of magnitude (Fig. 3.10). Furthermore, we implement an [active galactic nucleus \(AGN\)](#) feedback model, following the methodologies outlined in [Rosas-Guevara et al. \(2015\)](#), [Schaye et al. \(2015\)](#), [Crain et al. \(2015\)](#). This model approaches the [AGN](#) feedback as a stochastic thermal energy injection process.

The main points of this thesis can be summarized as follows:

- Our [SN](#) feedback model incorporates both kinetic and thermal feedback in the form of momentum injection and stochastic thermal energy injection. In isolated galaxy simulations, we have demonstrated that the kinetic feedback suppresses star formation by sustaining the galactic disk against gravitational collapse, and the thermal feedback drives galactic scale outflow transporting metals to [circumgalactic medium \(CGM\)](#) and [intergalactic medium \(IGM\)](#).
- Our simulations reproduce the observed stellar mass function across a broad spectrum of galaxy stellar masses, ranging from $10^8 M_\odot$ to $10^{11} M_\odot$ as illustrated in Figure 4.3. Notably, at $z \lesssim 3$, our [SN](#) feedback model, incorporating a top-heavy [IMF](#), effectively suppresses the formation of low-mass galaxies at $M_* < 10^{10.5} M_\odot$. At $z \sim 0.1$, [AGN](#) feedback plays a crucial role in reducing the number of massive

galaxies with $M_* \gtrsim 10^{11.8} M_\odot$ (bottom right panel of Figure 4.3). We anticipate that the influence of **AGN** feedback will be even more pronounced at the higher-mass end of the stellar mass function in a larger cosmological box of 100 Mpc, which we will perform in the near future.

- Our simulations that incorporate a metallicity- and redshift-dependent **IMF** (including **HN** contributions) can reproduce the stellar mass function at $z \lesssim 2$ relatively well, as shown in Figure 4.10. In stark contrast, the run without this IMF treatment (NoZdepSN run) significantly overpredicts the stellar mass function.
- Our simulations generally agree with the observed star formation main sequence across all redshifts, except for the runs without **SN** feedback (AGNonly and NoFB runs) as depicted in Figure 4.4. The latter two runs significantly overestimate the stellar mass function and mass–metallicity relation, while simultaneously underestimating the star formation main sequence and **IGM** metallicity. This discrepancy underscores the critical role of **SN** feedback in cosmological galaxy evolution.
- Our super massive black hole result at $z = 0.1$ show a general agreement with the EAGLE Ref run within the mass range of $M_* = 10^8 - 10^{12} M_\odot$ and $M_{\text{BH}} = 10^5 - 10^{10} M_\odot$ (Fig. 4.6). With a low C_{visc} parameter, the mass accretion onto **BH** in the LowCvisc run is enhanced relative to the Fiducial run, leading to an overestimation of M_{BH} and a corresponding underestimation of both the stellar mass function and star formation main sequence (Fig. 4.8). Furthermore, the runs without **AGN** feedback (SNonly and NoFB runs) consistently overpredict the M_{BH} .
- We find that the **SN** feedback is the dominant mechanism to transport metals into the **IGM** (Figure 5.2 and 5.3). In addition, the **AGN** feedback generates bipolar, metal-rich outflow (Fiducial and NoSNGalWind panels of Fig. 5.1), effectively enriching the CGM and extending into the **IGM** up to a few Mpc scales, as observed in the power spectrum of metal distribution with scales $k < 10 h \text{ Mpc}^{-1}$ (right panel of Fig. 5.4).

In this thesis, we primarily focused on the broad distributions of metals as functions of overdensities and spatial scales. Given that our simulation tracks multiple chemical species, we are well-positioned to extend our analysis to more detailed ionization calculations for individual elements. This will enable us to conduct comparative studies with a variety of metal absorption lines observed in quasar spectra. Additionally, our simulation incorporates sophisticated models for the formation and destruction of dust (Aoyama et al., 2017, Romano et al., 2022a), which allows us to investigate dust distribution within galaxies, **CGM**, and **IGM** in the future. By conducting cross-correlation

studies between galaxies, H I, dust, and metals, we anticipate gaining a more comprehensive understanding of galaxy evolution and the dynamics of the baryonic universe.

Future observations of [IGM](#) tomography, line intensity mapping, and X-ray mapping, as well as sensitive observation of Ly α and H α halo, will reveal the baryon distribution in the local and distant universe and revolutionize the understanding of structure formation. The rich observational data will first clarify the matter distribution around galaxy clusters, where we expect bright emissions of intercluster medium.

The formation, growth, and feedback of supermassive black holes will remain a central challenge in structure formation for the next decades. The development of physically-motivated black hole models is a central task in cosmological simulation, which we could not complete in this work. The range of the spatial and temporal scale they involve is much wider than that of supernova feedback, and a lot of effort is still necessary. Simulations are expanding the scale they treat, as highlighted by the recent work by [Hopkins et al. \(2023a\)](#), which solves the accretion disk of the central black hole within the realistic cosmological simulation. The continuous effort in this line, along with larger-box cosmological simulation comparable to observational volume, would be the two major approaches in numerical cosmology.

The usage of artificial intelligence (AI) and machine learning (ML) is promising in treating big data from observations and simulations. With the help of social requirements in the development of AI, the study of AI will keep accelerating, and the knowledge will be imported into astronomical research. I expect the AI to learn the behavior of matter and substitute numerical simulation for the current position, but direct simulations will remain a tool for making an *ab initio* prediction of the structure formation of the universe.

Appendix A

Evolution of a superbubble in idealized ISM

In this appendix, we describe the details of the simulation, as well as the basic analytic theory of superbubble evolution. The content in this appendix is a part of my master's thesis work.

A.1 Analytic theory

When multiple [SN](#) explosions occur clustered in space and time in stellar clusters, superbubbles are formed with the shell-formation time being a critical timescale for their growth. In Section [A.1.1](#), we analytically calculate the shell-formation time and investigate its dependence on metallicity.

A.1.1 Shell-formation time

We first consider the shell-formation time of an [SN](#) remnant formed by a single [SN](#) and extend it to the case of a superbubble formed by multiple [SNe](#).

A.1.1.1 Single [SN](#)

After [SN](#) explosion occurs, heated gas adiabatically expands and forms an [SN](#) remnant. The adiabatic phase is called the Sedov–Taylor phase, during which the [SN](#) remnant time evolution is described by Sedov–Taylor solutions. When the cooling effect is no

longer negligible, the **SN** remnant can no longer be considered adiabatic, terminating the Sedov–Taylor phase.

SN remnant cooling is most effective at the shock front, where its density is its highest. The cooling time immediately after the shock wave is estimated to be

$$t_c = \frac{e}{de/dt} = \frac{n_t k_B T_{\text{ST}}}{(\gamma + 1) n_H n_e \Lambda(T_{\text{ST}})} = \frac{2.3}{1.2} \frac{k_B T_{\text{ST}}}{(\gamma + 1) n_H \Lambda(T_{\text{ST}})}, \quad (\text{A.1})$$

where n_H , n_e , and n_t are the number densities of hydrogen, electrons, and total ions and electrons, respectively, while Λ represents the cooling function. Here, we assume the ratio of the number densities of hydrogen to helium atoms to be 10:1. T_{ST} is the temperature at the post-shock layer of the shock wave, obtained from the Sedov–Taylor solution and the Rankine–Hugoniot relation (Kim and Ostriker, 2015):

$$T_{\text{ST}} = 5.3 \times 10^7 \text{ K } E_{51}^{2/5} n_0^{-2/5} t_3^{-6/5}, \quad (\text{A.2})$$

where $E_{51} = E/(10^{51} \text{ erg})$, $n_0 = n_H/(1 \text{ cm}^{-3})$, $t_3 = t/(1 \text{ kyr})$ denote the energy injected by the **SN** explosion, the number density of hydrogen atoms in the **ISM**, and the time from the **SN** explosion.

Cooling via metal-line emission is most effective at $T \sim 10^5 \text{ K}$, and the cooling function at $10^5 \text{ K} < T < 10^7 \text{ K}$ is well-approximated as

$$\Lambda(T) = 10^{-22} \text{ erg cm}^3 \text{ s}^{-1} \Lambda_{6,-22} \left(\frac{T}{10^6 \text{ K}} \right)^{-0.7}, \quad (\text{A.3})$$

where $\Lambda_{6,-22} = \Lambda(10^6 \text{ K})/(10^{-22} \text{ erg cm}^3 \text{ s}^{-1})$ depicts the value of the cooling function at $T = 10^6 \text{ K}$ (see Fig. A.1). From equations (A.1), (A.2), and (A.3), the cooling time of the gas at the shock front at time t_s is

$$t_c(t_s) = 2.6 \times 10^7 \text{ yr } \left(\frac{t_s}{1 \text{ kyr}} \right)^{-2.04} E_{51}^{0.68} n_0^{-1.68} \Lambda_{6,-22}^{-1}. \quad (\text{A.4})$$

Kim and Ostriker (2015) found that when the cooling time is set to $t_c = 0.6 e/(de/dt)$, the shell-formation time obtained from Eq. (A.6) is in good agreement with the numerical results (Kim et al., 2017).

The gas that is stirred up at time t_s cools down to form a low-temperature ($T < 10^5 \text{ K}$) dense shell at

$$t_{\text{sf}}(t_s) = t_s + t_c(t_s). \quad (\text{A.5})$$

The shell-formation time is determined as the minimum value of $t_{\text{sf}}(t_s)$ following the method of Cox and Anderson (1982), Cox (1986):

$$t_{\text{sf}} = 4.5 \times 10^4 \text{ yr } E_{51}^{0.22} n_0^{-0.55} \Lambda_{6,-22}^{-0.33}. \quad (\text{A.6})$$

Combining Eq. (A.6) with the Sedov–Taylor self-similar solution, we obtain the radius, mass, and momentum at shell formation as:

$$R_{\text{sf}} = \xi_0 \left(\frac{E}{\rho} \right) t_{\text{sf}}^{2/5} = 23 \text{ pc } E_{51}^{0.29} n_0^{-0.42} \Lambda_{6,-22}^{-0.13}, \quad (\text{A.7})$$

$$M_{\text{sf}} = \frac{4}{3} \pi R_{\text{sf}}^3 \rho = 1.8 \times 10^3 \text{ M}_\odot E_{51}^{0.87} n_0^{-0.26} \Lambda_{6,-22}^{-0.39}, \quad (\text{A.8})$$

$$p_{\text{sf}} = 2.69 \frac{3}{4\pi} M_{\text{sf}} \dot{R}_{\text{sf}} = 2.2 \times 10^5 \text{ M}_\odot \text{ km s}^{-1} E_{51}^{0.93} n_0^{-0.13} \Lambda_{6,-22}^{-0.19}, \quad (\text{A.9})$$

where the coefficient 2.69 is the value obtained when integrating the profiles of the Sedov–Taylor self-similar solution (see Eq. (16) of Kim and Ostriker, 2015). The $\Lambda_{6,-22}$ value depends on metallicity. Since the cooling rate due to metal-line emission is proportional to the metal abundance, it proportionally varies with metallicity for a fixed metal abundance ratio. In this study, we use the cooling function of Sutherland and Dopita (1993). They assumed a solar abundance ratio (Anders and Grevesse, 1989) for $\log(Z/Z_\odot) > 0.0$, and a primordial abundance ratio (Wheeler et al., 1989, Bessell et al., 1991) for $\log(Z/Z_\odot) \leq -1.0$, where $Z_\odot = 0.0194$ is the solar metallicity. Here, we fit the cooling function at $T = 10^6 \text{ K}$ as follows:

$$\Lambda_{6,-22}(Z) = \max \left(1.9 - 0.85 \frac{Z}{Z_\odot}, 1.05 \right) \frac{Z}{Z_\odot} + 10^{-1.33} \quad (\text{A.10})$$

Combining Eqs. (A.6) and (A.10), we obtained the metallicity-dependent shell-formation time.

A.1.1.2 Multiple SNe

One can estimate the average time interval between the SN explosions in a stellar cluster by multiplying the stellar initial mass function with stellar age, which is approximately evenly spaced (Ferrand and Marcowith, 2010). The temporal evolution of the superbubble can be thought of in the same way as that of an SN remnant formed by a single SN explosion, by assuming SN explosions to occur at regular time intervals with a continuous injection of energy.

The superbubble evolves adiabatically until the cooling effect manifests and a shell forms. Its time evolution is represented by a self-similar solution, where the dimensionless quantity ξ is a combination of the radius r , the energy released in a single SN explosion E_{SN} ,

the **SN** explosion interval Δt_{SN} , the density of the **ISM** ρ , and the time t :

$$\xi = \left(\frac{\rho}{E_{\text{SN}}/\Delta t_{\text{SN}}} \right)^{1/5} \frac{r}{t^{3/5}}. \quad (\text{A.11})$$

Compared to the case of a single **SN** explosion, the energy E in the dimensionless quantity of the Sedov–Taylor solution is replaced by the energy injection rate $E/\Delta t_{\text{SN}}$, resulting in a difference in the time dependence from $t^{2/5}$ to $t^{3/5}$. The value of ξ at the shock is $\xi_0 = 0.88$, and the ratio of kinetic and thermal energies is $E_{\text{k}} : E_{\text{th}} = 22 : 78$ (Weaver et al., 1977).

The shell-formation time can be estimated by replacing the energy E in Eq. (A.6) with the total energy injected until time t , $E_{\text{SN}}(t/\Delta t_{\text{SN}})$, and solving for t :

$$t_{\text{sf,m}} = 1.7 \times 10^4 \text{ yr } E_{51}^{0.28} \Delta t_{\text{SN},6}^{-0.28} n_0^{-0.71} \Lambda_{6,-22}^{-0.42}. \quad (\text{A.12})$$

The radius, velocity, mass, and momentum at this point in time are

$$R_{\text{sf,m}} = 5.3 \text{ pc } E_{51}^{0.37} \Delta t_{\text{SN},6}^{-0.37} n_0^{-0.63} \Lambda_{6,-22}^{-0.25}, \quad (\text{A.13})$$

$$V_{\text{sf,m}} = 1.8 \times 10^2 \text{ km s}^{-1} E_{51}^{0.088} \Delta t_{\text{SN},6}^{-0.088} n_0^{0.084} \Lambda_{6,-22}^{0.17}, \quad (\text{A.14})$$

$$M_{\text{sf,m}} = 22 \text{ M}_\odot E_{51}^{1.11} \Delta t_{\text{SN},6}^{-1.11} n_0^{-0.89} \Lambda_{6,-22}^{-0.75}, \quad (\text{A.15})$$

$$p_{\text{sf,m}} = 3.3 \times 10^3 \text{ M}_\odot \text{ km s}^{-1} E_{51}^{1.2} \Delta t_{\text{SN},6}^{-1.2} n_0^{-0.80} \Lambda_{6,-22}^{-0.59}. \quad (\text{A.16})$$

We use Eqns. (A.12), (A.13), and (A.16) to normalize each physical quantity while examining the time evolution in Fig. A.8 & A.9.

A.2 ATHENA++ simulation of superbubbles

A.2.1 Numerical Method

We carried out 3D hydrodynamical simulations with the ATHENA++ code¹ (Stone et al., 2020) with the second-order accurate van Leer time integrator, the HLLC solver, and

¹<https://www.athena-astro.app>

second-order spatial reconstruction. We solved for the equations of continuity, momentum conservation, and energy while incorporating cooling, heating, and thermal conduction:

$$\frac{\partial \rho}{\partial t} + \nabla \cdot (\rho \mathbf{v}) = 0 \quad (\text{A.17})$$

$$\frac{\partial(\rho \mathbf{v})}{\partial t} + \nabla \cdot (\rho \mathbf{v} \mathbf{v} + P) = 0 \quad (\text{A.18})$$

$$\frac{\partial E}{\partial t} + \nabla \cdot \{(E + P) \cdot \mathbf{v}\} = \nabla \cdot (\kappa \nabla T) + n_{\text{H}} \Gamma(T) - n_{\text{H}}^2 \Lambda(T), \quad (\text{A.19})$$

where E is the energy density. We did not consider self-gravity and magnetic fields in our simulation. Assuming a mean molecular weight of $\mu = 1.4$, the gas temperature is taken at $T = P/(1.1n_{\text{H}}k_{\text{B}})$, where the hydrogen number density is $n_{\text{H}} = \rho/(1.4m_{\text{H}})$. We followed [Kim and Ostriker \(2015\)](#) for the implementation of radiative cooling and heating. For the cooling function $\Lambda(T)$ at low ($T < 10^4$ K) and high ($T > 10^4$ K) temperatures of gas, we adopted the fitting formulae from [Koyama and Inutsuka \(2002\)](#)² and piecewise power-law fits to the cooling function of [Sutherland and Dopita \(1993\)](#) with collisional ionization equilibrium³, respectively, as shown in Fig. A.1. Heating was applied, with the following heating function, only at $T < 10^4$ K to model the photoelectric heating of warm/cold ISM:

$$\Gamma(T) = \begin{cases} 10^{-26} \left(\frac{n_{\text{H}}}{1 \text{ cm}^{-3}} \right) \text{ erg s}^{-1} & (T < 10^4 \text{ K}) \\ 0 \text{ erg s}^{-1} & (T > 10^4 \text{ K}). \end{cases} \quad (\text{A.20})$$

We used different cooling functions at $T > 10^4$ K for different metallicities, but we did not take into account the metallicity dependence at $T < 10^4$ K. We did not consider the metallicity dependence of the heating function. At $Z \ll 1$, the low-temperature cooling and heating rates would be quite different due to reduced photoelectric heating and cooling by fine-structure C and O lines when the metal abundance is low. However, these differences do not affect the results of our simulations, because the shell formation time is determined by the cooling time of shock-heated gas at high temperatures. We imposed a temperature floor of 10^3 K.

We followed [El-Badry et al. \(2019\)](#) to implement thermal conduction. For thermal conductivity κ at low ($T \leq 6.6 \times 10^4$ K) and high ($T > 6.6 \times 10^4$ K) temperatures of gas, we applied, respectively, the thermal conductivities due to the neutral atomic collision ([Parker, 1963](#)):

$$\kappa = 2.5 \times 10^5 T_4^{1/2} \text{ erg s}^{-1} \text{ cm}^{-1} \text{ K}^{-1}, \quad (\text{A.21})$$

²The cooling function given by Eq. (4) of [Koyama and Inutsuka \(2002\)](#) contains two typographical errors. See Eq. (4) of [Vázquez-Semadeni et al. \(2007\)](#) for the corrected functional form.

³<https://www.mso.anu.edu.au/~ralph/data/cool/>

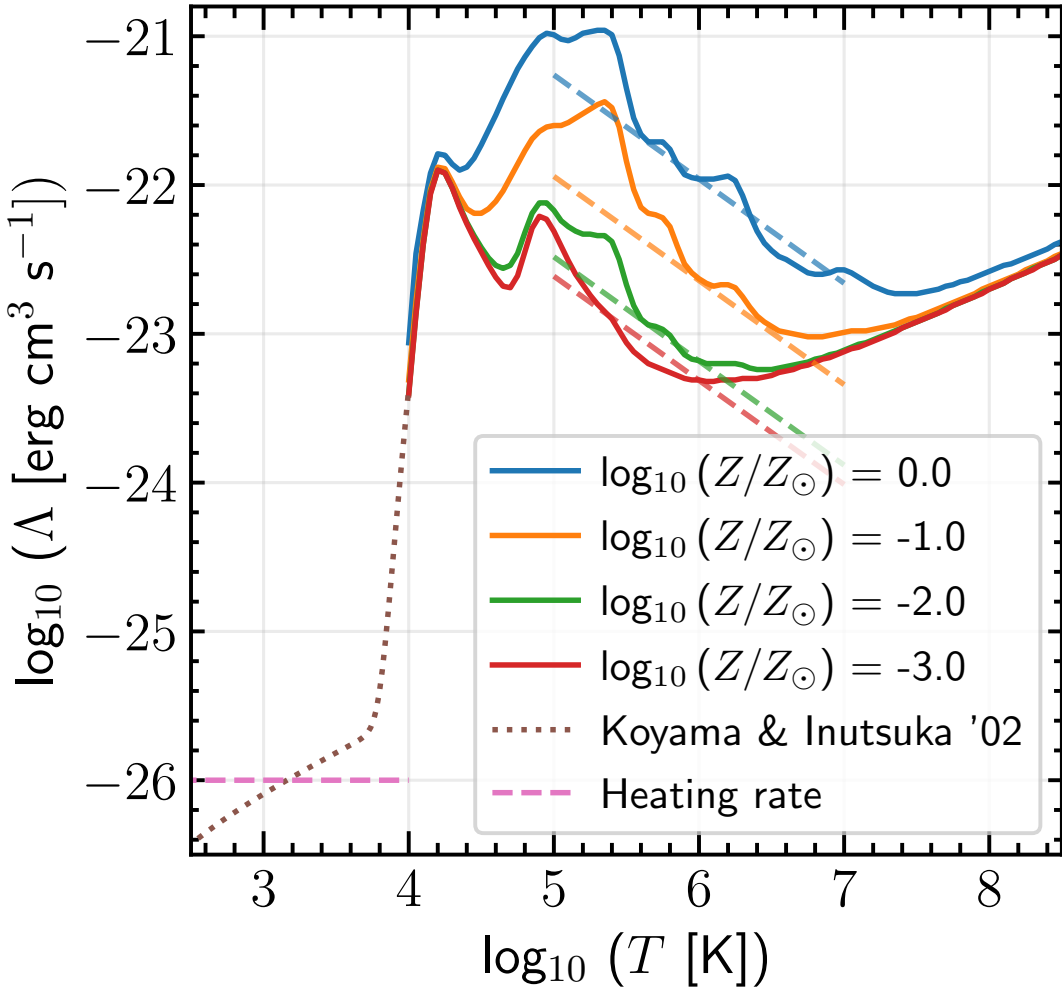


FIGURE A.1: Cooling curves used in this work at different metallicities from [Sutherland and Dopita \(1993\)](#) combined with those of [Koyama and Inutsuka \(2002\)](#). The dashed colored lines show approximations given in Eq. (A.3) for the same metallicities given in the legend. The horizontal line indicates the constant photoelectric heating function $\Gamma = 1 \times 10^{-26} (n_H/1 \text{ cm}^{-3}) \text{ erg s}^{-1}$ at $T < 10^4 \text{ K}$.

where $T_4 = T/10^4 \text{ K}$, and hydrogen plasma ([Spitzer, 1962](#)):

$$\kappa = \frac{1.7 \times 10^{11} T_7^{5/2}}{1 + 0.029 \ln(T_7 n_{e,-2}^{-1/2})} \text{ erg s}^{-1} \text{ cm}^{-1} \text{ K}^{-1}, \quad (\text{A.22})$$

where $T_7 = T/10^7 \text{ K}$, $n_{e,-2} = n_e/10^{-2} \text{ cm}^{-3}$ and n_e denotes the electron number density. The conductive heat flux $q = \kappa \nabla T$ is limited by the energy flux that can actually be transported by the electrons $q_{\max} = \frac{3}{2} \rho c_{s,\text{iso}}^3$ ([Parker, 1963](#), [Cowie and McKee, 1977](#)). The effective thermal conductivity κ_{eff} , which includes the saturation resulting from limiting the heat flux, becomes

$$\kappa_{\text{eff}}^{-1} = \kappa^{-1} + \frac{|\nabla T|}{q_{\max}}. \quad (\text{A.23})$$

TABLE A.1: Initial conditions of the suprebubble simulations.

Number density n_{H} [cm $^{-3}$]	0.1, 1, 10
Metallicity Z [Z_{\odot}]	$10^{-3}, 10^{-2}, 10^{-1}, 1$
Time interval of SN explosions Δt_{SN} [Myr]	0.01, 0.1, 1

To save calculation time, we imposed a ceiling on the thermal conductivity at the following value:

$$\kappa_{\text{ceiling}} = 1.8 \times 10^{12} \left(\frac{n_{\text{H}}}{1 \text{ cm}^{-3}} \right) \text{ erg s}^{-1} \text{ cm}^{-1} \text{ K}^{-1}. \quad (\text{A.24})$$

This value is sufficiently high and has negligible effects on our results. We note that our resolution is not high enough to resolve the conductive interface.

We ran 36 simulations by varying the initial values of the parameters as listed in Table A.1. The spatial resolution was fixed in time and uniform over the simulation box with periodic boundary conditions (we did not use static mesh refinement, SMR, or adaptive mesh refinement, AMR). The spatial resolutions were $\Delta x = 6, 3$, and 0.75 pc for number densities of $n_{\text{H}} = 0.1, 1$, and 10 cm^{-3} , respectively, to satisfy the convergence condition by [Kim and Ostriker \(2015\)](#), $\Delta x < R_{\text{sf}}/10$. To set up a turbulent initial condition, we start from a uniform density field with pressure of $2.0 \times 10^3 (n_{\text{H}}/1 \text{ cm}^{-3}) k_{\text{B}} \text{ K cm}^{-3}$. We then generate the decaying turbulence with only initial forcing and evolve to 1 Myr. The initial forcing field was normalized to a [Kolmogorov \(1941\)](#) power spectrum $E(k) \propto k^{-5/3}$, while the range of driving was set to $2 \leq kL/2\pi \leq 20$. The velocity dispersion in the box was set to $\sigma = 5 \text{ km s}^{-1}$ adopted based on Larson's law ([Larson, 1981](#), [Ohlin et al., 2019](#)). We note that this velocity dispersion of 5 km s^{-1} is lower than observed values at the scale of the simulation box, and that the initial evolution of 1 Myr is not long enough for multiphase **ISM** to develop via thermal instability. As a result, the inhomogeneity in the background is very weak, and the bubble expansion can be much more spherical than in realistic cases, which in turn affects the development of the Kelvin–Helmholtz instabilities that are normally driven by the shear at interfaces.

Thermal energy of 10^{51} erg per **SN** was injected into cells whose centers were at a distance $< r_{\text{init}}$ from the site of the **SN** explosion, where r_{init} is the radius within which the mass is 1 M_{\odot} . When thermal energy was injected, a mass of 1 M_{\odot} was also simultaneously injected. We repeated this ten times, at intervals of Δt_{SN} , setting $t = 0$ at the time of the initial energy injection.

To study the time evolution of the physical quantities of the superbubble, we define the bubble radius R_{bub} as the largest radius which satisfies following two criteria: (i) $v_r > 3 \text{ km s}^{-1}$, and (ii) $t_{\text{dens}} < 4t_{\text{sc}}$, where v_r is the radial velocity averaged over a spherical shell of radius r , $t_{\text{dens}} = \rho/\dot{\rho}$ indicates the timescale of the density change, and $t_{\text{sc}} = \Delta x/c_s$ depicts the sound-crossing time. In practice, we compute v_r , t_{dens} , and t_{sc}

for each cell, draw averaged radial profiles of these quantities, and then apply the above criteria. We have described the time evolution of total mass, energy, and momentum within R_{bub} in Section A.2.2.1.

To discuss the time evolution of the hot bubble, we also define the hot-gas radius as $R_{\text{hot}} = (V_{\text{hot}}/(4/3)\pi)^{1/3}$, where V_{hot} is the region at which $T > 10^4$ K. The time evolution of R_{hot} is discussed in Section A.2.3.

A.2.2 Results from Athena++ simulations

A.2.2.1 Results for $n_{\text{H}} = 1 \text{ cm}^{-3}$, $Z = 1 Z_{\odot}$, $\Delta t_{\text{SN}} = 0.1 \text{ Myr}$

Figure A.2 shows a slice plot of density and temperature at 0.03 Myr after the fifth energy injection for the case of $n_{\text{H}} = 1 \text{ cm}^{-3}$, $Z = Z_{\odot}$, $\Delta t_{\text{SN}} = 0.1 \text{ Myr}$. The collected gas forms a low-temperature, high-density shell, inside which exists a high-temperature, low-density gas. The shell grows almost spherically, but with a slight distortion due to the density fluctuations caused by turbulence. We see that R_{hot} adequately captures the size of the hot bubble inside the shell, with R_{bub} enclosing the shell itself.

Figure A.3 shows the phase diagram at this time. The low-temperature ($T < 2 \times 10^3$ K) gas at the bottom right corner is the **ISM** gas. The gas swept up at the front of the shell is heated by the shock, but as the temperature rises to $T > 10^4$ K, it loses energy due to hydrogen recombination. Since the shock compresses the gas to a high density, its cooling time is shorter than the dynamical time, and a shell of $T \sim 10^4$ K, $n_{\text{H}} \sim 10 \text{ cm}^{-3}$ is formed. At the post-shock layer of the shell, the gas can be heated by compression (if a shock propagates through the layer), or by mixing (if hot gas is advected into a cell containing cool gas), or by thermal conduction (if conduction is resolved). In our simulation, the upper left plume of hot gas in Figure A.3 is heated by compression and thermal conduction.

Figure A.4 shows the time evolution of the superbubble. The shell forms when it grows to a radius of about 20 pc, after which its growth slows down from the adiabatic phase. The subsequent energy injection stirs up the gas inside the shell and reduces its density. However, the density increases again due to the evaporation from the shell to the interior, and the mass is transferred from the cold shell to the hot interior.

A.2.2.2 Results for $\Delta t_{\text{SN}} = 0.01 \text{ Myr}$

The time evolution of mass, energy, and momentum for an **SN** explosion with a time interval of 0.01 Myr is shown in Figure A.5.

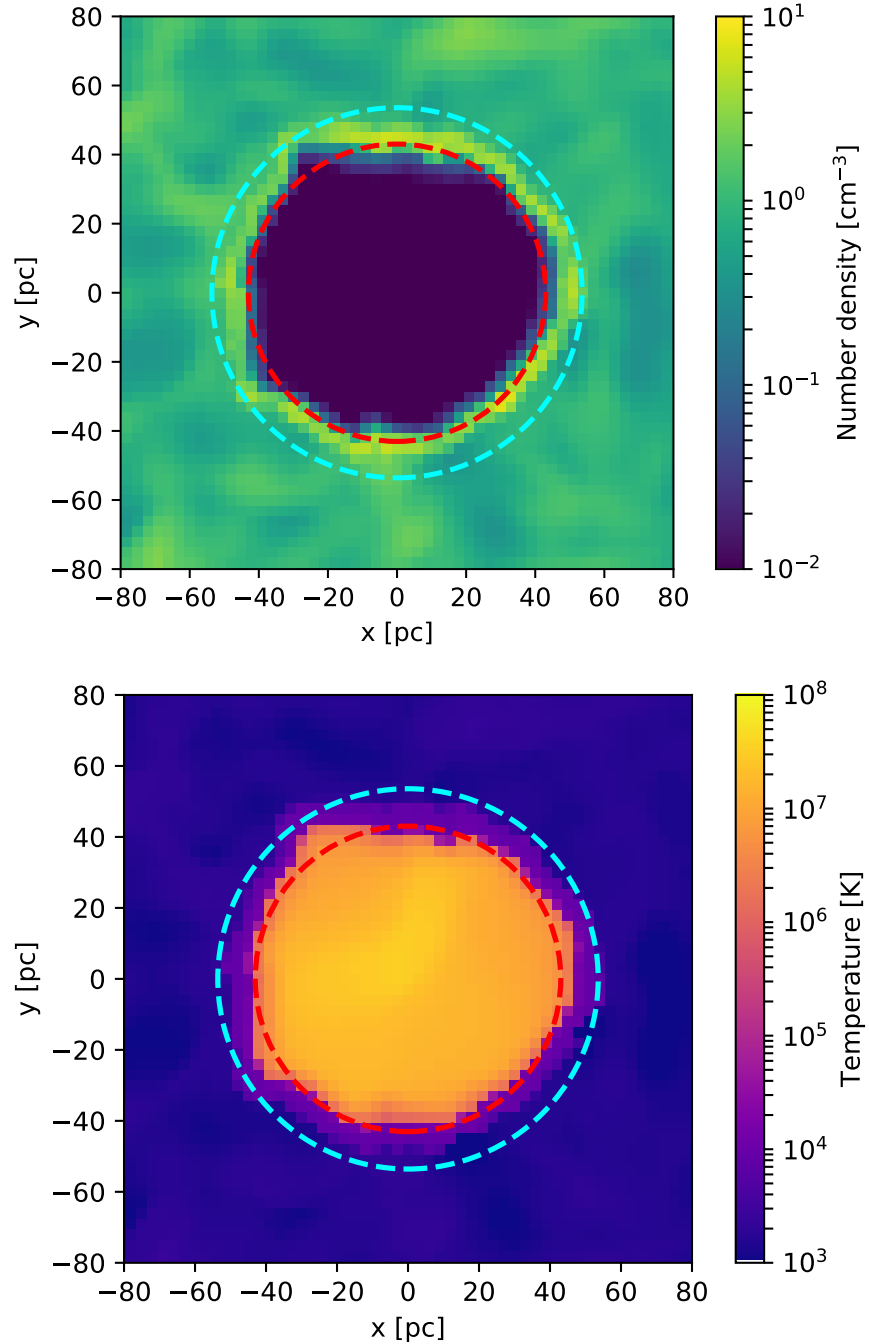


FIGURE A.2: Slice plot of gas number density and temperature distribution at $t = 0.53$ Myr for the case of $n_{\text{H}} = 1 \text{ cm}^{-3}$, $Z = Z_{\odot}$, $\Delta t_{\text{SN}} = 0.1$ Myr. The inner red circle shows R_{hot} , while the outer cyan circle shows R_{bub} .

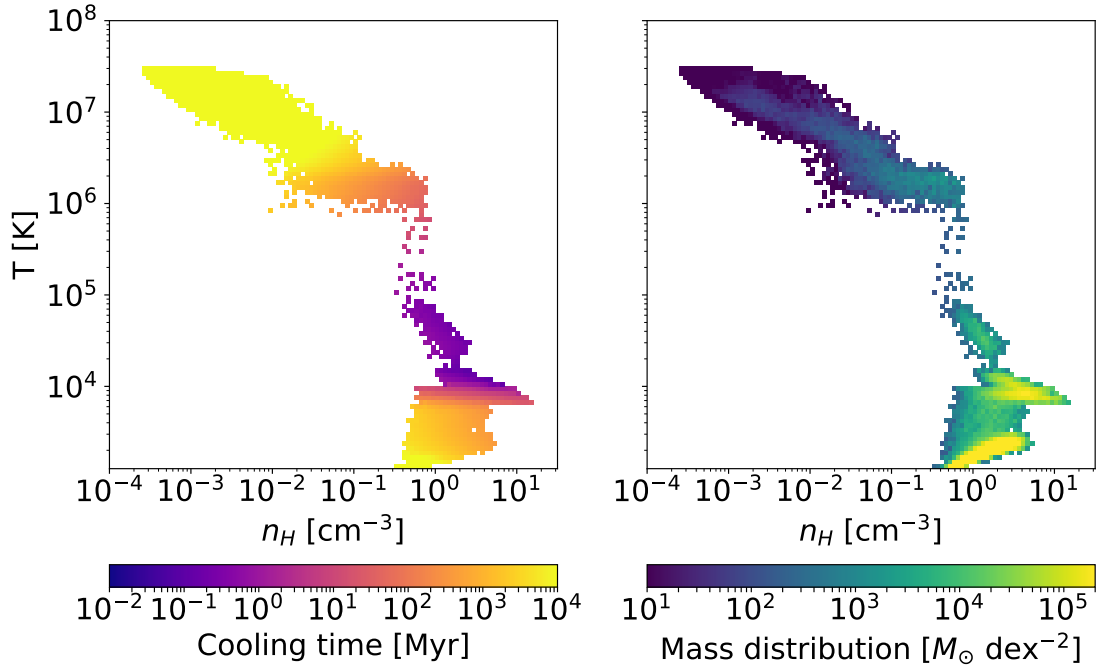


FIGURE A.3: Phase diagram of gas in computational box, weighted for its cooling time (left panel) and mass (right panel), at the same time as in Fig. A.2. In the left panel, one can see that the cooling time is short in the shell of $T \sim 10^4$ K and $n_H \sim 10 \text{ cm}^{-3}$.

For $n_H = 0.1 \text{ cm}^{-3}$, the system evolves adiabatically because the shell-formation time is longer than 0.1 Myr for any metallicity. Since the metallicity affects the shell-formation time but not the system's dynamics, no metallicity dependence is observed in this case. Since the system evolves adiabatically, its total energy after 10 SN explosions is 10^{52} erg. In the case of $n_H = 1 \text{ cm}^{-3}$, the cooling time is shorter due to the higher density, and this cooling effect is seen for $\log(Z/Z_\odot) = 0, -1$. The cooling effect is seen earlier for $\log(Z/Z_\odot) = 0$ because the larger the metallicity is, the shorter the cooling time is. Shell formation does not immediately get completed and, in the case of $\log(Z/Z_\odot) = 0$, the cooling effect begins to appear at $t \sim 0.04$ Myr, while shell formation completes at $t \sim 0.1$ Myr. During shell formation, the mass of the shell increases while that of the hot gas remains constant because it proceeds from the dense and short cooling time gas gathered in front of the superbubble.

In the case of $n_H = 10 \text{ cm}^{-3}$, the shell-formation time is shorter than 0.1 Myr at all metallicities, and a low-temperature, high-density shell is formed. After shell formation, most of the system's mass is in the shell, and at $t = 0.1$ Myr, the mass of the hot gas is about 2% of the total. Comparing the cases of $\log(Z/Z_\odot) = -2.0, -3.0$, there is little difference in the time evolution of the physical quantities. In the low-metallicity environment, bremsstrahlung is a more dominant cooling mechanism than metal line emission at $T > 10^6$ K, and hence the difference in metallicity becomes less apparent.

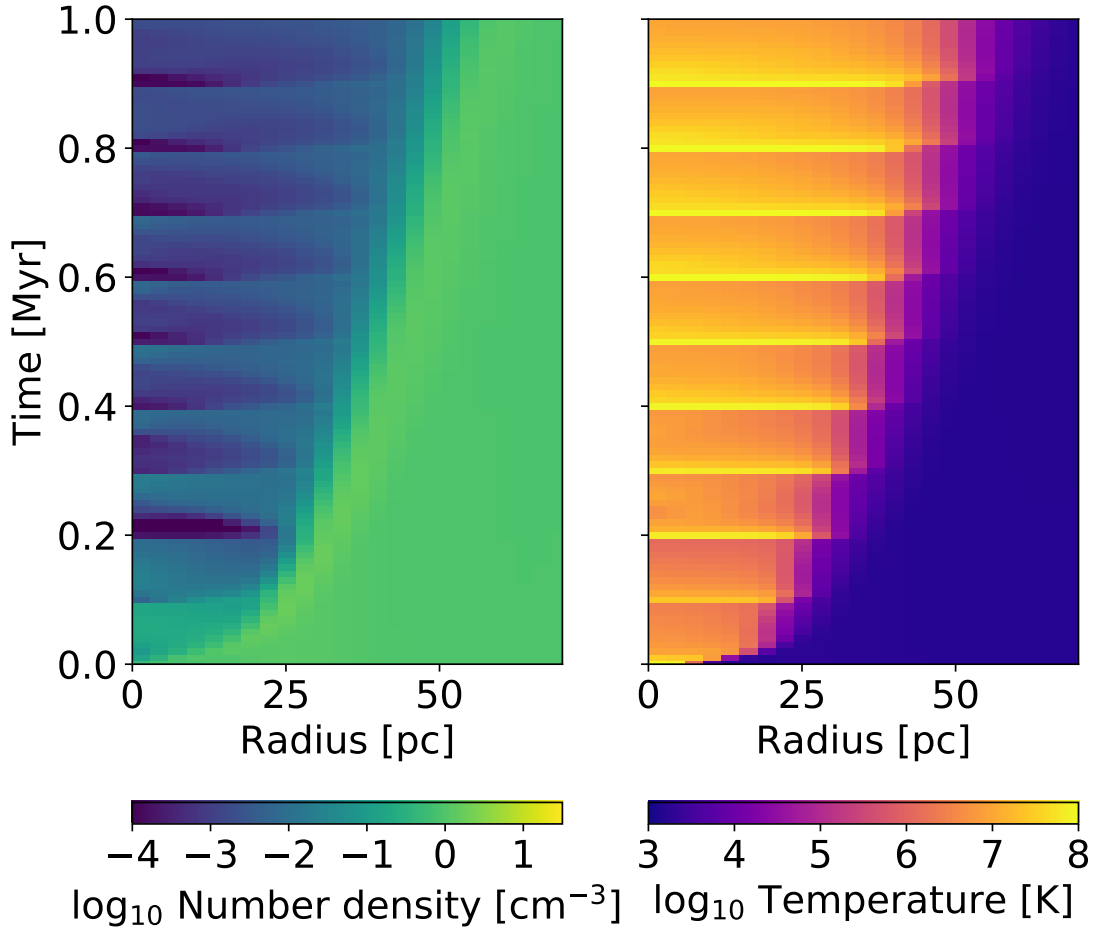


FIGURE A.4: Evolution of superbubble as a function of radius, weighted for gas number density (left panel) and gas temperature (right panel), for the case of $n_{\text{H}} = 1 \text{ cm}^{-3}$, $Z = Z_{\odot}$, $\Delta t_{\text{SN}} = 0.1 \text{ Myr}$. One can see the power-law expansion of the hot bubble. The horizontal features indicate the intermittent [SN](#) injection.

A.2.2.3 Results for $\Delta t_{\text{SN}} = 0.1 \text{ Myr}$

The time evolution of mass, energy, and momentum of a superbubble in the cases of $\Delta t_{\text{SN}} = 0.1 \text{ Myr}$ is shown in Fig. A.6. In this case, the shell-formation time is shorter due to the lower energy injection rate than $\Delta t_{\text{SN}} = 0.01 \text{ Myr}$.

In cases of $n_{\text{H}} = 0.1 \text{ cm}^{-3}$ and $\log(Z/Z_{\odot}) = 0.0, -1.0$, the shell formation is completed within the simulation time, after which the kinetic energy becomes roughly constant as shown by the red solid line in the left middle panel of the Fig. A.6.

In cases of $n_{\text{H}} = 1 \text{ cm}^{-3}$, the shell formation completes before the second [SN](#) explosion. Each [SN](#) explosion injects 10^{51} erg of thermal energy; some of it is converted to kinetic energy by PdV work on the shell, and the rest is dissipated by cooling so that most of the thermal energy is lost within 0.1 Myr following energy injection. From the phase diagram at $t = 0.53 \text{ Myr}$ for $\log(Z/Z_{\odot}) = 0.0$ (Fig. A.3), the cooling time of the gas

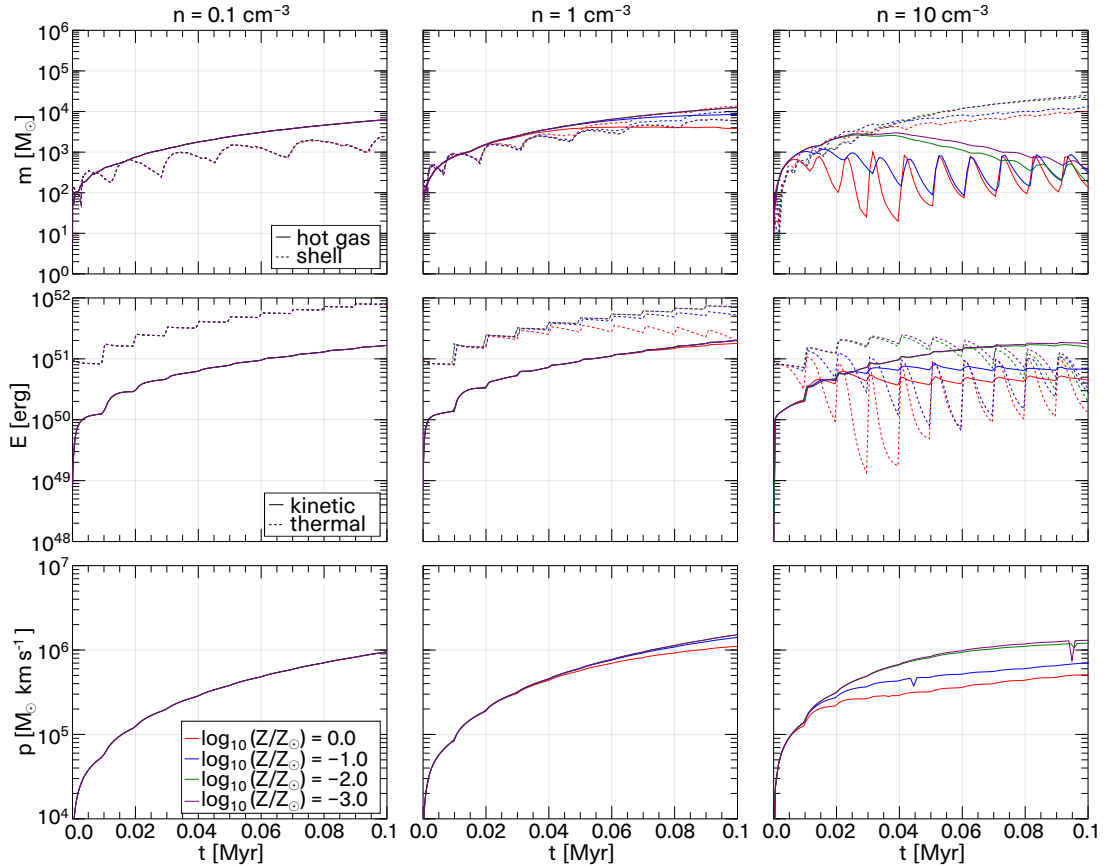


FIGURE A.5: Time evolution of mass (top row), energy (middle row) and momentum (bottom row) of the superbubble for [SN](#) injection time intervals of $\Delta t_{\text{SN}} = 0.01$ Myr. For each component, we also show four different metallicities as indicated in the legend. Left column: $n_{\text{H}} = 0.1 \text{ cm}^{-3}$. Middle column: $n_{\text{H}} = 1 \text{ cm}^{-3}$. Right column: $n_{\text{H}} = 10 \text{ cm}^{-3}$. In the top panels for mass, the solid lines are for the hot gas inside the superbubble while dotted lines are for the shell. In the middle panels for energy, the solid lines are for kinetic energy while the dotted lines are for the thermal energy of superbubble gas including the shell. In the left column, the lines for the four metallicities overlap because of low density and long shell-formation time, which prolongs the adiabatic phase with little metal-cooling. In the right column, the effect of intermittent [SN](#) injection is visible.

inside the shell is longer than 1 Myr. However, heat is transported to the shell by gas mixing at its rear surface and then radiated away (El-Badry et al., 2019, Fielding et al., 2020, Lancaster et al., 2021a,b), resulting in the loss of thermal energy within a duration shorter than 1 Myr. We note that our resolution is not high enough to resolve the conductive interfaces, and some of the thermal energy could be lost due to numerical diffusion. As shown in the top middle panel of Fig. A.6, the shell grows in mass while conserving momentum after each [SN](#) injection. At the same time, the kinetic energy decreases as shown in the central panel of Fig. A.6.

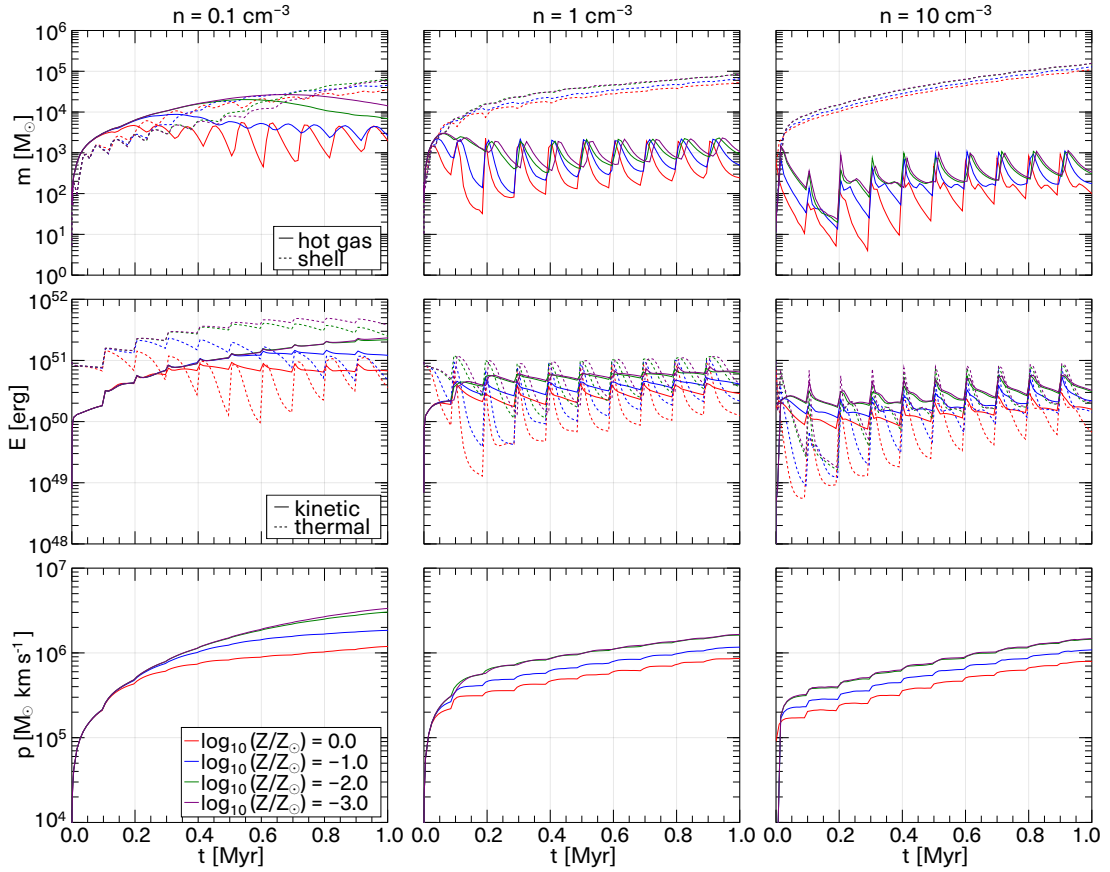


FIGURE A.6: Same as Figure A.5, but for **SN** injection time interval $\Delta t_{\text{SN}} = 0.1$ Myr. Note that the time range in the abscissa is different from that in Figure A.5.

A.2.2.4 Results for $\Delta t_{\text{SN}} = 1$ Myr

The time evolution of superbubble mass, energy, and momentum in the case of $\Delta t_{\text{SN}} = 1$ Myr is shown in Fig. A.7. In this case, the shell is formed before the second **SN** explosion occurs in all cases; therefore the time evolution is similar to that for $\Delta t_{\text{SN}} = 0.1$ Myr, $n_{\text{H}} = 1, 10 \text{ cm}^{-3}$. At $t > 4$ Myr, thermal energy exceeds kinetic energy. At this time, most of the mass is in the shell with its interior being cooled. Therefore, the gas in the shell contains most of the thermal energy of the superbubble. As shell mass increases while conserving momentum, its kinetic energy decreases. Let the velocity, temperature, and density of the shell be v_{shell} , T_{shell} , and ρ_{shell} , respectively. When the kinetic energy decreases to $(1/2)\rho_{\text{shell}}v_{\text{shell}}^2 < (3/2)(\rho_{\text{shell}}/\mu m_{\text{H}})k_{\text{B}}T_{\text{shell}}$, the thermal energy becomes larger. If the temperature of the shell is around the **ISM** temperature $T_{\text{ISM}} \sim 2 \times 10^3$ K, then the thermal energy exceeds kinetic energy when $v_{\text{shell}} < 7 \text{ km s}^{-1}$. When $n_{\text{H}} = 10 \text{ cm}^{-3}$, the mass and momentum appear to be decreasing when t is large. This is because the shell velocity has fallen below 3 km s^{-1} , whereby we can no longer follow its time evolution. In such a case, the shell is expected to gradually mix with the **ISM**.

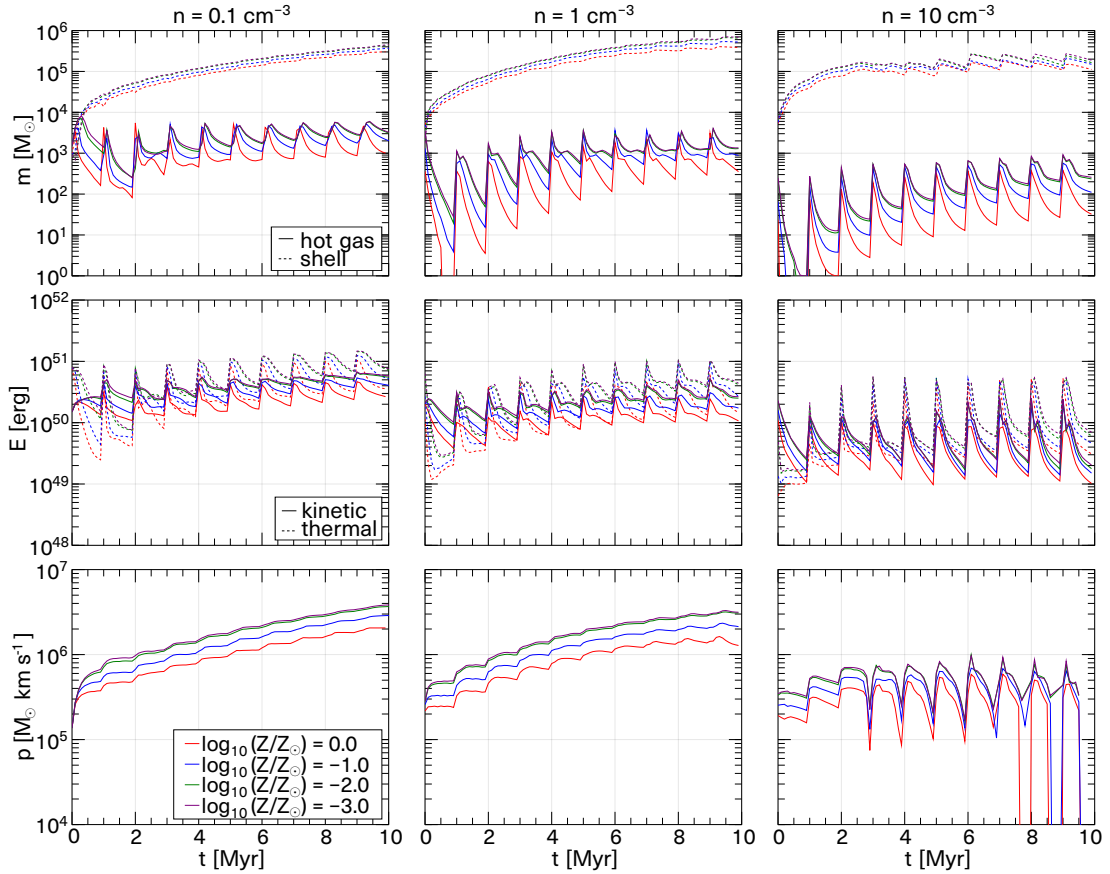


FIGURE A.7: Same as Figure A.5, but for [SN](#) injection time interval $\Delta t_{\text{SN}} = 1$ Myr. Note that the time range in the abscissa is different from that in Figure A.5.

A.2.3 Application to SN feedback model in galaxy simulations

In this section, we derive the scaling relations for the time evolution of superbubble momentum and radius for the application to the [SN](#) feedback model in galaxy simulations.

To discuss the environmental dependence of the superbubble in a unified manner, we normalize each physical quantity by its value at the shell-formation time. The same was done for single [SN](#) explosion simulations by [Kim and Ostriker \(2015\)](#), and also by [Kim et al. \(2017\)](#) for only the time variable for multiple [SN](#) explosion simulations.

Figure A.8 shows the time evolution of the radius, normalized by its value at the shell-formation time. The time evolution of the radius shows some deviations, but in all cases, we can see that the radius evolves according to

$$\frac{R_{\text{hot}}}{R_{\text{sf,m}}} = \left(\frac{t}{t_{\text{sf,m}}} \right)^{0.5}, \quad (\text{A.25})$$

as was also found by [Kim et al. \(2017\)](#). When $t < t_{\text{sf,m}}$, the superbubble is in an adiabatic period and expected to evolve with $R \propto t^{3/5}$ (Eq. A.11). The good fit of the straight

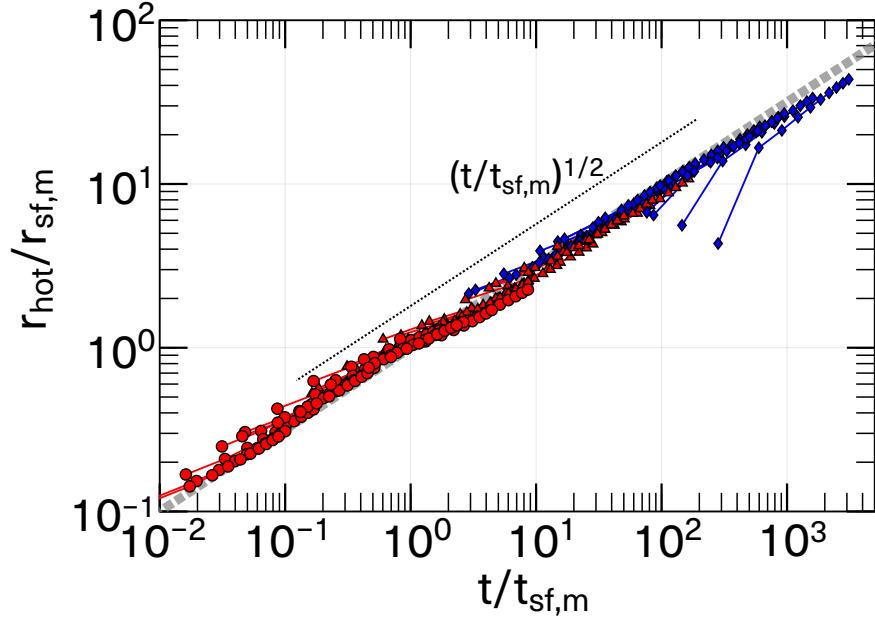


FIGURE A.8: Evolution of R_{hot} normalized by $R_{\text{sf,m}}$, versus time normalized by $t_{\text{sf,m}}$. Red and blue points depict the runs with $\Delta t_{\text{SN}} < 0.1 t_{\text{PDS}}$ and $\Delta t_{\text{SN}} > 0.1 t_{\text{PDS}}$, respectively. Different symbols connected by line correspond to runs at different SN intervals: $\Delta t_{\text{SN}} = 0.01$ Myr (circle), $\Delta t_{\text{SN}} = 0.1$ Myr (triangle), $\Delta t_{\text{SN}} = 1$ Myr (diamond). The thick black dotted line shows the power-law of Eq. (A.25).

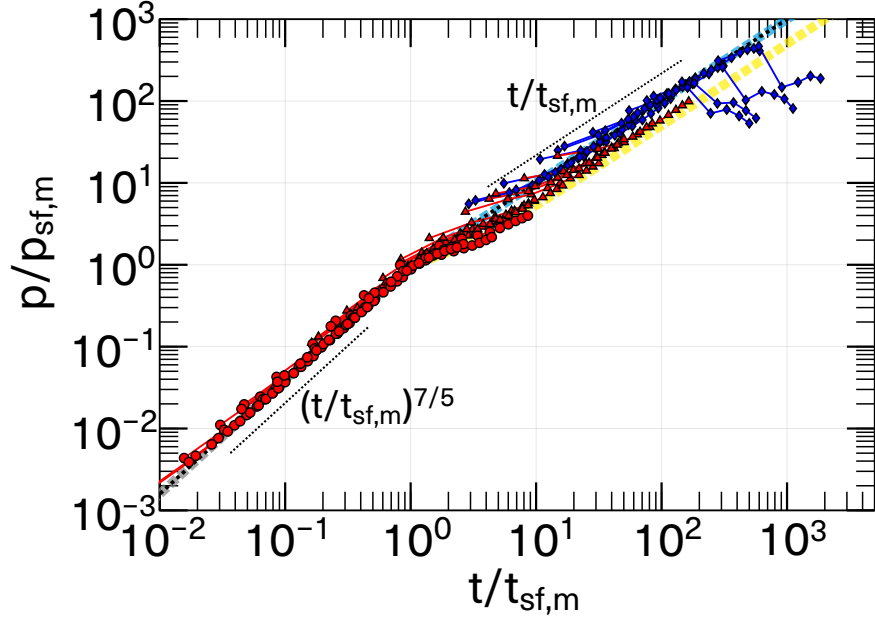


FIGURE A.9: Evolution of momentum p normalized by $p_{\text{sf,m}}$, versus time normalized by $t_{\text{sf,m}}$. Red and blue points depict the runs with $\Delta t_{\text{SN}} < 0.1 t_{\text{PDS}}$ and $\Delta t_{\text{SN}} > 0.1 t_{\text{PDS}}$, respectively. Different symbols connected by line correspond to runs at different SN intervals: $\Delta t_{\text{SN}} = 0.01$ Myr (circle), $\Delta t_{\text{SN}} = 0.1$ Myr (triangle), $\Delta t_{\text{SN}} = 1$ Myr (diamond). The black dotted lines indicates the $(p/p_{\text{sf,m}}) \propto (t/t_{\text{sf,m}})^{7/5}$ and $(p/p_{\text{sf,m}}) \propto (t/t_{\text{sf,m}})$ power-law, respectively. The thick gray, yellow and cyan dotted lines indicate the fitting function of Eq. (A.29).

line with a slope of 0.5 can be attributed to the fact that the energy injection is discrete rather than continuous, resulting in an intermediate time evolution with the Sedov–Taylor solution $R \propto t^{2/5}$. The asymptote of the fitting line is due to the transition from the Sedov–Taylor solution to the adiabatic solution of the superbubble. Time evolution after shell formation can also be approximated by a straight line with a slope of 0.5. The asymptotic behavior of the blue lines from the bottom is because the hot-gas radius R_{hot} could not correctly follow the radius of the inside of the shell when it was cooled down to $T < 2 \times 10^4$ K. The scaling relation $R \propto t^{1/2}$ agrees with the prediction from the momentum-driven model and not with that from the pressure-driven model (Ostriker and McKee, 1988). Substituting the values of $R_{\text{sf,m}}$, $t_{\text{sf,m}}$ (Eqs. (A.13), (A.12)), the time evolution of radius and velocity are obtained as

$$R = 40 \text{ pc } t_6^{1/2} E_{51}^{0.23} \Delta t_{\text{SN},6}^{-0.23} n_0^{-0.28} \Lambda_{6,-22}^{-0.040}, \quad (\text{A.26})$$

$$V = 20 \text{ km s}^{-1} t_6^{-1/2} E_{51}^{0.23} \Delta t_{\text{SN},6}^{-0.23} n_0^{-0.28} \Lambda_{6,-22}^{-0.040}. \quad (\text{A.27})$$

Next, we show the time evolution of momentum in Figure A.9. It shows two different trends after the shell-formation time. If the interval between **SN** explosions is longer than the duration of the **pressure-driven snowplow (PDS)** phase of a single **SN** explosion,

$$t_{\text{PDS}} = 5.0 \times 10^6 \text{ yr } T_{\text{ISM},3}^{-0.7} E_{51}^{0.32} n_0^{-0.36} \Lambda_{6,-22}^{-0.053}, \quad (\text{A.28})$$

where $T_{\text{ISM},3} = T_{\text{ISM}}/(10^3 \text{ K})$ is the temperature of the **ISM**, energy injection is considered to be discrete and the superbubble is expected to display an evolution over time that is different from the continuous case. Since thermal transfer to the shell was not considered in the derivation of t_{PDS} , the actual duration of the **PDS** phase will be shorter than t_{PDS} .

Here we find that the following fitting functions can describe the two separate regimes continuously, as shown in Fig. A.9:

$$\frac{p}{p_{\text{sf,m}}} = \begin{cases} \tau^{7/5} & (t < t_{\text{sf,m}}) \\ \frac{1}{2} (\tau + \tau^{-1/5}) & (t > t_{\text{sf,m}} \text{ \& } \frac{\Delta t_{\text{SN}}}{t_{\text{PDS}}} < 0.1) \\ \tau & (t > t_{\text{sf,m}} \text{ \& } \frac{\Delta t_{\text{SN}}}{t_{\text{PDS}}} > 0.1), \end{cases} \quad (\text{A.29})$$

where $\tau = t/t_{\text{sf,m}}$. Since the momentum can be estimated as $p = (4/3)\pi R^3 \rho \dot{R}$, when the time evolution of the radius is expressed as $R \propto t^\alpha$, $p \propto t^{4\alpha-1}$. Before shell formation, the superbubble grows adiabatically, and the time evolution of its radius is $R \propto t^{3/5}$; thus, the time evolution of momentum is $p \propto t^{7/5}$.

When $t \gg t_{\text{sf,m}}$, there occurs a deviation from the fitting line. This was also seen when $\Delta t_{\text{SN}} = 1 \text{ Myr}$, $n_{\text{H}} = 10 \text{ cm}^{-3}$ (Fig. A.7), because the shell velocity dropped below

3 km s^{-1} and its time evolution could not be followed.

In passing, we note that [El-Badry et al. \(2019\)](#) derived a criterion to distinguish discrete energy injection versus continuous limit in their Eq.(53). They derived this criterion only by considering the blast waves from individual [SNe](#) before reaching the shell, and their simulation results asymptote to their modified energy-driven solution with cooling at $t > t_{\text{subsonic}}$. We only simulated ten [SN](#) explosions, while [El-Badry et al. \(2019\)](#) examined the evolution all the way to the continuous energy injection limit (although with 1-D simulation); therefore, our time-scale shown in Fig. 9 is somewhat of a shorter time range than that of [El-Badry et al. \(2019\)](#)’s work (see their Fig. 6). The subsonic timescale t_{subsonic} in Eq.(53) of [El-Badry et al. \(2019\)](#) is much longer than our t_{PDS} , and therefore it is not straightforward to compare our results using their criteria based on t_{subsonic} .

Appendix B

Implementation of supernova feedback

In this appendix, we describe the implementation of supernova feedback in **SPH** simulation. The content in this appendix is a part of my master’s thesis work.

A schematic description of the ‘Spherical superbubble model’ developed in this thesis is illustrated in Fig. B.1. When the **SN** event occurs, we first calculate the density and metallicity at the **SN** site. An iterative solver is used to find a smoothing length for the stellar particle that satisfies

$$h_{\text{sml},i} = \left(\frac{3N_{\text{ngb}}}{4\pi \sum_j W(r_{ij}, h_{\text{sml},i})} \right)^{1/3}, \quad (\text{B.1})$$

where r_{ij} is the distance from the i -th stellar particle to the j -th gas particle, N_{ngb} is the number of neighboring **SPH** particles, and W is the kernel function adopted in the **SPH** simulation. We then compute the shock radius R_{shock} using local density and metallicity, using equation (2.18). We search for the gas particles within the shock radius and project them from the position of the star onto a sphere centered at the star with radius R_{shock} . Then, we construct a Voronoi polyhedron using STRIPACK¹ (Renka, 1997), which is an algorithm that constructs a Voronoi diagram of a set of points on the surface of a sphere. After constructing the Voronoi polyhedron on the spherical surface, we calculate Ω , which is the solid angle of the corresponding face on the Voronoi polyhedron from the star. We distribute physical quantities from the **SN** to neighboring gas particles weighted

¹https://people.sc.fsu.edu/~jb Burkardt/f_src/stripack/stripack.html

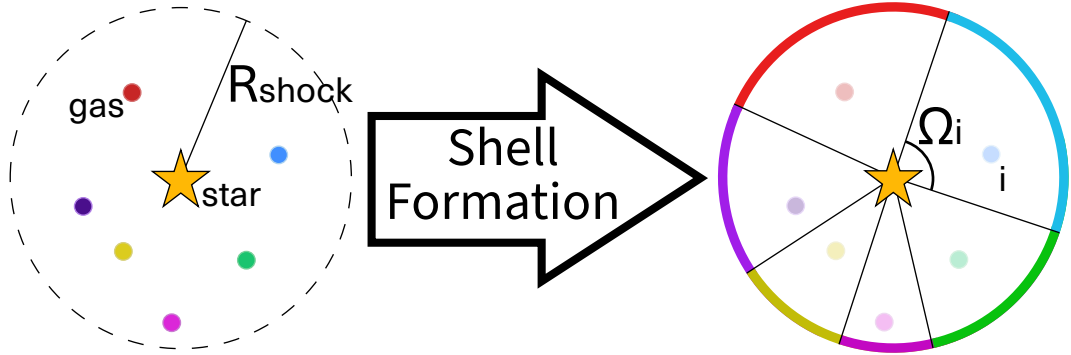


FIGURE B.1: Schematic description of the spherical superbubble feedback model developed in this paper. The left hand side shows the particle distribution of gas and star particles when the supernova explosions begin, whereas the right hand side shows the superbubble shell formation, and how we split the shell using Voronoi tessellation based on the gas particle distribution inside the bubble.

by Ω . The mass and metal deposited on the i -th gas particle are

$$\Delta m_i = m_{\text{SN}} \left(\frac{\Omega_i}{4\pi} \right), \quad (\text{B.2})$$

$$\Delta m_{Z,i} = m_{Z,\text{SN}} \left(\frac{\Omega_i}{4\pi} \right), \quad (\text{B.3})$$

where m_{SN} and $m_{Z,\text{SN}}$ are the mass and metal inputs from feedback and Ω_i is the solid angle of the corresponding face on the Voronoi polyhedron from the star. If the number of gas particles inside the shock radius is less than four, the Voronoi polyhedron cannot be constructed. In that case, we search for at least two nearest gas particles and equally assign mass and metals to them. Note that our method is similar to, but different in detail from, that of [Hopkins et al. \(2018\)](#).

Bibliography

B. Abolfathi, D. S. Aguado, G. Aguilar, C. Allende Prieto, A. Almeida, T. T. Ananna, F. Anders, S. F. Anderson, B. H. Andrews, B. Anguiano, and et al. The Fourteenth Data Release of the Sloan Digital Sky Survey: First Spectroscopic Data from the Extended Baryon Oscillation Spectroscopic Survey and from the Second Phase of the Apache Point Observatory Galactic Evolution Experiment. *ApJS*, 235(2):42, Apr. 2018. doi: 10.3847/1538-4365/aa9e8a.

O. Agertz, B. Moore, J. Stadel, D. Potter, F. Miniati, J. Read, L. Mayer, A. Gawryszczak, A. Kravtsov, Å. Nordlund, F. Pearce, V. Quilis, D. Rudd, V. Springel, J. Stone, E. Tasker, R. Teyssier, J. Wadsley, and R. Walder. Fundamental differences between SPH and grid methods. *MNRAS*, 380(3):963–978, Sept. 2007. doi: 10.1111/j.1365-2966.2007.12183.x.

O. Agertz, A. V. Kravtsov, S. N. Leitner, and N. Y. Gnedin. Toward a Complete Accounting of Energy and Momentum from Stellar Feedback in Galaxy Formation Simulations. *ApJ*, 770(1):25, June 2013. doi: 10.1088/0004-637X/770/1/25.

E. Anders and N. Grevesse. Abundances of the elements: Meteoritic and solar. *Geochim. Cosmochim. Acta*, 53(1):197–214, Jan. 1989. doi: 10.1016/0016-7037(89)90286-X.

B. H. Andrews and P. Martini. The Mass-Metallicity Relation with the Direct Method on Stacked Spectra of SDSS Galaxies. *ApJ*, 765(2):140, Mar. 2013. doi: 10.1088/0004-637X/765/2/140.

R. E. Angulo and A. Pontzen. Cosmological N-body simulations with suppressed variance. *MNRAS*, 462(1):L1–L5, Oct. 2016. doi: 10.1093/mnrasl/slw098.

S. Aoyama, K.-C. Hou, I. Shimizu, H. Hirashita, K. Todoroki, J.-H. Choi, and K. Nagamine. Galaxy simulation with dust formation and destruction. *MNRAS*, 466(1):105–121, Apr. 2017. doi: 10.1093/mnras/stw3061.

S. Arata, H. Yajima, K. Nagamine, M. Abe, and S. Khochfar. Starbursting [O III] emitters and quiescent [C II] emitters in the reionization era. *MNRAS*, 498(4):5541–5556, Nov. 2020. doi: 10.1093/mnras/staa2809.

L. Armillotta, M. R. Krumholz, E. M. Di Teodoro, and N. M. McClure-Griffiths. The life cycle of the Central Molecular Zone - I. Inflow, star formation, and winds. *MNRAS*, 490(3):4401–4418, Dec. 2019. doi: 10.1093/mnras/stz2880.

A. Arth, J. Donnert, U. Steinwandel, L. Böss, T. Halbesma, M. Pütz, D. Hubber, and K. Dolag. WVTICs – SPH initial conditions for everyone. *arXiv e-prints*, art. arXiv:1907.11250, July 2019. doi: 10.48550/arXiv.1907.11250.

M. Asplund, N. Grevesse, A. J. Sauval, and P. Scott. The Chemical Composition of the Sun. *ARA&A*, 47(1):481–522, Sept. 2009. doi: 10.1146/annurev.astro.46.060407.145222.

J. S. Bagla. TreePM: A Code for Cosmological N-Body Simulations. *Journal of Astrophysics and Astronomy*, 23(3-4):185–196, Dec. 2002. doi: 10.1007/BF02702282.

N. A. Bahcall, J. P. Ostriker, S. Perlmutter, and P. J. Steinhardt. The Cosmic Triangle: Revealing the State of the Universe. *Science*, 284:1481, May 1999. doi: 10.1126/science.284.5419.1481.

I. K. Baldry, S. P. Driver, J. Loveday, E. N. Taylor, L. S. Kelvin, J. Liske, P. Norberg, A. S. G. Robotham, S. Brough, A. M. Hopkins, S. P. Bamford, J. A. Peacock, J. Bland-Hawthorn, C. J. Conselice, S. M. Croom, D. H. Jones, H. R. Parkinson, C. C. Popescu, M. Prescott, R. G. Sharp, and R. J. Tuffs. Galaxy And Mass Assembly (GAMA): the galaxy stellar mass function at $z < 0.06$. *MNRAS*, 421(1):621–634, Mar. 2012. doi: 10.1111/j.1365-2966.2012.20340.x.

J. E. Barnes. A modified tree code: Don't laugh; It runs. *Journal of Computational Physics*, 87(1):161–170, Mar. 1990. doi: 10.1016/0021-9991(90)90232-P.

M. Bernardi, A. Meert, R. K. Sheth, V. Vikram, M. Huertas-Company, S. Mei, and F. Shankar. The massive end of the luminosity and stellar mass functions: dependence on the fit to the light profile. *MNRAS*, 436(1):697–704, Nov. 2013. doi: 10.1093/mnras/stt1607.

M. S. Bessell, R. S. Sutherland, and K. Ruan. Oxygen Abundances in Halo Stars. *ApJ*, 383:L71, Dec. 1991. doi: 10.1086/186244.

F. Bigiel, A. Leroy, F. Walter, E. Brinks, W. J. G. de Blok, B. Madore, and M. D. Thornley. The Star Formation Law in Nearby Galaxies on Sub-Kpc Scales. *AJ*, 136(6):2846–2871, Dec. 2008. doi: 10.1088/0004-6256/136/6/2846.

S. Bird, Y. Ni, T. Di Matteo, R. Croft, Y. Feng, and N. Chen. The ASTRID simulation: galaxy formation and reionization. *MNRAS*, 512(3):3703–3716, May 2022. doi: 10.1093/mnras/stac648.

D. Blas, J. Lesgourgues, and T. Tram. The Cosmic Linear Anisotropy Solving System (CLASS). Part II: Approximation schemes. *J. Cosmology Astropart. Phys.*, 2011(7):034, July 2011. doi: 10.1088/1475-7516/2011/07/034.

G. R. Blumenthal, S. M. Faber, J. R. Primack, and M. J. Rees. Formation of galaxies and large-scale structure with cold dark matter. *Nature*, 311:517–525, Oct. 1984. doi: 10.1038/311517a0.

H. Bondi. On spherically symmetrical accretion. *MNRAS*, 112:195, Jan. 1952. doi: 10.1093/mnras/112.2.195.

J. Borrow, M. Schaller, and R. G. Bower. Inconsistencies arising from the coupling of galaxy formation sub-grid models to pressure-smoothed particle hydrodynamics. *MNRAS*, 505(2):2316–2327, Aug. 2021. doi: 10.1093/mnras/stab1423.

J. Borrow, M. Schaller, R. G. Bower, and J. Schaye. SPHENIX: smoothed particle hydrodynamics for the next generation of galaxy formation simulations. *MNRAS*, 511(2):2367–2389, Apr. 2022. doi: 10.1093/mnras/stab3166.

R. Bouwens, G. Illingworth, P. Oesch, M. Stefanon, R. Naidu, I. van Leeuwen, and D. Magee. UV luminosity density results at $z > 8$ from the first JWST/NIRCam fields: limitations of early data sets and the need for spectroscopy. *MNRAS*, 523(1):1009–1035, July 2023. doi: 10.1093/mnras/stad1014.

R. G. Bower, J. Schaye, C. S. Frenk, T. Theuns, M. Schaller, R. A. Crain, and S. McAlpine. The dark nemesis of galaxy formation: why hot haloes trigger black hole growth and bring star formation to an end. *MNRAS*, 465(1):32–44, Feb. 2017. doi: 10.1093/mnras/stw2735.

J. Braspenning, J. Schaye, J. Borrow, and M. Schaller. Sensitivity of non-radiative cloud-wind interactions to the hydrodynamic solver. *MNRAS*, 523(1):1280–1295, July 2023. doi: 10.1093/mnras/stad1243.

J. S. Bullock and M. Boylan-Kolchin. Small-Scale Challenges to the Λ CDM Paradigm. *ARA&A*, 55(1):343–387, Aug. 2017. doi: 10.1146/annurev-astro-091916-055313.

A. Butler Contreras, E. T. Lau, B. D. Oppenheimer, Á. Bogdán, M. Tillman, D. Nagai, O. E. Kovács, and B. Burkhardt. X-ray absorption lines in the warm-hot intergalactic medium: probing Chandra observations with the CAMEL simulations. *MNRAS*, 519(2):2251–2261, Feb. 2023. doi: 10.1093/mnras/stac3631.

R. Cen and J. P. Ostriker. Galaxy Formation and Physical Bias. *ApJ*, 399:L113, Nov. 1992. doi: 10.1086/186620.

R. Cen and J. P. Ostriker. Where Are the Baryons? *ApJ*, 514(1):1–6, Mar. 1999. doi: 10.1086/306949.

S. Chabanier, M. Millea, and N. Palanque-Delabrouille. Matter power spectrum: from Ly α forest to CMB scales. *MNRAS*, 489(2):2247–2253, Oct. 2019. doi: 10.1093/mnras/stz2310.

G. Chabrier. Galactic Stellar and Substellar Initial Mass Function. *PASP*, 115(809):763–795, July 2003. doi: 10.1086/376392.

E. Chaikin, J. Schaye, M. Schaller, A. Benítez-Llambay, F. S. J. Nobels, and S. Ploeckinger. A thermal-kinetic subgrid model for supernova feedback in simulations of galaxy formation. *MNRAS*, 523(3):3709–3731, Aug. 2023. doi: 10.1093/mnras/stad1626.

I. Chemerynska, H. Atek, L. J. Furtak, A. Zitrin, J. E. Greene, P. Dayal, A. Weibel, V. Kokorev, A. D. Goulding, C. C. Williams, T. Nanayakkara, R. Bezanson, G. Brammer, S. E. Cutler, I. Labbe, J. Leja, R. Pan, S. H. Price, B. Wang, J. R. Weaver, and K. E. Whitaker. JWST UNCOVER: The Overabundance of Ultraviolet-luminous Galaxies at $z > 9$. *arXiv e-prints*, art. arXiv:2312.05030, Dec. 2023. doi: 10.48550/arXiv.2312.05030.

S. Chon, H. Ono, K. Omukai, and R. Schneider. Impact of the cosmic background radiation on the initial mass function of metal-poor stars. *MNRAS*, 514(3):4639–4654, Aug. 2022. doi: 10.1093/mnras/stac1549.

M. Cirasuolo, J. Afonso, M. Carollo, H. Flores, R. Maiolino, E. Oliva, S. Paltani, L. Vanzi, C. Evans, M. Abreu, D. Atkinson, C. Babusiaux, S. Beard, F. Bauer, M. Bellazzini, R. Bender, P. Best, N. Bezwada, P. Bonifacio, A. Bragaglia, I. Bryson, D. Busher, A. Cabral, K. Caputi, M. Centrone, F. Chemla, A. Cimatti, M. R. Cioni, G. Clementini, J. Coelho, D. Crnojevic, E. Daddi, J. Dunlop, S. Eales, S. Feltzing, A. Ferguson, M. Fisher, A. Fontana, J. Fynbo, B. Garilli, G. Gilmore, A. Glauer, I. Guinouard, F. Hammer, P. Hastings, A. Hess, R. Ivison, P. Jagourel, M. Jarvis, L. Kaper, G. Kauffmann, A. T. Kitching, A. Lawrence, D. Lee, B. Lemasle, G. Licausi, S. Lilly, D. Lorenzetti, D. Lunney, R. Maiolino, F. Mannucci, R. McLure, D. Minniti, D. Montgomery, B. Muschielok, K. Nandra, R. Navarro, P. Norberg, S. Oliver, L. Origlia, N. Padilla, J. Peacock, F. Pedichini, J. Peng, L. Pentericci, J. Pragt, M. Puech, S. Randich, P. Rees, A. Renzini, N. Ryde, M. Rodrigues, I. Roseboom, F. Royer, R. Saglia, A. Sanchez, R. Schiavon, H. Schnetler, D. Sobral, R. Speziali, D. Sun, R. Stuik, A. Taylor, W. Taylor, S. Todd, E. Tolstoy, M. Torres, M. Tosi, E. Vanzella, L. Venema, F. Vitali, M. Wegner, M. Wells, V. Wild, G. Wright, G. Zamorani, and M. Zuccali. MOONS: the Multi-Object Optical and Near-infrared Spectrograph for the VLT. In S. K. Ramsay, I. S. McLean, and H. Takami, editors, *Ground-based and Airborne Instrumentation for Astronomy V*, volume 9147 of *Society of Photo-Optical Instrumentation Engineers (SPIE) Conference Series*, page 91470N, July 2014. doi: 10.1117/12.2056012.

L. L. Cowie and C. F. McKee. The evaporation of spherical clouds in a hot gas. I. Classical and saturated mass loss rates. *ApJ*, 211:135–146, Jan. 1977. doi: 10.1086/154911.

D. P. Cox. The Terrain of Evolution of Isotropic Adiabatic Supernova Remnants. *ApJ*, 304:771, May 1986. doi: 10.1086/164214.

D. P. Cox and P. R. Anderson. Extended adiabatic blast waves and a model of the soft X-ray background. *ApJ*, 253:268–289, Feb. 1982. doi: 10.1086/159632.

R. A. Crain, J. Schaye, R. G. Bower, M. Furlong, M. Schaller, T. Theuns, C. Dalla Vecchia, C. S. Frenk, I. G. McCarthy, J. C. Helly, A. Jenkins, Y. M. Rosas-Guevara, S. D. M. White, and J. W. Trayford. The EAGLE simulations of galaxy formation: calibration of subgrid physics and model variations. *MNRAS*, 450(2):1937–1961, June 2015. doi: 10.1093/mnras/stv725.

C. Dalla Vecchia and J. Schaye. Simulating galactic outflows with thermal supernova feedback. *MNRAS*, 426(1):140–158, Oct. 2012. doi: 10.1111/j.1365-2966.2012.21704.x.

S. Das, Y.-K. Chiang, and S. Mathur. Detection of Thermal Sunyaev-Zel'dovich Effect in the Circumgalactic Medium of Low-mass Galaxies-A Surprising Pattern in Self-similarity and Baryon Sufficiency. *ApJ*, 951(2):125, July 2023. doi: 10.3847/1538-4357/acd764.

R. Davé, R. Thompson, and P. F. Hopkins. MUFASA: galaxy formation simulations with meshless hydrodynamics. *MNRAS*, 462(3):3265–3284, Nov. 2016. doi: 10.1093/mnras/stw1862.

R. Davé, D. Anglés-Alcázar, D. Narayanan, Q. Li, M. H. Rafieferantsoa, and S. Appleby. SIMBA: Cosmological simulations with black hole growth and feedback. *MNRAS*, 486(2):2827–2849, June 2019. doi: 10.1093/mnras/stz937.

J. J. Davies, R. A. Crain, B. D. Oppenheimer, and J. Schaye. The quenching and morphological evolution of central galaxies is facilitated by the feedback-driven expulsion of circumgalactic gas. *MNRAS*, 491(3):4462–4480, Jan. 2020. doi: 10.1093/mnras/stz3201.

M. Davis, G. Efstathiou, C. S. Frenk, and S. D. M. White. The evolution of large-scale structure in a universe dominated by cold dark matter. *ApJ*, 292:371–394, May 1985. doi: 10.1086/163168.

W. Dehnen and H. Aly. Improving convergence in smoothed particle hydrodynamics simulations without pairing instability. *MNRAS*, 425(2):1068–1082, Sept. 2012. doi: 10.1111/j.1365-2966.2012.21439.x.

A. Dekel and J. Silk. The Origin of Dwarf Galaxies, Cold Dark Matter, and Biased Galaxy Formation. *ApJ*, 303:39, Apr. 1986. doi: 10.1086/164050.

A. Dekel, K. C. Sarkar, Y. Birnboim, N. Mandelker, and Z. Li. Efficient formation of massive galaxies at cosmic dawn by feedback-free starbursts. *MNRAS*, 523(3):3201–3218, Aug. 2023. doi: 10.1093/mnras/stad1557.

C. L. Doherty, P. Gil-Pons, H. H. B. Lau, J. C. Lattanzio, and L. Siess. Super and massive AGB stars - II. Nucleosynthesis and yields - $Z = 0.02, 0.008$ and 0.004 . *MNRAS*, 437(1):195–214, Jan. 2014. doi: 10.1093/mnras/stt1877.

J. M. F. Donnert, A. M. Beck, K. Dolag, and H. J. A. Röttgering. Simulations of the galaxy cluster CIZA J2242.8+5301 - I. Thermal model and shock properties. *MNRAS*, 471(4):4587–4605, Nov. 2017. doi: 10.1093/mnras/stx1819.

B. T. Draine. *Physics of the Interstellar and Intergalactic Medium*. Princeton University Press, 2011.

S. P. Driver, S. Bellstedt, A. S. G. Robotham, I. K. Baldry, L. J. Davies, J. Liske, D. Obreschkow, E. N. Taylor, A. H. Wright, M. Alpaslan, S. P. Bamford, A. E. Bauer, J. Bland-Hawthorn, M. Bilicki, M. Bravo, S. Brough, S. Casura, M. E. Cluver, M. Colless, C. J. Conselice, S. M. Croom, J. de Jong, F. D'Eugenio, R. De Propris, B. Dogruel, M. J. Drinkwater, A. Dvornik, D. J. Farrow, C. S. Frenk, B. Giblin, A. W. Graham, M. W. Grootes, M. L. P. Gunawardhana, A. Hashemizadeh, B. Häufslér, C. Heymans, H. Hildebrandt, B. W. Holwerda, A. M. Hopkins, T. H. Jarrett, D. Heath Jones, L. S. Kelvin, S. Koushan, K. Kuijken, M. A. Lara-López, R. Lange, Á. R. López-Sánchez, J. Loveday, S. Mahajan, M. Meyer, A. J. Moffett, N. R. Napolitano, P. Norberg, M. S. Owers, M. Radovich, M. Raouf, J. A. Peacock, S. Phillipps, K. A. Pimbblet, C. Popescu, K. Said, A. E. Sansom, M. Seibert, W. J. Sutherland, J. E. Thorne, R. J. Tuffs, R. Turner, A. van der Wel, E. van Kampen, and S. M. Wilkins. Galaxy And Mass Assembly (GAMA): Data Release 4 and the $z < 0.1$ total and $z < 0.08$ morphological galaxy stellar mass functions. *MNRAS*, 513(1):439–467, June 2022. doi: 10.1093/mnras/stac472.

F. Durier and C. Dalla Vecchia. Implementation of feedback in smoothed particle hydrodynamics: towards concordance of methods. *MNRAS*, 419(1):465–478, Jan. 2012. doi: 10.1111/j.1365-2966.2011.19712.x.

K. El-Badry, E. C. Ostriker, C.-G. Kim, E. Quataert, and D. R. Weisz. Evolution of supernovae-driven superbubbles with conduction and cooling. *MNRAS*, 490(2):1961–1990, Dec. 2019. doi: 10.1093/mnras/stz2773.

R. Feldmann, E. Quataert, C.-A. Faucher-Giguère, P. F. Hopkins, O. Çatmabacak, D. Kereš, L. Bassini, M. Bernardini, J. S. Bullock, E. Cenci, J. Gensior, L. Liang, J. Moreno, and A. Wetzel. FIREbox: simulating galaxies at high dynamic range in a cosmological volume. *MNRAS*, 522(3):3831–3860, July 2023. doi: 10.1093/mnras/stad1205.

G. J. Ferland, R. L. Porter, P. A. M. van Hoof, R. J. R. Williams, N. P. Abel, M. L. Lykins, G. Shaw, W. J. Henney, and P. C. Stancil. The 2013 Release of Cloudy. *Rev. Mexicana Astron. Astrofis.*, 49:137–163, Apr. 2013. doi: 10.48550/arXiv.1302.4485.

G. Ferrand and A. Marcowith. On the shape of the spectrum of cosmic rays accelerated inside superbubbles. *A&A*, 510:A101, Feb. 2010. doi: 10.1051/0004-6361/200913520.

D. Fielding, E. Quataert, and D. Martizzi. Clustered supernovae drive powerful galactic winds after superbubble breakout. *MNRAS*, 481(3):3325–3347, Dec. 2018. doi: 10.1093/mnras/sty2466.

D. B. Fielding, E. C. Ostriker, G. L. Bryan, and A. S. Jermyn. Multiphase Gas and the Fractal Nature of Radiative Turbulent Mixing Layers. *ApJ*, 894(2):L24, May 2020. doi: 10.3847/2041-8213/ab8d2c.

S. L. Finkelstein, G. C. K. Leung, M. B. Bagley, M. Dickinson, H. C. Ferguson, C. Papovich, H. B. Akins, P. Arrabal Haro, R. Dave, A. Dekel, J. S. Kartaltepe, D. D. Kocevski, A. M. Koekeboer, N. Pirzkal, R. S. Somerville, L. Y. A. Yung, R. Amorin, B. E. Backhaus, P. Behroozi, L. Bisigello, V. Bromm, C. M. Casey, O. A. Chavez Ortiz, Y. Cheng, K. Chwiorowsky, N. J. Cleri, M. C. Cooper, K. Davis, A. de la Vega, D. Elbaz, M. Franco, A. Fontana, S. Fujimoto, M. Giavalisco, N. A. Grogan, B. W. Holwerda, M. Huertas-Company, M. Hirschmann, K. G. Iyer, S. Jogee, I. Jung, R. L. Larson, R. A. Lucas, B. Mobasher, A. M. Morales, C. V. Morley, S. Mukherjee, P. G. Perez-Gonzalez, S. Ravindranath, G. Rodighiero, M. Rowland, S. Tacchella, A. J. Taylor, J. R. Trump, and S. Wilkins. The Complete CEERS Early Universe Galaxy Sample: A Surprisingly Slow Evolution of the Space Density of Bright Galaxies at $z \sim 8.5-14.5$. *arXiv e-prints*, art. arXiv:2311.04279, Nov. 2023. doi: 10.48550/arXiv.2311.04279.

C. S. Frenk, S. D. M. White, P. Bode, J. R. Bond, G. L. Bryan, R. Cen, H. M. P. Couchman, A. E. Evrard, N. Gnedin, A. Jenkins, A. M. Khokhlov, A. Klypin, J. F. Navarro, M. L. Norman, J. P. Ostriker, J. M. Owen, F. R. Pearce, U. L. Pen, M. Steinmetz, P. A. Thomas, J. V. Villumsen, J. W. Wadsley, M. S. Warren, G. Xu, and G. Yepes. The Santa Barbara Cluster Comparison Project: A Comparison of Cosmological Hydrodynamics Solutions. *ApJ*, 525(2):554–582, Nov. 1999. doi: 10.1086/307908.

N. Frontiere, C. D. Raskin, and J. M. Owen. CRKSPH - A Conservative Reproducing Kernel Smoothed Particle Hydrodynamics Scheme. *Journal of Computational Physics*, 332:160–209, Mar. 2017. doi: 10.1016/j.jcp.2016.12.004.

K. Fukushima, K. Nagamine, and I. Shimizu. Star formation and chemical enrichment in protoclusters. *MNRAS*, 525(3):3760–3780, Nov. 2023. doi: 10.1093/mnras/stad2526.

A. Gal-Yam. The Most Luminous Supernovae. *ARA&A*, 57:305–333, Aug. 2019. doi: 10.1146/annurev-astro-081817-051819.

S. Genel, M. Vogelsberger, V. Springel, D. Sijacki, D. Nelson, G. Snyder, V. Rodriguez-Gomez, P. Torrey, and L. Hernquist. Introducing the Illustris project: the evolution of galaxy populations across cosmic time. *MNRAS*, 445(1):175–200, Nov. 2014. doi: 10.1093/mnras/stu1654.

J. Greene, R. Bezanson, M. Ouchi, J. Silverman, and the PFS Galaxy Evolution Working Group. The Prime Focus Spectrograph Galaxy Evolution Survey. *arXiv e-prints*, art. arXiv:2206.14908, June 2022. doi: 10.48550/arXiv.2206.14908.

F. Haardt and P. Madau. Radiative Transfer in a Clumpy Universe. IV. New Synthesis Models of the Cosmic UV/X-Ray Background. *ApJ*, 746(2):125, Feb. 2012. doi: 10.1088/0004-637X/746/2/125.

M. Habouzit, Y. Li, R. S. Somerville, S. Genel, A. Pillepich, M. Volonteri, R. Davé, Y. Rosas-Guevara, S. McAlpine, S. Peirani, L. Hernquist, D. Anglés-Alcázar, A. Reines, R. Bower, Y. Dubois, D. Nelson, C. Pichon, and M. Vogelsberger. Supermassive black holes in cosmological simulations I: M_{BH} - M_* relation and black hole mass function. *MNRAS*, 503(2):1940–1975, May 2021. doi: 10.1093/mnras/stab496.

O. Hahn and T. Abel. Multi-scale initial conditions for cosmological simulations. *MNRAS*, 415(3):2101–2121, Aug. 2011. doi: 10.1111/j.1365-2966.2011.18820.x.

O. Hahn, C. Rampf, and C. Uhlemann. Higher order initial conditions for mixed baryon-CDM simulations. *MNRAS*, 503(1):426–445, May 2021. doi: 10.1093/mnras/staa3773.

N. Hand, Y. Feng, F. Beutler, Y. Li, C. Modi, U. Seljak, and Z. Slepian. nbbodykit: An Open-source, Massively Parallel Toolkit for Large-scale Structure. *AJ*, 156(4):160, Oct. 2018. doi: 10.3847/1538-3881/aadae0.

Y. Harikane, M. Ouchi, M. Oguri, Y. Ono, K. Nakajima, Y. Isobe, H. Ueda, K. Mawatari, and Y. Zhang. A Comprehensive Study of Galaxies at $z \geq 9$ Found in the Early JWST Data: Ultraviolet Luminosity Functions and Cosmic Star Formation History at the Pre-reionization Epoch. *ApJS*, 265(1):5, Mar. 2023. doi: 10.3847/1538-4365/acaaa9.

M. Hirschmann, K. Dolag, A. Saro, L. Bachmann, S. Borgani, and A. Burkert. Cosmological simulations of black hole growth: AGN luminosities and downsizing. *MNRAS*, 442(3):2304–2324, Aug. 2014. doi: 10.1093/mnras/stu1023.

S. Höfner and H. Olofsson. Mass loss of stars on the asymptotic giant branch. Mechanisms, models and measurements. *A&A Rev.*, 26(1):1, Jan. 2018. doi: 10.1007/s00159-017-0106-5.

P. F. Hopkins. A general class of Lagrangian smoothed particle hydrodynamics methods and implications for fluid mixing problems. *MNRAS*, 428(4):2840–2856, Feb. 2013. doi: 10.1093/mnras/sts210.

P. F. Hopkins. A new class of accurate, mesh-free hydrodynamic simulation methods. *MNRAS*, 450(1):53–110, June 2015. doi: 10.1093/mnras/stv195.

P. F. Hopkins, E. Quataert, and N. Murray. Self-regulated star formation in galaxies via momentum input from massive stars. *MNRAS*, 417(2):950–973, Oct. 2011. doi: 10.1111/j.1365-2966.2011.19306.x.

P. F. Hopkins, A. Wetzel, D. Kereš, C.-A. Faucher-Giguère, E. Quataert, M. Boylan-Kolchin, N. Murray, C. C. Hayward, and K. El-Badry. How to model supernovae in simulations of star and galaxy formation. *MNRAS*, 477(2):1578–1603, June 2018. doi: 10.1093/mnras/sty674.

P. F. Hopkins, M. Y. Grudic, K.-Y. Su, S. Wellons, D. Angles-Alcazar, U. P. Steinwandel, D. Guszejnov, N. Murray, C.-A. Faucher-Giguere, E. Quataert, and D. Keres. FORGE'd in FIRE: Resolving the End of Star Formation and Structure of AGN Accretion Disks from Cosmological Initial Conditions. *arXiv e-prints*, art. arXiv:2309.13115, Sept. 2023a. doi: 10.48550/arXiv.2309.13115.

P. F. Hopkins, A. Wetzel, C. Wheeler, R. Sanderson, M. Y. Grudić, O. Sameie, M. Boylan-Kolchin, M. Orr, X. Ma, C.-A. Faucher-Giguère, D. Kereš, E. Quataert, K.-Y. Su, J. Moreno, R. Feldmann, J. S. Bullock, S. R. Loebman, D. Anglés-Alcázar, J. Stern, L. Necib, C. R. Choban, and C. C. Hayward. FIRE-3: updated stellar evolution models, yields, and micro-physics and fitting functions for applications in galaxy simulations. *MNRAS*, 519(2):3154–3181, Feb. 2023b. doi: 10.1093/mnras/stac3489.

N. Hosono, T. R. Saitoh, and J. Makino. A Comparison of SPH Artificial Viscosities and Their Impact on the Keplerian Disk. *ApJS*, 224(2):32, June 2016. doi: 10.3847/0067-0049/224/2/32.

C.-Y. Hu. Supernova-driven winds in simulated dwarf galaxies. *MNRAS*, 483(3):3363–3381, Mar. 2019. doi: 10.1093/mnras/sty3252.

C.-Y. Hu, T. Naab, S. Walch, B. P. Moster, and L. Oser. SPHGal: smoothed particle hydrodynamics with improved accuracy for galaxy simulations. *MNRAS*, 443(2):1173–1191, Sept. 2014. doi: 10.1093/mnras/stu1187.

L. Hui and N. Y. Gnedin. Equation of state of the photoionized intergalactic medium. *MNRAS*, 292(1):27–42, Nov. 1997. doi: 10.1093/mnras/292.1.27.

J. Japelj, C. Laigle, M. Puech, C. Pichon, H. Rahmani, Y. Dubois, J. E. G. Devriendt, P. Petitjean, F. Hammer, E. Gendron, L. Kaper, S. Morris, N. Pirzkal, R. Sánchez-Janssen, A. Slyz, S. D. Vergani, and Y. Yang. Simulating MOS science on the ELT: Ly α forest tomography. *A&A*, 632:A94, Dec. 2019. doi: 10.1051/0004-6361/201936048.

S. Jin, S. C. Trager, G. B. Dalton, J. A. L. Aguerri, J. E. Drew, J. Falcón-Barroso, B. T. Gänsicke, V. Hill, A. Iovino, M. M. Pieri, and et al. The wide-field, multiplexed, spectroscopic facility WEAVE: Survey design, overview, and simulated implementation. *MNRAS*, Mar. 2023. doi: 10.1093/mnras/stad557.

A. I. Karakas. Updated stellar yields from asymptotic giant branch models. *MNRAS*, 403(3):1413–1425, Apr. 2010. doi: 10.1111/j.1365-2966.2009.16198.x.

A. Karim, E. Schinnerer, A. Martínez-Sansigre, M. T. Sargent, A. van der Wel, H. W. Rix, O. Ilbert, V. Smolčić, C. Carilli, M. Pannella, A. M. Koekemoer, E. F. Bell, and M. Salvato. The Star Formation History of Mass-selected Galaxies in the COSMOS Field. *ApJ*, 730(2):61, Apr. 2011. doi: 10.1088/0004-637X/730/2/61.

N. Katz. Dissipational Galaxy Formation. II. Effects of Star Formation. *ApJ*, 391:502, June 1992. doi: 10.1086/171366.

N. Katz, D. H. Weinberg, and L. Hernquist. Cosmological Simulations with TreeSPH. *ApJS*, 105:19, July 1996. doi: 10.1086/192305.

S. Kaviraj, C. Laigle, T. Kimm, J. E. G. Devriendt, Y. Dubois, C. Pichon, A. Slyz, E. Chisari, and S. Peirani. The Horizon-AGN simulation: evolution of galaxy properties over cosmic time. *MNRAS*, 467(4):4739–4752, June 2017. doi: 10.1093/mnras/stx126.

B. W. Keller and J. M. D. Kruijssen. Uncertainties in supernova input rates drive qualitative differences in simulations of galaxy evolution. *MNRAS*, 512(1):199–215, May 2022. doi: 10.1093/mnras/stac511.

B. W. Keller, J. Wadsley, and H. M. P. Couchman. Cosmological galaxy evolution with superbubble feedback - I. Realistic galaxies with moderate feedback. *MNRAS*, 453(4):3499–3509, Nov. 2015. doi: 10.1093/mnras/stv1789.

B. W. Keller, J. Wadsley, and H. M. P. Couchman. Cosmological galaxy evolution with superbubble feedback - II. The limits of supernovae. *MNRAS*, 463(2):1431–1445, Dec. 2016. doi: 10.1093/mnras/stw2029.

B. W. Keller, J. M. D. Kruijssen, and J. W. Wadsley. Entropy-driven winds: Outflows and fountains lifted gently by buoyancy. *MNRAS*, 493(2):2149–2170, Apr. 2020. doi: 10.1093/mnras/staa380.

N. Khandai, T. Di Matteo, R. Croft, S. Wilkins, Y. Feng, E. Tucker, C. DeGraf, and M.-S. Liu. The MassiveBlack-II simulation: the evolution of haloes and galaxies to $z \sim 0$. *MNRAS*, 450(2):1349–1374, June 2015. doi: 10.1093/mnras/stv627.

C.-G. Kim and E. C. Ostriker. Momentum Injection by Supernovae in the Interstellar Medium. *ApJ*, 802(2):99, Apr. 2015. doi: 10.1088/0004-637X/802/2/99.

C.-G. Kim and E. C. Ostriker. Three-phase Interstellar Medium in Galaxies Resolving Evolution with Star Formation and Supernova Feedback (TIGRESS): Algorithms, Fiducial Model, and Convergence. *ApJ*, 846(2):133, Sept. 2017. doi: 10.3847/1538-4357/aa8599.

C.-G. Kim and E. C. Ostriker. Numerical Simulations of Multiphase Winds and Fountains from Star-forming Galactic Disks. I. Solar Neighborhood TIGRESS Model. *ApJ*, 853(2):173, Feb. 2018. doi: 10.3847/1538-4357/aaa5ff.

C.-G. Kim, E. C. Ostriker, and R. Raileanu. Superbubbles in the Multiphase ISM and the Loading of Galactic Winds. *ApJ*, 834(1):25, Jan. 2017. doi: 10.3847/1538-4357/834/1/25.

C.-G. Kim, E. C. Ostriker, D. B. Fielding, M. C. Smith, G. L. Bryan, R. S. Somerville, J. C. Forbes, S. Genel, and L. Hernquist. A Framework for Multiphase Galactic Wind Launching Using TIGRESS. *ApJ*, 903(2):L34, Nov. 2020a. doi: 10.3847/2041-8213/abc252.

C.-G. Kim, E. C. Ostriker, R. S. Somerville, G. L. Bryan, D. B. Fielding, J. C. Forbes, C. C. Hayward, L. Hernquist, and V. Pandya. First Results from SMAUG: Characterization of Multiphase Galactic Outflows from a Suite of Local Star-forming Galactic Disk Simulations. *ApJ*, 900(1):61, Sept. 2020b. doi: 10.3847/1538-4357/aba962.

J.-h. Kim, T. Abel, O. Agertz, G. L. Bryan, D. Ceverino, C. Christensen, C. Conroy, A. Dekel, N. Y. Gnedin, N. J. Goldbaum, J. Guedes, O. Hahn, A. Hobbs, P. F. Hopkins, C. B. Hummels, F. Iannuzzi, D. Keres, A. Klypin, A. V. Kravtsov, M. R. Krumholz, M. Kuhlen, S. N. Leitner, P. Madau, L. Mayer, C. E. Moody, K. Nagamine, M. L. Norman, J. Onorbe, B. W. O'Shea, A. Pillepich, J. R. Primack, T. Quinn, J. I. Read, B. E. Robertson, M. Rocha, D. H. Rudd, S. Shen, B. D. Smith, A. S. Szalay, R. Teyssier, R. Thompson, K. Todoroki, M. J. Turk, J. W. Wadsley, J. H. Wise, A. Zolotov, and t. AGORA Collaboration29. The AGORA High-resolution Galaxy Simulations Comparison Project. *ApJS*, 210(1):14, Jan. 2014. doi: 10.1088/0067-0049/210/1/14.

J.-h. Kim, O. Agertz, R. Teyssier, M. J. Butler, D. Ceverino, J.-H. Choi, R. Feldmann, B. W. Keller, A. Lupi, T. Quinn, Y. Revaz, S. Wallace, N. Y. Gnedin, S. N. Leitner, S. Shen, B. D. Smith, R. Thompson, M. J. Turk, T. Abel, K. S. Arraki, S. M. Benincasa, S. Chakrabarti, C. DeGraf, A. Dekel, N. J. Goldbaum, P. F. Hopkins, C. B. Hummels, A. Klypin, H. Li, P. Madau, N. Mandelker, L. Mayer, K. Nagamine, S. Nickerson, B. W. O'Shea, J. R. Primack, S. Roca-Fàbrega, V. Semenov, I. Shimizu, C. M. Simpson, K. Todoroki, J. W. Wadsley, J. H. Wise, and AGORA Collaboration. The AGORA High-resolution Galaxy Simulations Comparison Project. II. Isolated Disk Test. *ApJ*, 833(2):202, Dec. 2016. doi: 10.3847/1538-4357/833/2/202.

T. Kimm and R. Cen. Escape Fraction of Ionizing Photons during Reionization: Effects due to Supernova Feedback and Runaway OB Stars. *ApJ*, 788(2):121, June 2014. doi: 10.1088/0004-637X/788/2/121.

C. Kobayashi, H. Umeda, K. Nomoto, N. Tominaga, and T. Ohkubo. Galactic Chemical Evolution: Carbon through Zinc. *ApJ*, 653(2):1145–1171, Dec. 2006. doi: 10.1086/508914.

A. Kolmogorov. The Local Structure of Turbulence in Incompressible Viscous Fluid for Very Large Reynolds' Numbers. *Akademii Nauk SSSR Doklady*, 30:301–305, Jan. 1941.

O. E. Kovács, Á. Bogdán, R. K. Smith, R. P. Kraft, and W. R. Forman. Detection of the Missing Baryons toward the Sightline of H1821+643. *ApJ*, 872(1):83, Feb. 2019. doi: 10.3847/1538-4357/aaef78.

H. Koyama and S.-i. Inutsuka. An Origin of Supersonic Motions in Interstellar Clouds. *ApJ*, 564(2):L97–L100, Jan. 2002. doi: 10.1086/338978.

M. R. Krumholz, C. F. McKee, and J. Bland-Hawthorn. Star Clusters Across Cosmic Time. *ARA&A*, 57:227–303, Aug. 2019. doi: 10.1146/annurev-astro-091918-104430.

L. Lancaster, E. C. Ostriker, J.-G. Kim, and C.-G. Kim. Efficiently Cooled Stellar Wind Bubbles in Turbulent Clouds. I. Fractal Theory and Application to Star-forming Clouds. *ApJ*, 914(2):89, June 2021a. doi: 10.3847/1538-4357/abf8ab.

L. Lancaster, E. C. Ostriker, J.-G. Kim, and C.-G. Kim. Efficiently Cooled Stellar Wind Bubbles in Turbulent Clouds. II. Validation of Theory with Hydrodynamic Simulations. *ApJ*, 914(2):90, June 2021b. doi: 10.3847/1538-4357/abf8ac.

R. B. Larson. Turbulence and star formation in molecular clouds. *MNRAS*, 194:809–826, Mar. 1981. doi: 10.1093/mnras/194.4.809.

K.-G. Lee, J. F. Hennawi, C. Stark, J. X. Prochaska, M. White, D. J. Schlegel, A.-C. Eilers, A. Arinyo-i-Prats, N. Suzuki, R. A. C. Croft, K. I. Caputi, P. Cassata, O. Ilbert, B. Garilli, A. M. Koekemoer, V. Le Brun, O. Le Fèvre, D. Maccagni, P. Nugent, Y. Taniguchi, L. A. M. Tasca, L. Tresse, G. Zamorani, and E. Zucca. Ly α Forest Tomography from Background Galaxies: The First Megaparsec-resolution Large-scale Structure Map at $z > 2$. *ApJ*, 795(1):L12, Nov. 2014. doi: 10.1088/2041-8205/795/1/L12.

K.-G. Lee, A. Krolewski, M. White, D. Schlegel, P. E. Nugent, J. F. Hennawi, T. Müller, R. Pan, J. X. Prochaska, A. Font-Ribera, N. Suzuki, K. Glazebrook, G. G. Kacprzak, J. S. Kartaltepe, A. M. Koekemoer, O. Le Fèvre, B. C. Lemaux, C. Maier, T. Nanayakkara, R. M. Rich, D. B. Sanders, M. Salvato, L. Tasca, and K.-V. H. Tran. First Data Release of the COSMOS Ly α Mapping and Tomography Observations: 3D Ly α Forest Tomography at $2.05 < z < 2.55$. *ApJS*, 237(2):31, Aug. 2018. doi: 10.3847/1538-4365/aace58.

C. Leitherer, D. Schaerer, J. D. Goldader, R. M. G. Delgado, C. Robert, D. F. Kune, D. F. de Mello, D. Devost, and T. M. Heckman. Starburst99: Synthesis Models for Galaxies with Active Star Formation. *ApJS*, 123(1):3–40, July 1999. doi: 10.1086/313233.

C. Leitherer, P. A. Ortiz Otálvaro, F. Bresolin, R.-P. Kudritzki, B. Lo Faro, A. W. A. Pauldrach, M. Pettini, and S. A. Rix. A Library of Theoretical Ultraviolet Spectra of Massive, Hot Stars for Evolutionary Synthesis. *ApJS*, 189(2):309–335, Aug. 2010. doi: 10.1088/0067-0049/189/2/309.

C. Leitherer, S. Ekström, G. Meynet, D. Schaerer, K. B. Agienko, and E. M. Levesque. The Effects of Stellar Rotation. II. A Comprehensive Set of Starburst99 Models. *ApJS*, 212(1):14, May 2014. doi: 10.1088/0067-0049/212/1/14.

M. Li and G. L. Bryan. Simple Yet Powerful: Hot Galactic Outflows Driven by Supernovae. *ApJ*, 890(2):L30, Feb. 2020. doi: 10.3847/2041-8213/ab7304.

M. Li, G. L. Bryan, and J. P. Ostriker. Quantifying Supernovae-driven Multiphase Galactic Outflows. *ApJ*, 841(2):101, June 2017. doi: 10.3847/1538-4357/aa7263.

P. Madau and M. Dickinson. Cosmic Star-Formation History. *ARA&A*, 52:415–486, Aug. 2014. doi: 10.1146/annurev-astro-081811-125615.

R. Maiolino, M. Haehnelt, M. T. Murphy, D. Queloz, L. Origlia, J. Alcalá, Y. Alibert, P. J. Amado, C. Allende Prieto, M. Ammler-von Eiff, M. Asplund, M. Barstow, G. Becker, X. Bonfils, F. Bouchy, A. Bragaglia, M. R. Burleigh, A. Chiavassa, D. A. Cimatti, M. Cirasuolo, S. Cristiani, V. D’Odorico, D. Dravins, E. Emsellem, J. Farihi, P. Figueira, J. Fynbo, B. T. Gansicke, M. Gillon, B. Gustafsson, V. Hill, G. Israelyan, A. Korn, S. Larsen, P. De Laverny, J. Liske, C. Lovis, A. Marconi, C. Martins, P. Molero, B. Nisini, E. Oliva, P. Petitjean, M. Pettini, A. Recio Blanco, R. Rebolo, A. Reiners, C. Rodriguez-Lopez, N. Ryde, N. C. Santos, S. Savaglio, I. Snellen, K. Strassmeier, N. Tanvir, L. Testi, E. Tolstoy, A. Triaud, L. Vanzi, M. Viel, and M. Volonteri. A Community Science Case for E-ELT HIRES. *arXiv e-prints*, art. arXiv:1310.3163, Oct. 2013. doi: 10.48550/arXiv.1310.3163.

D. Maoz and F. Mannucci. Type-Ia Supernova Rates and the Progenitor Problem: A Review. *PASA*, 29(4):447–465, Jan. 2012. doi: 10.1071/AS11052.

F. Marinacci, L. V. Sales, M. Vogelsberger, P. Torrey, and V. Springel. Simulating the interstellar medium and stellar feedback on a moving mesh: implementation and isolated galaxies. *MNRAS*, 489(3):4233–4260, Nov. 2019. doi: 10.1093/mnras/stz2391.

N. J. McConnell and C.-P. Ma. Revisiting the Scaling Relations of Black Hole Masses and Host Galaxy Properties. *ApJ*, 764(2):184, Feb. 2013. doi: 10.1088/0004-637X/764/2/184.

D. J. McLeod, R. J. McLure, J. S. Dunlop, F. Cullen, A. C. Carnall, and K. Duncan. The evolution of the galaxy stellar-mass function over the last 12 billion years from a combination of ground-based and HST surveys. *MNRAS*, 503(3):4413–4435, May 2021. doi: 10.1093/mnras/stab731.

M. McQuinn. The Evolution of the Intergalactic Medium. *ARA&A*, 54:313–362, Sept. 2016. doi: 10.1146/annurev-astro-082214-122355.

M. Michaux, O. Hahn, C. Rampf, and R. E. Angulo. Accurate initial conditions for cosmological N-body simulations: minimizing truncation and discreteness errors. *MNRAS*, 500(1):663–683, Jan. 2021. doi: 10.1093/mnras/staa3149.

T. J. Moriya, E. I. Sorokina, and R. A. Chevalier. Superluminous Supernovae. *Space Sci. Rev.*, 214(2):59, Mar. 2018. doi: 10.1007/s11214-018-0493-6.

J. P. Morris. A study of the stability properties of smooth particle hydrodynamics. *PASA*, 13(1):97–102, Jan. 1996.

T. Naab and J. P. Ostriker. Theoretical Challenges in Galaxy Formation. *ARA&A*, 55(1):59–109, Aug. 2017. doi: 10.1146/annurev-astro-081913-040019.

K. Nagamine, M. Fukugita, R. Cen, and J. P. Ostriker. Star Formation History and Stellar Metallicity Distribution in a Cold Dark Matter Universe. *ApJ*, 558(2):497–504, Sept. 2001. doi: 10.1086/322293.

K. Nagamine, I. Shimizu, K. Fujita, N. Suzuki, K.-G. Lee, R. Momose, S. Mukae, Y. Liang, N. Kashikawa, M. Ouchi, and J. D. Silverman. Probing Feedback via IGM tomography and the Ly α Forest with Subaru PFS, TMT/ELT, and JWST. *ApJ*, 914(1):66, June 2021. doi: 10.3847/1538-4357/abfa16.

S. Nakashima, Y. Inoue, N. Yamasaki, Y. Sofue, J. Kataoka, and K. Sakai. Spatial Distribution of the Milky Way Hot Gaseous Halo Constrained by Suzaku X-Ray Observations. *ApJ*, 862(1):34, July 2018. doi: 10.3847/1538-4357/aacceb.

A. B. Newman, G. C. Rudie, G. A. Blanc, D. D. Kelson, S. Rhoades, T. Hare, V. Pérez, A. J. Benson, A. Dressler, V. Gonzalez, J. A. Kollmeier, N. P. Konidaris, J. S. Mulchaey, M. Rauch, O. Le Fèvre, B. C. Lemaux, O. Cucciati, and S. J. Lilly. LATIS: The Ly α Tomography IMACS Survey. *ApJ*, 891(2):147, Mar. 2020. doi: 10.3847/1538-4357/ab75ee.

Y. Ni, T. Di Matteo, S. Bird, R. Croft, Y. Feng, N. Chen, M. Tremmel, C. DeGraf, and Y. Li. The ASTRID simulation: the evolution of supermassive black holes. *MNRAS*, 513(1):670–692, June 2022. doi: 10.1093/mnras/stac351.

Y. Ni, S. Genel, D. Anglés-Alcázar, F. Villaescusa-Navarro, Y. Jo, S. Bird, T. Di Matteo, R. Croft, N. Chen, N. S. M. de Santi, M. Gebhardt, H. Shao, S. Pandey, L. Hernquist, and R. Dave. The CAMELS Project: Expanding the Galaxy Formation Model Space with New ASTRID and 28-parameter TNG and SIMBA Suites. *ApJ*, 959(2):136, Dec. 2023. doi: 10.3847/1538-4357/ad022a.

K. Nomoto, C. Kobayashi, and N. Tominaga. Nucleosynthesis in Stars and the Chemical Enrichment of Galaxies. *ARA&A*, 51(1):457–509, Aug. 2013. doi: 10.1146/annurev-astro-082812-140956.

L. Ohlin, F. Renaud, and O. Agertz. Supernovae feedback propagation: the role of turbulence. *MNRAS*, 485(3):3887–3894, May 2019. doi: 10.1093/mnras/stz705.

Y. Oku and K. Nagamine. Osaka Feedback Model III: Cosmological Simulation CROCODYLE. *arXiv e-prints*, art. arXiv:2401.06324, Jan. 2024. doi: 10.48550/arXiv.2401.06324.

Y. Oku, K. Tomida, K. Nagamine, I. Shimizu, and R. Cen. Osaka Feedback Model. II. Modeling Supernova Feedback Based on High-resolution Simulations. *ApJS*, 262(1):9, Sept. 2022. doi: 10.3847/1538-4365/ac77ff.

M. E. Orr, D. B. Fielding, C. C. Hayward, and B. Burkhardt. Bursting Bubbles: Clustered Supernova Feedback in Local and High-redshift Galaxies. *ApJ*, 924(2):L28, Jan. 2022a. doi: 10.3847/2041-8213/ac479f.

M. E. Orr, D. B. Fielding, C. C. Hayward, and B. Burkhardt. Bursting Bubbles: Feedback from Clustered Supernovae and the Trade-off Between Turbulence and Outflows. *ApJ*, 932(2):88, June 2022b. doi: 10.3847/1538-4357/ac6c26.

E. C. Ostriker and C.-G. Kim. Pressure-regulated, Feedback-modulated Star Formation in Disk Galaxies. *ApJ*, 936(2):137, Sept. 2022. doi: 10.3847/1538-4357/ac7de2.

J. P. Ostriker and C. F. McKee. Astrophysical blastwaves. *Reviews of Modern Physics*, 60(1): 1–68, Jan. 1988. doi: 10.1103/RevModPhys.60.1.

J. P. Ostriker and P. J. Steinhardt. The observational case for a low-density Universe with a non-zero cosmological constant. *Nature*, 377(6550):600–602, Oct. 1995. doi: 10.1038/377600a0.

R. Pakmor, V. Springel, J. P. Coles, T. Guillet, C. Pfrommer, S. Bose, M. Barrera, A. M. Delgado, F. Ferlito, C. Frenk, B. Hadzhiyska, C. Hernández-Aguayo, L. Hernquist, R. Kannan, and S. D. M. White. The MillenniumTNG Project: the hydrodynamical full physics simulation and a first look at its galaxy clusters. *MNRAS*, 524(2):2539–2555, Sept. 2023. doi: 10.1093/mnras/stac3620.

E. N. Parker. *Interplanetary dynamical processes*. Interscience Publishers, 1963.

S. Perlmutter, G. Aldering, M. della Valle, S. Deustua, R. S. Ellis, S. Fabbro, A. Fruchter, G. Goldhaber, D. E. Groom, I. M. Hook, A. G. Kim, M. Y. Kim, R. A. Knop, C. Lidman, R. G. McMahon, P. Nugent, R. Pain, N. Panagia, C. R. Pennypacker, P. Ruiz-Lapuente, B. Schaefer, and N. Walton. Discovery of a supernova explosion at half the age of the Universe. *Nature*, 391(6662):51–54, Jan. 1998. doi: 10.1038/34124.

A. Pillepich, D. Nelson, L. Hernquist, V. Springel, R. Pakmor, P. Torrey, R. Weinberger, S. Genel, J. P. Naiman, F. Marinacci, and M. Vogelsberger. First results from the IllustrisTNG simulations: the stellar mass content of groups and clusters of galaxies. *MNRAS*, 475(1):648–675, Mar. 2018a. doi: 10.1093/mnras/stx3112.

A. Pillepich, V. Springel, D. Nelson, S. Genel, J. Naiman, R. Pakmor, L. Hernquist, P. Torrey, M. Vogelsberger, R. Weinberger, and F. Marinacci. Simulating galaxy formation with the IllustrisTNG model. *MNRAS*, 473(3):4077–4106, Jan. 2018b. doi: 10.1093/mnras/stx2656.

Planck Collaboration, P. A. R. Ade, N. Aghanim, M. Arnaud, M. Ashdown, J. Aumont, C. Baccigalupi, A. J. Banday, R. B. Barreiro, J. G. Bartlett, and et al. Planck 2015 results. XIII. Cosmological parameters. *A&A*, 594:A13, Sept. 2016. doi: 10.1051/0004-6361/201525830.

Planck Collaboration, N. Aghanim, Y. Akrami, M. Ashdown, J. Aumont, C. Baccigalupi, M. Ballardini, A. J. Banday, R. B. Barreiro, N. Bartolo, S. Basak, R. Battye, K. Benabed, J. P. Bernard, M. Bersanelli, P. Bielewicz, J. J. Bock, J. R. Bond, J. Borrill, F. R. Bouchet, F. Boulanger, M. Bucher, C. Burigana, R. C. Butler, E. Calabrese, J. F. Cardoso, J. Carron, A. Challinor, H. C. Chiang, J. Chluba, L. P. L. Colombo, C. Combet, D. Contreras, B. P. Crill, F. Cuttaia, P. de Bernardis, G. de Zotti, J. Delabrouille, J. M. Delouis, E. Di Valentino, J. M. Diego, O. Doré, M. Douspis, A. Ducout, X. Dupac, S. Dusini, G. Efstathiou,

F. Elsner, T. A. Enßlin, H. K. Eriksen, Y. Fantaye, M. Farhang, J. Fergusson, R. Fernandez-Cobos, F. Finelli, F. Forastieri, M. Frailis, A. A. Fraisse, E. Franceschi, A. Frolov, S. Galeotta, S. Galli, K. Ganga, R. T. Génova-Santos, M. Gerbino, T. Ghosh, J. González-Nuevo, K. M. Górski, S. Gratton, A. Gruppuso, J. E. Gudmundsson, J. Hamann, W. Handley, F. K. Hansen, D. Herranz, S. R. Hildebrandt, E. Hivon, Z. Huang, A. H. Jaffe, W. C. Jones, A. Karakci, E. Keihänen, R. Keskitalo, K. Kiiveri, J. Kim, T. S. Kisner, L. Knox, N. Krachmalnicoff, M. Kunz, H. Kurki-Suonio, G. Lagache, J. M. Lamarre, A. Lasenby, M. Lattanzi, C. R. Lawrence, M. Le Jeune, P. Lemos, J. Lesgourgues, F. Levrier, A. Lewis, M. Liguori, P. B. Lilje, M. Lilley, V. Lindholm, M. López-Caniego, P. M. Lubin, Y. Z. Ma, J. F. Macías-Pérez, G. Maggio, D. Maino, N. Mandolesi, A. Mangilli, A. Marcos-Caballero, M. Maris, P. G. Martin, M. Martinelli, E. Martínez-González, S. Matarrese, N. Mauri, J. D. McEwen, P. R. Meinholt, A. Melchiorri, A. Mennella, M. Migliaccio, M. Millea, S. Mitra, M. A. Miville-Deschénes, D. Molinari, L. Montier, G. Morgante, A. Moss, P. Natoli, H. U. Nørgaard-Nielsen, L. Pagano, D. Paoletti, B. Partridge, G. Patanchon, H. V. Peiris, F. Perrotta, V. Pettorino, F. Piacentini, L. Polastri, G. Polenta, J. L. Puget, J. P. Rachen, M. Reinecke, M. Remazeilles, A. Renzi, G. Rocha, C. Rosset, G. Roudier, J. A. Rubiño-Martín, B. Ruiz-Granados, L. Salvati, M. Sandri, M. Savelainen, D. Scott, E. P. S. Shellard, C. Sirignano, G. Sirri, L. D. Spencer, R. Sunyaev, A. S. Suur-Uski, J. A. Tauber, D. Tavagnacco, M. Tenti, L. Toffolatti, M. Tomasi, T. Trombetti, L. Valenziano, J. Valiviita, B. Van Tent, L. Vibert, P. Vielva, F. Villa, N. Vittorio, B. D. Wandelt, I. K. Wehus, M. White, S. D. M. White, A. Zacchei, and A. Zonca. Planck 2018 results. VI. Cosmological parameters. *A&A*, 641:A6, Sept. 2020. doi: 10.1051/0004-6361/201833910.

S. F. Portegies Zwart, S. L. W. McMillan, and M. Gieles. Young Massive Star Clusters. *ARA&A*, 48:431–493, Sept. 2010. doi: 10.1146/annurev-astro-081309-130834.

L. Portinari, C. Chiosi, and A. Bressan. Galactic chemical enrichment with new metallicity dependent stellar yields. *A&A*, 334:505–539, June 1998.

D. J. Price. Modelling discontinuities and Kelvin Helmholtz instabilities in SPH. *Journal of Computational Physics*, 227(24):10040–10057, Dec. 2008. doi: 10.1016/j.jcp.2008.08.011.

D. J. Price. Smoothed particle hydrodynamics and magnetohydrodynamics. *Journal of Computational Physics*, 231(3):759–794, Feb. 2012. doi: 10.1016/j.jcp.2010.12.011.

D. J. Price and G. Laibe. A solution to the overdamping problem when simulating dust-gas mixtures with smoothed particle hydrodynamics. *MNRAS*, 495(4):3929–3934, July 2020. doi: 10.1093/mnras/staa1366.

T.-E. Rathjen, T. Naab, P. Girichidis, S. Walch, R. Wünsch, F. Dinnbier, D. Seifried, R. S. Klessen, and S. C. O. Glover. SILCC VI - Multiphase ISM structure, stellar clustering, and outflows with supernovae, stellar winds, ionizing radiation, and cosmic rays. *MNRAS*, 504(1):1039–1061, June 2021. doi: 10.1093/mnras/stab900.

B. A. Reid, W. J. Percival, D. J. Eisenstein, L. Verde, D. N. Spergel, R. A. Skibba, N. A. Bahcall, T. Budavari, J. A. Frieman, M. Fukugita, J. R. Gott, J. E. Gunn, Ž. Ivezić, G. R. Knapp, R. G. Kron, R. H. Lupton, T. A. McKay, A. Meiksin, R. C. Nichol, A. C. Pope, D. J. Schlegel, D. P. Schneider, C. Stoughton, M. A. Strauss, A. S. Szalay, M. Tegmark, M. S. Vogeley, D. H. Weinberg, D. G. York, and I. Zehavi. Cosmological constraints from the clustering of the Sloan Digital Sky Survey DR7 luminous red galaxies. *MNRAS*, 404(1):60–85, May 2010. doi: 10.1111/j.1365-2966.2010.16276.x.

R. J. Renka. Algorithm 772: Stripack: Delaunay triangulation and voronoi diagram on the surface of a sphere. *ACM Transactions on Mathematical Software (TOMS)*, 23(3):416–434, 1997.

S. Roca-Fàbrega, J.-H. Kim, L. Hausammann, K. Nagamine, A. Lupi, J. W. Powell, I. Shimizu, D. Ceverino, J. R. Primack, T. R. Quinn, Y. Revaz, H. Velázquez, T. Abel, M. Buehlmann, A. Dekel, B. Dong, O. Hahn, C. Hummels, K.-W. Kim, B. D. Smith, C. Strawn, R. Teyssier,

M. J. Turk, and AGORA Collaboration. The AGORA High-resolution Galaxy Simulations Comparison Project. III. Cosmological Zoom-in Simulation of a Milky Way-mass Halo. *ApJ*, 917(2):64, Aug. 2021. doi: 10.3847/1538-4357/ac088a.

L. E. C. Romano, K. Nagamine, and H. Hirashita. Dust diffusion in SPH simulations of an isolated galaxy. *MNRAS*, 514(1):1441–1460, July 2022a. doi: 10.1093/mnras/stac1385.

L. E. C. Romano, K. Nagamine, and H. Hirashita. The co-evolution of molecular hydrogen and the grain size distribution in an isolated galaxy. *MNRAS*, 514(1):1461–1476, July 2022b. doi: 10.1093/mnras/stac1386.

Y. M. Rosas-Guevara, R. G. Bower, J. Schaye, M. Furlong, C. S. Frenk, C. M. Booth, R. A. Crain, C. Dalla Vecchia, M. Schaller, and T. Theuns. The impact of angular momentum on black hole accretion rates in simulations of galaxy formation. *MNRAS*, 454(1):1038–1057, Nov. 2015. doi: 10.1093/mnras/stv2056.

S. Rosswog. Astrophysical smooth particle hydrodynamics. *New A Rev.*, 53(4-6):78–104, Apr. 2009. doi: 10.1016/j.newar.2009.08.007.

S. Rosswog. The Lagrangian hydrodynamics code MAGMA2. *MNRAS*, 498(3):4230–4255, Nov. 2020. doi: 10.1093/mnras/staa2591.

T. R. Saitoh. Chemical Evolution Library for Galaxy Formation Simulation. *AJ*, 153(2):85, Feb. 2017. doi: 10.3847/1538-3881/153/2/85.

T. R. Saitoh and J. Makino. A Necessary Condition for Individual Time Steps in SPH Simulations. *ApJ*, 697(2):L99–L102, June 2009. doi: 10.1088/0004-637X/697/2/L99.

T. R. Saitoh and J. Makino. A Density-independent Formulation of Smoothed Particle Hydrodynamics. *ApJ*, 768(1):44, May 2013. doi: 10.1088/0004-637X/768/1/44.

D. Salak, N. Nakai, Y. Miyamoto, A. Yamauchi, and T. G. Tsuru. Large-Field CO($J = 1 \rightarrow 0$) Observations of the Starburst Galaxy M 82. *PASJ*, 65:66, June 2013. doi: 10.1093/pasj/65.3.66.

B. Salmon, C. Papovich, S. L. Finkelstein, V. Tilvi, K. Finlator, P. Behroozi, T. Dahlen, R. Davé, A. Dekel, M. Dickinson, H. C. Ferguson, M. Giavalisco, J. Long, Y. Lu, B. Mobasher, N. Reddy, R. S. Somerville, and R. H. Wechsler. The Relation between Star Formation Rate and Stellar Mass for Galaxies at $3.5 \leq z \leq 6.5$ in CANDELS. *ApJ*, 799(2):183, Feb. 2015. doi: 10.1088/0004-637X/799/2/183.

R. L. Sanders, A. E. Shapley, T. Jones, N. A. Reddy, M. Kriek, B. Siana, A. L. Coil, B. Mobasher, I. Shivaei, R. Davé, M. Azadi, S. H. Price, G. Leung, W. R. Freeman, T. Fetherolf, L. de Groot, T. Zick, and G. Barro. The MOSDEF Survey: The Evolution of the Mass-Metallicity Relation from $z = 0$ to $z = 3.3$. *ApJ*, 914(1):19, June 2021. doi: 10.3847/1538-4357/abf4c1.

J. Schaye, A. Aguirre, T.-S. Kim, T. Theuns, M. Rauch, and W. L. W. Sargent. Metallicity of the Intergalactic Medium Using Pixel Statistics. II. The Distribution of Metals as Traced by C IV. *ApJ*, 596(2):768–796, Oct. 2003. doi: 10.1086/378044.

J. Schaye, R. A. Crain, R. G. Bower, M. Furlong, M. Schaller, T. Theuns, C. Dalla Vecchia, C. S. Frenk, I. G. McCarthy, J. C. Helly, A. Jenkins, Y. M. Rosas-Guevara, S. D. M. White, M. Baes, C. M. Booth, P. Camps, J. F. Navarro, Y. Qu, A. Rahmati, T. Sawala, P. A. Thomas, and J. Trayford. The EAGLE project: simulating the evolution and assembly of galaxies and their environments. *MNRAS*, 446(1):521–554, Jan. 2015. doi: 10.1093/mnras/stu2058.

J. Schaye, R. Kugel, M. Schaller, J. C. Helly, J. Braspennning, W. Elbers, I. G. McCarthy, M. P. van Daalen, B. Vandenbroucke, C. S. Frenk, J. Kwan, J. Salcido, Y. M. Bahé, J. Borrow, E. Chaikin, O. Hahn, F. Huško, A. Jenkins, C. G. Lacey, and F. S. J. Nobels. The FLAMINGO project: cosmological hydrodynamical simulations for large-scale structure and galaxy cluster surveys. *MNRAS*, 526(4):4978–5020, Dec. 2023. doi: 10.1093/mnras/stad2419.

M. Schmidt. The Rate of Star Formation. *ApJ*, 129:243, Mar. 1959. doi: 10.1086/146614.

I. J. Schoenberg. Contributions to the problem of approximation of equidistant data by analytic functions. part b. on the problem of osculatory interpolation. a second class of analytic approximation formulae. *Quarterly of Applied Mathematics*, 4(2):112–141, 1946.

A. Schruba, A. K. Leroy, F. Walter, F. Bigiel, E. Brinks, W. J. G. de Blok, G. Dumas, C. Kramer, E. Rosolowsky, K. Sandstrom, K. Schuster, A. Usero, A. Weiss, and H. Wiesemeyer. A Molecular Star Formation Law in the Atomic-gas-dominated Regime in Nearby Galaxies. *AJ*, 142(2):37, Aug. 2011. doi: 10.1088/0004-6256/142/2/37.

I. R. Seitzenzahl, F. Ciaraldi-Schoolmann, F. K. Röpke, M. Fink, W. Hillebrandt, M. Kromer, R. Pakmor, A. J. Ruiter, S. A. Sim, and S. Taubenberger. Three-dimensional delayed-detonation models with nucleosynthesis for Type Ia supernovae. *MNRAS*, 429(2):1156–1172, Feb. 2013. doi: 10.1093/mnras/sts402.

F. Sembolini, G. Yepes, F. R. Pearce, A. Knebe, S. T. Kay, C. Power, W. Cui, A. M. Beck, S. Borgani, C. Dalla Vecchia, R. Davé, P. J. Elahi, S. February, S. Huang, A. Hobbs, N. Katz, E. Lau, I. G. McCarthy, G. Murante, D. Nagai, K. Nelson, R. D. A. Newton, V. Perret, E. Puchwein, J. I. Read, A. Saro, J. Schaye, R. Teyssier, and R. J. Thacker. nIFTy galaxy cluster simulations - I. Dark matter and non-radiative models. *MNRAS*, 457(4):4063–4080, Apr. 2016. doi: 10.1093/mnras/stw250.

S. Shen, J. Wadsley, and G. Stinson. The enrichment of the intergalactic medium with adiabatic feedback - I. Metal cooling and metal diffusion. *MNRAS*, 407(3):1581–1596, Sept. 2010. doi: 10.1111/j.1365-2966.2010.17047.x.

R. K. Sheth, H. J. Mo, and G. Tormen. Ellipsoidal collapse and an improved model for the number and spatial distribution of dark matter haloes. *MNRAS*, 323(1):1–12, May 2001. doi: 10.1046/j.1365-8711.2001.04006.x.

I. Shimizu, K. Todoroki, H. Yajima, and K. Nagamine. Osaka feedback model: isolated disc galaxy simulations. *MNRAS*, 484(2):2632–2655, Apr. 2019. doi: 10.1093/mnras/stz098.

I. Shimizu, Y. Oku, K. Nagamine, K. Todoroki, and H. Yajima. Erratum: Osaka feedback model: isolated disc galaxy simulations. *MNRAS*, 494(1):598–599, Apr. 2020. doi: 10.1093/mnras/staa772.

E.-J. Shin, J.-H. Kim, and B. K. Oh. How Metals Are Transported Into and Out of a Galactic Disk: Dependence on Hydrodynamic Schemes in Numerical Simulations. *ApJ*, 917(1):12, Aug. 2021. doi: 10.3847/1538-4357/abffd0.

P. L. Shopbell and J. Bland-Hawthorn. The Asymmetric Wind in M82. *ApJ*, 493(1):129–153, Jan. 1998. doi: 10.1086/305108.

J. Smagorinsky. General circulation experiments with the primitive equations: I. the basic experiment. *Monthly Weather Review*, 91(3):99 – 164, 1963. doi: [https://doi.org/10.1175/1520-0493\(1963\)091<0099:GCEWTP>2.3.CO;2](https://doi.org/10.1175/1520-0493(1963)091<0099:GCEWTP>2.3.CO;2). URL https://journals.ametsoc.org/view/journals/mwre/91/3/1520-0493_1963_091_0099_gcewtp_2_3_co_2.xml.

B. D. Smith, G. L. Bryan, S. C. O. Glover, N. J. Goldbaum, M. J. Turk, J. Regan, J. H. Wise, H.-Y. Schive, T. Abel, A. Emerick, B. W. O’Shea, P. Anninos, C. B. Hummels, and S. Khochfar. GRACKLE: a chemistry and cooling library for astrophysics. *MNRAS*, 466(2):2217–2234, Apr. 2017. doi: 10.1093/mnras/stw3291.

R. S. Somerville and R. Davé. Physical Models of Galaxy Formation in a Cosmological Framework. *ARA&A*, 53:51–113, Aug. 2015. doi: 10.1146/annurev-astro-082812-140951.

M. Song, S. L. Finkelstein, M. L. N. Ashby, A. Grazian, Y. Lu, C. Papovich, B. Salmon, R. S. Somerville, M. Dickinson, K. Duncan, S. M. Faber, G. G. Fazio, H. C. Ferguson, A. Fontana, Y. Guo, N. Hathi, S.-K. Lee, E. Merlin, and S. P. Willner. The Evolution of the Galaxy Stellar Mass Function at $z = 4.8$: A Steepening Low-mass-end Slope with Increasing Redshift. *ApJ*, 825(1):5, July 2016. doi: 10.3847/0004-637X/825/1/5.

L. Spitzer. *Physics of Fully Ionized Gases*. Interscience Publishers, 1962.

V. Springel. The cosmological simulation code GADGET-2. *MNRAS*, 364(4):1105–1134, Dec. 2005. doi: 10.1111/j.1365-2966.2005.09655.x.

V. Springel. Smoothed Particle Hydrodynamics in Astrophysics. *ARA&A*, 48:391–430, Sept. 2010a. doi: 10.1146/annurev-astro-081309-130914.

V. Springel. E pur si muove: Galilean-invariant cosmological hydrodynamical simulations on a moving mesh. *MNRAS*, 401(2):791–851, Jan. 2010b. doi: 10.1111/j.1365-2966.2009.15715.x.

V. Springel and L. Hernquist. Cosmological smoothed particle hydrodynamics simulations: a hybrid multiphase model for star formation. *MNRAS*, 339(2):289–311, Feb. 2003. doi: 10.1046/j.1365-8711.2003.06206.x.

V. Springel, S. D. M. White, G. Tormen, and G. Kauffmann. Populating a cluster of galaxies - I. Results at $z=0$. *MNRAS*, 328(3):726–750, Dec. 2001. doi: 10.1046/j.1365-8711.2001.04912.x.

V. Springel, T. Di Matteo, and L. Hernquist. Modelling feedback from stars and black holes in galaxy mergers. *MNRAS*, 361(3):776–794, Aug. 2005. doi: 10.1111/j.1365-2966.2005.09238.x.

V. Springel, R. Pakmor, O. Zier, and M. Reinecke. Simulating cosmic structure formation with the GADGET-4 code. *MNRAS*, 506(2):2871–2949, Sept. 2021. doi: 10.1093/mnras/stab1855.

M. Stefanon, R. J. Bouwens, I. Labb  , A. Muzzin, D. Marchesini, P. Oesch, and V. Gonzalez. The Rest-frame Optical (900 nm) Galaxy Luminosity Function at $z \sim 4.7$: Abundance Matching Points to Limited Evolution in the M_{STAR}/M_{HALO} Ratio at $z \geq 4$. *ApJ*, 843(1):36, July 2017. doi: 10.3847/1538-4357/aa72d8.

M. Stefanon, R. J. Bouwens, I. Labb  , G. D. Illingworth, V. Gonzalez, and P. A. Oesch. Galaxy Stellar Mass Functions from $z = 10$ to $z = 6$ using the Deepest Spitzer/Infrared Array Camera Data: No Significant Evolution in the Stellar-to-halo Mass Ratio of Galaxies in the First Gigayear of Cosmic Time. *ApJ*, 922(1):29, Nov. 2021. doi: 10.3847/1538-4357/ac1bb6.

G. Stinson, A. Seth, N. Katz, J. Wadsley, F. Governato, and T. Quinn. Star formation and feedback in smoothed particle hydrodynamic simulations - I. Isolated galaxies. *MNRAS*, 373(3):1074–1090, Dec. 2006. doi: 10.1111/j.1365-2966.2006.11097.x.

J. M. Stone, T. A. Gardiner, P. Teuben, J. F. Hawley, and J. B. Simon. Athena: A New Code for Astrophysical MHD. *ApJS*, 178(1):137–177, Sept. 2008. doi: 10.1086/588755.

J. M. Stone, K. Tomida, C. J. White, and K. G. Felker. The Athena++ Adaptive Mesh Refinement Framework: Design and Magnetohydrodynamic Solvers. *ApJS*, 249(1):4, July 2020. doi: 10.3847/1538-4365/ab929b.

C. Strawn, S. Roca-F  brega, J. R. Primack, J. hoon Kim, A. Genina, L. Hausammann, H. Kim, A. Lupi, K. Nagamine, J. W. Powell, Y. Revaz, I. Shimizu, H. Vel  zquez, T. Abel, D. Ceverino, B. Dong, M. Jung, T. R. Quinn, E. jin Shin, K. S. S. Barrow, A. Dekel, B. K. Oh, N. Mandelker, R. Teyssier, C. Hummels, S. Maji, A. Man, P. Mayerhofer, and the AGORA Collaboration. The agora high-resolution galaxy simulations comparison project. vi. similarities and differences in the circumgalactic medium. *ApJ*, 962(1):29, feb 2024. doi: 10.3847/1538-4357/ad12cb. URL <https://dx.doi.org/10.3847/1538-4357/ad12cb>.

D. K. Strickland and T. M. Heckman. Supernova Feedback Efficiency and Mass Loading in the Starburst and Galactic Superwind Exemplar M82. *ApJ*, 697(2):2030–2056, June 2009. doi: 10.1088/0004-637X/697/2/2030.

A. L. Strom, G. C. Rudie, C. C. Steidel, and R. F. Trainor. Chemical Abundance Scaling Relations for Multiple Elements in $z \simeq 2\text{-}3$ Star-forming Galaxies. *ApJ*, 925(2):116, Feb. 2022. doi: 10.3847/1538-4357/ac38a3.

K.-Y. Su, P. F. Hopkins, C. C. Hayward, X. Ma, C.-A. Faucher-Giguère, D. Kereš, M. E. Orr, T. K. Chan, and V. H. Robles. The failure of stellar feedback, magnetic fields, conduction, and morphological quenching in maintaining red galaxies. *MNRAS*, 487(3):4393–4408, Aug. 2019. doi: 10.1093/mnras/stz1494.

R. S. Sutherland and M. A. Dopita. Cooling Functions for Low-Density Astrophysical Plasmas. *ApJS*, 88:253, Sept. 1993. doi: 10.1086/191823.

The MSE Science Team, C. Babusiaux, M. Bergemann, A. Burgasser, S. Ellison, D. Haggard, D. Huber, M. Kaplinghat, T. Li, J. Marshall, and et al. The Detailed Science Case for the Maunakea Spectroscopic Explorer, 2019 edition. *arXiv e-prints*, art. arXiv:1904.04907, Apr. 2019. doi: 10.48550/arXiv.1904.04907.

A. R. Tomczak, R. F. Quadri, K.-V. H. Tran, I. Labbé, C. M. S. Straatman, C. Papovich, K. Glazebrook, R. Allen, G. B. Brammer, M. Cowley, M. Dickinson, D. Elbaz, H. Inami, G. G. Kacprzak, G. E. Morrison, T. Nanayakkara, S. E. Persson, G. A. Rees, B. Salmon, C. Schreiber, L. R. Spitler, and K. E. Whitaker. The SFR-M* Relation and Empirical Star-Formation Histories from ZFOURGE* at $0.5 < z < 4$. *ApJ*, 817(2):118, Feb. 2016. doi: 10.3847/0004-637X/817/2/118.

T. Totani, T. Morokuma, T. Oda, M. Doi, and N. Yasuda. Delay Time Distribution Measurement of Type Ia Supernovae by the Subaru/XMM-Newton Deep Survey and Implications for the Progenitor. *PASJ*, 60:1327, Dec. 2008. doi: 10.1093/pasj/60.6.1327.

M. Tremmel, M. Karcher, F. Governato, M. Volonteri, T. R. Quinn, A. Pontzen, L. Anderson, and J. Bellovary. The Romulus cosmological simulations: a physical approach to the formation, dynamics and accretion models of SMBHs. *MNRAS*, 470(1):1121–1139, Sept. 2017. doi: 10.1093/mnras/stx1160.

C. A. Tremonti, T. M. Heckman, G. Kauffmann, J. Brinchmann, S. Charlot, S. D. M. White, M. Seibert, E. W. Peng, D. J. Schlegel, A. Uomoto, M. Fukugita, and J. Brinkmann. The Origin of the Mass-Metallicity Relation: Insights from 53,000 Star-forming Galaxies in the Sloan Digital Sky Survey. *ApJ*, 613(2):898–913, Oct. 2004. doi: 10.1086/423264.

M. A. Troxel, N. MacCrann, J. Zuntz, T. F. Eifler, E. Krause, S. Dodelson, D. Gruen, J. Blazek, O. Friedrich, S. Samuroff, J. Prat, L. F. Secco, C. Davis, A. Ferté, J. DeRose, A. Alarcon, A. Amara, E. Baxter, M. R. Becker, G. M. Bernstein, S. L. Bridle, R. Cawthon, C. Chang, A. Choi, J. De Vicente, A. Drlica-Wagner, J. Elvin-Poole, J. Frieman, M. Gatti, W. G. Hartley, K. Honscheid, B. Hoyle, E. M. Huff, D. Huterer, B. Jain, M. Jarvis, T. Kacprzak, D. Kirk, N. Kokron, C. Krawiec, O. Lahav, A. R. Liddle, J. Peacock, M. M. Rau, A. Refregier, R. P. Rollins, E. Rozo, E. S. Rykoff, C. Sánchez, I. Sevilla-Noarbe, E. Sheldon, A. Stebbins, T. N. Varga, P. Vielzeuf, M. Wang, R. H. Wechsler, B. Yanny, T. M. C. Abbott, F. B. Abdalla, S. Allam, J. Annis, K. Bechtol, A. Benoit-Lévy, E. Bertin, D. Brooks, E. Buckley-Geer, D. L. Burke, A. Carnero Rosell, M. Carrasco Kind, J. Carretero, F. J. Castander, M. Crocce, C. E. Cunha, C. B. D’Andrea, L. N. da Costa, D. L. DePoy, S. Desai, H. T. Diehl, J. P. Dietrich, P. Doel, E. Fernandez, B. Flaugher, P. Fosalba, J. García-Bellido, E. Gaztanaga, D. W. Gerdes, T. Giannantonio, D. A. Goldstein, R. A. Gruendl, J. Gschwend, G. Gutierrez, D. J. James, T. Jeltema, M. W. G. Johnson, M. D. Johnson, S. Kent, K. Kuehn, S. Kuhlmann, N. Kuropatkin, T. S. Li, M. Lima, H. Lin, M. A. G. Maia, M. March, J. L. Marshall, P. Martini, P. Melchior, F. Menanteau, R. Miquel, J. J. Mohr, E. Neilsen, R. C. Nichol, B. Nord, D. Petravick, A. A. Plazas, A. K. Romer, A. Roodman, M. Sako, E. Sanchez, V. Scarpine, R. Schindler, M. Schubnell, M. Smith, R. C. Smith, M. Soares-Santos, F. Sobreira, E. Suchyta, M. E. C. Swanson, G. Tarle, D. Thomas, D. L. Tucker, V. Vikram, A. R. Walker, J. Weller, Y. Zhang, and DES Collaboration. Dark Energy Survey Year 1 results: Cosmological constraints from cosmic shear. *Phys. Rev. D*, 98(4):043528, Aug. 2018. doi: 10.1103/PhysRevD.98.043528.

J. K. Truelove, R. I. Klein, C. F. McKee, I. Holliman, John H., L. H. Howell, and J. A. Greenough. The Jeans Condition: A New Constraint on Spatial Resolution in Simulations of Isothermal Self-gravitational Hydrodynamics. *ApJ*, 489(2):L179–L183, Nov. 1997. doi: 10.1086/310975.

G. A. Vázquez and C. Leitherer. Optimization of Starburst99 for Intermediate-Age and Old Stellar Populations. *ApJ*, 621(2):695–717, Mar. 2005. doi: 10.1086/427866.

E. Vázquez-Semadeni, G. C. Gómez, A. K. Jappsen, J. Ballesteros-Paredes, R. F. González, and R. S. Klessen. Molecular Cloud Evolution. II. From Cloud Formation to the Early Stages of Star Formation in Decaying Conditions. *ApJ*, 657(2):870–883, Mar. 2007. doi: 10.1086/510771.

F. Villaescusa-Navarro, S. Genel, D. Anglés-Alcázar, L. A. Pérez, P. Villanueva-Domingo, D. Wadekar, H. Shao, F. G. Mohammad, S. Hassan, E. Moser, E. T. Lau, L. F. Machado Poletti Valle, A. Nicola, L. Thiele, Y. Jo, O. H. E. Philcox, B. D. Oppenheimer, M. Tillman, C. Hahn, N. Kaushal, A. Pisani, M. Gebhardt, A. M. Delgado, J. Caliendo, C. Kreisch, K. W. K. Wong, W. R. Coulton, M. Eickenberg, G. Parimbelli, Y. Ni, U. P. Steinwandel, V. La Torre, R. Dave, N. Battaglia, D. Nagai, D. N. Spergel, L. Hernquist, B. Burkhardt, D. Narayanan, B. Wandelt, R. S. Somerville, G. L. Bryan, M. Viel, Y. Li, V. Irsic, K. Kraljic, F. Marinacci, and M. Vogelsberger. The CAMELS Project: Public Data Release. *ApJS*, 265(2):54, Apr. 2023. doi: 10.3847/1538-4365/acbf47.

M. Vogelsberger, F. Marinacci, P. Torrey, and E. Puchwein. Cosmological simulations of galaxy formation. *Nature Reviews Physics*, 2(1):42–66, Jan. 2020. doi: 10.1038/s42254-019-0127-2.

J. W. Wadsley, G. Veeravalli, and H. M. P. Couchman. On the treatment of entropy mixing in numerical cosmology. *MNRAS*, 387(1):427–438, June 2008. doi: 10.1111/j.1365-2966.2008.13260.x.

R. Weaver, R. McCray, J. Castor, P. Shapiro, and R. Moore. Interstellar bubbles. II. Structure and evolution. *ApJ*, 218:377–395, Dec. 1977. doi: 10.1086/155692.

R. Weinberger, V. Springel, L. Hernquist, A. Pillepich, F. Marinacci, R. Pakmor, D. Nelson, S. Genel, M. Vogelsberger, J. Naiman, and P. Torrey. Simulating galaxy formation with black hole driven thermal and kinetic feedback. *MNRAS*, 465(3):3291–3308, Mar. 2017. doi: 10.1093/mnras/stw2944.

H. Wendland. Piecewise polynomial, positive definite and compactly supported radial functions of minimal degree. *Advances in Computational Mathematics*, 4:389–396, 1995.

J. C. Wheeler, C. Sneden, and J. Truran, James W. Abundance ratios as a function of metallicity. *ARA&A*, 27:279–349, Jan. 1989. doi: 10.1146/annurev.aa.27.090189.001431.

K. E. Whitaker, P. G. van Dokkum, G. Brammer, and M. Franx. The Star Formation Mass Sequence Out to $z = 2.5$. *ApJ*, 754(2):L29, Aug. 2012. doi: 10.1088/2041-8205/754/2/L29.

A. H. Wright, A. S. G. Robotham, S. P. Driver, M. Alpaslan, S. K. Andrews, I. K. Baldry, J. Bland-Hawthorn, S. Brough, M. J. I. Brown, M. Colless, E. da Cunha, L. J. M. Davies, A. W. Graham, B. W. Holwerda, A. M. Hopkins, P. R. Kafle, L. S. Kelvin, J. Loveday, S. J. Maddox, M. J. Meyer, A. J. Moffett, P. Norberg, S. Phillipps, K. Rowlands, E. N. Taylor, L. Wang, and S. M. Wilkins. Galaxy And Mass Assembly (GAMA): the galaxy stellar mass function to $z = 0.1$ from the r-band selected equatorial regions. *MNRAS*, 470(1):283–302, Sept. 2017. doi: 10.1093/mnras/stx1149.

G. Xu. A New Parallel N-Body Gravity Solver: TPM. *ApJS*, 98:355, May 1995. doi: 10.1086/192166.

L. Y. A. Yung, R. S. Somerville, S. L. Finkelstein, S. M. Wilkins, and J. P. Gardner. Are the ultra-high-redshift galaxies at $z > 10$ surprising in the context of standard galaxy formation models? *MNRAS*, 527(3):5929–5948, Jan. 2024. doi: 10.1093/mnras/stad3484.